THÈSE

Pour obtenir le grade de

DOCTEUR DE L'UNIVERSITÉ GRENOBLE ALPES

École doctorale : I-MEP² - Ingénierie - Matériaux, Mécanique, Environnement, Energétique, Procédés, Production
Spécialité : 2MGE - Matériaux, Mécanique, Génie civil, Electrochimie
Unité de recherche : Laboratoire d'Electrochimie et de Physico-Chimie des Matériaux et des Interfaces.

Compréhension des limitations cinétiques de l'électrode de graphite : des propriétés du matériau à la microstructure de l'électrode

Understanding Kinetic Limitations in the Graphite Electrode: From Material Properties to Electrode Microstructure

Présentée par :

Corentin RENAIS

Direction de thèse :

Claire VILLEVIEILLE DIRECTRICE DE RECHERCHE, CNRS	Directrice de thèse
Fannie ALLOIN DIRECTRICE DE RECHERCHE, CNRS DELEGATION ALPES	Co-encadrante de thèse
Céline BARCHASZ INGENIEURE HDR, VERKOR	Co-encadrante de thèse

Rapporteurs :

Claire HEROLD
DIRECTRICE DE RECHERCHE, CNRS délégation Centre-Est
Karim ZAGHIB
FULL PROFESSOR, Concordia University

Thèse soutenue publiquement le **6 novembre 2025**, devant le jury composé de :

Yann BULTEL, PROFESSEUR DES UNIVERSITES, Grenoble INP - UGA	Président
Claire VILLEVIEILLE, DIRECTRICE DE RECHERCHE, CNRS délégation Alpes	Directrice de thèse
Claire HEROLD, DIRECTRICE DE RECHERCHE, CNRS délégation Centre-Est	Rapporteure
Marie-Liesse DOUBLET, DIRECTRICE DE RECHERCHE, CNRS délégation Occitanie Est	Examinatrice
Hubert GIRAULT, PROFESSEUR EMERITE, Ecole polytechnique fédérale de Lausanne	Examinateur

Invités :

Anthony Bonnet
DOCTEUR EN SCIENCES, ARKEMA
Fannie ALLOIN
DIRECTRICE DE RECHERCHE, CNRS Alpes

ACKNOWLEDGMENTS

A doctoral thesis is a profoundly enriching journey, both intellectually and socially. It is a transformative life experience, blending deep personal commitment with encounters with individuals who are passionate about their craft. Three years of doctoral research are demanding and challenging, yet they are also intensely emotional and invigorating on a daily basis. These years will remain etched in my memory as a personal achievement in the pursuit of knowledge and scientific enrichment, marking the most beautiful beginning to a career in both fundamental and applied research.

This thesis would not have come to fruition without the passion and dedication of my research supervisor, Claire Villevieille, whose pronounced appetite for challenging and unconventional research projects serves the battery research community so well. Of course, a doctoral thesis is never undertaken alone, and the commitment of my co-supervisor, Fannie Alloin, has undoubtedly contributed to the scientific and human successes of this endeavour. I am deeply grateful to these two researchers, who have imparted to me their love for both fundamental and applied research, and who have provided the keys to a doctoral experience that has been as enjoyable as it has been rewarding.

A thesis is, of course, also about significant human connections, involving colleagues whose bonds deepen with each passing day in the unique environment of a French research laboratory. For many, these bonds have blossomed into friendship: Benjamin, Maxime, Arno, Enzo, Marie, Emma, Sergio, Ove, Oskar, Hippolyte, Xavier, Pierre, and Patrice. It is also about shared projects with a certain BMG, a seasoned post-doctoral researcher, whom history will remember as the co-inventor of the revolutionary LBS support in the world of batteries.

Scientifically, I have had the privilege of conducting numerous experiments at the ESRF and ILL, the synchrotron and neutron sources of Grenoble. These experiments, sometimes conducted through the night, were all the more enriching thanks to the dedicated beamline scientists of ID31 and ID16b, Marta and Victor. I extend my sincere thanks to these scientists, whose contributions have undoubtedly enhanced the story of this thesis.

A thesis is also a cross-generational adventure, marked by encounters with sometimes eminent researchers who have much to impart. I am deeply grateful to Hubert Girault, who introduced me to the fundamental aspects of electrochemistry and instilled in me an appreciation for scientific semantics; our exchanges have always been profoundly enriching.

To anyone embarking on a doctoral journey, I wish the same fulfilment and joy that I have experienced during this adventure. This deep personal investment - sometimes emotionally demanding - has the merit of yielding learning, achievements, and satisfactions that are all the more intense. It is an adventure truly worth living.

TABLE OF CONTENTS

Table of Contents ..... *iii*

Abbreviations ..... *v*

Introduction *1*

Chapter I *7*

1 Energy and power densities, the challenges 9

2 How to optimise power densities in LiBs? 12

3 Fundamental background in intercalation compounds 24

4 The exception of graphite 29

5 Perspectives for the thesis 55

Chapter II *57*

1 Graphite electrode elaboration 59

2 Electrochemical tests 61

3 Electrode morphology characterisations 68

4 Operando characterisations 70

5 Mechanical characterisations 79

6 ^{6}Li-isotope 81

Chapter III *85*

1 Electrochemical characterisation of thin graphite electrodes 87

2 Structural characterisation of thin electrodes 97

3 Conclusion – Chapter 3 122

Chapter IV *125*

1 Context 127

2 Electrochemical characterisation 127

3 Morphological characterisation 136

4 Structural characterisation 140

5 Conclusion – Chapter 4 155

Chapter V *157*

1 State of the art 159

2 Graphite electrode dilatometry 161

3 NMC | graphite commercial cell ultrasound study 168

4 Conclusion – Chapter 5 180

Chapter VI 181

1 Context 183

2 State of the art 184

3 Investigation of the lithium isotope effect 191

4 Conclusion – Chapter VI 197

Conclusion 199

Appendices I

1 Chapter III I

2 Chapter IV IV

3 Chapter V VII

4 Chapter VI IX

References XI

Abstract XXIX

Résumé XXX

ABBREVIATIONS

AAD	Absolute Average Deviation
ARPLS	Asymmetrically Reweighted Penalized Least Squares Smoothing
BET	Brunauer, Emmett, Teller
BMS	Battery Management System
CBD	Carbon Binder Domain
CE	Counter Electrode
CMC	Carboxymethyl Cellulose
CMOS	Complementary Metal Oxide Semiconductor
DCA	Differential Capacity Analysis
DFPT	Density Functional Perturbation Theory
DFT	Density Functional Theory
DMC	Dimethyl Carbonate
DMSO	Dimethyl Sulfoxide
EC	Ethylene Carbonate
EDLC	Electric Double Layer Capacitor
EDS	Energy Dispersive Spectroscopy
EHT	Electron High Tension
EIS	Electrochemical Impedance Spectroscopy
ESS	Energy Storage System
FEA	Finite Element Analysis
FEC	Fluoroethylene Carbonate
FIB	Focused Ion Beam
FWHM	Full Width at Half Maximum
GITT	Galvanostatic Intermittent Titration Technique
HC	Hard Carbon
ICL	Irreversible Capacity Loss
ICP	Induced Coupled Plasma
IPCC	Intergovernmental Panel on Climate Change
IUPAC	International Union of Pure and Applied Chemistry

LCO	Lithium Cobalt Oxide
LFP	Lithium Iron Phosphate
LiB	Lithium Ion Battery
LMO	Lithium Manganese Oxide
LNMO	Lithium Nickel Manganese Oxide
LSO	Lutetium Oxyorthosilicate
LTO	Lithium Tin Oxide
NAAD	Normalised Absolute Average Deviation
NCA	Nickel Cobalt Aluminium
NDP	Neutron Depth Profiling
NMC	Nickel Manganese Cobalt
NMP	N-methyl-2-pyrrolidone
NMR	Nuclear Magnetic Resonance
OCV	Open Circuit Voltage
PFA	Perfluoroalcoxy
PITT	Potential Intermittent Titration Technique
PTFE	Polytetrafluoroethylene
PVDF	Polyvinylidene Fluoride
SAXS	Small-Angle X-ray Scattering
SBR	Styrene-Butadiene Rubber
SEI	Solid Electrolyte Interphase
SEM	Scanning Electron Microscope
SIMS	Secondary Ion Mass Spectroscopy
SNIP	Statistics-sensitive Non-linear Iterative Peak-clipping
TEM	Transmission Electron Microscope
TLM	Transmission Line Model
TRL	Technology Readiness Level
WAXS	Wide-Angle X-ray Scattering
XPS	X-ray Photoelectron Spectroscopy
XRD	X-ray Diffraction
ZPE	Zero-Point Energy

INTRODUCTION

June 26, 1800.

Alessandro Volta addresses to the Royal Society of London a thesis describing the first electrochemical cell[1]. In this paper (excerpt of the title page in **Figure 1a**), the Milanese author describes an autonomous generator capable of delivering a continuous current. At that time, the new invention contrasts with the Leyden jar (capacitor ancestor) only able to discharge discontinuously. Briefly, the cell consists in the assembly of zinc discs, copper discs and fabrics soaked by salt water (**Figure 1b**). It involves the consumption of zinc discs by oxidation into Zn^{2+} ions in solution, whereas water is reduced into H_2 at the copper surface. Volta insisted on the necessity of using salty water to create a current; since the voltmeter did not exist, Volta only had his finger dipped in the salty solution to gauge the current through the felt discharge. Physically, the thesis highlighted for the first time a difference of potential emerging from the contact of two metals with different work functions, and it resulted later to the creation of the *volt* unit in 1881[2].

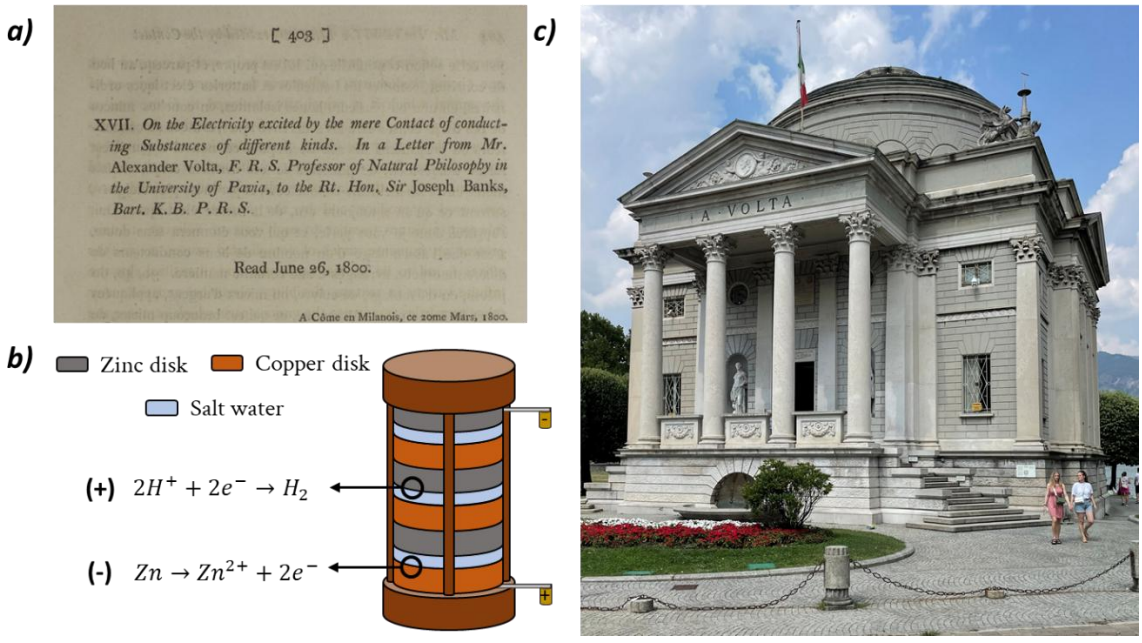


Figure 1: a) Excerpt from Volta's thesis written in 1800 and sent to the Royal Society of London[1]. b) Illustration of the Volta's electrochemical cell. c) Alessandro Volta's temple, memorial established in his hometown Como, Italy.

19th – 20th century.

The Volta's breakthrough is the origin of numerous important advances in the development of modern electricity and actual batteries. This led to several battery technologies such as rechargeable lead-acid batteries developed by Gaston Planté in the late 19th century and the supply of starters of vehicle engines[3]. If at the time the development of batteries was mainly driven by scientific curiosity and the creation of the first autonomous devices, the motivations changed in the 1980s. Indeed, during this period oil consumption exceeded proven and yet-to-be-discovered reserves (**Figure 2**)[4]. Consequently, the research progressively shifted with the motivation of supplying renewable energy, and the development of electric and hybrid vehicles to decrease the global consumption of fossil fuel. With the idea of developing batteries with higher energy densities, Ni-based batteries were developed such as Ni-Cd and Ni-MH, providing a power source for portable devices. Then, the Li-ion technology emerged in the late 1960s[5] and pushed further the progress in powering hybrid and electric vehicles.

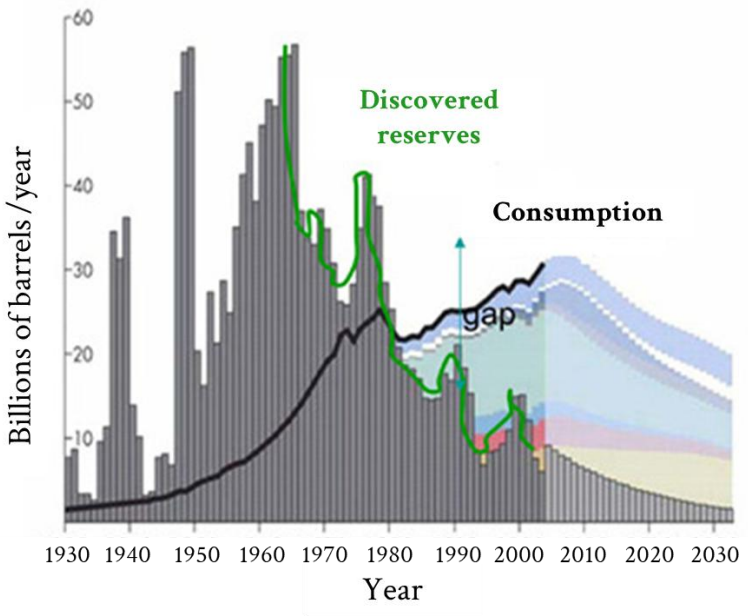


Figure 2: Growing gap between oil consumption and the discovered/yet-to-be-discovered reserves. Reprinted with permission from ref. [4].

Today.

From the 6th IPCC report, stronger warnings are issued regarding global warming and its consequences on human health and our planet. Green mobility, based on E-mobility, is one of the solutions envisaged to reduce greenhouse emissions[6]. However, even if the production of electric and hybrid vehicles increases every year, they only represent 10 – 15% of the French vehicle fleet.

Multiple reasons can explain such a number, like the poor infrastructure network making difficult the car charge during a trip, the cost of an E-vehicle easily 30% higher than a combustion engine vehicle, the mentality related to shorter driving range. One of our responsibilities as academic researchers and industrials rely on tackling the last challenge related to driving range by improving Li-ion batteries (LiBs). The latter is the most mature electrochemical energy storage systems to date[7], and the only one allowing to compete with thermal vehicles. If the increase of driving range relies on new chemical materials delivering more energy, another challenge is the power capability of the batteries to decrease charging times (nowadays around 1 – 2h)[8], while maintaining a suitable energy density.

If new Li-based technologies emerge in the academic field to fill the gaps in LiBs such as all solid-state Li-batteries, Li-sulphur or water-in-salt batteries, a lot of research in the improvement of the actual LiBs technology is still undergoing. For this purpose, graphite, which dominates the worldwide market as negative electrode, is still being investigated, as evidenced by the number of publications associated to this keyword (**Figure 3**). Indeed, the number of publications associated to "Li ion" increases exponentially since the 1990s, and the research on "graphite" for LiBs follows the same trend without slowing down. This highlights that even if the graphite electrode has been investigated for the last 70 years, challenges and misunderstanding persist.

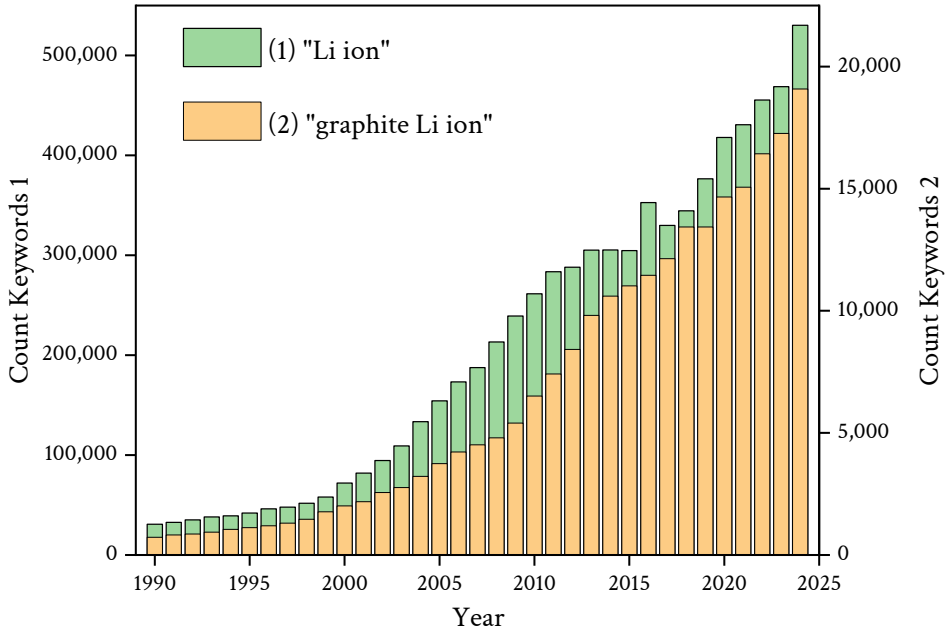


Figure 3: Number of publications strictly containing the keywords (1) "Li ion" and (2) "graphite Li ion" as a function of the year. The analysis was performed in Semantic Scholar.*

* The analysis is over-simplified and excludes a lot of publications probably dealing with the same topics without the same keywords. However, it represents a simple and fast analysis of the interest in graphite for LiBs from 1990 to todays-life.

Thesis objectives.

In this PhD thesis, the core objective is the investigation of the power limitation of the graphite electrode for LiBs, which limits the fast-charging ability of this technology. The principal questions motivating these investigations are the following:

What are the causes of this power limitation?

How can the power capabilities of graphite electrode be enhanced?

The plan of this thesis manuscript is illustrated in **Figure 4**, presenting the main questions and investigations carried out chapter by chapter. Answering these questions first requires establishing a proper state of the art, in order to highlight current knowledge, discuss the open questions, and identify existing limitations. To ensure reproducibility and a clear understanding of the investigations, Chapter II provides a detailed description of the materials and methods used and developed throughout the thesis.

The first experimental results are presented in Chapter III, which focuses on the study of thin graphite electrodes under quasi-thermodynamic conditions, with the objective of characterising the lithiation mechanism of graphite. Chapter IV then addresses the first key question regarding the origin of the power limitations of graphite. A multi-probe approach, combining structural and electrochemical characterisations, is employed and reveals the kinetic limitations of thick electrodes.

In Chapter V, the investigations turn to the mechanical aspects of lithiation, with the goal of understanding how mechanical changes during cycling affect power performance. These effects are mainly examined using dilatometric measurements and ultrasonic characterisations.

Finally, Chapter VI introduces an innovative and unique strategy based on the use of the lithium isotope ^{6}Li as a lithium source. The investigations in this chapter aim to determine whether this isotope can serve as a booster for the power capability of graphite electrodes.

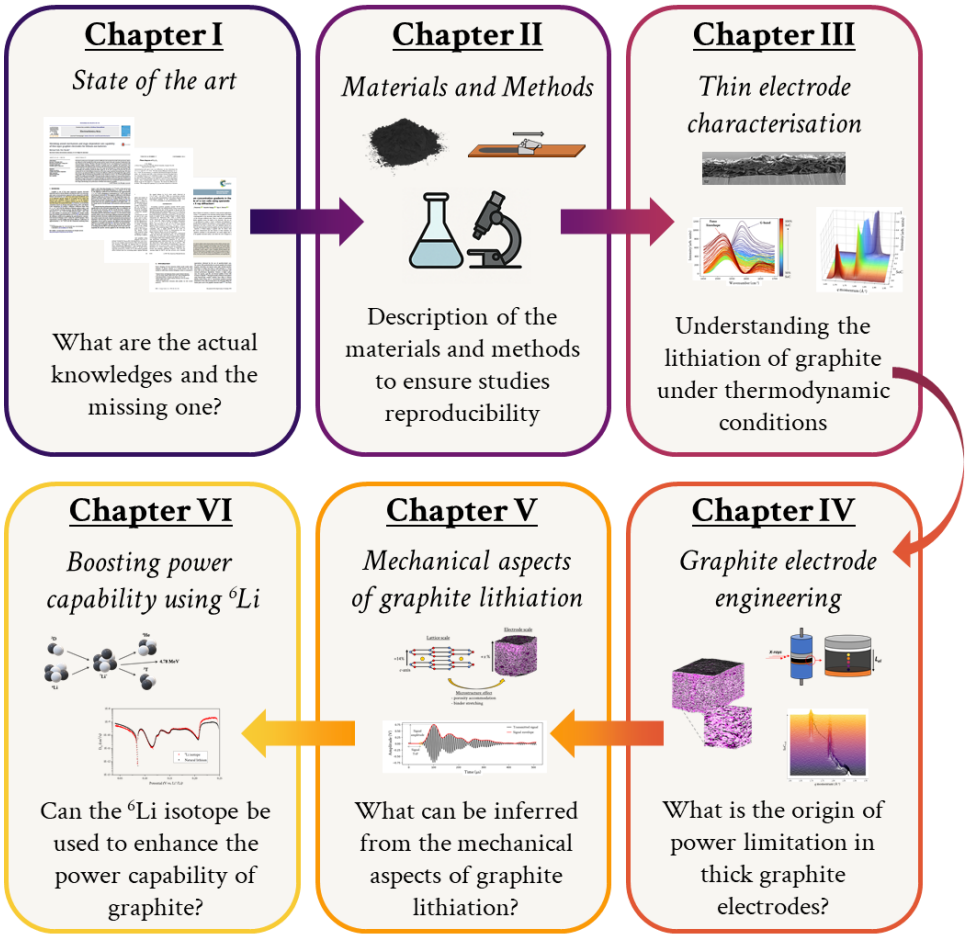


Figure 4: Illustration of the manuscript plan.

CHAPTER I

STATE OF THE ART

In this first chapter, the actual state of the art is discussed, focusing on aspects related to energy and power of energy storage systems to highlight the advantages and drawbacks of Li-ion batteries. Then, the working principle of Li-ions batteries along with the transport processes will be presented.

As the thesis focuses on the power properties of the graphite electrode, the power limitations encountered for different positive and negative electrodes will be introduced along with the impact of the electrode engineering. Finally, the last part will be dedicated to the *operando* characterisations allowing a better understanding of the power limitations.

1 ENERGY AND POWER DENSITIES, THE CHALLENGES

A broad range of energy storage systems (ESS) are available to supply energy, each of them having different properties based on the targeted application. In this regard, the main parameters rely on the energy density and the power density[9]. Ideally, energy and power densities are decoupled, and one can achieve both i) high energy densities enabling long operation time without charge and ii) high power densities providing high amount of energy for short times. Typical examples of coupled and decoupled ESS are described in **Figure 5**. A perfect illustration is the production of energy *via* a hydroelectric dam, the theoretical energy produced depends on the water volume and on the dam height (gravitational potential) whereas the power depends on the alternators used[10]. The decoupling between energy and power densities is possible because the elements responsible for the energy and power production are different.

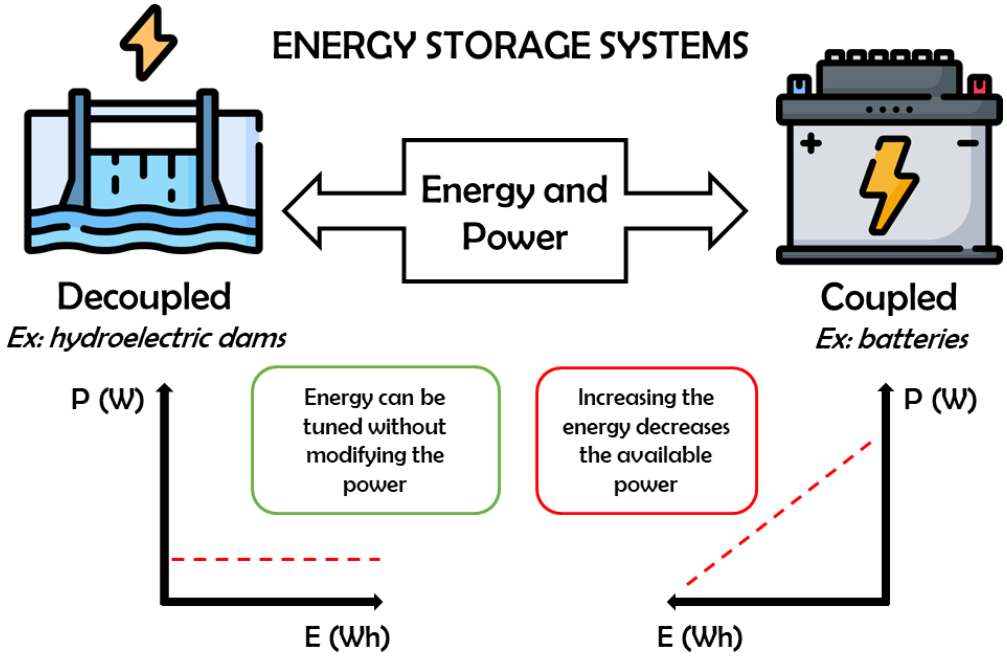
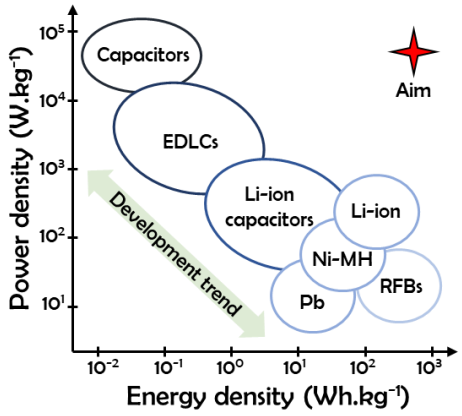


Figure 5: Illustration of energy storage systems with coupled / decoupled energy and power properties.

Based on this principle, redox-flow batteries represent a promising but still recent ESS decoupling these two parameters. The decoupling comes from an energy storage achieved by the volume tank providing the amount of electro-active material, and the delivered power depends on the flow stack (electro-active surface)[11]. Beside these specific applications, most of the ESS display energy and power densities that are coupled, with, unfortunately, antagonistic behaviour: a high energy density induces a low power density (and *vice versa*). This is the case with an electrochemical double-layer capacitor (EDLC) that uses the adsorption of ions at the surface of the electroactive material as electrical energy storage. The adsorption of ions being a very fast process involving electrostatic interactions, a very high power density is associated to this technology[12]. The price to

pay is a low energy density because of the low specific capacity associated with charge adsorption (surface process)[13,14], even if a new research avenue tends to use advanced electroactive materials with large storage capacity. Inversely, the batteries provide energy by converting chemical energy into electrical energy using redox reactions, and the associated energy density is much higher than that of charge adsorption. Since redox reactions involve oxidations and reductions of chemical species (*i.e.* the complete removal/addition of one or more electrons to a molecule[15]), the associated characteristic times are much longer providing lower power densities compared to EDLC[16,17]. Ragone diagram, presented in **Figure 6a**, compares the aforementioned ESS technologies, one can notice the development trend (double arrow) nicely summarising the antagonistic coupling between energy and power densities. Indeed, all commercial ESS are distributed along the high power/low energy to low power/high energy axis, whereas the targeted performance for future application are symbolised by a red star. In addition to performance indicators, the storage mechanism strongly impacts the lifetime of the ESS. In **Figure 6b**, some ESSs are summarised with their approximate lifetime. Capacitors-type devices display high cycling lifetime as a result of the charge adsorption process (surface process) that does not cause materials fatigue. However, battery-type systems suffer from a limited cycling lifetime, since, among other things, the bulk of electroactive materials is solicited implying structural modifications and volume expansion.



Energy Storage System	Lifetime
Electrochemical Double Layer Capacitors (EDLCs)	> 100 000
Li-ion capacitors	~ 10 000
Li-ion	1 000 – 2 000
Redox Flow Batteries (RFBs)	> 10 000

Figure 6: Left) Ragone diagram of several ESS. The red star represents the targeted performance to be achieved in the future, whereas the historical trend is symbolised by the double arrow. Adapted from [18–21]. Right) Associated metrics from the different ESS.

In the context of the energetical transition, the electric and hybrid vehicles (EVs and HEVs) impose the use of mobile technology combining high autonomy (high energy density), fast charging (high power density), safety, and low cost (at least in the range of combustion engines). Since their commercialisation by Sony® in 1991[22], Li-ion batteries (LiBs) have been set as the most promising ESS. Compared to other battery technologies, LiBs provide appealing features, such as a high energy density because lithium is the lightest alkali metal[23], a very small self-discharge, and

long lifespan. However, LiBs suffer from relatively low power density, leading to poor fast-charging ability.

Figure 7 illustrates the working principle of a Li-ion battery. The cell is composed of positive (higher potential) and negative (lower potential) electrodes, separated by a porous separator (*e.g.,* Celgard®). This separator prevents short-circuits in the cell and is soaked by an organic liquid electrolyte that contains the lithium ions. The liquid electrolyte also soaks the two electrodes, providing to the active material the accessibility to lithium ions. The two electrodes are coated on current collectors (usually copper or aluminium) which allow electric connection to the external parts (a charger or the device to power). LiBs are based on the rocking chair principle[24], with lithium ions going back and forth between the positive and negative electrodes. Upon charge, lithium ions are extracted from the positive electrode (electroactive material containing lithium), while other lithium ions are inserted into the negative electrode. As a consequence, the cell voltage (potential difference between the two-electrode materials) increases, and the energy is stored through a chemical form. Upon discharge, closing the electrical circuit allows the spontaneous removal of lithium ions from the negative electrode, and the lithium ions return to the positive electrode. In parallel to this ionic current, an electronic current exists with electrons leaving the negative electrode and going to the positive one. This discharge current serves as a power source for devices; during this step, the chemical energy is converted back to an electrical one.

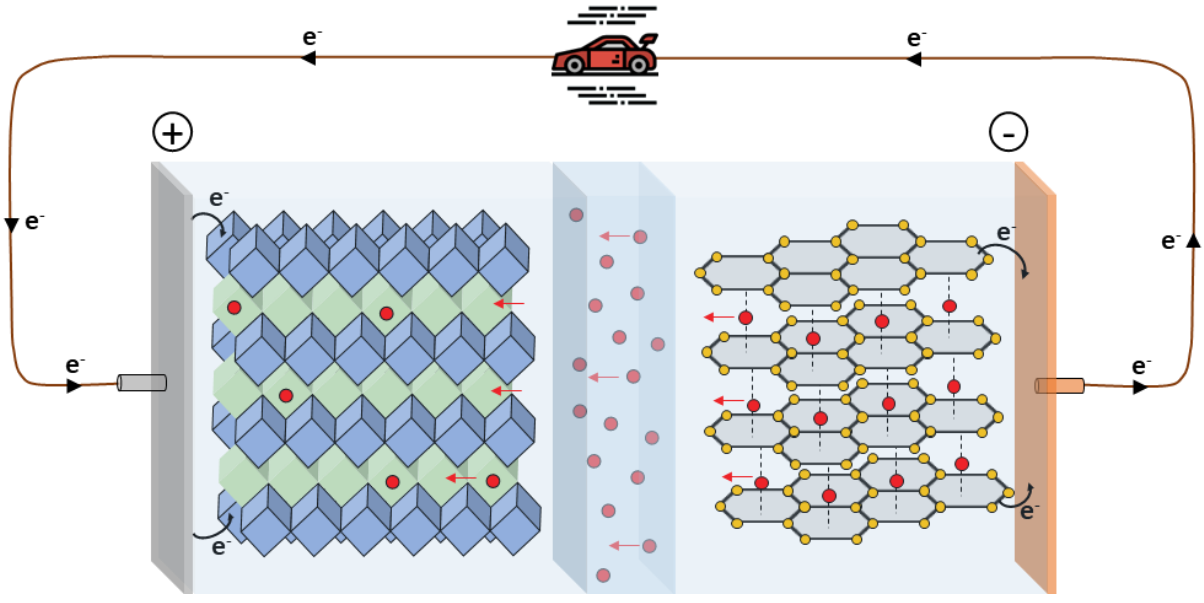


Figure 7: Illustration of the working principle of a lithium ion battery upon discharge.

2 HOW TO OPTIMISE POWER DENSITIES IN LIBS?

Whereas the energy depends on the amount of active material that is accessible for lithium reaction, the power property depends on multiple transport processes and their respective timescales. Because the electrodes for LiBs are complex systems, optimisation of the power density is a real challenge that takes place at different scales, mainly at the bulk (active material) level and electrode level, as shown in **Figure 8**. Several axes can be seen for the investigation of power density, presented below:

- For the active material, the power properties can be assessed through "model" electrode systems, *i.e.* thin-film like electrodes. In this configuration, only the ionic transport at the solid-state and the charge transfer matter whereas the role of ionic transport in liquid phase and the electronic transport are negligible. In these conditions, the response to the electric stimuli depends on the timescale at which lithium ions can diffuse/migrate inside the active material, but also on the charge transfer kinetic. In the literature, the charge transfer kinetic is most of the time considered as fast compared to the transport processes in "normal" condition of cycling (25°C and reasonable C-rate). However, this transfer phenomenon can limit the system under low temperature operation (-30 to -40°C)[25] and for extreme fast charging (4C)[26]. The charge transfer is a complete subject of research, one can refer to the following reference [27] as example.

- The properties linked to the electrode engineering can be probed using "realistic" systems with a porous structure. For thick electrodes, the liquid-phase transport of lithium is also playing a role in the transport processes. In this configuration, the electronic and ionic properties depend on the electrode engineering, *i.e.* a modification of the electrode microstructure can influence the properties.

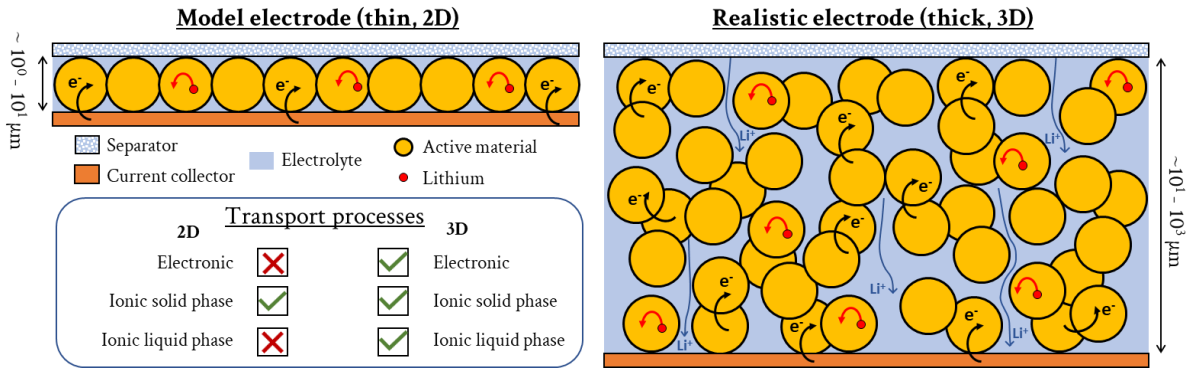


Figure 8: Differences between the model and realistic electrodes in terms of transport processes.

By distinguishing these two configurations, the multiple transport processes that take place at the material level and at the electrode scale are discussed here.

2.1 Transport processes in Li-ion batteries*

2.1.1 Electronic transport, at the material level

The electronic transport is ensured by multiple materials in classical composite electrodes that are all in contact, with electrons migrating through the conduction bands of metals and semi-conductors. For example, in the case of negative electrodes, the electronic conduction is ensured by the copper current collector, the carbon additives, and possibly by the active material phase.

In copper, electrons are conducted through the 4s and 3d orbitals that slightly overlap to form a high density of states around the Fermi level (conduction band)[28]. For carbon-based materials (graphite and black carbon), electrons are transported through the π^* orbitals of carbon atoms. It is interesting to note that disordered carbons are usually added in composite electrodes to improve the electronic conductivity. But looking closer to electronic conductivities of carbon materials, one can notice that the disordered forms of carbon display lower electronic conductivities at the single particle scale, with graphite displaying 10^5 $S.m^{-1}$ whereas black carbon "only" displays 10^3 $S.m^{-1}$ [29]. The same applies to compacted powders with graphite, which displays a slightly higher electronic conductivity than the black carbon. This was investigated by Pantea *et al.* that correlated the electrical conductivity with the graphitic character of the disordered carbons. This graphitic character was described as regions that approach the honey-comb structure of pure graphite[30]. Indeed, for disordered carbons, the hybridised domains sp^3 are more preponderant and do not provide electrical conductivity as sp^2 hybridisation. One should keep in mind that agglomerates of black carbon will be worse conductors than graphite flakes; it is of interest to properly disperse these carbon nanoparticles and avoid their agglomeration in the composite electrode.

2.1.2 Electronic transport, at the electrode level

In a 3D and porous structure, electrons need to be transported from the current collector to the active particles near the electrode/separator interface. To ensure a proper electronic transport, a high contact surface should be developed among all the electronic conductors, known as electronic percolation. If black carbon does not provide better intrinsic electronic conductivity compared to graphite, interest is found with its morphology and size. Indeed, being nanoparticles, their small size and spherical morphology enable optimal dispersion in the electrode volume, improving the electronic percolation. In contrast, the binder that provides the mechanical strength of the electrode is a pure insulator and can hinder the electronic transport. In addition, the porosity of the electrode, which enables the accessibility of lithium ions to the active material through the liquid electrolyte, is an obstacle to electronic transport. Then, tuning the volumetric fractions of

* The transport processes will mainly concern the negative electrodes, even if a lot of transport processes are common with the positive electrodes.

the electrode components is an important step to optimise both electronic and ionic transports that will be discussed later.

With this in mind, Ma *et al.* demonstrated the interest in adding graphene nanosheets and carbon nanotubes (CNTs) to hard carbon (HC) composite electrodes to improve the power capability[31]. Using this strategy, a reallocation of electronic current operates with favoured pathways along the CNTs and graphene additives (see **Figure 9a, b**). At the electrode scale, a better current distribution is observed when using these additives (see **Figure 9c, d**). This must be attributed to the particle's form factor, which improves the percolation even for low weight fraction compared to spherical particles.

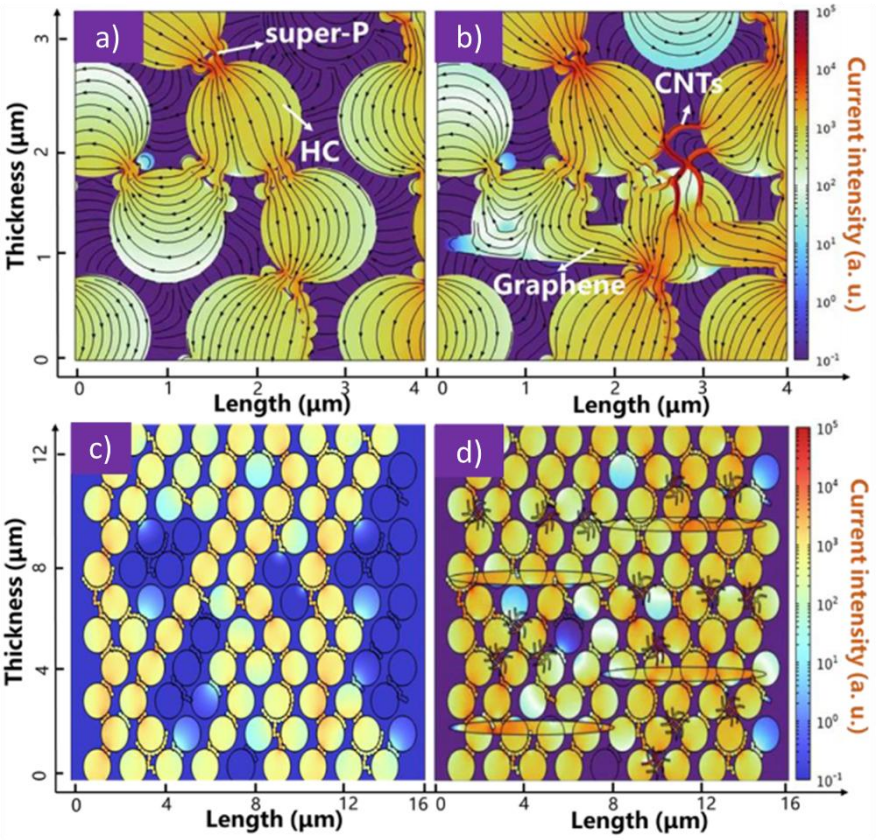


Figure 9: Charge transport pathway in a) hard carbon – super P composite (HC) and b) hard carbon – super P – carbon nanotubes – graphene composite (M-HC), simulated by finite element analysis (FEA). Current distribution at the electrode scale for the c) HC electrode and d) M-HC electrode, simulated by FEA. Reprinted with permission from ref. [31].

2.1.3 Ionic transport in liquid phase, at the electrolyte level

The liquid phase (organic based electrolyte), wetting the porous structure of the separator, is the place for lithium-ion diffusion/migration in a solvated state. This transport phenomenon depends on the electrolyte used: common electrolytes are composed of a lithium salt dissolved in organic solvents, such as LP30 electrolyte composed of a $LiPF_6$ salt (1 M) in ethylene carbonate (EC) and

dimethyl carbonate (DMC) (50/50 v/v). The electrolyte displays specific properties such as ionic conductivity, species diffusion coefficient, and transference number. Although the ionic conductivity and the diffusion coefficient are related to the motion of ions in solution, the transference number reflects the fraction of current carried by the ion[32] (t_+ for lithium and t_- for counter-anion, with $t_+ + t_- = 1$). In the case of liquid electrolytes, the current carrier is ensured by both the cations (lithium) and the counter-anion because each of them is free to move. This is the reason for transference numbers $t_+ < 1$ for lithium cations in such electrolytes, and because both the cation and counter-anion act as charge carriers, the diffusion corresponds to the mean diffusion of both lithium cations and the counter-anions, called bipolar diffusion. A wide range of literature focuses on electrolytes, trying to improve the motion of lithium ions and the current carrier[33,34]. As an example, Diederichsen *et al.*[35] demonstrated based on simulations the beneficial effect of slightly improving the cationic transference number of electrolyte for LiBs (from $t_+ < 0.5$ to ~0.7), allowing to reach higher state of charge at a high charging rate*.

2.1.4 Ionic transport in liquid phase, at the electrode level

The Li-ion diffusion/migration not only depend on the electrolyte nature but also on the electrode microstructure, introducing the concept of tortuosity[36†]. Electrochemically, tortuosity represents an increase in resistance associated with the transport of charges through a porous structure[37]. As a consequence, effective conductivities (Eq. 1) and effective diffusion‡ coefficients (Eq. 2) are expressed as a function of the bulk properties of the electrolyte and on the electrode microstructure.

$$\sigma_{eff} = \frac{\varepsilon}{\tau}\sigma \qquad \textit{Eq. 1}$$

$$D_{eff} = \frac{\varepsilon}{\tau}D \qquad \textit{Eq. 2}$$

Where σ_{eff} and D_{eff} are the effective ionic conductivity and diffusivity on the electrode scale, σ and D are the ionic conductivity and the bipolar diffusion coefficient of the liquid electrolyte. These terms are related to the electrode porosity, ε and the tortuosity factor§, τ.

The MacMullin number is commonly used to describe the link between effective and bulk ionic conductivities or diffusion coefficients[38], with Eq. 3:

* In this study, the simulations were realised on thick electrodes of ~100 µm, favouring a limitation by the transport in the electrolyte.

† The separator of the battery also induces a tortuosity, usually low because of very porous structures.

‡ Here, it corresponds to a bipolar diffusion.

§ This electrode tortuosity factor is usually determined by EIS in a symmetric cell (with two similar electrodes) with the desired electrolyte. A method describing this analysis is given in Materials and Methods (p**56**).

$$N_M = \frac{\tau}{\varepsilon} = \frac{\sigma}{\sigma_{eff}} = \frac{D}{D_{eff}} \qquad \textit{Eq. 3}$$

In works dating from the 1930s, Bruggeman built a model predicting the relationship between porosity and tortuosity of a medium, providing the following power-law Eq. 4:

$$\tau = f.\varepsilon^{-\alpha} \qquad \textit{Eq. 4}$$

Where ε is the porosity, α and f are power and proportionality factors depending on the particle shape. For spherical particles, a α factor of 1/2 is predicted while cylindrical particles imply a α factor of 1[39].

Using this power-law equation, one can determine the α factor of a medium to get information about the particle isotropy, with factors approaching 1/2 for spherical shape and increasing toward higher values by increasing the particle anisotropy.

In addition to this electrochemical tortuosity, a geometric tortuosity can also be used and rely on 3D image reconstruction. Simply, this microscopic approach (Eq. 5) describes the elongation path of the transport pathway due to the porous structure with respect to a theoretical straight path, the electrode thickness in LiBs[40].

$$\tau_{geo} = \frac{d_{path}}{d} \qquad \textit{Eq. 5}$$

Where d_{path} is the elongated distance and d is the straightest path for lithium ions mobility (e.g. electrode thickness).

This geometric tortuosity is determined *via* image analysis using several techniques such as focused ion beam – scanning electron microscope (FIB-SEM) or X-ray tomography. Compared to the electrochemical tortuosity factor, this geometric tortuosity can distinguish the mobility along the three space dimensions and can provide useful information about the anisotropy of electrode microstructure along *x, y* and *z* directions[41]. The comparison between both tortuosity factors (electrochemical and geometric) is not straightforward because they do not probe the same physical phenomenon. Although electrochemical determination account for interactions between ions and the electrode structure (active material particles, binder, etc.), geometrical determination is a physical representation of the electrode tortuosity not considering electrical effects. Still, the two methods are complementary and discussed together in the literature.

2.1.5 Ionic transport in solid phase, at the material level

In the case of negative electrodes working at rather low potential compared to the redox couple Li^+/Li, a passivation layer is formed by reduction of the organic electrolyte. This passivation layer, known as solid electrolyte interphase (SEI), is the first "barriers" that lithium ions cross at the solid-state level. With a thickness of few nanometres, the SEI is characterised as an electronic

insulator and ionic conductor[42]. This buffers further reduction of the electrolyte upon cell operation and provides an electrochemical stability[43]. The SEI is then inevitable when dealing with negative electrode at low working potential (< 0.8 V vs. Li^+/Li), and can also cause some problems of self-discharge, rate capability and safety[44]. For a better comprehension of the SEI and its intrinsic properties, reader can refer to several papers and reviews[45–47].

Once lithium ions reach the particle surface (under reductive conditions), a de-solvation step is needed to enable the insertion of the non-solvated ion in the active material. This insertion generates a concentration gradient from the surface of the particle to its centre. This gradient is responsible for the diffusion of lithium ions, characterised by a diffusion coefficient that depends on the active material. The type of lithium diffusion mechanism greatly depends on the crystallographic structure of the host materials and the type of connectivity between the guest sites[48]. Three dimensional (3D) materials enable lithium diffusion through empty/vacant sites that can be occupied by lithium ions, and can be reached through a 3D network as schematised in **Figure 10a**.

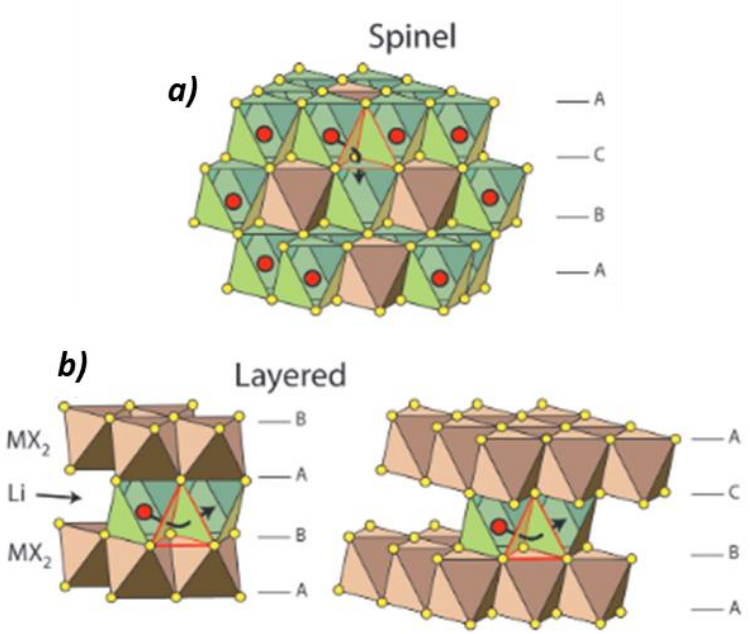


Figure 10: Crystal structures and lithium diffusion paths for a) spinel materials (3D) and b) layered materials (2D). Reprinted with permission from ref. [48].

It is commonly claimed that 3D networks provide high-rate lithium ion conduction, making materials such as $LiNi_{0.5}Mn_{1.5}O_4$[49] (LNMO), $LiMn_2O_4$[50,51] (LMO) or $Li_4Ti_5O_{12}$ (LTO) good candidates for power applications. These materials are part of the spinel family, providing 3D connectivity between the guest sites and creating multiple ways for lithium ion to diffuse in the bulk material. Similarly, two dimensional (2D) materials such as the layered oxide family display lithium diffusion occurring in a 2D plane, usually in between the oxide layers as schematised in

Figure 10b. Regarding one-dimensional (1D) materials such as $LiFePO_4$ (LFP), belonging to the olivine family, lithium ions diffuse through a 1D tunnel as computed by first principles calculations by Morgan *et al.*[52].

In addition to the several diffusion processes, the interaction between lithium and the active material differs between graphite and other electrode materials. For $LiNi_xMn_yCo_zO_2$ (NMC) or other positive electrode materials (as illustrated in **Figure 11**), lithium ions are de/inserted into interstitial sites and the addition or the removal of a positive charge (Li ion) compensate the reduction/oxidation of transition metals (Ni and Co for NMC, Fe for LFP)[53]. Peljo *et al.* described these systems as redox solids for which the electrochemical activity depends on the electroactive metal (Ni^{3+}/Ni^{2+}) that are compensated by the lithium de/insertion[54]. Within these types of active materials, lithium ions 'only' act as charge carrier and their oxidation state is constant and equal to +1.

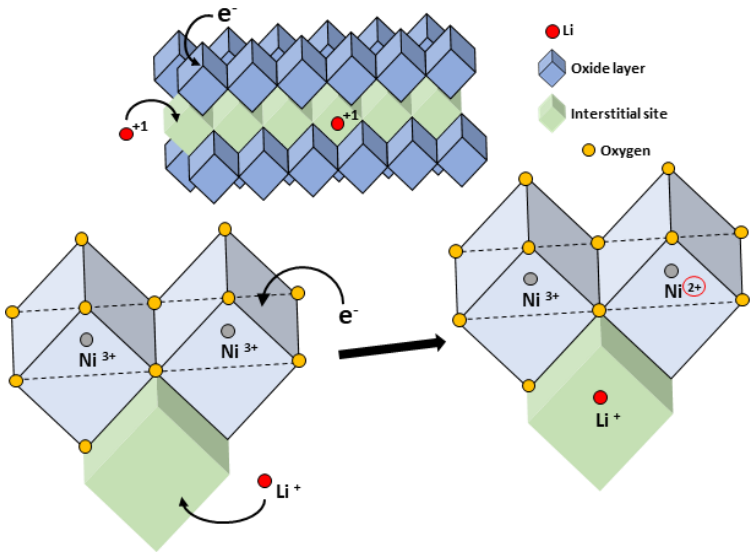


Figure 11: Illustration of layered oxide material lithiation such as NMC. The lithium ion is inserted to compensate for the nickel ion reduction.

In the case of graphite, the lithium ions intercalate between the graphene sheets, and the nature of the interaction between the carbon planes and the lithium is still debated. Holzwarth and Rabii calculated the energy band structure of LiC_6 using *ab initio* method[55]. A charge transfer between the 2s orbitals of lithium and the graphite π^* orbital suggests covalent interactions. Although the Li 2s character of the Fermi level of LiC_6 was negligible, covalent contributions were noticed for other electronic states. Later, Hazrati *et al.* calculated the phonon density of states of LiC_{12} and LiC_6 compounds using van der Waals density functional theory (DFT)[56]. The vibrational modes clearly involved contributions from 2s orbitals of lithium and graphite π^* orbital, supporting a charge transfer between the two entities. Similar results from Kganyago and Ngoepe[57] support the partial

delocalisation of the π^* orbital density of carbon atoms onto the 2s orbitals of lithium atom, lithium acting as an electron acceptor.

Compared with other insertion materials, the lithium entity is involved in the band structure of the lithiated phases of graphite. This suggests that lithium can be considered as partially reduced during its intercalation with the following Reaction I, as illustrated in **Figure 12**.

$$C_6 + xLi^+ + xe^- \Leftrightarrow \left[Li_x^{\delta+} - C_6^{\delta-}\right] \qquad \textit{Reaction I}$$

With $1 > \delta^+ > 0$, *and the Li-C interaction being partially covalent.*

Even if the lithium is partially reduced with a non-net charge and should not be considered as an ion*, the term "lithium ion" will be used.

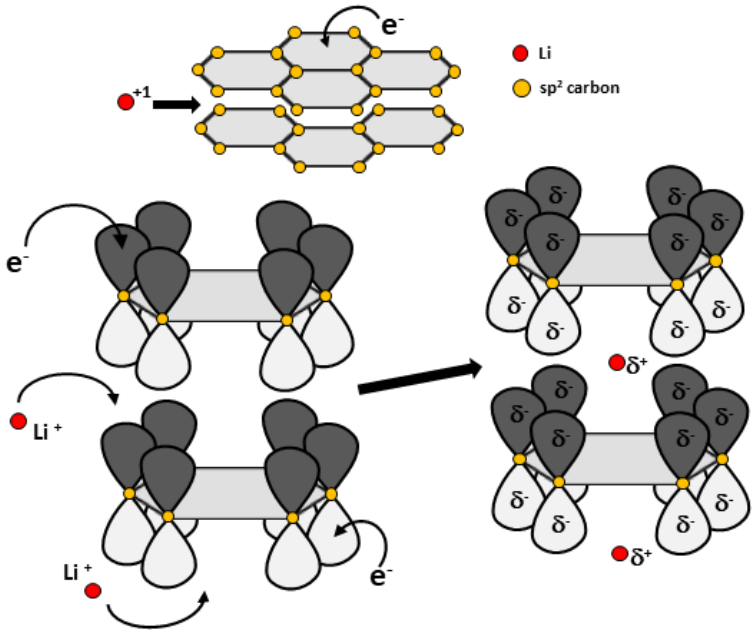


Figure 12: Illustration of lithium intercalation in graphite sheets with a slight charge transfer occurring between the antibonding π orbitals of carbon atoms and the lithium 2s orbital.

2.1.6 Summary

In this section, one could see the multiple transport processes that take place in LiBs at different scales, from the active material to the electrode level. It demonstrates the complexity associated with the charge and discharge of electrodes. As a consequence, several axes of improvement are available to increase the power capability of these complex systems. Starting from the material level, one can take advantages of certain active materials suitable for power. At the electrode scale, the engineering of the microstructure is also very crucial and will be discussed later.

* Following the IUPAC definition given in the Gold Book[15], an "ion" is an atomic or molecular particle having a net electric charge.

2.2 Practical comparison of power capabilities between electrode materials for LiBs

Practically, a lot of positive[58] and negative[59] electrode materials for LiBs were investigated and many studies tried to classify these materials in terms of kinetic properties. Here, the kinetic properties of well-known electrode materials are correlated with their mechanism of solid-state diffusion; one will observe that both are not necessarily correlated. The impact of particle morphology is also discussed.

2.2.1 Kinetic properties of electrode materials

To evaluate the power capabilities of an electrode material, the usual strategy is to compare the available specific capacity obtained for high C-rates of charge/discharge (1 C corresponds to the charge of the electrode in 1 h) with the deliverable specific capacity under quasi-thermodynamic conditions. However, the power capability strongly relies on the electrode microstructure, thus an electrode should be investigated in a realistic system (3D, thick electrode), with a loading higher than several mg/cm^2, and one should keep in mind that the power limitation for a 2D (thin) electrode would originate from a different transport phenomenon. Unfortunately, as there is no relevant standardisation protocol in the literature, it is difficult to rely on the literature data[42,60]. As an example, several parameters can lead to bias results, the electrode loading (amount of active material per cm^2 of electrode), the porosity of the electrode, the amount of carbon additive added to the system, and the electrolyte formulation (in particular salt concentration). Without a proper access to these parameters, it is highly difficult to compare several studies. Indeed, a high loading of electrode induces low power capabilities because of the low mobility through all the electrode microstructure (a dedicated section is further discussing this point in p**127**). Still, some studies compared LiBs electrode materials, and some results are given in **Table 1**. Keeping in mind the lack of standardisation and the difficulty to obtain the electrode loadings from these studies, a trend can be seen, correlating the type of electrode material (3D, 2D or 1D) and the kinetic properties at the electrode level. As an example, 3D materials-based electrodes display high-rate specific capacities in the upper range up to 20 C, while 1D material-based electrodes such as $LiFePO_4$ provide lower performance with 5 C. Overall, the 2D materials display power capabilities in the middle range around 10 C, except for graphite which displays by far the lower kinetic properties.

Table 1: High rate properties reported in the literature for different electrode materials at the electrode level. The practical specific capacities are usually obtained under low cycling rate such as 0.1 C (quasi-thermodynamic). Kinetic properties are expressed by the highest C-rate at which at least 70% of the practical specific capacity is obtained. The values reported are taken from [61–63].

Electrode material	Type	Practical specific capacity (thermodynamic)	High rate specific capacities
$\mathbf{Li_4Ti_5O_{12}}$ (LTO)	3D – Spinel	~ 175 mAh.g^{-1}	150 mAh.g^{-1} @10 - 20 C
$\mathbf{LiNi_{0.5}Mn_{1.5}O_2}$ (LNMO)	3D – Spinel	~ 130 mAh.g^{-1}	120 mAh.g^{-1} @20 C
$\mathbf{LiMn_2O_4}$ (LMO)	3D – Spinel	~ 120 mAh.g^{-1}	110 mAh.g^{-1} @20 C
$\mathbf{LiNi_{0.8}Co_{0.15}Al_{0.05}O_2}$ (NCA)	2D – Layered oxide	~ 210 mAh.g^{-1}	160 mAh.g^{-1} @10 C
$\mathbf{LiNi_{1/3}Mn_{1/3}Co_{1/3}O_2}$ (NMC111)	2D – Layered oxide	~ 180 mAh.g^{-1}	130 mAh.g^{-1} @10 C
Graphite	2D	~ 372 mAh.g^{-1}	330 mAh.g^{-1} @1 - 2 C
$\mathbf{LiFePO_4}$ (LFP)	1D – Olivine	~ 165 mAh.g^{-1}	140 mAh.g^{-1} @5 C

These results demonstrate the high variability of power properties depending on the electrode material. To understand whether the rate capabilities are linked to the type of solid-state lithium diffusion path (3D, 2D, or 1D), solid-state diffusion coefficients are compared in the following section.

2.2.2 Solid-state diffusion of lithium in electrode materials

Based on the different lithium diffusion pathways in 3D, 2D, and 1D materials, a recurring statement is observed in the literature: materials involving 3D lithium diffusion pathways display better diffusion rate than their peers with 2D and 1D paths. To verify this statement, the diffusion rate of lithium ions can be compared in those materials. The diffusion rate of lithium ions is described by a diffusion coefficient obtained through several electrochemical methods such as the Galvanostatic Intermittent Titration Technique (GITT), the Potentiostatic Intermittent Titration Technique (PITT) or the Electrochemical Impedance Spectroscopy (EIS). **Figure 13** provides a comparison of diffusion coefficient from the literature for different electrode materials, classified by the dimensionality of diffusion paths. Again, the comparison between different methods (GITT, PITT or EIS) and the differences between particle morphologies can provide biased interpretation; even for the same material, several orders of magnitude difference can be reported. Here, diffusion coefficients of the same magnitude order for some 3D and 2D materials are

noticed. As an example, LNMO displays values similar to those of 2D electrode materials such as NCA or graphite. Moreover, for NMC 111, diffusion coefficients are in the upper range, demonstrating that 2D materials can provide high diffusion coefficients. The only case following the expected trend is LFP which exhibits a very low diffusion rate of lithium compared to other materials, probably due to the one-dimensional path for lithium diffusion.

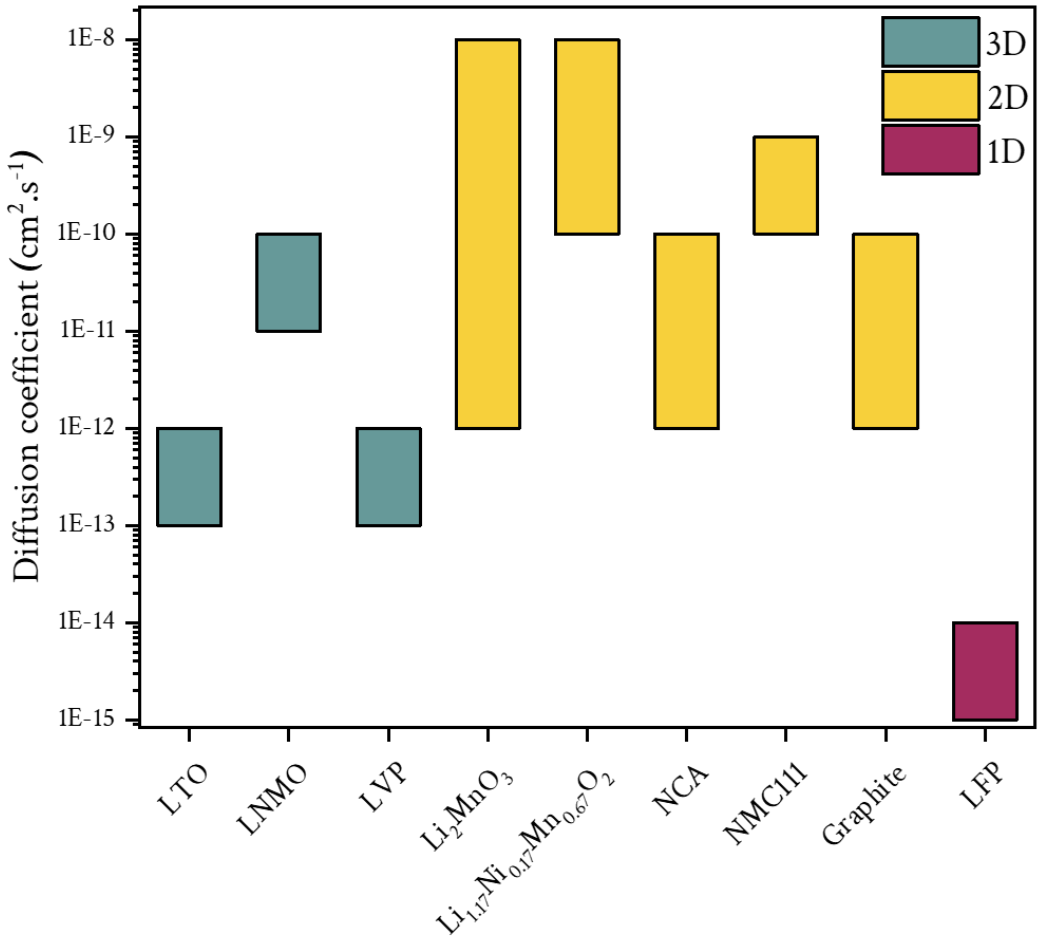


Figure 13: Lithium diffusion coefficient for several LiBs electrode materials classified by the dimensionality of diffusion network. The values are taken from refs. [64–73].

A key parameter in the lithium transport mechanism is the activation energy, associated to the energy required for lithium ions to move from one guest site to another. Taking the example of LTO, lithium ions jump from tetrahedral guest sites to octahedral one, both sharing a face. This diffusion mechanism is faster for lithiated-LTO ($Li_7Ti_5O_{12}$), justified by a decrease in the activation barrier energy from 0.55 eV (LTO) to 0.45 eV ($Li_7Ti_5O_{12}$)[74]. This phenomenon results in a higher diffusion coefficient, determined by electrochemical impedance measurement by Ma *et al.*[64], increasing from 10^{-13} $cm^2.s^{-1}$ (LTO) to 10^{-12} $cm^2.s^{-1}$ ($Li_7Ti_5O_{12}$). Similarly, Sarkar *et al.* [65] demonstrated that by doping the layered-oxide Li_2MnO_3 with nickel into $Li_{1.17}Ni_{0.17}Mn_{0.67}O_2$, a significant decrease of the activation energy barrier for lithium diffusion was obtained, changing

from ~0.5 eV to 0.1 – 0.2 eV, respectively. This is responsible for a higher diffusion coefficient for the doped material. These results demonstrate that not only the dimensionality of diffusion paths is important but the electronic environment of lithium ions in those diffusion paths also impacts the diffusion rate.

By comparing the kinetic properties and the diffusion coefficient of these electrode materials, a correlation between these two properties cannot be established. The measurement and comparison of lithium diffusion coefficient is not a good indicator to classify materials in terms of power capabilities. One convincing example is that of graphite which displays a diffusion coefficient in the middle range (~10^{-11} $cm^2.s^{-1}$) but exhibits very low-rate capabilities compared to other positive and negative electrode materials. As mentioned earlier, parameters such as the particle morphology/size can influence the power capabilities. Here are some studies that improve the power capabilities of LiBs electrodes by playing with particle engineering.

2.2.3 Impact of particle engineering on the power capability

To understand the effect of particle's engineering on power performance, $LiFePO_4$ is a very good example being limited by a one-dimensional lithium diffusion path. In 1996, Padhi *et al.* used $LiFePO_4$ for the first time, as an electrode material for a LiB[75]. The authors suggested that LFP was a good material for low power applications because of the limited practical capacity under high rate of charge (100 - 110 $mAh.g^{-1}$ *vs.* 170 $mAh.g^{-1}$ as theoretical specific capacity), due to its low electronic conductivity. Following this pioneering work, Ravet *et al.* improved the power capability of LFP by adding a carbon coating on its surface[76]. By carbonisation of aromatic compounds in natural LFP samples, carbon coated samples systematically provided better practical capacities (~150 $mAh.g^{-1}$) and enhanced stability upon cycling.

More recently, Zhao *et al.* employed an efficient strategy based on the synthesis of single-crystalline carbon-coated nanosheets of LFP[77]. Generally, lithium ions diffuse along the [010] crystal direction. To improve the power properties, the authors reduced the crystal size along the [010] direction to form a nanosheet, as schematised in **Figure 14a**. An SEM image of the LFP nanosheets is presented in **Figure 14b**. Compared to classical LFP/C electrodes, the LFP nanosheet displayed much higher rate capability with 120 $mAh.g^{-1}$ @5 C and 72 $mAh.g^{-1}$ @20 C, while the classical electrode displayed 85 $mAh.g^{-1}$ @5 C and 40 $mAh.g^{-1}$ @20 C (**Figure 14c**). This increase in rate capability was attributed to the higher contact surface between the carbon coating, the electrolyte, and the [010] facets of the crystal, increasing the accessibility of lithium ion to active material. In addition, the decreased diffusion length enables lower solid-state diffusion time.

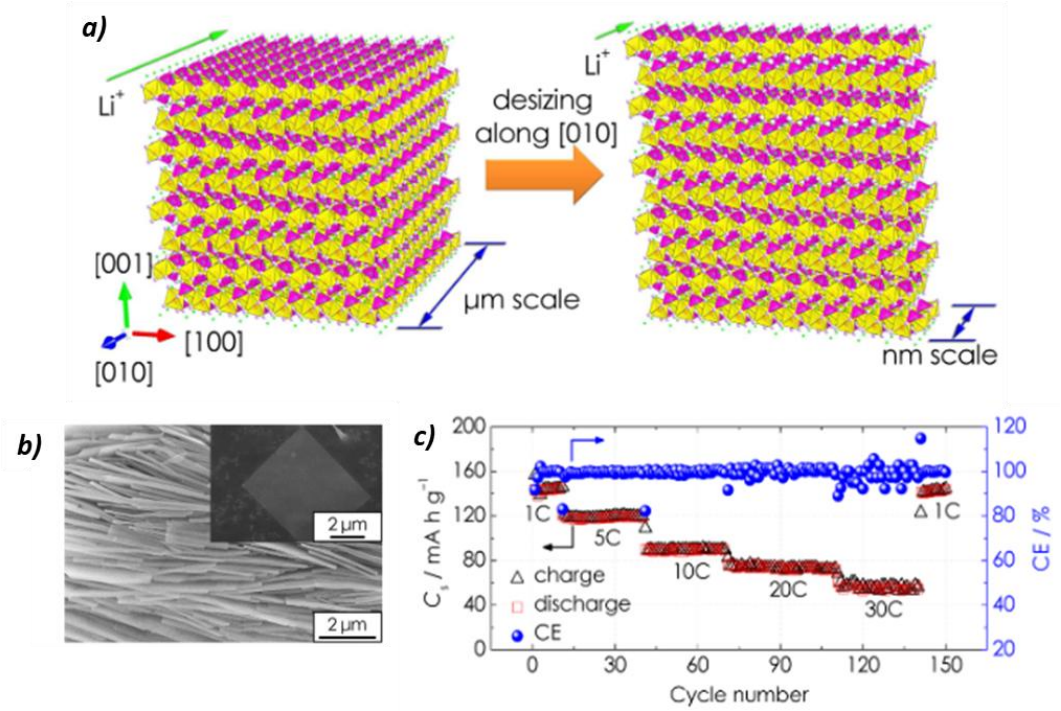


Figure 14: a) Schematic illustration of the size reduction in the [010] direction. b) SEM image of the carbon-coated LFP nanosheets. c) Rate capability of the carbon-coated LFP nanosheets. Reprinted with permission from ref.[77].

Similarly, Van Den Bergh *et al.* discussed the size of the crystallites and the effect on the rate capabilities, especially for NMC material. Single-crystal layered oxide materials are significantly larger in grain size compared to primary particles of polycrystalline materials. This difference in particle size directly impacts the diffusion lengths, decreasing the kinetics of lithiation/delithiation[78].

In conclusion, these studies demonstrate the importance of the diffusion lengths which plays a key role in decreasing the diffusion times in LiBs electrode materials and, then the power densities.

3 FUNDAMENTAL BACKGROUND IN INTERCALATION COMPOUNDS

Prior to pursuing with the exception of graphite as an electrode material, the development of the fundamental background of lithium insertion in intercalation compounds is necessary. In LiBs, there are several types of electrode with different reaction mechanisms to insert or remove lithium. Some are considered as conversion materials[79], others use an alloying-dealloying process[80], but most active materials rely on the insertion principle[81]. Here, the discussion is focused on intercalation compounds, and the thermodynamic and structural aspects of lithium insertion.

3.1 Should we use the term 'insertion' or 'intercalation' when dealing with such materials?

In the literature, both terms 'insertion' and 'intercalation' are used to describe materials that involve lithiation and delithiation processes. So far with literature, it is difficult to highlight the difference between these two terms since some authors speak about lithium 'intercalation' [82], while others use the term lithium 'insertion' [83] for the same active materials with no tendency associated with the publication year. Following the IUPAC definitions[15], 'insertion' is defined as an exact term and describes a 'reaction involving the transfer of a guest atom, ion or molecule into a host crystal lattice'. The term 'intercalation' is associated with other nouns such as 'intercalation reaction' or 'intercalation compound' and is very similar to the 'insertion' definition. The term 'intercalation reaction' refers to 'the penetration of a host material by guest species without causing a major structural modification of the host'. IUPAC suggests with a note that 'Intercalation can refer to the insertion of a guest species …' and 'Examples of intercalation reactions are the insertion of […] potassium into the layers of graphite (C_8K)'.

It is very difficult to find definitions that properly differentiate both terms, and the definitions can vary between different fields of science. Here, based on IUPAC definitions given in material science and chemistry, the term 'insertion' will be preferred when talking about the transfer or integration of guest entities (lithium) into the host structure, such as the 'lithium insertion', whereas 'intercalation' will be associated with other nouns to form terms that describe the insertion of a guest, such as 'intercalation mechanism' or 'intercalation compounds'.

3.2 Thermodynamic and structural aspects of lithium insertion

In electrochemistry, the characterisation of materials is based on the measurement of the cell voltage under open-circuit voltage (OCV). This voltage measurement depends on the chemical equilibrium established at both electrodes. Here, the chemical equilibrium implies the insertion/removal of lithium ions in the two electrodes and depends on the chemical potential of lithium in the two phases. For intercalation compounds, it depends on the way lithium organises and interacts with the host crystal structure, and any change in the local environment of lithium (at the crystal lattice scale) impacts the chemical potential. This chemical potential is related to the Gibbs free energy (G), a thermodynamic term used in the description of a chemical equilibrium. The chemical potential of lithium depends on its environment in the interstitial site[48], and evolves with the variation of free energy (Eq. 21).

$$\mu_{Li^+} = \left(\frac{\partial G}{\partial x}\right)_{T,P,n_i} \qquad \textit{Eq. 6}$$

Where μ_{Li^+} is the chemical potential of lithium in the host material and ∂x is the variation of electric charge.

In electrochemical cells, the voltage difference (Eq. 7) that is measured depends on the difference of chemical potential of lithium in the two electrodes.

$$E_{cell} = \frac{\mu_{Li^+}^{pos} - \mu_{Li^+}^{neg}}{-ne} \qquad \textit{Eq. 7}$$

Where $\mu_{Li^+}^{pos}$ and $\mu_{Li^+}^{neg}$ are the chemical potentials of lithium in the positive and negative electrodes, n is the number of exchanged electrons and e is the elementary charge.

In the case of a half-cell* composed of a positive electrode and metallic lithium as negative electrode, one can assume that the electrochemical potential of lithium in the metallic lithium electrode is constant upon dis/charging. This is true because the variation of free energy associated with lithium plating and stripping (Reaction II) on the negative electrode is constant.

$$Li_{(l)}^{+} + e^{-} \rightleftharpoons Li_{(s)}^{0} \qquad \textit{Reaction II}$$

Where $Li_{(l)}^{+}$ is the lithium ion solvated in the liquid electrolyte and $Li_{(s)}^{0}$ is the reduced lithium ion on the metallic lithium electrode.

In reality, one could consider that the lithium plating and stripping reactions take place on surface of lithium metal that is passivated by the SEI. If this interphase changes in chemical composition upon dis/charging, one should consider the chemical potential of electrons in the negative electrode as variable. This is not the case for sufficiently low current densities, and the cell voltage variations reflect the lithium chemical potential variations of the positive electrode.

It appears that the electrochemical behaviour (or signature) of a material strictly depends on its structural evolution upon de/lithiation, from a thermodynamic point of view. This introduces the different mechanism of lithium insertion in intercalation compounds, by distinguishing first-order and solid solutions transitions.

* In this manuscript, a half-cell is defined as an electrochemical cell composed of an electrode to study with respect to a reference electrode. This configuration enables the characterisation of the charge and discharge processes of an electrode (*e.g.* graphite). The half-cell term is selected with respect to the full cell term that concerns an electrochemical cell composed of two electrodes that are not considered as references. As an example, an NMC | graphite full cell is composed of two half-cells (NMC | Li and graphite | Li), where each electrode of interest is investigated versus the lithium reference electrode.

3.2.1 First-order transition, biphasic state

A first-order transition[84] involves the coexistence of two phases that remain stable in composition upon the transition. Structurally, a phase appears to the extent of another that disappears, with the coexistence of two crystallographic phases. This biphasic mechanism involves, *in fine,* an electrochemical reaction that is constant with phases of stable composition, and the variation of free energy is constant. Therefore, the chemical potential of lithium in the host structures is constant and the cell voltage (in the case of half-cells with a reference electrode, *i.e.* Li metal) should be perfectly stable, as schematised in **Figure 15a, b**. Another interesting representation is the analysis of accumulated electric charge as a function of the cell voltage (also called Differential Capacity Analysis, DCA). In first-order transition, a divergence should be observed on the derivative of accumulated electric charge as a function of the material potential. In practice, a very narrow peak is usually observed due to kinetic effects, as schematised in **Figure 15d**. The first-order transitions involve an hysteresis between charge and discharge with potential plateaus at a lower potential in lithiation than in delithiation, even under quasi-thermodynamic conditions[84].

A well-known material that illustrates this ordered insertion is $LiFePO_4$ (LFP), which undergoes the following electrochemical Reaction III:

$$LiFePO_4 \rightleftharpoons FePO_4 + Li^+_{(l)} + e^- \qquad \textit{Reaction III}$$

Using X-ray diffraction (XRD), Hess *et al.* observed the coexistence of two phases and their exchange in relative content[85]. In the X-ray diffraction patterns, this biphasic mechanism is characterised by a decrease of a phase to the extent of another one (**Figure 15c**). In parallel, the 2 theta (or q scattering vector) position of these two peaks is stable due to the constant diffraction plane length. Electrochemically, a potential plateau characterises the dis/charging of LFP electrodes in half-cells (vs. a stable reference electrode). The following schematics (**Figure 15**) illustrate this first order transition on structural, thermodynamic, and electrochemical aspects.

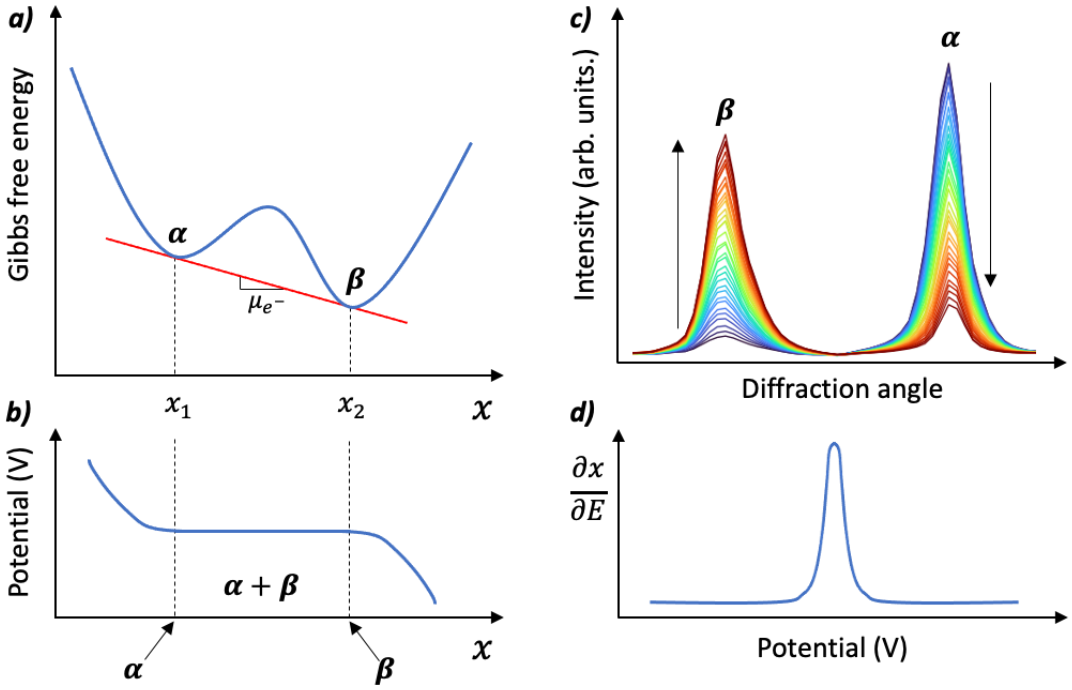


Figure 15: Illustration of a first-order transition. a) Gibbs free energy of the material as a function of the electric charge. b) Potential of the material as a function of the electric charge. c) Diffraction pattern illustrating the disappearance of the α phase and the appearance of the β phase with increasing the electric charge. d) Derivative of the accumulated charge as a function of the material potential (vs. a reference electrode). Inspired by ref. [48,84].

3.2.2 Solid solution transition, single phase state

Solid solutions are characteristic of materials that involve the insertion of lithium ions into interstitial sites without generating any additional phase. This insertion results in small modifications of the lattice parameters but without drastic symmetrical change most of the time inducing an increase in unit cell volume upon lithiation and *vice-versa*. This solid solution mechanism involves a phase that constantly changes in composition, and the variation of free energy is not constant upon dis/charging. The chemical potential of lithium in the host structure is no longer constant and no potential plateau is observed (**Figure 16a, b**). A good example of solid solution mechanism is $LiNi_xMn_yCo_zO_2$ (NMC) material that reacts exclusively through solid solution processes upon dis/charging[86,87]. Structurally speaking, a shift of the peak is observed by XRD because of the fluctuation of the Li content leading to modification of lattice parameters, while no change in the peak amplitude occurs[88] (**Figure 16c**). Electrochemically, no potential plateau is observed, instead, a smooth sloping of the potential curve (**Figure 16b**) occurs.

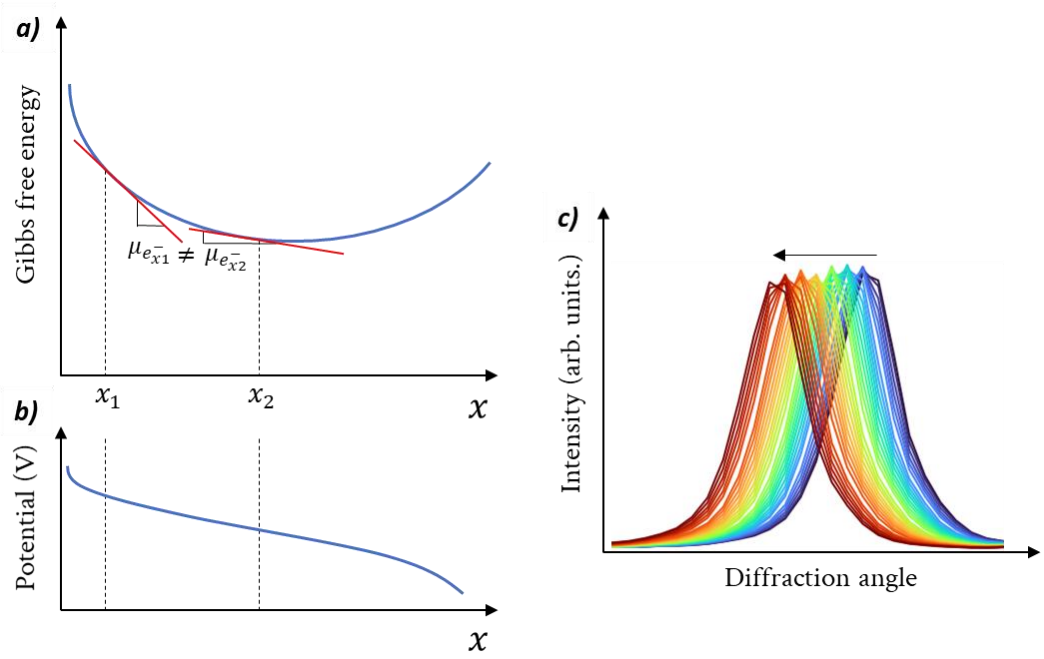


Figure 16: Illustration of a solid solution transition. a) Gibbs free energy of the material as a function of the electric charge. b) Potential of the material (vs. a reference electrode) as a function of the electric charge. c) Diffraction pattern illustrating the shift in diffraction angle with increasing the electric charge. Inspired by ref. [48,84].

4 THE EXCEPTION OF GRAPHITE

Graphite is the most commonly used negative electrode by dominating over more than 95% of the actual market[89]. This success relies on the abundancy of carbon and the low-cost associated to its implementation in LiBs. In parallel, graphite displays a high specific capacity (372 $mAh.g^{-1}$) compared to other electrode materials (reaching 150 - 200 $mAh.g^{-1}$), and the de/lithiation potential is low (0.08 – 0.2 V *vs.* Li^+/Li) enabling a high cell voltage[90]. Graphite is not only interesting for LiBs but also for potassium ion batteries, because of the possible insertion of this alkali metal inside the graphite sheets[91]. In addition, the SEI stability is by far the best on carbonaceous electrodes[46], contrasting with other materials such as silicon[92].

On the drawback side, graphite is suffering from poor power capabilities as seen in p**20**, which is urgent to overcome for EVs application. The low working potential, near the Li^+/Li redox couple, is also an issue because of the risk of metallic lithium deposition on the graphite particle surface, generating dendrite formation and growing that can short-circuit the cells. This plating phenomenon is an important research topic that still needs to be addressed[93].

Before trying to understand the issues related to graphite electrodes in terms of power capability, one has to address the lithium intercalation mechanism at the material level. This implies an understanding of the electrochemical signature of graphite and the structural evolution of this material upon de/lithiation. Obviously, both aspects will be linked in the next section.

4.1 Lithium intercalation mechanism in graphite

4.1.1 Structural aspects, graphite stages

Graphite is composed of graphene layers that are stacked along two crystalline forms, the hexagonal phase (2H, **Figure 17**) displays an ABAB stacking sequence, and the rhombohedral form (3R, **Figure 17**) is arranged following an ABCABC sequence. According to Shi *et al.*[94], the two phases are interchangeable and the 3R phase is favoured by grinding the graphite particles. Thermodynamically, a slight enthalpy difference of 0.6 kJ.mol^{-1} exists with the 2H phase more stable at normal temperature, distinguishing electrochemically the two phases is thus very difficult because only 6 mV/mol of graphite in potential difference exists. Structurally, the difference is visible, and appropriate refinement can help distinguishing both phases. By decreasing the particle size, a higher proportion of rhombohedral phase is observed, reaching around 30% of 3R for 6 µm graphite particles. In both cases, the insertion of lithium ions induces a rearrangement of the stacking sequence leading to a AAA form with a hexagonal unit cell, as illustrated in **Figure 17**.

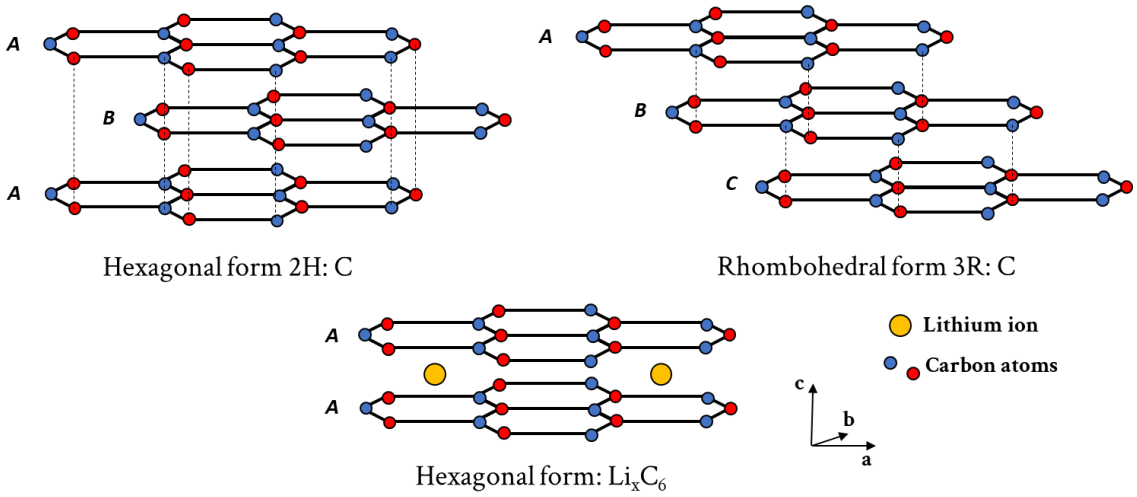


Figure 17: Illustration of the hexagonal and rhombohedral forms of graphite, and the hexagonal lattice of lithiated forms of graphite. Inspired from ref. [95].

Historically, the lithium insertion in graphite was evidenced by Herold in 1955[96], who observed the formation of a yellow compound resulting from the chemical reaction between graphite and lithium vapours around 500°C. Later on, Juzza and Wehle[97] described the LiC_6, LiC_{12} and LiC_{18} compounds, attributing the yellow colour observed by Herold to the LiC_6 phase. Starting from the 1970s, the lithiated forms of graphite were investigated by XRD and several phases, commonly called 'stages', were evidenced. This staging process consists in the insertion of lithium ions every nth layer of graphite. Along the through-plane direction (*c*-axis), a periodic sequence with empty and filled layers is established[98]. A nomenclature has been created defining a graphite stage as the occupancy frequency in the graphite layers, *e.g.* stage II corresponds to lithium ions inserted every two-graphite layer. Guerard and Herold chemically synthetized lithiated forms of graphite using

vapour of lithium and powder compression[99]. Based on the calculation of lithium content inserted in graphite, four stages were evidenced with stages I and II corresponding respectively to LiC_6 and LiC_{12} stoichiometries. Stages III and IV were also evidenced but uncertainties in the stoichiometries were noticed in the range LiC_{18}-LiC_{30} and LiC_{36}-LiC_{44}, respectively. These stages were characterised by XRD and the authors concluded on a hexagonal crystal lattice from the space group P6/mmm, for the LiC_6 and LiC_{12} phases. Pursuing with the characterisation of those stages, a binary phase diagram of Li - C was established by Fisher *et al.*[98] and Dahn *et al.*[100]. The authors mainly followed the (002) Bragg reflections that correspond to the plane containing a minimal periodic sequence of carbon honeycombs. In addition, the periodic insertion of lithium ions generates a superlattice structure (or supercell, with dimensions larger than the crystal lattice), creating Bragg reflections that do not exist in pure graphite. Following these peaks enabled the establishment of phase diagrams, *e.g.* LiC_{12} (stage II) has a distinct (002) reflection compared to both pure graphite (002) and LiC_6 (001). From these reports, it was widely admitted that the electrochemical insertion of lithium in graphite leads to a maximal stoichiometry of LiC_6. **Table 2** summarises the different stages and their stoichiometry that were evidenced in the literature, considering that these phases were all chemically synthesised or electrochemically obtained and isolated to be measured by XRD.

Table 2: Phases of Li_xC_6 compounds, reported from the literature.

Stage number	Phase stoichiometry (Li_xC_6)	References
I-L or VIII (8^{th})	LiC_{72} ($Li_{0.08}C_6$)	101–103
IV (4^{th})	LiC_{36} ($Li_{0.16}C_6$)	101–103
III (3^{rd})	$LiC_{30\text{-}27}$ ($Li_{0.2\text{-}0.22}C_6$)	101–105
II-L (2^{nd})	LiC_{18} ($Li_{0.33}C_6$)	101,102,105,106
II (2^{nd})	LiC_{12} ($Li_{0.5}C_6$)	101–103,105–108
I (1^{st})	LiC_6	101–103,105,107,108

Beside the through-plane ordering (along the *c*-axis) that is induced by lithium insertion, an in-plane ordering was also observed for several stages. For stages I and II, the same in-plane ordering was observed with a $P\left(\sqrt{3}\times\sqrt{3}\right) R\ 30°$ supercell. The P letter represents a primitive unit cell, $\sqrt{3}\times\sqrt{3}$ that corresponds to the unit cell's vectors length in units of lattice parameter a = 2.456 Å (a parameter of the hexagonal unit cell of pure graphite) and R gives the rotation angle compared to the graphite unit cell's angle ($\gamma = 120°$)[109,110]. This in-plane ordering is schematised in **Figure 18**. It can be seen that for stage II, the in-plane ordering corresponds to LiC_6 stoichiometry whereas in the through-plane direction, ½ layer is occupied leading to a LiC_{12} stoichiometry in average.

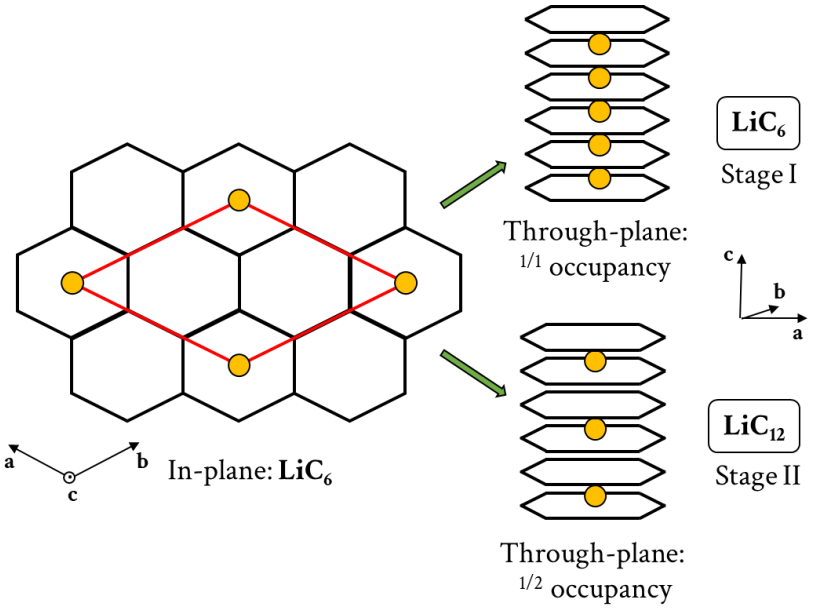


Figure 18: Illustration of the in-plane and through-plane crystal structures of stages I and II.

For higher stages, other superlattice structures were observed corresponding to $P(3 \times 3)\ R\ 0°$. **Figure 19** illustrates the in-plane and through-plane ordering for stages II-L and III, the in-plane average stoichiometry is LiC_9. In the case of stage II-L, ½ layer occupancy of lithium ions is observed through plane (being the reason for the order II denomination). *In fine*, an average stoichiometry of LiC_{18} is obtained. The same supercells were observed for stages III, IV and VIII[109,110].

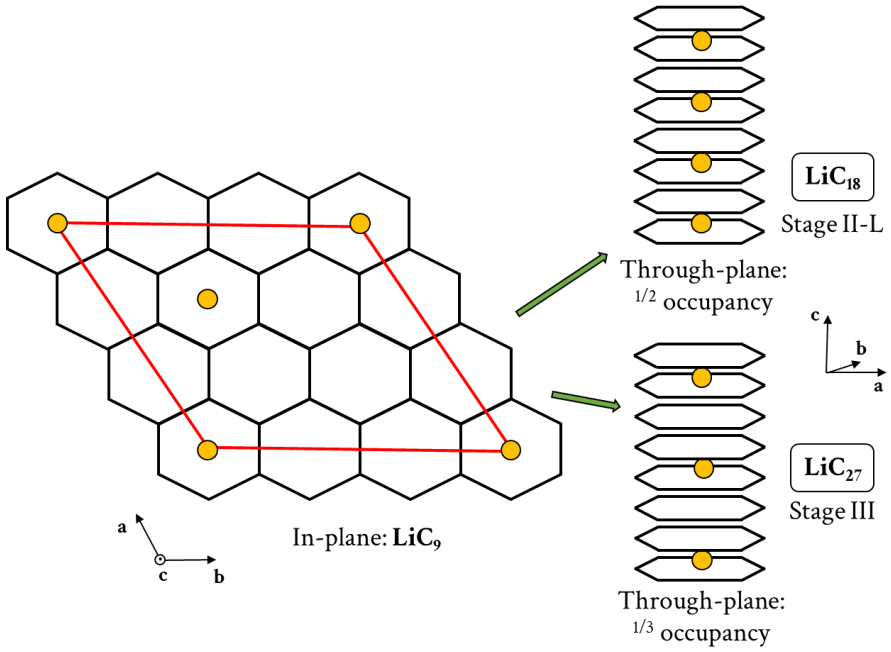


Figure 19: Illustration of the in-plane and through-plane crystal structures of stages II-L and III.

In the literature, the 'liquid-like' denomination is used to characterise some Li_xC_6 stages. This was attributed to stages that present a liquid character depending on the temperature. At specific temperatures, the "liquid-like" stages are stabilised and a long-range order exists in the through and in-plane directions; otherwise the localisation of lithium ions is very difficult due to the lack of long-range order. It is commonly accepted that a liquid-like form of stage II is observed (stage II-L, LiC_{18}), and Dahn claimed the disappearance of this stage II-L below 10°C[100]. For the stage I-L (or stage VIII), a debate in the literature is still observed. Based on Dahn's work[100], this phase is a diluted stage I (I-L), without in-plane order with intercalants in every graphite interlayer. Based on this, some consider this phase to be a solid solution[105,111], whereas some consider this intermediate to be a stage VIII with lithium intercalant in every eight graphite layers, supporting a "pure" LiC_{72} solid phase[109,110,112].

4.1.2 Dynamic evolution between Li_xC_6 phases and electrochemical signature

In terms of dynamic, the transition between these several graphite stages is achieved through two types of mechanism, solid solution transitions or first-order transitions (described in p**25**). In the 1990s, the phase transitions occurring during electrochemical cycling were obtained through *in situ* XRD measurement, where diffractograms were collected after a relaxation period (waiting to reach a quasi-thermodynamic equilibrium). Most of the papers denoted several two-phase coexistence at different state of charge of graphite, associated to first-order transition, and the following Reaction IV - Reaction VII were reported[101,103,112]:

$$LiC_{12} + e^- + Li^+ \rightleftharpoons 2\ LiC_6 \qquad \textit{Reaction IV}$$

$$2\ LiC_{27} + e^- + Li^+ \rightleftharpoons 3\ LiC_{18} \qquad \textit{Reaction V}$$

$$3\ LiC_{36} + e^- + Li^+ \rightleftharpoons 4LiC_{27} \qquad \textit{Reaction VI}$$

$$LiC_{72} + e^- + Li^+ \rightleftharpoons 2\ LiC_{36} \qquad \textit{Reaction VII}$$

For all of these reactions, two phases were systematically observed by XRD, and it was generally accepted that the insertion mechanism was achieved through first-order transition. Electrochemically, the graphite signature is shown in **Figure 20a** and the corresponding structural evolutions are given in **Figure 20b**. As explained in p**27**, a first-order transition (biphasic mechanism) is associated with a stable chemical potential of lithium, responsible for several potential plateaus. In contrast, several regions of high potential variations are attributed to solid solutions domains. Hess[113] highlighted a solid solution region right after the stage I formation; this point will be discussed later.

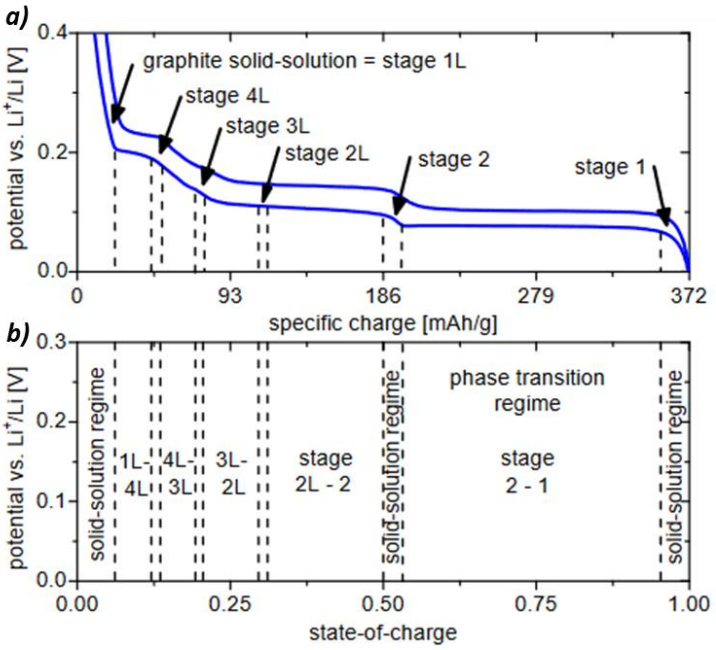


Figure 20: Electrochemical and structural evolution of graphite upon lithium insertion in half-cell. a) Potential vs. specific capacity plot. b) Structural states as a function of the state of charge. Reprinted with permission from ref. [113].

Using cyclic voltammetry, Levi and Aurbach characterised graphite electrodes in a three electrode cell (lithium as counter and reference electrodes) at very low scanning rate (4 μV/s)[103]. In **Figure 21**, one can notice the attribution of the peaks observed to the following Reaction IV - Reaction VII. The hysteresis, characteristic of first-order transition, is visible with a clear shift of the cathodic and anodic peaks. On the peak width, the authors attributed the larger width for thicker electrodes to different relaxation processes, probably suffering from lower kinetics of relaxation.

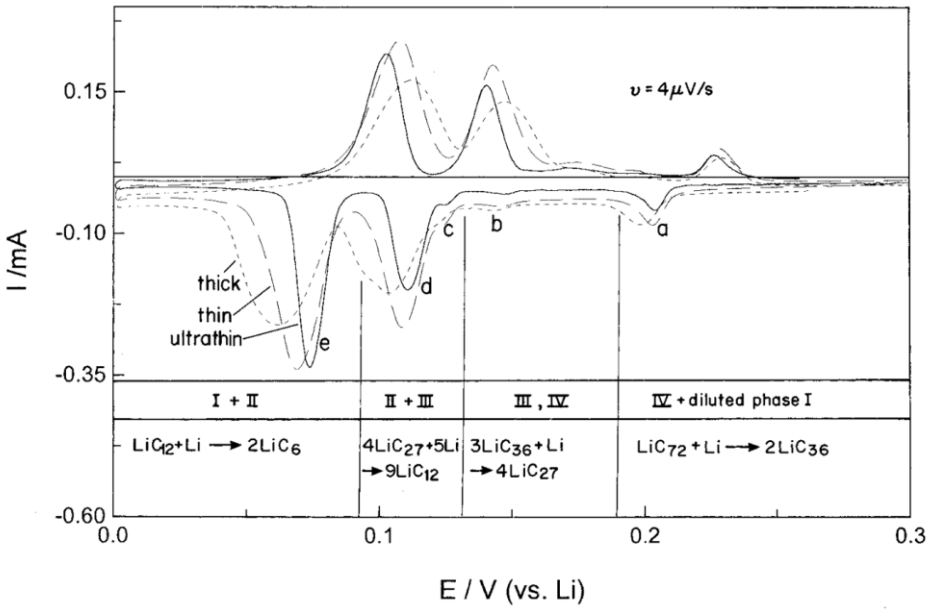


Figure 21: Cyclic voltammograms of thick, thin, and ultrathin graphite electrodes. Reprinted with permission from ref.[103].

In terms of structural evolution, the development of synchrotron facilities in the 1990s enabled the acquisition of diffraction patterns in a few seconds, leading to operando* characterisations. By scanning graphite electrodes upon de/lithiation, scientists reported the dynamic evolution of Bragg reflections of Li_xC_6 compounds with an excellent temporal resolution, offering new insight into the graphite phase evolution. Takagi et al. analysed the delithiation of a graphite half-cell and provided the evolution of the (00l) (**Figure 22a**) and (110) / (300) reflections (**Figure 22b**).

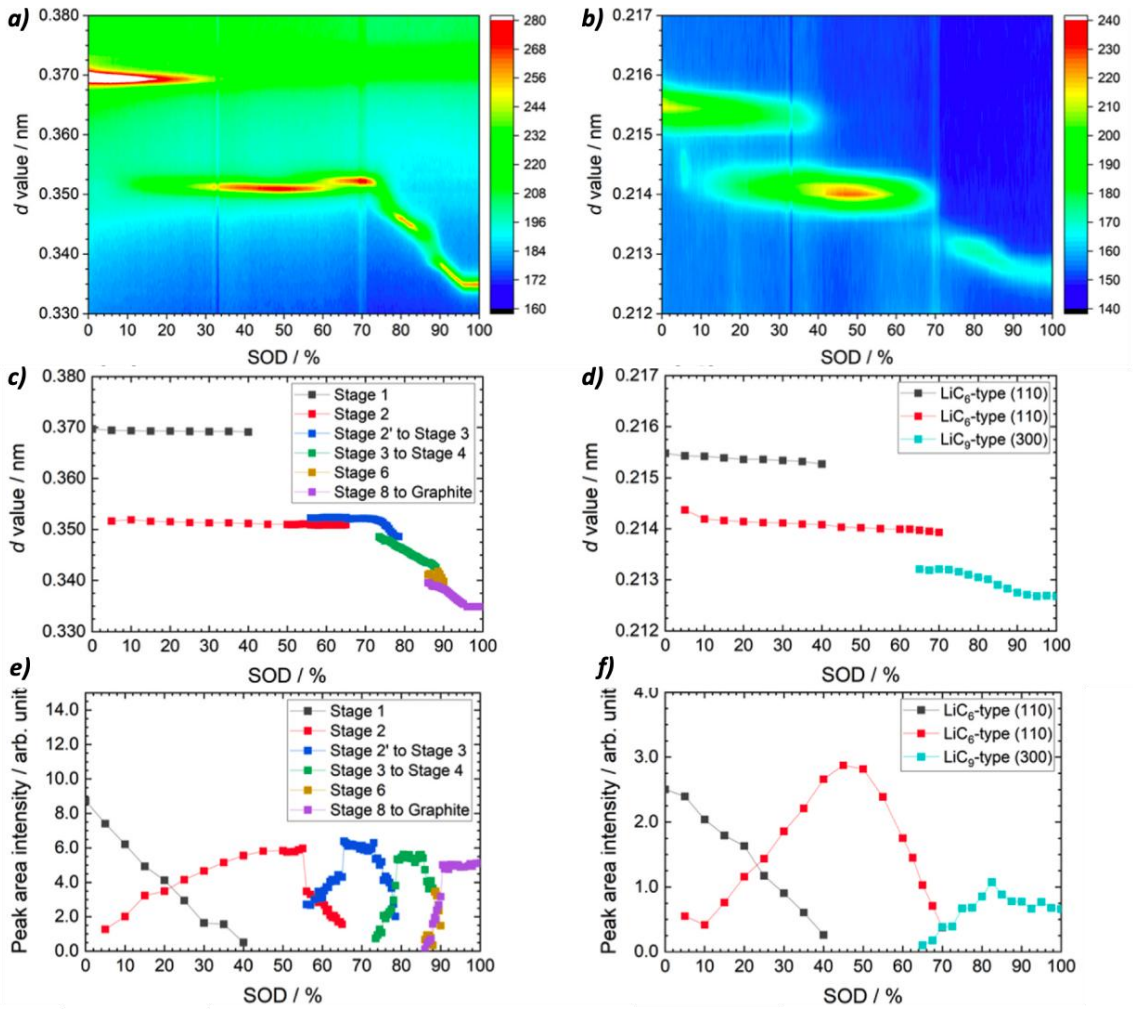


Figure 22: Contour plots of XRD profiles obtained upon delithiation of a graphite half-cell. a) 00l reflections and b) 110/300 reflections of Li_xC_6 compounds. c, d) d-values of the corresponding reflections. e, f) Amplitude of the several reflections. Reprinted with permission from ref. [112].

* *Operando* measurement has to be distinguished from *in situ* measurement, even if both terms were used for the same type of investigations few years ago. I*n situ* measurement stand for the characterisation of a system in equilibrium after bringing it to a desired state. In the case of batteries, it could be the acquisition of a diffraction pattern after charging a cell at a specific state of charge and waiting for the system to relax, reaching quasi thermodynamic equilibrium. *Operando* measurement refer to a "live" characterisation of the system, without pausing the system during the measurement. For batteries, it corresponds for example to the acquisition of diffraction patterns upon cycling of cell[114].

The x-axis represents the state of discharge of the cell (SoD). By fitting the Bragg reflections, the authors identified several phase transitions (**Figure 22c, d**). The first-order transitions were observed with the coexistence of two phases; as an example, stage I and stage II coexist until 40% SoD. In **Figure 22d**, the (300) reflection appears at 65% SoD, which correlates with the appearance of high order stages (stage III – VIII) that display LiC9-type in-plane ordering. The phase amplitude is also plotted in **Figure 22e, f**, where the almost linear exchange of amplitude between peaks of stage I and stage II was observed, characteristic of a first-order transition. Within this dynamic evolution, three regions display a monophasic character, with a peak amplitude (**Figure 22e, f**) that is stable upon discharge. These three regions correlate with the transitions of stage II-L → stage III, stage III → stage IV and stage VIII → graphite, and are characteristic of solid solutions state.

4.1.3 Ordering of Li_xC_6 compounds

Rüdorff and Hofmann[115] proposed a first model in which a uniform distribution of lithium ions exists throughout the graphitic structure (**Figure 23a**). This model implies rigid and flat planes of graphene. With this model (from the 1930s), no lithium heterogeneity is considered and it implies perfect first-order transitions. Later (in the 1970s), Daumas and Hérold proposed a model based on the presence of defects and deformations in the graphene planes[116]. This model implies clusters of Li_xC_6 compounds (stages) that are separated from each other due to deformations or bending of the graphene layers (**Figure 23b**). With this, the coexistence of multiple stages of graphite is possible, and this hypothesis can explain the possibility of transition between different stages that was not possible with the Rüdorff-Hofmann model. The Daumas-Hérold model does not apply for stage I, which follows the Rüdorff-Hofmann model[117]. The Daumas-Hérold model includes clusters ordered along the Rüdorff-Hofmann model but adds flexibility in the graphene layers.

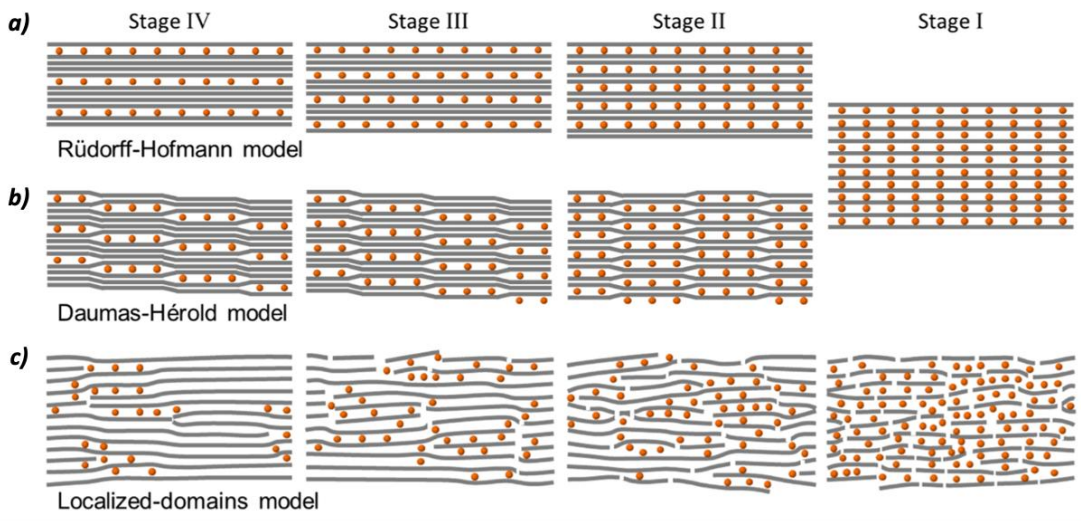


Figure 23: Illustrations of Li_xC_6 stages for different models. a) Rüdorff-Hofmann model, b) Daumas-Hérold model and c) localised-domains model. Reprinted with permission from ref. [118].

More recently, the use of advanced techniques of characterisation, such as cryo-transmission electron microscopy (TEM) enabled a better understanding of the graphite staging by probing the diffraction planes at the nanometer scale. Weng *et al.* analysed the different stages of Li_xC_6 compounds by cryo-TEM and provided a new model that combined the Rüdorff-Hofmann and Daumas-Hérold models[118]. In **Figure 24a-d**, the TEM images obtained for stages IV, III, II and I can be seen.

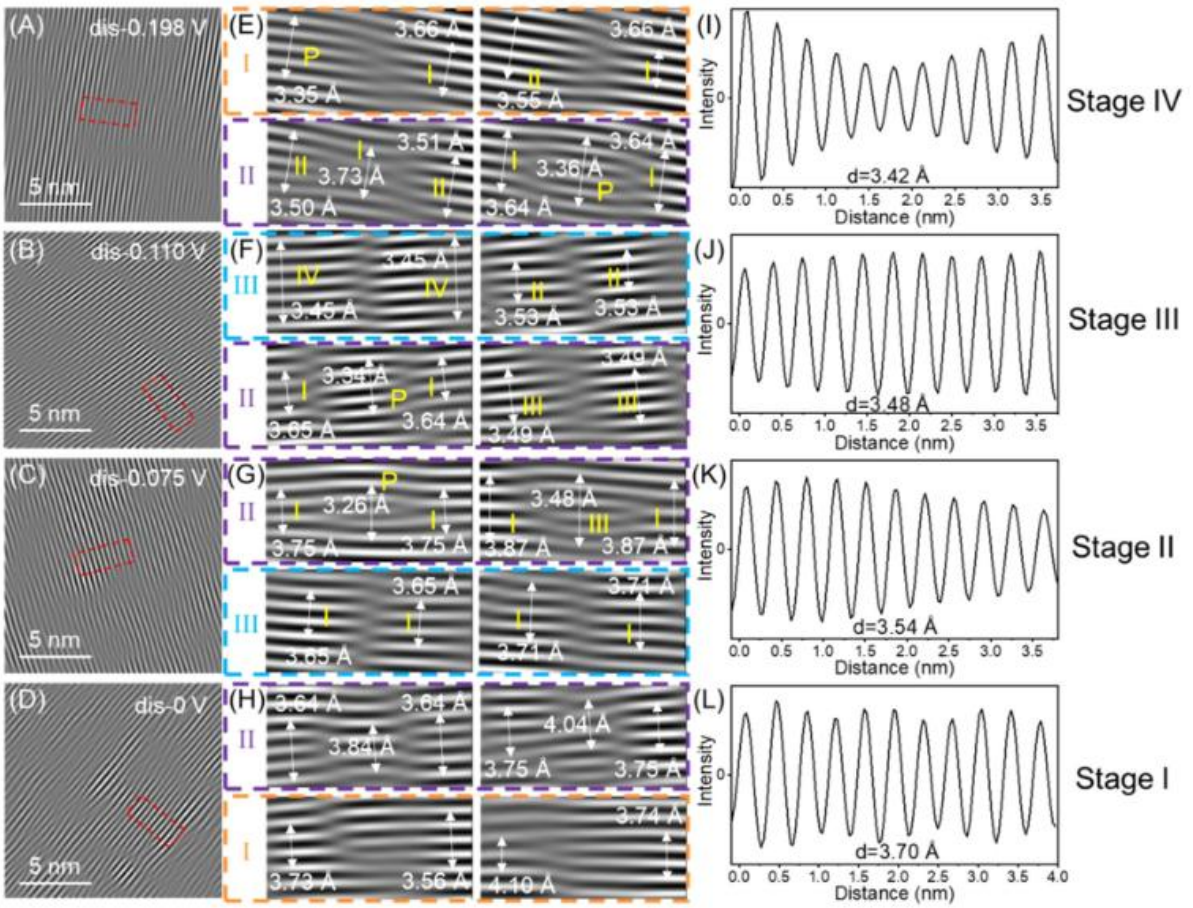


Figure 24: Long- and short-range orders of lithiated graphite. a-d) Cryo-TEM images. e-h) Defects in the structure with the corresponding d-spacing. i-l) Line scan profile of eleven graphene layers along the red marked regions in a-d panels. Reprinted with permission from ref.[118].

The authors attributed the discharge potential of 0.110 V to the formation of stage III (**Figure 24b**), while according to the literature, it corresponds to stage II-L formation. In their study, the authors used the terminology "macroscopic" and "microscopic" order, these terms have to be, respectively, interpreted as long-range order (obtained from XRD measurement) and short-range order (obtained from TEM measurement). From their observation, most of the stages observed at the macroscopic scale are composed of microscopic stages with different compositions (**Figure 24e-h)**; for example, the macroscopic stage II is composed of microscopic stages I and II-L that coexist. In **Figure 24g**, one can see the defect that separates the stages I and II-L (labelled III in the figure). With this 'Localised-domain model', schematised in **Figure 23c**, the macroscopic stages

(Rüdorff-Hofmann model) of graphite are composed of a mixture of microscopic domains that coexist (Daumas-Hérold model) with defects in the interphase regions.

At the particle scale, Hess and Novák investigated the dependence of graphite stages as a function of rate capability in thin-layer graphite electrodes and formulated a 'shrinking annuli' mechanism[119]. Similarly to the annuli of trees, graphite phases form at the edge of the particle and diffuse along the bulk (**Figure 25a**). With this model, lithium-ion diffusion takes place through several phases, *e.g.* starting in a pure stage I phase and diffusing toward interphase domains (Daumas-Hérold domains, see **Figure 25b**). This 'shrinking annuli' model has important implications, especially for the use of Fick's law, which cannot be applied over the entire particle volume because of the phase boundaries.

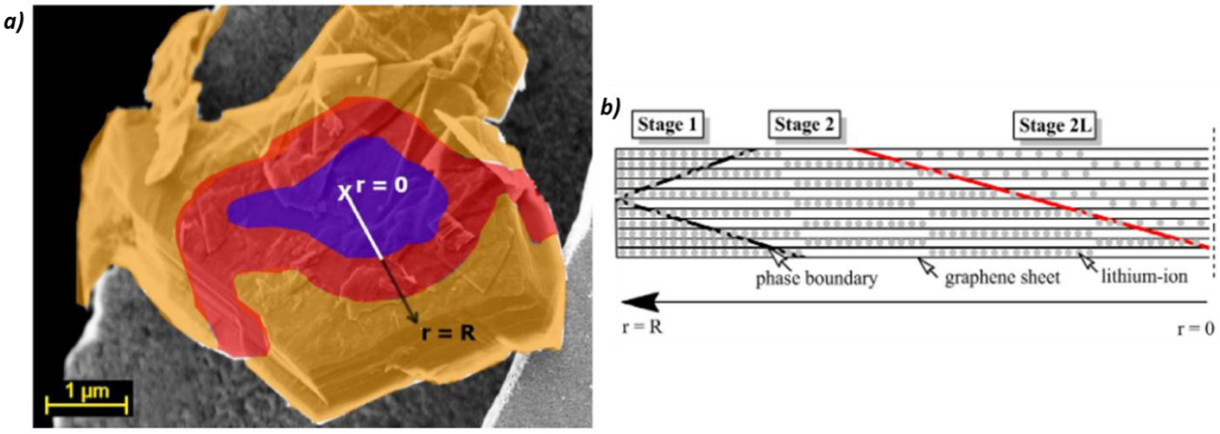


Figure 25: Shrinking annuli model. a) Single graphite particle (stage I in gold; stage II in red and stage II-L in blue) sketch. b) Simplified 2D phase distribution along the arrow on the left part. Reprinted with permission from ref.[119].

In this section, the lithium intercalation mechanism was discussed and the several stages of graphite were addressed with respect to structural and electrochemical aspects. On this basis, the next section focuses on the electrode level with the aim of understanding the impact of engineering on the power performance.

4.2 Engineering of the graphite electrode

4.2.1 Effect of the electrode casting and the binder

Wet-process

Historically, LiBs electrodes were prepared using a wet process as described in **Figure 26**. Active materials are usually mixed with carbon additives and binders in solvent. The slurry is casted on a current collector and dried using different possible methods, mainly based on heating[120].

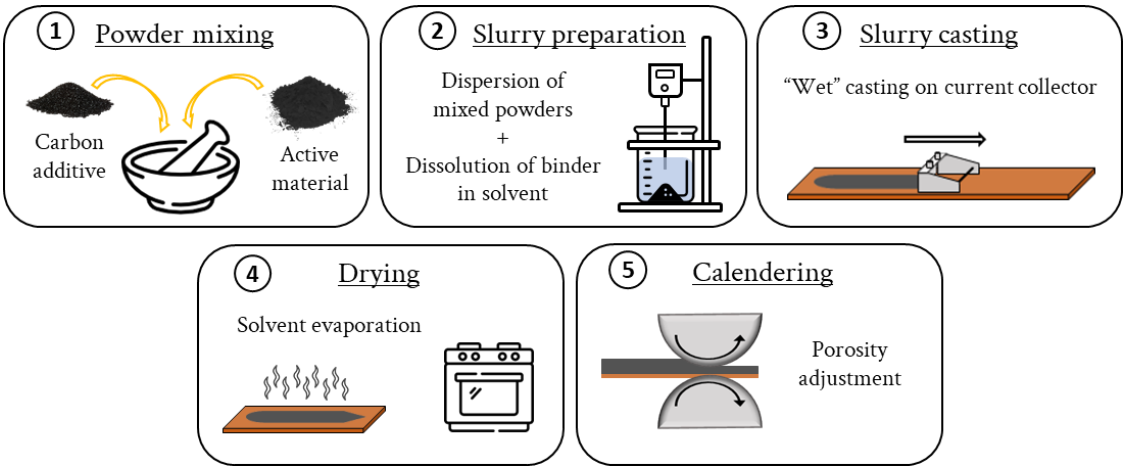


Figure 26: Illustration of an electrode elaboration based on wet process.

With wet-processing, multiple studies demonstrated a non-uniform distribution of components in the electrode due to the drying process. As an example, Li and Wang[121] studied the impact of using organic solvent (N-methyl-2-pyrrolidone, NMP) or water in the elaboration of $LiCoO_2$ (LCO) electrodes. With both solvents, a non-uniform distribution of binder was observed along the drying direction, with an increase in the amount of binder on the top of the electrode. This heterogeneity was attributed to the flow of solvent evaporation during the drying step. For the conductive additives, rearrangements were also observed with the organic-based process, whereas a water-based process was not subject to this. For the authors, this difference was attributed to the lower viscosity of the organic-based ink, but the different binders can also be responsible for different interactions with the particles and induce differences in the drying process.

Stein *et al.*[122] discussed the role of evaporation on electrode microstructure and cell performance. Especially, sedimentation was observed for particles of micrometric scale, whereas this effect was negligible for nanometric particles. Using Energy Dispersive Spectroscopy (EDS) on a Scanning Electron Microscope (SEM), disparities of secondary phases (carbon additives and binder) were observed with a larger amount of binder near the current collector. This study demonstrates that the rate of evaporation drives the structuration of the secondary phases, and a fast-drying process is recommended to prevent the particle sedimentation.

From these two examples, very different results were observed for electrodes prepared through a similar wet-process with polyvinylidene fluoride (PVDF) and NMP, with in one case the binder distribution following the evaporation rate and in the other one following the sedimentation. This highlights that using a wet-process can provide significant differences in electrode microstructures, only regarding the drying step. The heterogeneities of component distribution in electrodes should be avoided to minimise side effects such as non-uniform current distributions. To overcome these issues, one solution could be the elaboration of electrodes with a dry-process, also called a solvent-free process.

Dry-process

The dry-process relies on dry mixing of the material powders, implying the use of compatible binders such as polytetrafluoroethylene (PTFE). By mechanical mixing, the binder undergoes a stretching to form fibrils (fibrillation) that bridge the active material and carbon additives. The solid mixtures are then hot-laminated onto a current collector. Using wet-processing of electrodes, Hwang *et al.*[123] demonstrated that particles rearrangement in electrodes can lead to high local tortuosity that can decrease the kinetics of lithium intercalation/deintercalation. By proceeding with solvent free electrode casting using PTFE as binder, the authors claimed that larger active surface areas are obtained because of the PTFE bridges linking the graphite particles on the basis of the measurement of ionic resistance by EIS, compared to the wet-process, where the polymer binder probably covers the active particles. In the rate capability test performed at 5 C rate, the dry-processed electrodes systematically displayed higher specific capacities than the wet-processed electrodes, due to lower overpotentials. This effect was attributed to a lower ionic tortuosity value for the dry-process (determined by EIS), improving the mobility of lithium ions in the electrode porosity.

Other studies investigated the comparison of graphite electrodes prepared by wet-processing with carboxymethylcellulose (CMC)/styrene-butadiene rubber (SBR) binders and dry-processing with PTFE[124]. Suh *et al*[125]. demonstrated the relevance of the dry process. As illustrated in **Figure 27d, e**, the dry-processed electrode displays better rate capability with a higher Constant Current (CC) contribution at each cycling rate than the wet-processed electrode. The authors measured the effective diffusivity of lithium ions through the porosity of the electrode using GITT and CV (**Figure 27b, c**) and claimed higher diffusion coefficients for the dry process with both techniques. It is surprising to observe diffusion coefficients that vary with the electrode state of charge while measuring the effective diffusivity in the electrode porosity. One can suspect that the measured diffusion coefficient is representative of the solid-state transport of lithium (in the bulk of graphite particles), and not from the diffusivity of lithium in the porous structure. The authors also investigated the diffusion resistance and tortuosity factors by EIS and observed significant lower resistances for the dry-processed electrode, inducing lower tortuosity.

The obtained results agree with those of the study mentioned above, demonstrating that dry-processed electrodes provide better power capabilities than their wet-processed homologues by decreasing the ionic tortuosity and facilitating the diffusion/migration of lithium ions in the electrode microstructure.

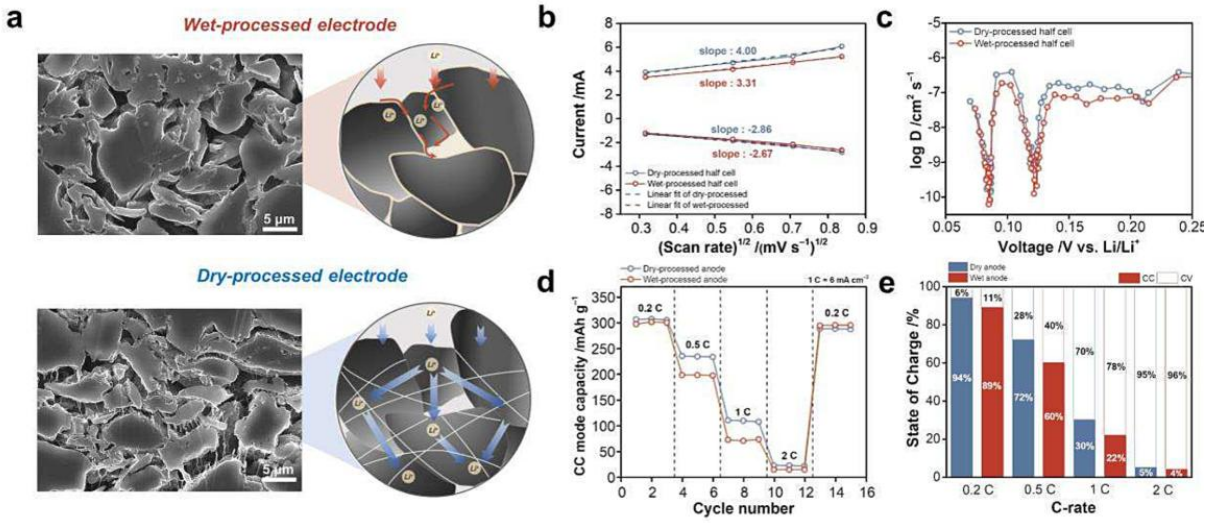


Figure 27: Comparison between wet-processed and dry-processed graphite electrodes. a) Cross-sectional SEM images of both electrode process. b) Evolution of peak current vs. the square root of scan rate. c) Diffusion coefficient obtained by GITT. d) Rate capability test. e) CC-CV charging capacities as a function of cycling rate. Reprinted with permission from ref.[125].

As a summary, **Table 3** highlights the advantages and drawbacks of wet and dry processes for the elaboration of electrodes.

Table 3: Advantages and drawbacks of wet and dry processes[*].

Criterion	Wet-processing	Dry-processing
Safety & Environmental impact	✗ Use of CMR solvents	✓ No solvent needed
Cost	✗ Higher (drying step)	✓ Lower, very fast process
Adaptability	✓ Flexible for many materials	✗ Limited in terms of binder
Coating quality	✓ Good uniformity and adhesion	✗ Homogeneity and adhesion issues

Other more exotic strategies can be employed to increase the power capabilities regarding the method of electrode casting. Billaud *et al.* worked on the magnetic alignment of graphite flakes on a highly loaded electrode (10 mg.cm^{-2}). The alignment was realised during the drying process of the graphite inks by applying a rotating magnetic field. As described in **Figure 28b**, the casted electrode obtained displays graphite flakes aligned along the thickness direction (*z*-axis), increasing the accessibility of the graphite edges for lithium ions (see **Figure 28c**). A lower geometric tortuosity factor along the *z*-axis, decreasing from 14.0 to 3.8. As a consequence, the rate capabilities (**Figure 28a**) obtained are significantly higher for the aligned graphite electrode,

[*] CMR: Carcinogenic, mutagenic or reprotoxic.

demonstrating the positive effect of electrode structuration[126]. However, this electrode structuration cannot support a calendering step that would collapse the flakes alignment.

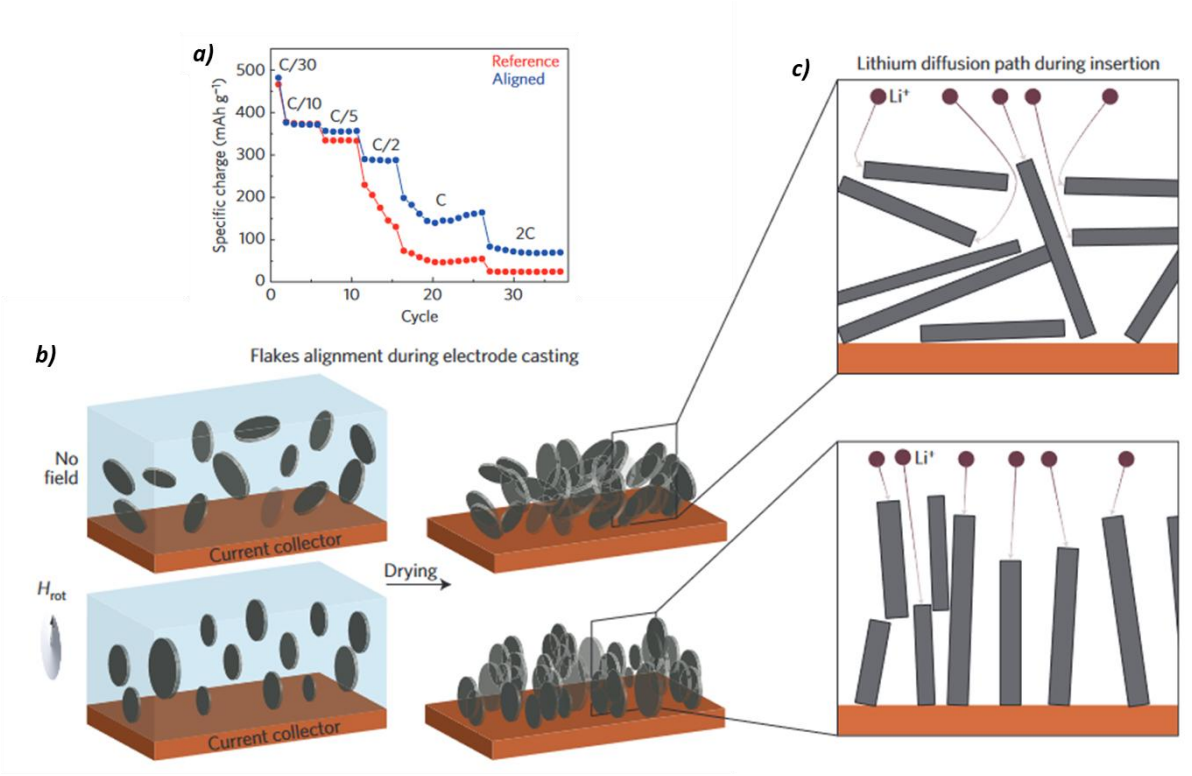


Figure 28: Effect of the graphite flakes alignment. a) Rate capability results for a classical electrode not magnetically aligned and for the aligned sample. b) Casting of the graphite electrodes with and without magnetic field applied during the drying process. c) Lithium diffusion paths for both electrode microstructure. Reprinted with permission from ref. [126].

4.2.2 Effect of electrode porosity and tortuosity

For EVs, the highest energy density is suitable for providing a high autonomy that requires a thick and dense electrode[127]. However, increasing the density of electrodes is far from having only beneficial effects because of the increase in tortuosity. As a consequence, one has to find the optimal electrode densities that provide the best energy/power combination. A standard and low-cost procedure for electrode compaction is calendering using hard pressure rollers as schematised in **Figure 29a.**

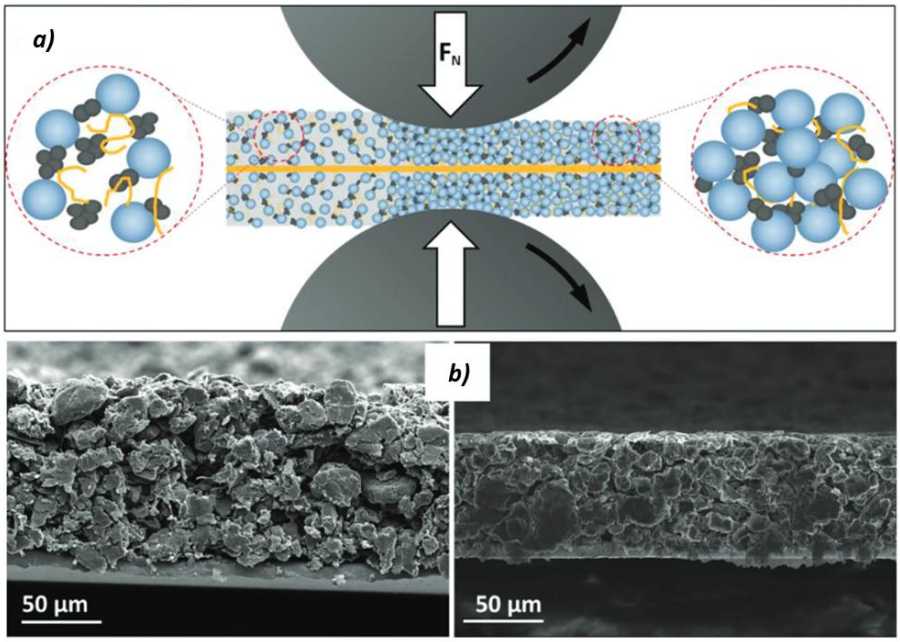


Figure 29: Illustration of the calendering process. a) Effect on the active material particles (blue), binder (yellow) and carbon additive (grey) contacts. b) SEM cross-sections of graphite electrodes before and after calendering. Reprinted with permission from ref.[127].

Antartis *et al.*[128] investigated the effect of porosity in graphite electrodes and their mechanical properties in response to stress-strain tests. For porosities ranging from 70% to 35%, the authors investigated the electrochemical response in terms of available capacity for the two first cycles and the capacity retention at C/5 rate and demonstrate optimal properties at 45% porosity for graphite particles below 20 µm. For the first two cycles (C/30), a decrease of the lithiation and delithiation capacities was observed while decreasing the porosity from 50% to 35%, whereas for higher porosities, similar capacities were obtained. These observations were attributed to the optimal electrode wetting in the case of sufficient number and size of opened-pores, the authors suggest that for porosities lower than 45%, the pore closing decreases the graphite particles accessibility to lithium ions. In terms of capacity retention at C/5 cycling rate, higher capacity fading was observed above 50% porosity whereas a stable retention was obtained below 50% porosity. To understand the origin of this difference, the stress-strain responses of the different electrodes were also investigated. The better mechanical integrity was obtained for electrodes with 40% porosity, and increasing the electrode porosity led to lower mechanical tensile strength. With this study, one can notice the complex relationship existing between the electrode porosity, the mechanical strength and the electrochemical performance.

Singh *et al.*[129] found a similar conclusion by investigating the effect of porosity on highly loaded and porous graphite electrodes (41 $mg.cm^{-2}$ and 48% - 58% porosity). To ensure a proper mechanical integrity and electronic conduction, the authors added carbon fibres to enhance the long-range electronic percolation. It was observed that calendaring the electrode decreases the

contact resistances by improving the electronic network. In addition, no gain in power capability (estimated by rate capability test) was noticed for porosities higher than 50%.

In these studies, the authors highlighted the relationship between the porosity of the electrode and their electrochemical performance without mentioning the tortuosity. Guo *et al.*[130] quantified the ionic tortuosity for graphite composite electrodes, with artificial holes along the electrode thickness. Two types of holes were realised (**Figure 30a-d**), with holes crossing the half-electrode thickness (blind holes, B-H) and with holes crossing the whole thickness (through holes, T-H). For a classical graphite electrode (without holes), a tortuosity of ~ 25 was obtained, whereas the presence of holes decreased the tortuosity to ~ 15 for B-H and ~ 9 for T-H (**Figure 30e**). Vertical pathways along the electrode thickness reduce the ionic resistance associated to lithium-ion mobility through the electrode microstructure. Additionally, the authors quantified the electronic resistivity R_{elec} of graphite electrodes by changing the porosity. A decrease in R_{elec} was observed by decreasing porosity from 77% to ~ 45%, whereas no gain in electronic conductivity was observed by further decreasing the porosity until ~ 30%, probably because the percolation threshold was reached.

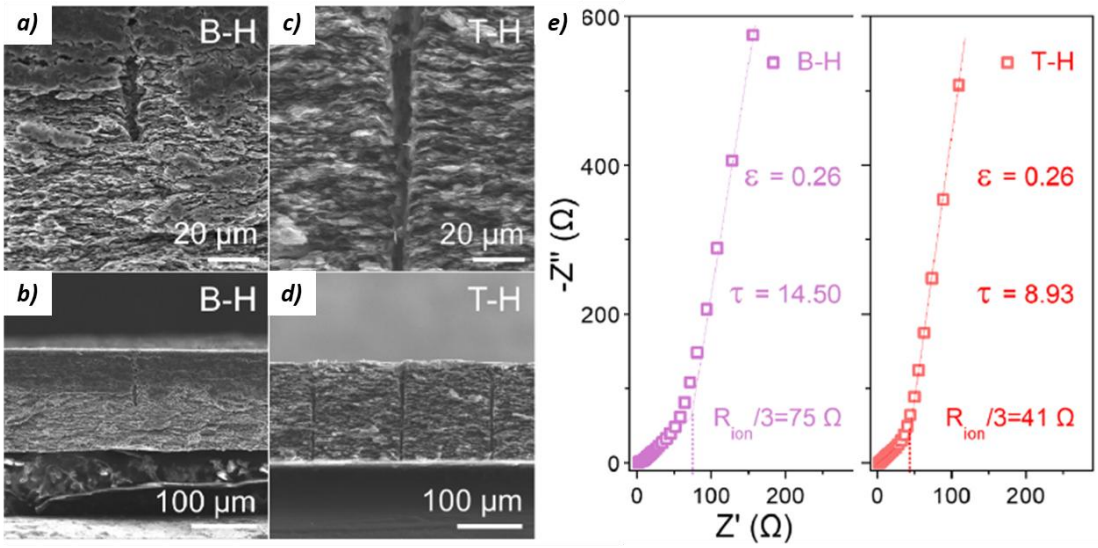
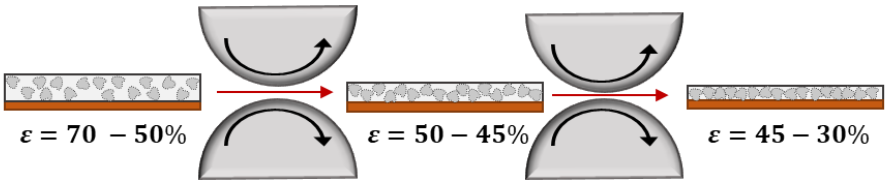


Figure 30: a, b) Cross sectional SEM images of graphite-flakes electrodes with blind-holes (B-H) and c, d) graphite-flakes electrodes with through-holes (T-H). e) EIS spectrum of symmetrical cells with B-H and T-H electrodes. Reprinted with permission from ref. [130].

Thus, an optimal porosity around 45 – 50% was found for graphite particles < 20 µm with flakes-shape. A summary of the effect of porosity is given in **Figure 31**.



Porosity	> 50%	50 – 45%	< 45%
Mechanical strength	✗ Poor tensile strength	✓ Excellent tensile strength	
Electrode capacity	✓ Maximal → optimal pores wetting		✗ Limited → bad pores wetting
Ionic transport	✓ Optimal → low τ_{ion}	~ Median	✗ Poor → high τ_{ion}
Electronic transport	✗ Poor → high R_{elec}	~ Median	✓ Optimal → low R_{elec}

Figure 31: Summary of different properties for graphite electrodes at different porosities. The suggestions made here refer to flakes-shape graphite particles < 20µm, and probably differ for other types of graphite particle shape or size.

4.2.3 Effect of the particle shape and size

The particle size is an important factor to adjust the power properties of graphite electrodes. Natural graphite, as illustrated in **Figure 32**, displays flakes-shape with large dimension along the basal plane (parallel to the graphene sheet plane) and much lower dimension along the edge plane (normal to the graphene sheet plane), generating a high particle anisotropy. The issue with this morphology is that the edge of the particles are the sites of lithium insertion, whereas the basal planes cannot achieve insertion. Also, electrolyte decomposition is much more catalysed on the edge sites[131]. It implies that the reactivity towards chemical (oxidation for example) and electrochemical reactions (lithium insertion) is very dependent on the volume to surface ratio, and then on the particle size and shape. As an example, the SEI formation highly depends on the particle size. During the first lithiation of a cell using graphite as negative electrode, a part of the electrons injected into the graphite conduction band serves to decompose the organic solvents, salt or electrolyte additives (around 0.8 V vs. Li^+/Li) and specific capacities larger than 372 $mAh.g^{-1}$ are achieved. During the delithiation of the graphite electrode (oxidative condition), this passivation layer is stable and is not oxidised for potential lower than 1.5 V* vs. Li^+/Li[132,133]. As a consequence, an irreversible capacity loss (ICL) is observed for the first charge/discharge step, with a coulombic efficiency (CE) easily lower than 90%.

* The oxidation potential of the SEI depends on the solvents used and the eventual additives such as fluoroethylene carbonate (FEC) or vinylene carbonate (VC).

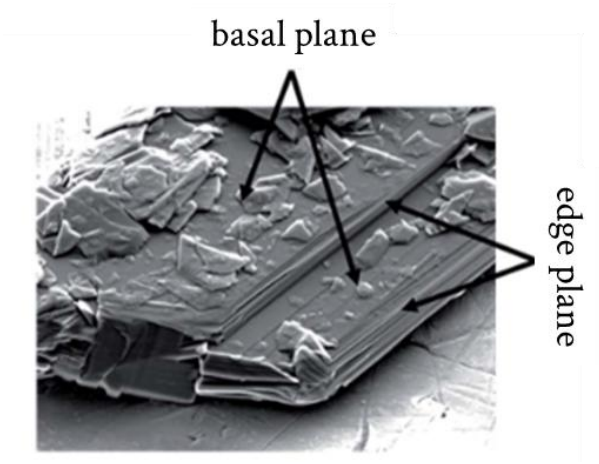


Figure 32: SEM image of a graphite flake. Reprinted with permission from ref.[134].

Zaghib *et al.*[135] investigated the effect of the particle size on the ICL. As expected, a larger ICL was observed for graphite particles with the lowest particle size (**Figure 33a**), with almost 100 $mAh.g^{-1}$ of ICL for particles of 12 $m^2.g^{-1}$ BET surface area and only 20 $mAh.g^{-1}$ for 2 – 4 $m^2.g^{-1}$ particles. Based on the ICL coming from the edge and basal planes, the authors calculated the reaction constant associated to the two sites with five times higher kinetics for the edge sites (k_e (edge) and k_b (basal), in $mAh.m^{-2}$). From their observation, k_b and k_e are independent from the particle size, supporting the following hypothesis: the magnitude of the ICL does not directly depend on the particle size but on the relative fraction of edge and basal plane sites, and this depends on the particle BET and its shape.

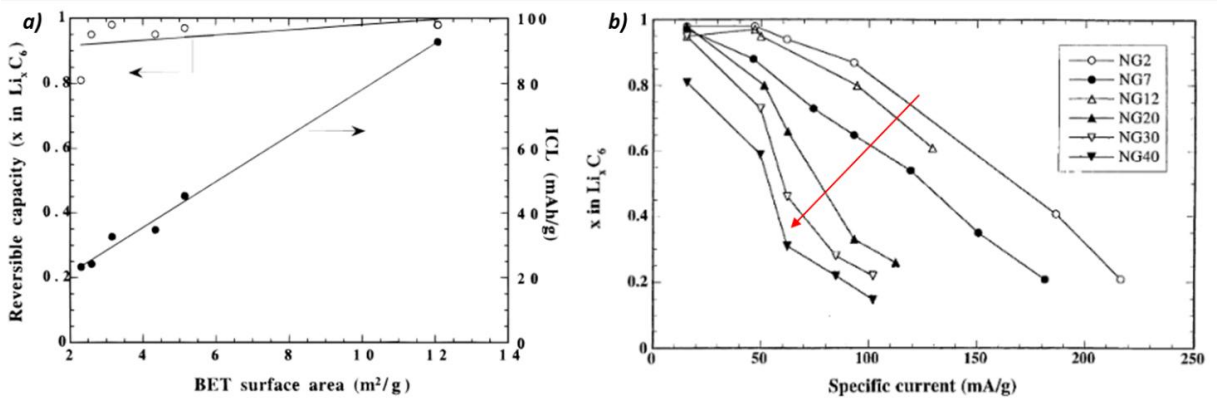


Figure 33: a) Relationship between reversible and irreversible capacities as a function of the surface area of natural graphite. b) State of charge of the natural graphite, x in Li_xC_6, as a function of specific current for different size particles. The red arrow shows the trend of increase in particle size. Reprinted with permission from ref. [135,136].

The authors investigated the effect of the particle size on the lithium intercalation rate in the same natural graphites[136]. In **Figure 33b**, lower specific capacities were observed when increasing the particle size, at an equivalent charging rate. The authors claimed that the Li-ion diffusion to the edge sites is not the limiting factor, but the solid-state diffusion of lithium would limit the specific capacity.

To improve the power capability of graphite electrodes, some authors opted for the spheroidisation of particles. Zaghib *et al.* synthesised spherical particles (potato-shaped, see the inset of **Figure 34**) from natural graphite flakes[137]. With this shape, the graphite particles display higher fractions of edge sites, and the accessibility for lithium ions is increased. As a result, the rate capability (**Figure 34**) is better for spherical particles that show a higher available capacity at an equivalent C-rate compared to the natural particle shape.

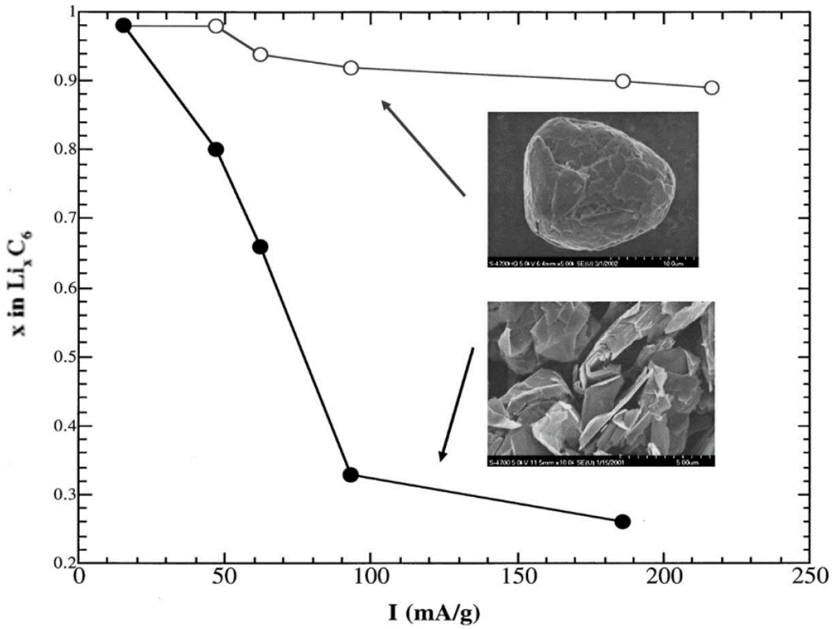


Figure 34: State of charge of graphite electrode, x in Li_xC_6, as a function of the specific current for flakes-shaped (black dotes) and potato-shaped (white dotes) graphite particles. Reprinted with permission from ref.[137].

Similarly, Fischer *et al.* studied the fast-charging capability of spherical, flakes-shaped, and pancake-shaped graphite particles[138]. Not surprisingly, the specific capacity available by increasing the charging rate is higher for spherical particles than for the flakes and pancake shapes. This was interpreted as the result of a lower diffusion resistance of lithium ions for spherical particles. If the authors did not mention tortuosity aspects, one can suspect that a lower ionic tortuosity is obtained for spherical graphite particles because of the higher particle isotropy[139]. The lower diffusion resistance could be attributed to both i) a higher fraction of edge sites, increasing the kinetic of lithium intercalation and ii) a lower ionic tortuosity, decreasing the diffusion time along the electrode thickness.

4.3 Understanding the rate capability limitation of graphite electrodes by *operando* characterisation

To go deeper into the understanding of power limitation of graphite electrodes, a powerful method is the combination of material characterisation and electrochemical cycling. O*perando* investigations can correlate the evolution of the material properties with the electrochemical signature.

4.3.1 Optical characterisations

Upon lithiation, the band structure of graphite changes and the optical properties change as well. In its pristine state, graphite exhibits an overlapping between π-π^* orbitals, and one considers it has a no bandgap material[140]. This overlap is responsible for the semi-metallic properties of graphite[141] and its black colour, indeed a lot of optical inter-band transition (electron promotion from π to π^* orbitals) are possible, enabling the absorption of the whole visible light spectra (between 1.65 eV and 3.26 eV[142]). As lithium is inserted, an increase of the delocalised electrons density is observed in the conduction band and favours intra-bands transitions[143]. These transitions can be induced by optical excitations of electrons and take place within a band as illustrated in **Figure 35**. As a result, plasmonic effects (synchronised oscillation of electrons) appear and are responsible for a discrete absorption of light in the visible domain. Depending on the lithiated graphite stage, the colour varies because of the change in the band structure, and very distinct colours are observable upon lithiation. As an example, LiC_{12} and LiC_6 phases were analysed by reflectivity measurements, and transitions of 1.75 eV (reddish colour) and 2.0 - 2.75 eV (gold colour) were observed by Basu *et al* [144].

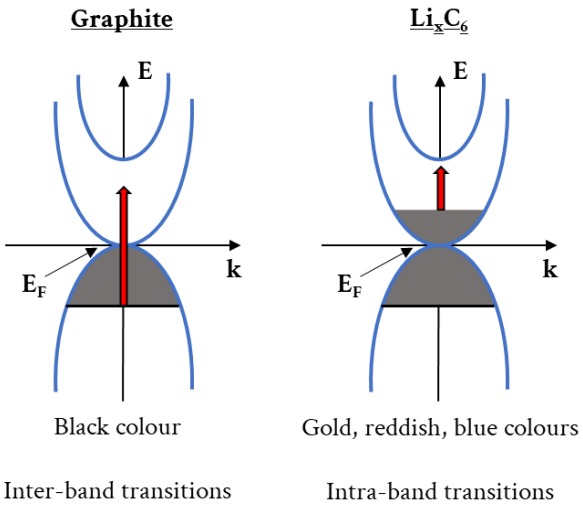


Figure 35: Illustration of inter-band and intra-band transitions in graphite and Li_xC_6 compounds.

Thus, *operando* optical characterisations of graphite electrodes can help to understand the heterogeneities of lithiation. Kang *et al.* studied the hysteresis between charge and discharge of a graphite half-cell using an optical microscope[145]. In **Figure 36**, the colour of the graphite electrode can be observed upon lithiation with the appearance of the goldish colour at the separator/electrode interface. A front of lithiation is observed with the propagation of the goldish phase (stage I) toward the current collector/electrode interface. According to the authors, the spatial distribution of lithium content was larger in transition regions (*a priori* two-phase domains). This front of lithiation indicates that the graphite electrode is limited by the liquid phase transport of lithium, with favoured kinetics near the separator/electrode interface. In addition, it was demonstrated that the electrode delithiation was more homogeneous, supporting better kinetics during delithiation.

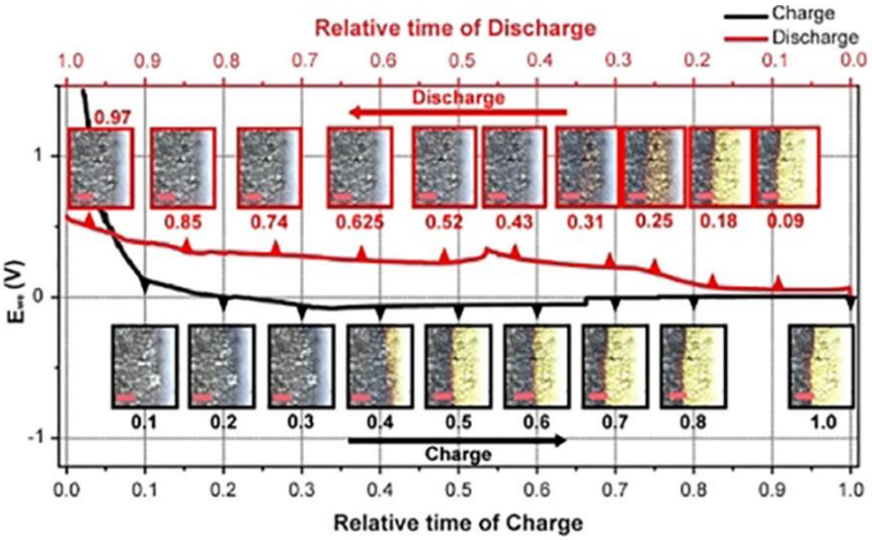


Figure 36: Optical images of the graphite electrode and its potential as a function of relative time of charge (scale bar 100 µm in red). Reprinted with permission from ref. [145].

Due to the changes in electrical conductivity upon lithiation, Raman spectroscopy is also adapted to probe graphite and Li_xC_6 compounds. Pristine graphite exhibits two main characteristic bands: i) the G band is associated to the vibration of the C-C bond in-plane (sp^2 orbitals) and ii) the D band is associated to disorder and defects on the graphitic surface (sp^3 orbitals)[146]. The G band is dominant in graphite and is highly impacted by the insertion of lithium. For this reason, many studies reported the lithiation of graphite *in situ* or *operando* measurement by Raman spectroscopy[147–150]. With the idea of studying the lithiation heterogeneities in thick graphite electrodes, Maruyama characterised by Raman spectroscopy the de/lithiation at the separator/electrode and electrode/current collector interfaces[151]. By comparing the evolution of the G band upon lithiation and delithiation at both interfaces, the author highlighted a reaction distribution with a higher kinetic near the electrolyte side. Despite the lack of a figure

summarising these observations, this study demonstrates the interest of Raman spectroscopy to probe the structural heterogeneities of de/lithiation upon cycling.

4.3.2 X-ray diffraction experiments

Because of the several stages and the through- and in-plane ordering that take place in graphite, X-ray and neutron diffraction can serve to probe the structural state of graphite upon de- and lithiation. Combining high spatial and high temporal resolution, Yao *et al.* investigated the diffraction signal of graphite electrode at different positions along its thickness upon cycling at 1 C rate[152]. **Figure 37a** is an X-ray radiograph of a full cell probed composed of graphite and NMC 532. In **Figure 37b-f**, the diffraction patterns acquired on charge and discharge are given as a function of the position in the graphite electrode.

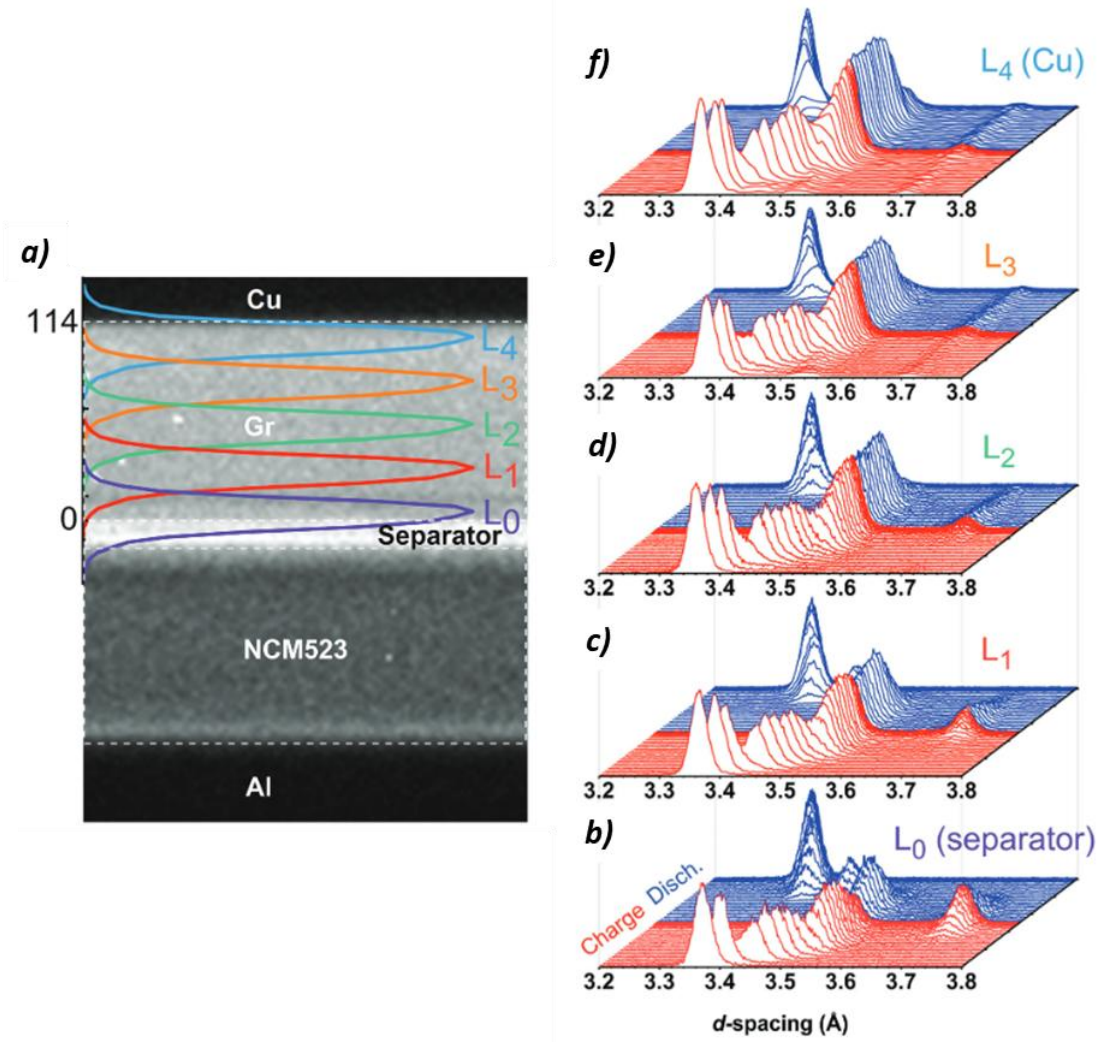


Figure 37: a) X-ray radiograph of the probed cell, with the graphite electrode of 114 µm on top. b-f) Evolution of XRD patterns upon charge and discharge for the different positions in the graphite electrode. Reprinted with permission from ref.[152].

As a preliminary result, the appearance of the stage I peak (around 3.7 Å) was observed at the end of the charge near the separator (L_0, **Figure 37b**). The maximum amplitude reached for this peak at the end of charge is greater at the L_0 position than for the others, and it should be noted that a gradual disappearance is observed for this phase towards the current collector side (L_4, **Figure 37f**).

In addition, the authors quantified the amount of lithium in the graphite phase for each L position. This quantification was performed by identifying the several stages present in a diffraction pattern, knowing the fractional content of lithium in each phase and the integrated flux of photons diffracted by each phase, the amount of *x* in Li_xC_6 was calculated. In **Figure 38**, the evolution of lithium content (*x* in Li_xC_6) for each L position was observed as a function the cell average lithium content determined electrochemically. A gradient of lithiation exists with favourable kinetic near the separator (L_0) that displays a faster increase in lithium content compared to other positions. Good agreement is observed between the straight line (x = y) and the average values (empty dots) in charge, but not in discharge. This could be explained by a poor fitting of the several phases that coexist in the diffraction patterns.

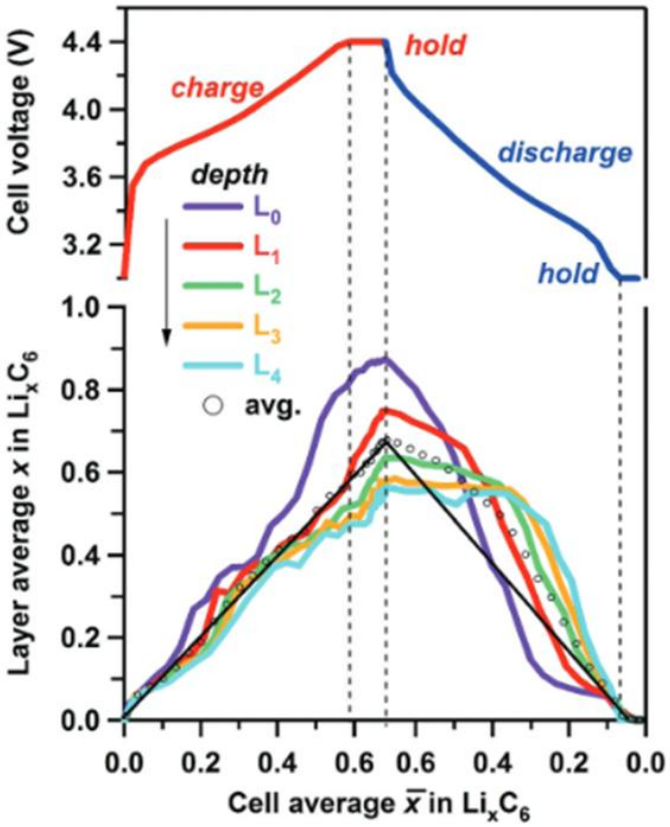


Figure 38: Average lithium content x in Li_xC_6 in the different layer as a function of the cell average lithium content determined electrochemically. Reprinted with permission from ref. [152].

Using a high temporal depth-profiling XRD experiment, Finegan *et al.* investigated the lithiation of a thick graphite electrode (100 µm) in full cell (versus NMC622) up to 6 C charging rate[153]. The quantification of lithium content in graphite (x in Li_xC_6) was estimated by adding the lithium content of each lithiation stage*. In **Figure 39a, b**, the 3D graphs show the evolution of lithium content in graphite (x in Li_xC_6) as a function of time and depth of the electrode, in lithiation and delithiation at 6 C, respectively. With a 2D representation in **Figure 39c, d** a lithiation gradient is established from the separator to the current collector side. Indeed, a faster increase of lithium content is observed in lithiation near the separator, whereas the kinetics of lithiation are slower near the collector. This is also observed in discharge with faster delithiation near the separator. An interesting thing to note is that even after a constant voltage period (time > 40 s in charge and > 100 s in discharge), heterogeneities due to mass transport limitation occurring during the CC step are still observed along the electrode thickness because of lithium depletion in the liquid phase (electrolyte) toward the collector side.

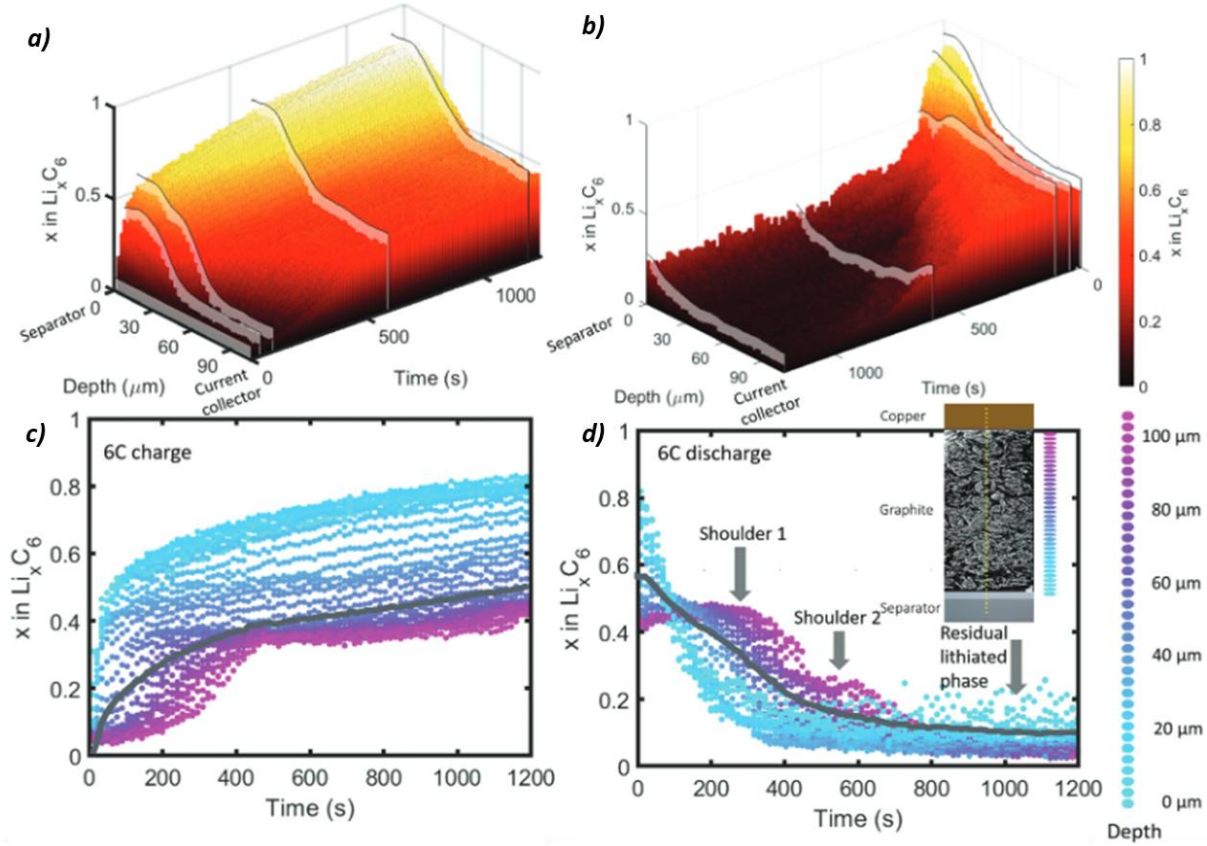


Figure 39: 3D plot of lithium content as a function of time and depth during a) charge and b) discharge. Constant current period lasted 40 s in charge and 100 s in discharge, then followed a constant voltage period. c, d) Lithium content as a function of time along the electrode depth and average x in Li_xC_6 along the electrode thickness (grey). Reprinted with permission from ref. [153].

* In this study, every stage involved between graphite and stage II were considered as stage III.

By measuring the local rate of lithiation (Δx / Δt), the authors estimated the kinetics of de/lithiation as a function of depth in the electrode. In **Figure 40a, b** a very high rate of de/lithiation (approximately a factor of four, with 6 C rate corresponding to a value of $1.6.10^{-3}$ s^{-1}) is reached at the beginning of charge near the separator/electrode interface, whereas the rest of the electrode depth inserts lithium at a rather low rate.

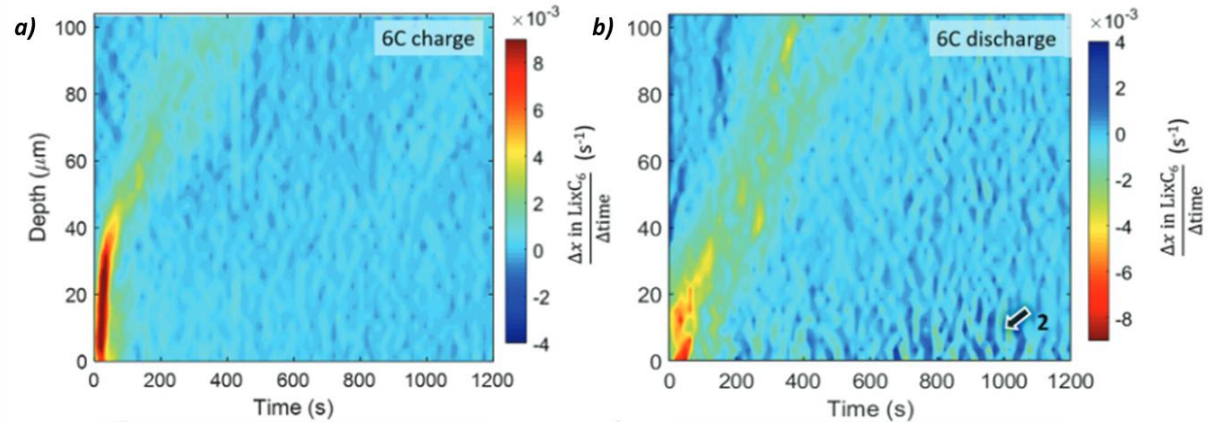


Figure 40: Colour maps of the de/lithiation rate (x in Li_xC_6) as a function of time and depth in a) charge and b) discharge at 6 C cycling rate. Reprinted with permission from ref. [153].

In a similar study, Tardif *et al.* combined X-ray experiments and modelling to characterise the heterogeneous lithiation of graphite electrodes in half-cell at C/5 rate[154]. By mapping the graphite electrode thickness with X-photons, the authors estimated the lithium content x in Li_xC_6 during graphite delithiation. This quantification was different from the previous study; here the authors summarised the average d-spacing values as a function of x in Li_xC_6 based on literature data **(Figure 41a**).

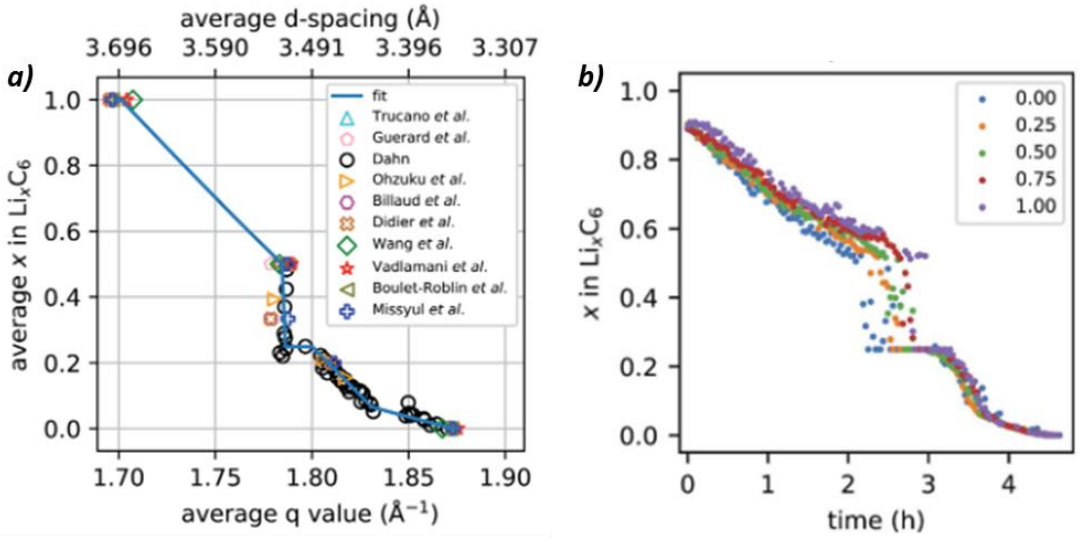


Figure 41: a) Average d-spacing as a function of the lithium content x in Li_xC_6, reported from literature. b) Lithium content at a given depth of the graphite electrode thickness (0 = separator/electrode interface, 1=electrode/collector interface). Reprinted with permission from ref.[154].

This curve was used as a calibration profile to estimate the lithium content from each diffraction pattern obtained during the experiment. The obtained results are given in **Figure 41b** as a function of the electrode depth (0 being near the separator and 1, near the collector). One can observe a gradient of delithiation, especially between 2-3 hours, with a lithium content decreasing earlier near the separator/electrode interface. These distributions of graphite state of charge testify a delithiation driven by a mass transport limitation in the electrode thickness.

A heterogeneity quantification was proposed by the authors using a Normalised Absolute Averaged Deviation (NAAD, Eq. 8) indicator.

$$NAAD(x_{Li}) = \frac{1}{L}\int_{z=0}^{z=L} \frac{|x_{Li}(z) - \langle x_{Li}\rangle_z|}{\langle x_{Li}\rangle_z} dz \qquad \textit{Eq. 8}$$

This function indicates the dispersion in lithium content along the electrode thickness and the authors obtained the evolution given in **Figure 42a**. The authors noticed a correlation between the maxima in the NAAD function and the two-phase domains. In comparison with simulation results based on classical Butler-Volmer equation to model the exchange current density, the authors noticed a missing maximum in their experimental results. According to them, in this last potential plateau the lithiation of the graphite electrode was not limited by the penetration of ions but by the charge transfer at the electrolyte/electrode interface. By modifying their models, a better agreement was obtained with the experimental results.

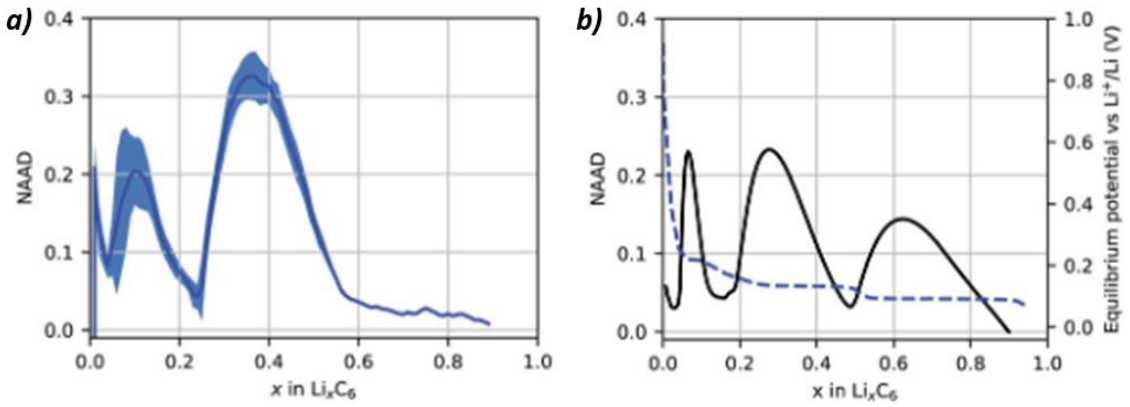


Figure 42: NAAD as a function of the average electrode lithium content upon delithiation. a) Experimental results from diffraction experiment. b) Simulations. Reprinted with permission from ref.[154].

To conclude on this section, these studies focusing on the characterisation of de/lithiation heterogeneities in graphite electrodes pointed out a recurrent phenomenon. Upon de/lithiation, heterogeneities of lithium content are observed along the electrode thickness, with favoured kinetics near the separator/electrode interface. These observations support a limitation coming from the mobility of lithium ions in the liquid phase, hindered by the electrode tortuosity.

5 PERSPECTIVES FOR THE THESIS

The literature is very rich when it comes to the investigation of graphite as active materials in negative electrodes for Li-ion batteries. It spans from fundamental aspects related to lithium intercalation mechanism to practical applications in commercial cells. A general statement concerns the poor power capabilities of graphite, limiting the fast charging of batteries. One of the reasons for the limited rate performance is often attributed to limitations by the ionic transport due to electrode microstructures.

The graphite electrode engineering is detailed in the literature, and multiple ways of improving power properties are already discussed. Unfortunately, a lack of correlation between electrode engineering and structural or morphological analysis is observed. In parallel, the growing accessibility to large-scale facilities enabled the investigation of graphite electrodes *in operando* with multiple characterisation tools, such as X-ray diffraction or tomography. Synchrotron radiation facilities are ideal for that purpose, since they enable the characterisation of the system from the bulk to the surface response in very short timescales, and with very high spatial resolution. Such studies would further improve the understanding of the interplay between the electrode's microstructure and the rate capabilities, combining structural, morphological, and electrochemical analyses. In addition, only a few studies tried to capture the current distribution inside the electrode microstructures, which would provide key information on the impact of the electrode engineering on the rate performances. The mechanical properties of graphite during cycling, from the material level to the electrode sale, is also an important factor that is not well documented, and is far from being discussed about the power properties.

On the basis of these observations, this thesis aims to investigate the relationship between graphite electrode engineering and the kinetic/mechanical properties at the electrode scale. Part of the investigations will focus on the characterisation of the microstructure morphology, and link it to the structural evolution at the electrode scale. Investigations on the mechanical evolution upon cycling will also be presented, with a special focus on the use of ultrasound as a probing tool. To move a little beyond standard studies, an innovative strategy will be presented on the use of ^{6}Li isotope in graphite half-cells to enhance power performance.

CHAPTER II

MATERIALS AND METHODS

This chapter provides a detailed overview of the materials, tools, and methods employed throughout the research. It outlines the electrode elaboration procedure, the cell assembly as well as the experimental protocols to ensure the reliability and reproducibility of the studies. By clearly describing each step, this chapter aims to facilitate the understanding of the research to enable replication of the results by other scientists.

1 GRAPHITE ELECTRODE ELABORATION

1.1 Materials

The graphite electrode elaboration was done using a wet-route in organic solvent. In this thesis, three different grades of graphite were used, SFG6L, SFG15L, and SFG44 from Imerys®. **Table 4** summarises the main characteristics of each graphite grade. Polyvinylidene fluoride (PVDF, HSV900 from Arkema) was used as binder to ensure the mechanical integrity of the composite electrodes. Super C65 (Imerys®) was used as an electrically conductive additive.

Table 4: Summary of the graphite powders and black carbon characteristics taken from supplier data.

Grade	SFG 6L	SFG 15L	SFG 44	C65
D_{90}	6.8 µm	16.3 µm	48.8 µm	50 – 100 nm
BET ($m^2.g^{-1}$)	17.0	9.5	5.0	62.0

1.2 Electrode elaboration

1.2.1 Thick electrodes

To obtain the ink, a PVDF solution (HSV900) was prepared by dissolution in N-methyl-2-pyrrolidone (NMP, Sigma Aldrich) at 10%$_{wt}$. In the case of thick electrodes (> 100 µm), 80%$_{wt}$ of graphite powder, 10%$_{wt}$ of PVDF and 10%$_{wt}$ of C65 were mixed. Graphite powder and Super C65 were mixed in an agate mortar during 10 min, cyclohexane was used to facilitate the particles mixing. The mixed powders were added in the adequate quantity to the PVDF solution, and all the components were mixed using a disperser (Ultra Turrax). Small amount of NMP was added to the slurry to decrease the viscosity until the obtention of a honey-texture. For 1 g of composite electrode, approximatively 4.2 mL of NMP was added to reach the desired viscosity. In the end, a dry extract of ~16% was a good parameter for the slurry casting.

Once mixed, the slurry was degassed using a rolling machine for at least 1 h. Then, the slurry was casted on a copper current collector (MTI) of 10 µm thickness using the doctor blade technique. For thick electrodes, a 600 µm blade was used. The casted slurry was dried at 70°C overnight to evaporate the NMP solvent.

1.2.2 Thin electrodes

The same procedure was used for the slurry preparation as in the case of thick electrodes, except that no Super C65 was added in the mixture; meaning a mixture of 90%$_{wt}$ of graphite powder and 10%$_{wt}$ of PVDF. The electrode casting was performed with an aerograph and was manually sprayed on the copper current collector. The electrode was then dried at 70°C overnight.

1.2.3 Electrode characteristics

The dry electrodes were systematically characterised by their loading (in $mg_{active\ material}.cm^{-2}$), thickness (μm) and porosity (ε). The porosity was calculated using the theoretical electrode density (ρ_{theo}) and the apparent one (ρ_{app}) using Eq. 9:

$$\varepsilon = 1 - \frac{\rho_{app}}{\rho_{theo}} \quad \textit{Eq. 9}$$

The theoretical density was estimated using the weighted density of each material as given in Eq. 10.

$$\rho_{theo} = w_{Gr} \times 2.26 + w_{C65} \times 1.6 + w_{PVDF} \times 1.78 \quad \textit{Eq. 10}$$

Where w_X is the mass fraction of each component. The numerical values correspond to the densities of each component in $g.cm^{-3}$.

Regardless of the graphite particle size, the dry electrodes obtained with this elaboration method systematically showed a porosity of ~70%. For the loading, the thick electrodes were around ~6.5 – 7 $mg.cm^{-2}$ of active material, whereas the thin electrodes were around 0.4 $mg.cm^{-2}$.

Depending on the targeted porosity, the electrodes were calendared using a calendering machine (MTI, MSK-HRP-01) at room-temperature. The electrode thickness was reduced by successive runs (3 – 4 times) between the two rollers and by changing the electrode direction to avoid non-uniform porosity reduction. In the end, thicknesses of ~75 – 80 μm were obtained for porosities of 50% and ~45 – 50 μm for porosities of 30%.

1.3 Half-cells preparation

1.3.1 Coin cells

Discs of graphite composite electrodes were punched at 12 mm and 14 mm diameter, the electrode diameter evolved during the thesis changing from 12 mm to 14 mm. A larger electrode diameter was preferred in the end to decrease as much as possible the effects of alignment in the coin cells between the two electrodes. Before being inserted in an argon filled glovebox, the electrodes were dried in a Büchi oven under dynamic vacuum (10^{-3} bar) at 90°C overnight. In parallel, the Whatman® separator (GF/D grade) was dried in dynamic vacuum (10^{-3} bar) at 180°C overnight. The half-cell assembly was performed in an Ar-filled glovebox with < 1 ppm O_2 and < 1 ppm H_2O. The half-cells were mounted in CR2032 coin cells (in 316L, Hosen) as shown in **Figure 43**. In the case of thin electrodes, two spacers with a total thickness of 1.5 mm were added, whereas for thick electrodes (50 – 100 μm) one spacer of 1 mm was used. A lithium counter electrode (S4R supplier) 750 μm thick was used. The separator was soaked by 100 – 130 μL of electrolyte using a 1000 μL micropipette. The coin cells were closed using a crimping machine (Hosen).

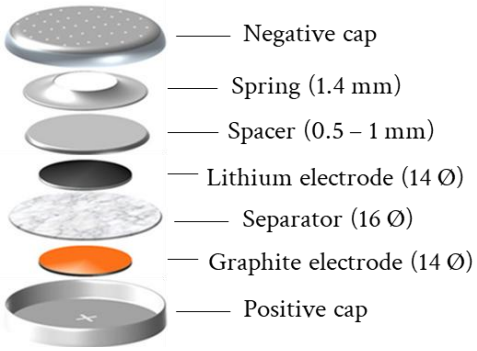


Figure 43: Illustration of a coin cell assembly. Reprinted with permission from ref.[155].

1.3.2 Swagelok cells

Disks of graphite composite electrodes were punched at 6 mm diameter. The same procedure was used as for the coin cells, *i.e.* drying under dynamic vacuum and assembly in an Ar-filled glovebox. The half-cells were mounted on a 6 mm diameter Swagelok® cell as shown in **Figure 44**. A lithium counter electrode (S4R supplier) 750 µm thick was used. The Swagelok cells were closed manually.

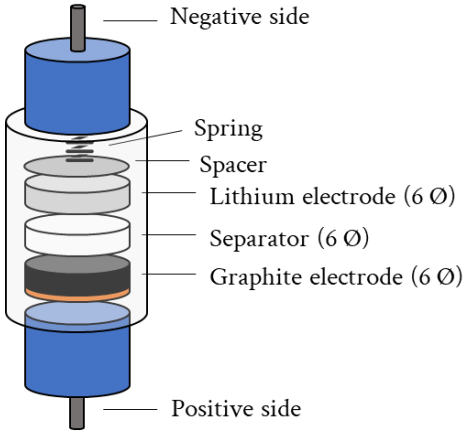


Figure 44: Illustration of a Swagelok cell assembly.

2 ELECTROCHEMICAL TESTS

All electrochemical tests were performed using Biologic® potentiostats and cycling devices. In the case of cycling experiments such as rate capability tests, BCS (815) cycling device were used. For more precise characterisations such as cyclic voltammetry or very low current cycling (few µA), SP potentiostats were used. After cell assembly, all cells rested for at least 1 h at 25°C in a thermoregulated oven (IPP30 from Memmert®), to ensure a stabilisation of the internal temperature and a relaxation of the open-circuit voltage (OCV). In the thesis, the coin cells were systematically cycled at 25°C in a thermoregulated oven. All the potentials expressed in the thesis always refer to the reference redox couple Li^+/Li, except if otherwise stated.

2.1 Rate capability test

Rate capability tests are commonly used in the battery field[63,156,157], using Constant Current – Constant Voltage protocols and by increasing the applied current. Upon the constant current period, the applied current is expressed by the charge/discharge rate (C-rate) and corresponds to the rate of charge or discharge as a function of the nominal capacity of the cell. This C-rate corresponds to the division of the charge or discharge current (in *A*) by the nominal capacity of the cell (in *Ah*). Practically, a C-rate of 1 C corresponds to the charge or discharge of the cell in 1 hour. In this manuscript, the C-rate term is used in charge and discharge. The first two cycles (formation cycle) were realised at C/20 rate. Then, a progressive increase of the C-rate was realised, with three charge/discharge cycles for each C-rate. A repetition of three cycles was used to ensure that the voltage response was representative of the used C-rate (reproducibility). Each charge/discharge cycle was composed of a Constant Current period (limited by the cell voltage at 0.01 V in lithiation and 1.2 V in delithiation), then a Constant Voltage (at 0.01 V and 1.2 V) was applied during 30 min in the end of lithiation and delithiation, respectively.

Each rate capability measurement was performed on at least 3 identical cells to ensure reproducibility and the standard deviations were calculated.

2.2 Potentiostatic Intermittent Titration Technique (PITT) experiment

The PITT experiments were performed on thin graphite electrodes in a half-cell using several potential steps (1, 0.4 and 0.2 mV) from 0.250 to 0.040 V. The relaxation of current was acquired until a rather constant current was obtained (I_{lim} ~ 0.8 – 0.4 µA), as shown in **Figure 45**.

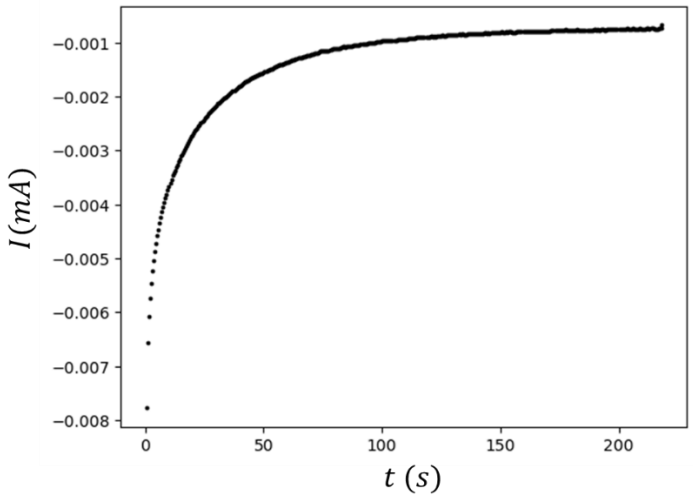


Figure 45: Current relaxation upon one potential step as a function of time.

During the current relaxation, two regimes are observed for intercalation compounds, as expressed in the following equations[158–160]. For short times, a Cottrellian regime occurs, and the current response depends on the Cottrell equation (Eq. 11):

$$I_{cottrell} = \frac{\Delta Q}{\sqrt{\pi t \tau_D}} \qquad \textit{Eq. 11}$$

Where ΔQ is the variation of charge (mA.s), τ_D is the characteristic diffusion time and t is the time response (s).

Two methods can be used to estimate the characteristic time of diffusion, τ_D, always for short-times. From Eq. 11, the following Eq. 12 expresses the current variation with the reverse square-root of time, as illustrated in **Figure 46a**, and one can fit the linear evolution to obtain the intercept.

$$\left(\frac{I\sqrt{t}}{\Delta E}\right)^{-1} = \frac{(\pi\tau_D)^{1/2}}{C_{diff}} + \frac{\tau_D}{\Lambda\, C_{diff}} t^{-1/2} \; with \; \Lambda = \frac{R_d}{R_\Omega + R_{ct}} \qquad \textit{Eq. 12}$$

Where C_{diff} is the differential capacity expressed in mAs.V^{-1}, ΔE is the potential step in V, and Λ is a dimensionless parameter depending on the diffusion R_d, charge transfer, R_{ct} and ohmic resistances, R_Ω.

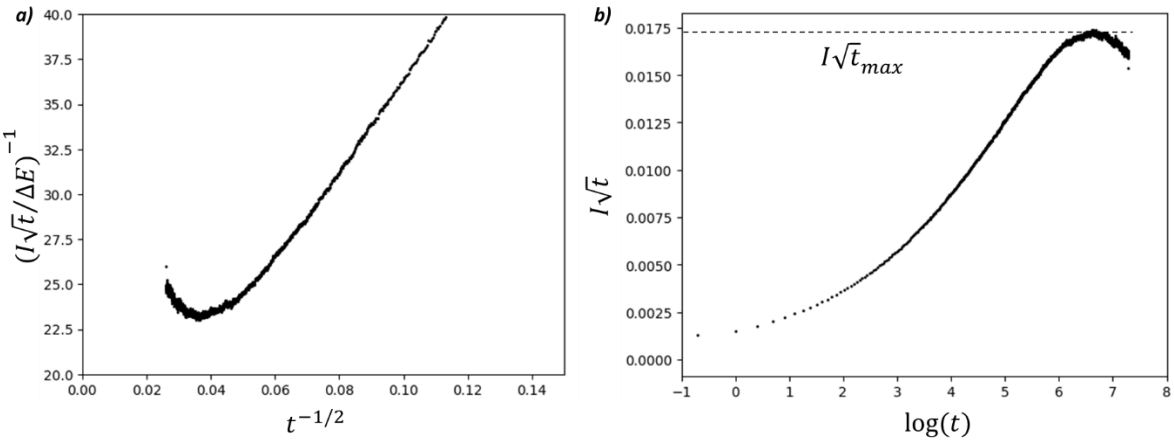


Figure 46: Illustration of the current relaxation upon one step of potential. a) Graphical evolution of Eq. 12. b) Graphical evolution of $I\sqrt{t} = f(\log(t))$.

With a second representation, shown in **Figure 46b**, one can estimate the diffusion time *via* the curve apex using Eq. 13:

$$I\sqrt{t}_{max} = \Delta Q(\tau_D \pi)^{-1/2} \qquad \textit{Eq. 13}$$

For long-times, an exponential decay of current is observed as expressed in Eq. 14:

$$I_D = \frac{2\Delta Q}{\tau_D} exp\left(\frac{-\pi^2 t}{4\tau_D}\right) \quad \textit{Eq. 14}$$

Based on Eq. 14, Eq. 15 is obtained and a linear regression at long-times enables the determination of the characteristic time of diffusion from both the intercept and the slope, as illustrated in **Figure 47**.

$$log\left(\frac{I_D}{2\Delta Q}\right) = -log\tau_D - \frac{\pi^2}{4\tau_D} t \quad \textit{Eq. 15}$$

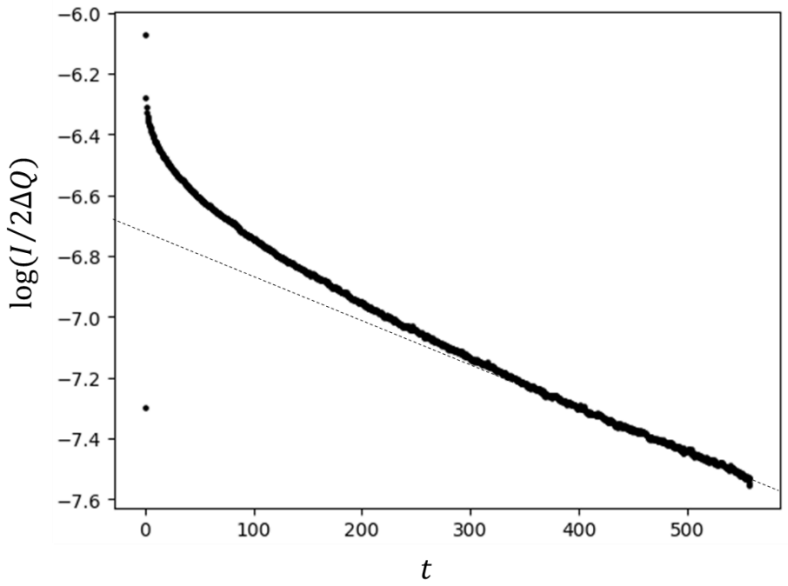


Figure 47: Illustration of the current relaxation following Eq. 15.

Both methods were compared to find the most reliable one comparing two potential step values (1 mV and 0.4 mV). Small potential steps are preferred for measuring the diffusion coefficient, to ensure that changes in lithium content "*x*" (in Li_xC_6) are not too important. The diffusion coefficient obtained based on short-time and long-time domains are plotted in **Figure 48,** considering a diffusion length (*L*) of 3 µm (graphite particle radius). The same trend was observed for both methods, but the order of magnitude between the two potential steps was different with the Eq. 12. For the long-time domain, the two methods are consistent with diffusion coefficient of the same magnitude order. The better consistency between the two potential steps was obtained using the long-time domain and the determination *via* the slope of the linear regressions. From this, the diffusion coefficients discussed on this manuscript were all obtained with this method.

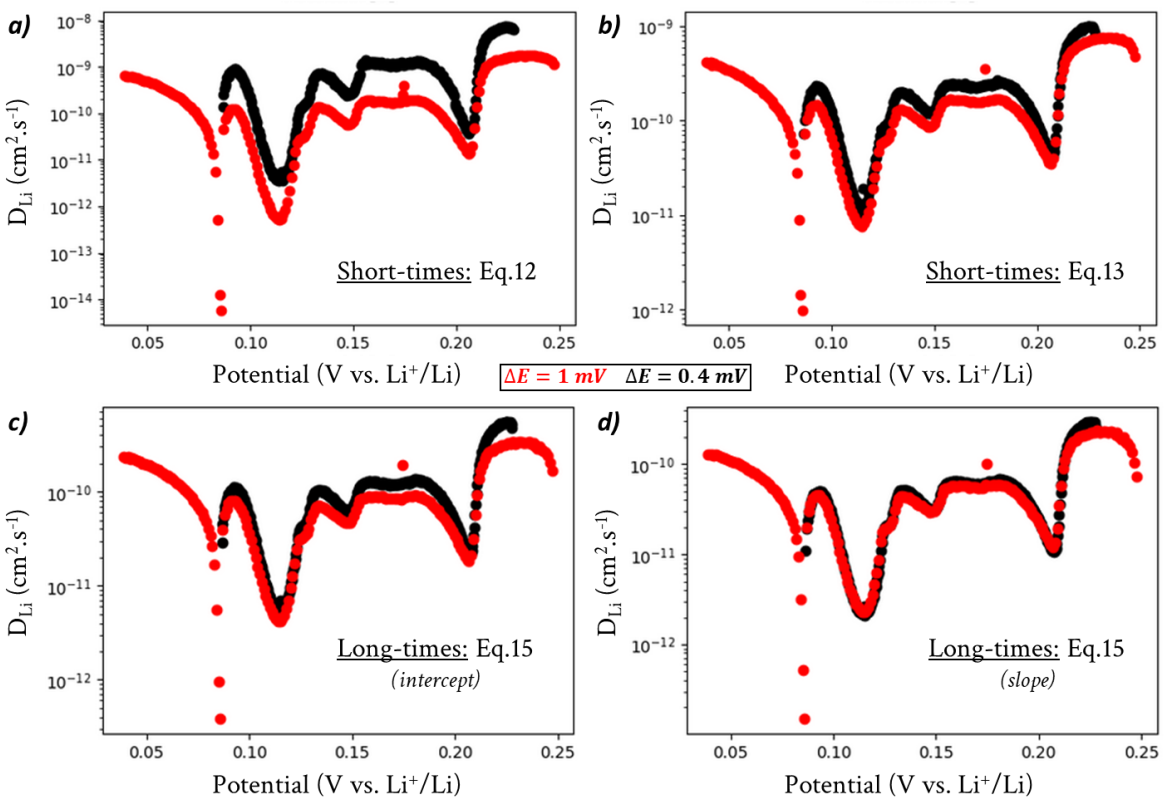


Figure 48: Diffusion coefficients as a function of graphite electrode potential obtained through different methods. a) From short-times domain using Eq. 12. b) From short-times domain using Eq. 13. c) From long-times domains using Eq. 15 and the intercept from the linear regression. d) From long-times domain using Eq. 15 and the slope from the linear regression.

2.3 Differential Capacity Analysis

From the electrode potential evolution with respect to the cell state of charge ($E = f(SoC)$) plotted in **Figure 49a**, the differential evolution of the accumulated charge with respect to the potential (DCA) provides information about the precise potential of the several electrochemical processes. In **Figure 49b**, the reversed DCA profile helps to understand the correlation between a potential plateau (from a galvanostatic curve) and a peak (on the DCA curve). Going further into data representation, the DCA profile can be represented as a function of the cell SoC using the curve in **Figure 49a**. **Figure 49c, d** plots the $d_{SoC}/d_E = f(SoC)$ profile, and demonstrates the translation of the initial potential plateaus into waves. The intensity of the wave corresponds to the DCA intensity, and its width corresponds to the potential plateau length.

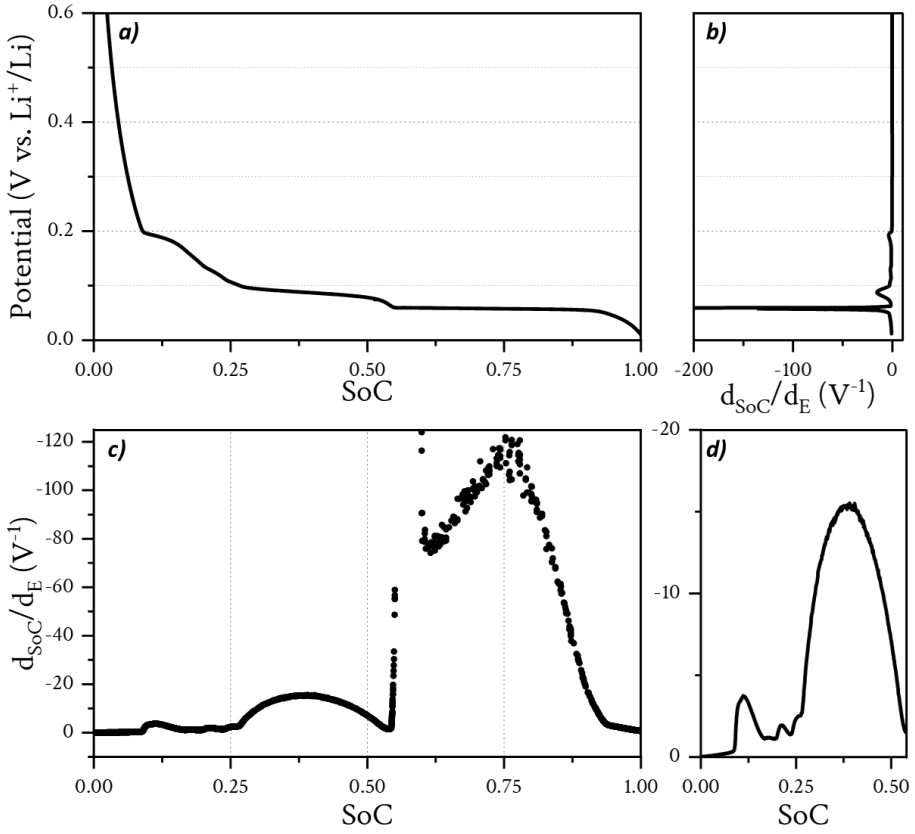


Figure 49: Different representation of the electrochemical profile of a thin graphite electrode cycled in half-cell. a) Electrode potential with respect to the SoC. b) Differential Capacity Analysis profile (reversed). c) DCA with respect to the SoC. d) Zoom on the c plot.

2.4 Tortuosity measurement by Electrochemical Impedance Spectroscopy (EIS)

Using electrochemical impedance spectroscopy, an alternative current or potential is applied at different frequencies to promote the diffusion and migration of electrons and lithium ions. In the case of pristine graphite electrodes, no intercalation is observed before a potential lower than 0.5 – 0.6 V in reductive conditions . For this reason, the impedance recorded at the pristine state is considered as being in blocking conditions, with lithium ions travelling the porous structure and adsorbing on the charged particles (graphite and carbon additives). The obtained impedance spectrum is generally analysed using a simplified transmission line model (TLM) that models the porous structure[161]. With this equivalent circuit, schematised in **Figure 50**, a resistive branch established along the electrode thickness accounts for the ionic resistance in the pores (the sum of incremental ionic resistances gives the total ionic resistance, $\sum r_{ion} = R_{ion}$). Similarly, a succession of charge transfer resistances and double layer capacitances account for the charge transfer processes in the pores ($\sum r_{ct} = R_{ct}, \sum q_{dl} = Q_{dl}$). In this simplified TLM, no resistances are added to the electronic branch since the electronic resistivity is considered as negligible compared to the ionic resistivity[162].

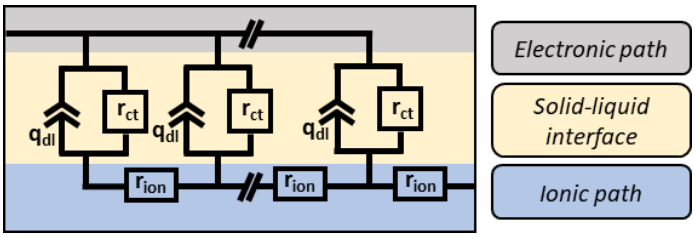


Figure 50: Schematic of a simplified transmission line model (TLM) used to extract the tortuosity parameter from an electrode.

Note that the total impedance includes the impedance of the two graphite electrodes, the ionic tortuosity was then calculated using Eq. 16.

$$\tau = \frac{R_{ion} . A . \sigma_{ion} . \varepsilon}{2\ d} \qquad \text{Eq. 16}$$

Where R_{ion} is the total ionic resistance (Ω), A is the cross-sectional area estimated based on the electrodes radius (cm^2), σ_{ion} is the ionic conductivity of the electrolyte ($S.cm^{-1}$), ε is the electrode porosity and d is the electrode thickness (cm).

A typical Nyquist impedance diagram and its corresponding fit are plotted in **Figure 51**. The semi-circle at low frequency can be attributed either to the copper/electrode interface as described in literature[163], or to internal polarisation phenomena of the composite electrode[164]. At medium frequency, the diffusion of ions in the electrode porosity induces a slope of ~35°, whereas the high frequency domain contains a capacitive signature caused by the blocking condition of the copper current collector.

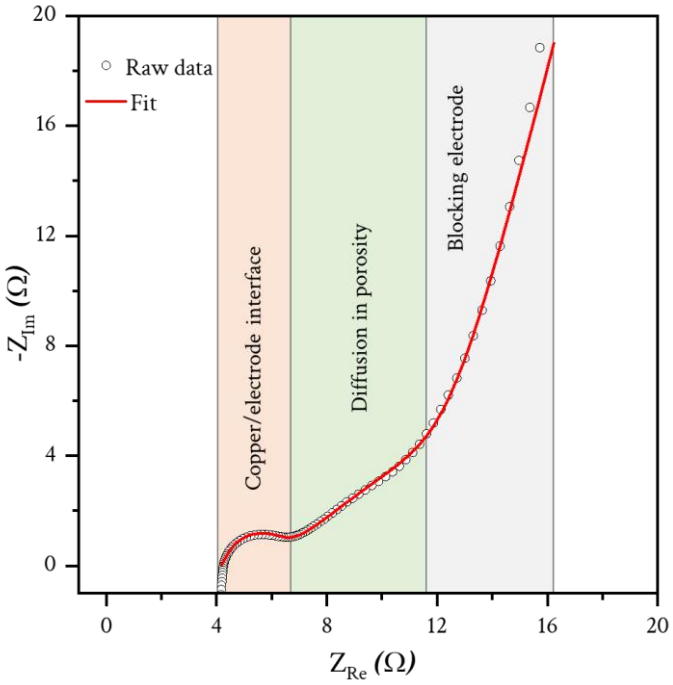


Figure 51: Nyquist impedance diagram obtained from symmetrical cell composed of two graphite electrodes of 70% porosity with 0.35 M $LiPF_6$ in EC/DMC (1:1%$_v$).

2.5 Conductivity measurement

Conductivity measurements consist in using a conductivity probe composed of two Pt electrodes of known geometry (**Figure 52**). The conductivity estimation is based on the following Eq. 17.

$$\sigma_{ion} = \frac{K_{cell}}{R_{ion}} = \frac{l}{S.R_{ion}} \qquad \textit{Eq. 17}$$

Where σ_{ion} is the ionic conductivity in S.cm^{-1}, R_{ion} is the ionic resistance in Ω, and K_{cell} is a geometric factor depending on the distance between the Pt electrodes (l, in m) and their surface (S, in m^2).

The cell geometric factor is determined using a solution of known specific conductivity, here KCl at 0.01 M was used with a specific conductivity of 1.413 mS.cm^{-1} at 25°C. The geometric factor was determined by measuring the ionic resistance in the KCl solution at 25°C by impedance spectroscopy using an applied voltage of 10 mV from 1 Hz to 7 MHz. The geometric factor (systematically around 1.5) was then used as cell constant in Eq. 17 to determine the conductivity of the probed solution from the measured ionic resistance.

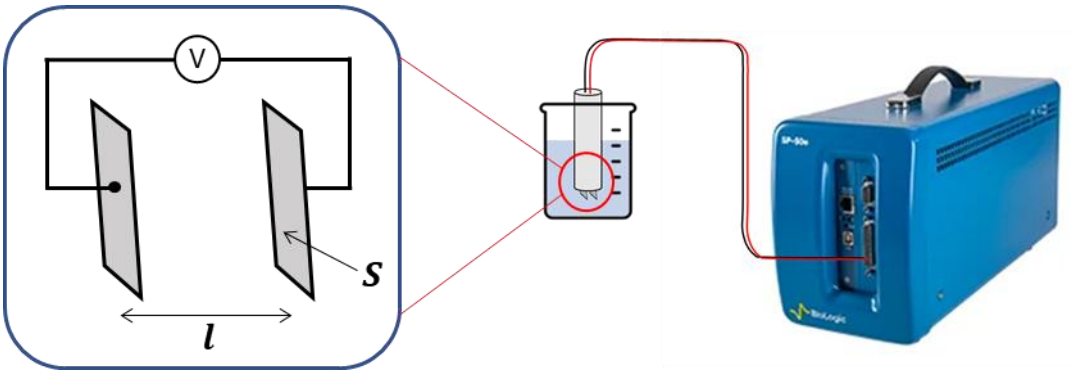


Figure 52: Illustration of a conductivity cell set-up.

3 ELECTRODE MORPHOLOGY CHARACTERISATIONS

3.1 Cross-sections and Scanning Electron Microscope (SEM)

Cross-sections of the electrode were realised using an ion-milling machine (Cross polisher HITACHI, IM 5000 CTC). First, the electrode disks were cut, along the Z axis using a razor blade to visualise the section of the electrode (their thickness). The samples were glued on a silicon piece using a silver lacquer and the whole was assembled on a machine support. The machine used an Ar-ion flux to dig in the electrode thickness on roughly 1 to 2 mm of lateral displacement, with an operation of 30 to 60 min. The samples were then transferred to the SEM chamber, and images of the cross-sections were acquired.

The SEM analyses were performed on a LEO 1530 model (ZEISS®, Germany). The electron high tension (EHT) was set to 2 kV with a working distance around 5 mm.

3.2 X-ray holotomography measurement

3.2.1 Experimental set-up and data acquisition

The data were acquired on the ID16b beamline at ESRF[165] using the holotomography technique[166], with the help of Dr. Victor Vanpeene for the acquisition, treatment and interpretation. An image of the experimental set-up is shown in **Figure 53**.

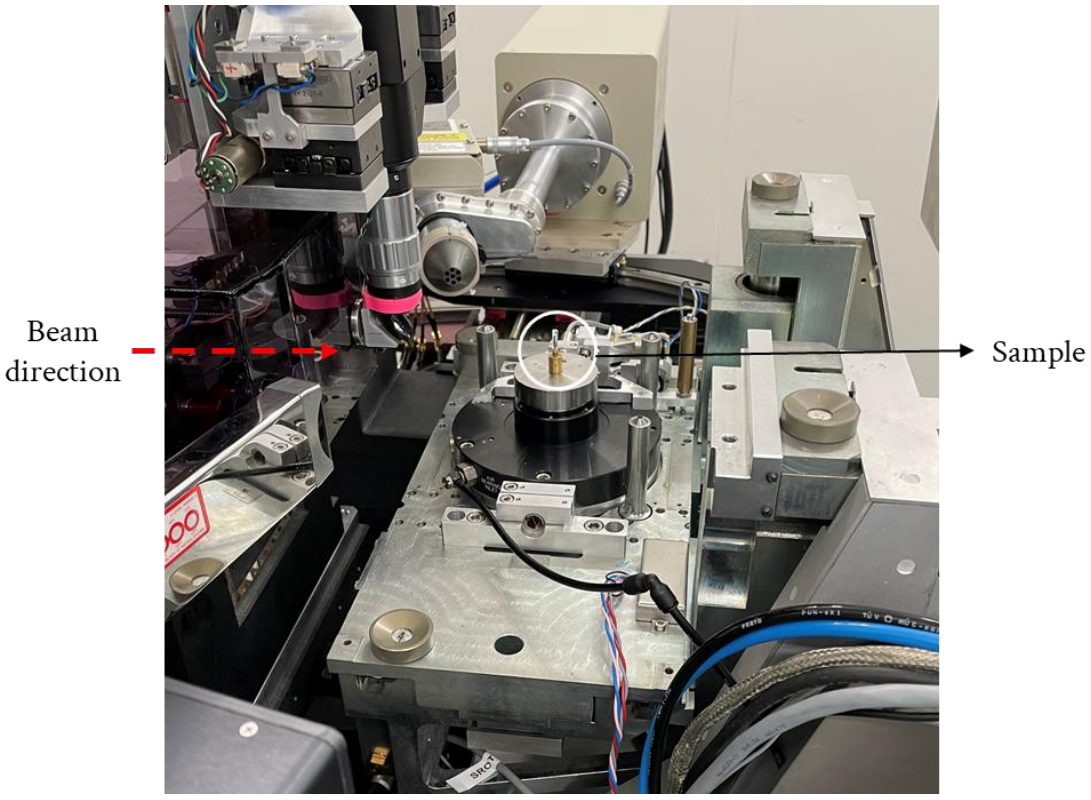


Figure 53: Image of the experimental set-up used at ID16b beamline from ESRF.

Graphite electrode disks of 50 % and 30% porosity were cut in thin lamella (few hundreds of micrometres in width) using a razor blade. The lamellas were glued to brass pins and placed in a sample holder made of PFA sealed under Ar thanks to a UV-curing glue. Scans composed of 4 consecutive acquisitions at each distance were constituted of 2505 projections, as well as 20 and 21 reference and dark images respectively, that were recorded on a PCO edge 5.5 CMOS camera (2048×2048pixels2) with a 17 µm thick LSO scintillator along a 360° rotation. For the incident X-ray beam, an energy of 29.45 keV and photon flux 3.4 10^{11} ph.s^{-1} were measured, hence an exposure time of 10 ms per projection. Acquisitions were performed at a voxel size of 50 nm, resulting in fields of view of 102×102 μm^2. 3D reconstructions were achieved in two steps: (i) phase retrieval calculation using an in-house developed octave script based on a Paganin-like approach using a

delta/beta ratio of 2740, and (ii) filtered back projection reconstruction using ESRF software PyHST2[167]. Final volumes of 102×102×102 μm^3 with a voxel size of 50 nm in a 32-bit floating point were obtained. Post-processing ring removal and 8-bit conversion was performed using a dedicated Matlab script[168]. Analyses were performed on the reconstructed 8-bit volumes using the ImageJ software[169]. The different phases were segmented using a machine learning based random forest classifier embedded within the Ilastik software[170].

4 OPERANDO CHARACTERISATIONS

4.1 Wide Angle X-ray Scattering (WAXS) at ID31

4.1.1 Experimental set-up

Data were acquired on the ID31 beamline at ESRF, and an image of the experimental set-up is given in **Figure 54**. The coin cells were mounted on a coin cell holder applying pressure on top of the coin cell with a spring, and the potentiostat connectors were connected on both sides of the coin cell. The coin cells were aligned with the beam direction, and the cell alignment was performed by following the shape of the graphite signal on the diffraction ring by successive acquisition of diffraction patterns. Once the graphite signal was roughly equal to the electrode thickness, the cell was considered aligned and the *z*-profiling experiment was realised. During the experiment, the cell was probed in its centre to ensure that a maximum amount of graphite was probed by the beam, and only the *z*-motor was moved to scan along the electrode thickness.

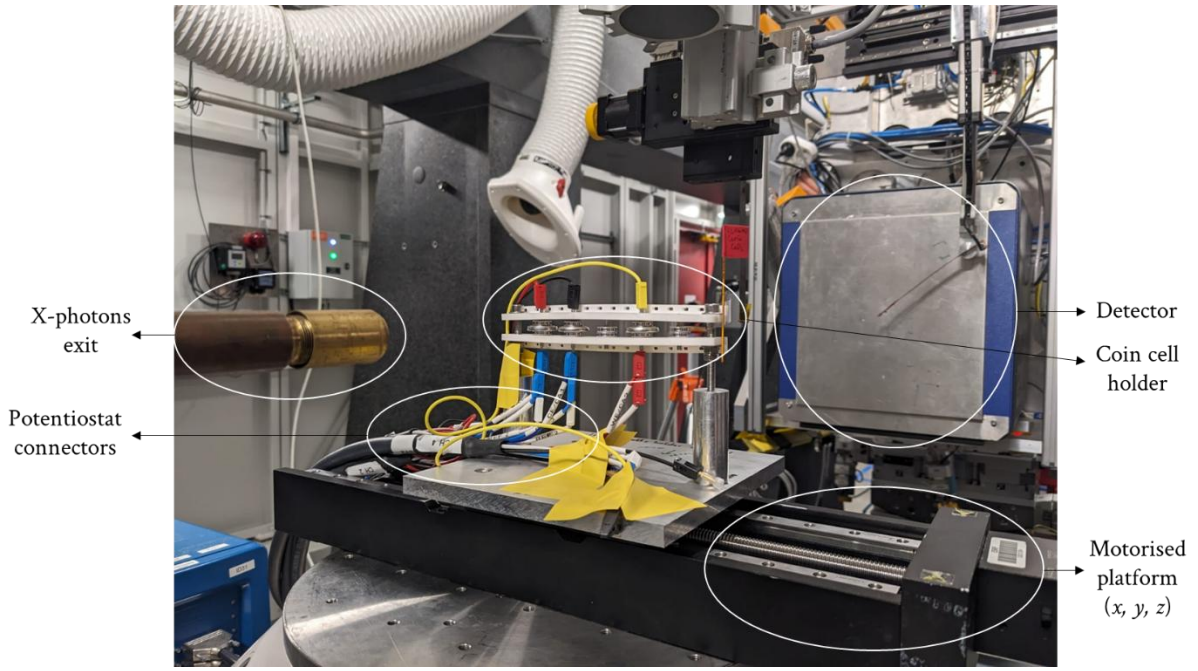


Figure 54: Image of the experimental set-up used at ID31 beamline for the probing of coin cells.

4.1.2 Data acquisition

A Pilatus 2M CdTe 2D detector (Dectris) was used for the acquisition of the diffracted signal, positioned roughly at 1 m from the sample. The beam energy is set at 75 keV, and the beam is focused on the sample (approximately 5 µm x 15 µm, vertical x horizontal). The 2D images are integrated into a 1D diffraction pattern using the pyFAY package[171].

4.1.3 Peak fitting analysis

Peak analysis was performed with home-made Python scripts based on the LMFIT library[172]. Before proceeding with peak fitting, the scattering background was removed, as illustrated in **Figure 55**, using a Statistics-sensitive Non-linear Iterative Peak-clipping (SNIP) function from PyBaseline library[173].

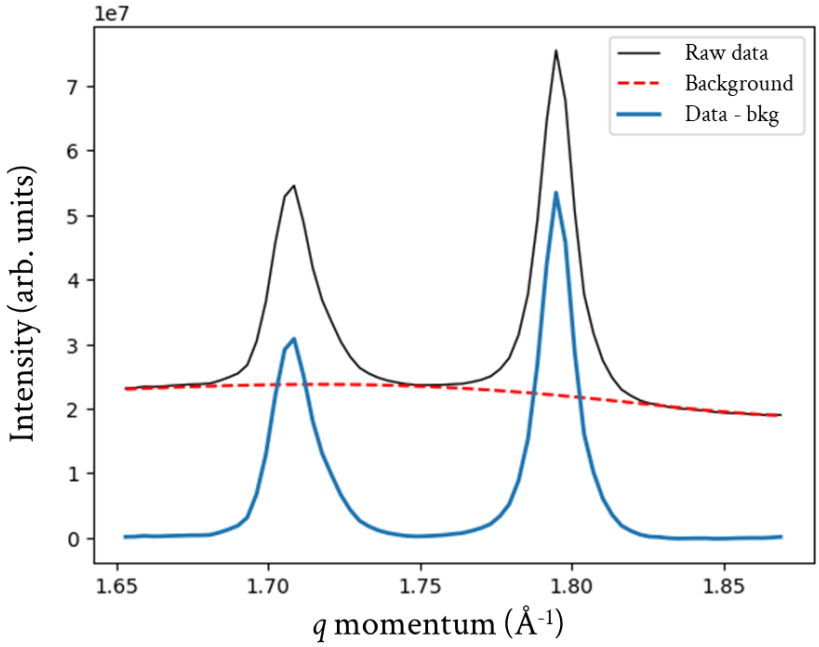


Figure 55: Example of a raw diffraction pattern (black), the computed background (red) and the corrected diffraction pattern (blue).

Most of the diffraction peaks were fitted using one or two PseudoVoigt (pV) contributions. In the case of the stage III to stage II-L transition, a SplitPseudoVoigt (spV) function was used. As stated in Eq. 18, the spV function consists of two pV functions (a right and left one), displaying different sigma and fraction parameters. Note that the implementation of the function in the Python script was inspired by these references[174,175].

$$f(x; A, \mu, \sigma_l, \sigma_r, \alpha_l, \alpha_r) = pV_l(x, A, \sigma_l, \alpha_l) \times H(\mu - x) + pV_r(x, A, \sigma_r, \alpha_r) \times H(x - \mu) \quad \textit{Eq. 18}$$

Where H is the Heaviside function, A the peak amplitude, σ_l and σ_r the peak width from its center to its left or right side at half maximum, μ the peak center, α_l and α_r the fraction of Lorentzian contribution of the two PseudoVoigt functions.

The detailed function is given in Eq. 19, which involves normalised Gaussian (G') and Lorentzian (L') functions, as described in the PseudoVoigt description of Mantid Project[176]. Since the spV can be asymmetric, the full width at half maximum (FWHM) corresponds to $\sigma_l + \sigma_r$.

$$f(x; A, \mu, \sigma_l, \sigma_r, \alpha_l, \alpha_r) = A[(1-\alpha_l)G'(x,\sigma_l) + \alpha_l L'(x,\sigma_l)]H(\mu - x) + A[(1-\alpha_r)G'(x,\sigma_r) + \alpha_r L'(x,\sigma_r)]H(x-\mu) \quad \textit{Eq. 19}$$

Figure 56 illustrates the use of a SplitPseudoVoigt function for the fitting of an asymmetric peak; one can notice a shoulder on the right part of the peak that is not properly fitted using a symmetric function. However, with the spV, a better fit quality is obtained. During the fitting procedure, this spV function was used for regions possibly involving two contributions without evident deconvolution.

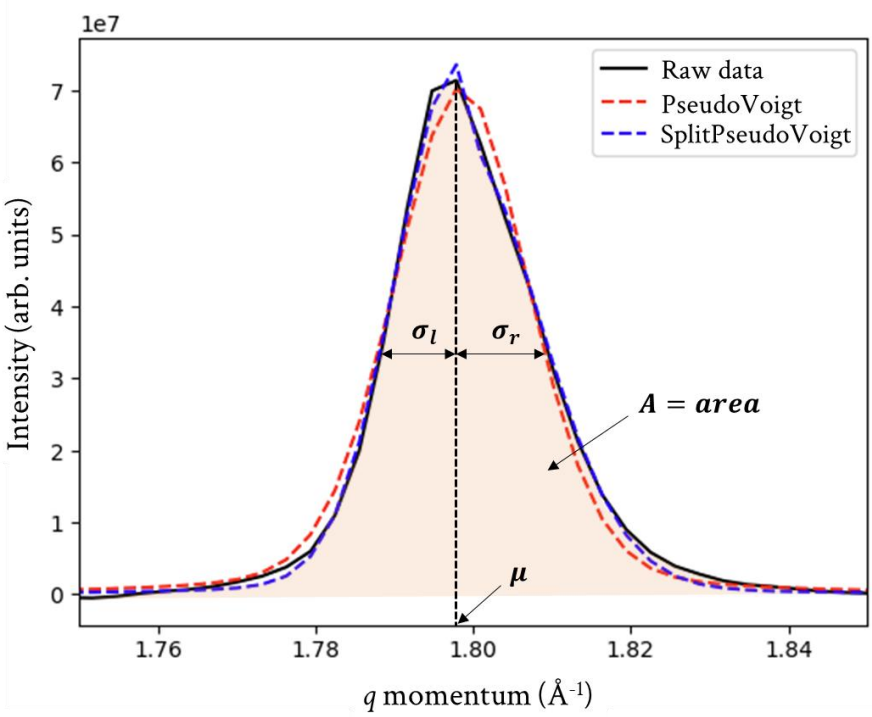


Figure 56: (002) Bragg reflection of lithiated graphite fitted with a PseudoVoigt contribution in red and using a SplitPseudoVoigt in blue.

4.1.4 Mass centre calculation

The collected diffraction patterns correspond physically to the collection of interlayers d-spacing (q momentum) that exist in the probed sample, weighted by the number of scattered X-photons. Based on this, a mean q momentum (or mass centre, mc) is calculated using a weighted arithmetic mean:

$$mc = \sum_{q_{min}}^{q_{max}} (I_q \times q) \Big/ \sum_{q_{min}}^{q_{max}} I_q \qquad \text{Eq. 20}$$

With I_q, the intensity at a given q momentum.

A schematic representation of the mass centre calculation is given in **Figure 57**.

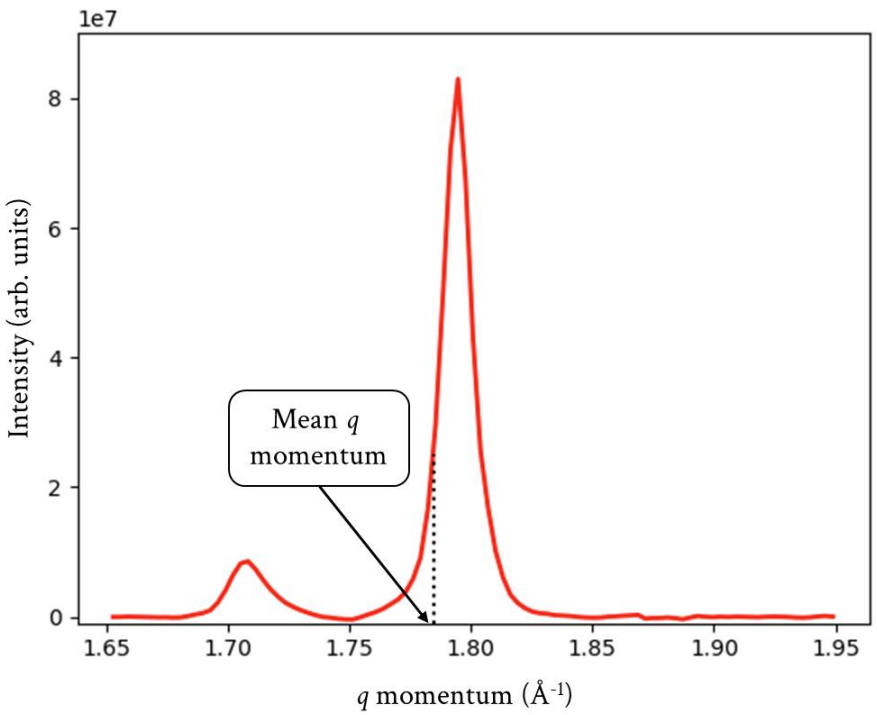


Figure 57: Illustration of a diffraction pattern and the calculated mean q momentum (mass centre).

4.1.5 Thick electrode characterisation

To visualise the z-positions and their relative position in the electrode's depth, the graphite electrodes were probed in pristine state along their thickness by moving the z-motor of the platform. By looking at the count number attributed to the graphite phase on the diffraction ring with respect to the motor position, the electrode shape is given in **Figure 58**. A coherent shape for the graphite electrode of 50% porosity is observed in **Figure 58a**, with a thickness of ~80 µm as expected. The electrode was probed at 5 z-positions spaced by 16 µm (the X-ray beam height

was ~5 µm), from z_1 = 0.1 L (with L the electrode thickness) to z_5 = 0.9 L. For the electrode of 30% porosity, a coherent electrode shape is also observed (**Figure 58b**) with a thickness of ~45 µm as expected. The electrode was probed at 9 *z*-positions spaced by 5 µm (limit of the spatial resolution) from z_0 = 0.1 L to z_8 = 0.9 L. In the case of the electrode of 30% porosity, all the electrode thickness was probed by the X-ray beam in the *z*-profiling protocol, whereas only ~30% of the 50% porosity electrode surface was probed. Nevertheless, the *z*-positions being at the same relative positions in both electrodes, a fair comparison was possible between the two samples.

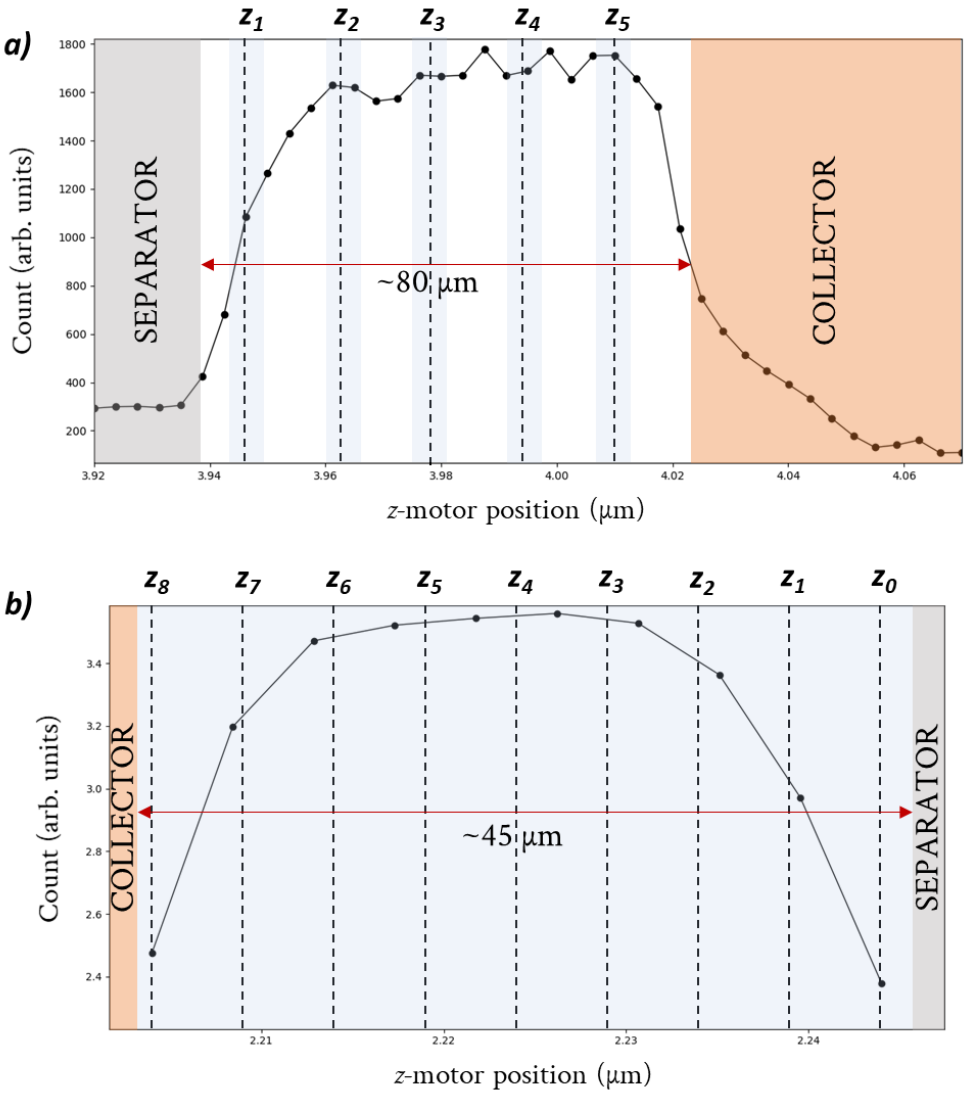


Figure 58: Visualisation of the graphite electrodes and the z-positions in their respective thickness. a) Graphite electrode of 50% porosity. b) Graphite electrode of 30% porosity. Note that the blue zones correspond to the regions probed by the X-ray beam.

4.2 Raman spectroscopy

4.2.1 Cell assembly

The Raman spectroscopy experiment was carried out with the ECC-OPTO-10 optical cell (EL-CELL®) schematised in **Figure 59**, using a Sapphire window. The cell was used in transmission configuration, with a lithium disk of 10 mm diameter placed on the piston and the thin graphite electrode directly coated on a Whatman separator of 10 mm diameter, so that the electrode was visible through the Sapphire window. A contact disk was used to electronically connect the graphite electrode to the potentiostat. The separator was soaked with 50 µL of LP30 as electrolyte. Once closed, a formation cycle was carried out at C/20 rate at 25°C.

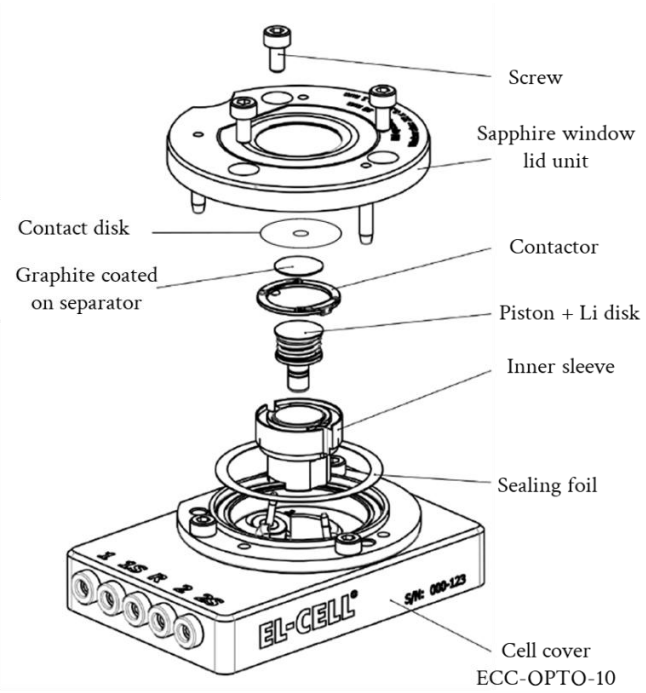


Figure 59: Schematic illustration of the ECC-OPTO-10 optical cell from EL-CELL®. Adapted from ECC-OPTO-10 manual.

4.2.2 Raman experiment

The Raman spectra were acquired with a 532 nm green laser. Preliminary Raman spectra (**Figure 60**) were acquired: the sapphire window alone, the electrolyte with the sapphire window, and the LiC_6 phase in the entire assembly. With respect to the electrolyte/sapphire spectrum, no Raman peak was observed, ensuring that no graphite peak would be merged with other signatures. Because the metallicity of graphite increases upon lithiation and then decreases the penetration depth of the beam, the LiC_6 phase was probed to estimate the optimal power and exposition time. From this, the laser power was set to 10% and an exposition time of 30 s was selected to enable the visualisation of signal in the end of the graphite lithiation.

The half-cell was cycled *in operando* condition using a SP10 Biologic potentiostat and Raman spectra were acquired each 30 s. The cell was charged at C/35 @20°C, corresponding to ~4200 Raman spectra acquired upon lithiation, whereas the discharge was performed at C/17 rate.

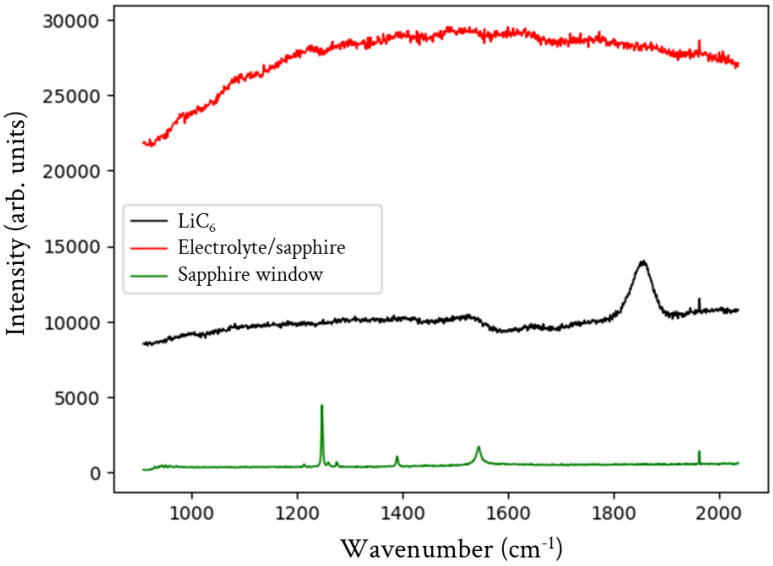


Figure 60: Raman spectra of the Sapphire window, the separator and the electrolyte, and the LiC_6 compound.

4.2.3 Spectra analysis and fitting

A pre-treatment of the acquired spectrum was realised using the spectrometer software to remove the spikes (intense pixel). Then, all the spectra were treated and analysed using Python. The background was removed from the raw data using an Asymmetrically Reweighted Penalized Least squares Smoothing (ARPLS) from PyBaseline[173], an example of background subtraction is shown in **Figure 61**.

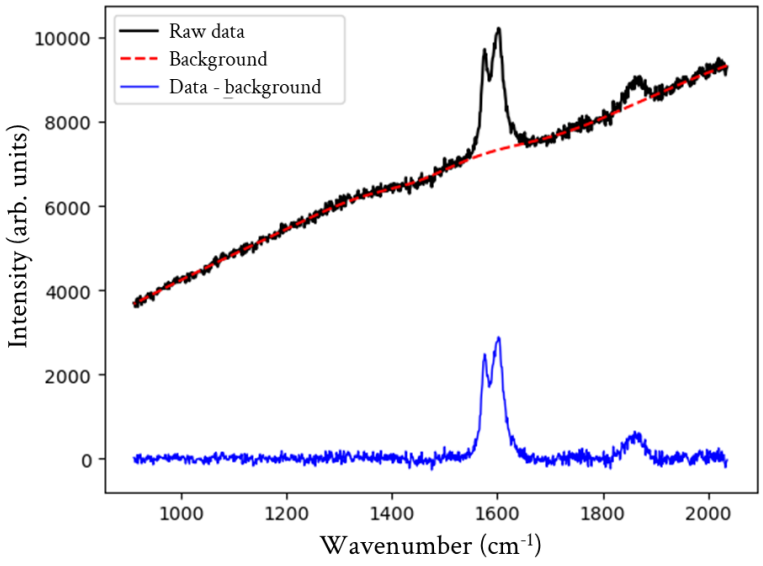


Figure 61: Example of background subtraction from a raw Raman spectrum.

Peak fitting was performed with PseudoVoigt functions using one or two contributions, and a dynamic procedure was used as for the XRD diffraction experiment (see p**100**).

For the fitting of Fano lineshapes, the deconvolution of the C-C bond vibration and the scattering background was practically impossible, so the fitting was complicated due to the combination of both signals.

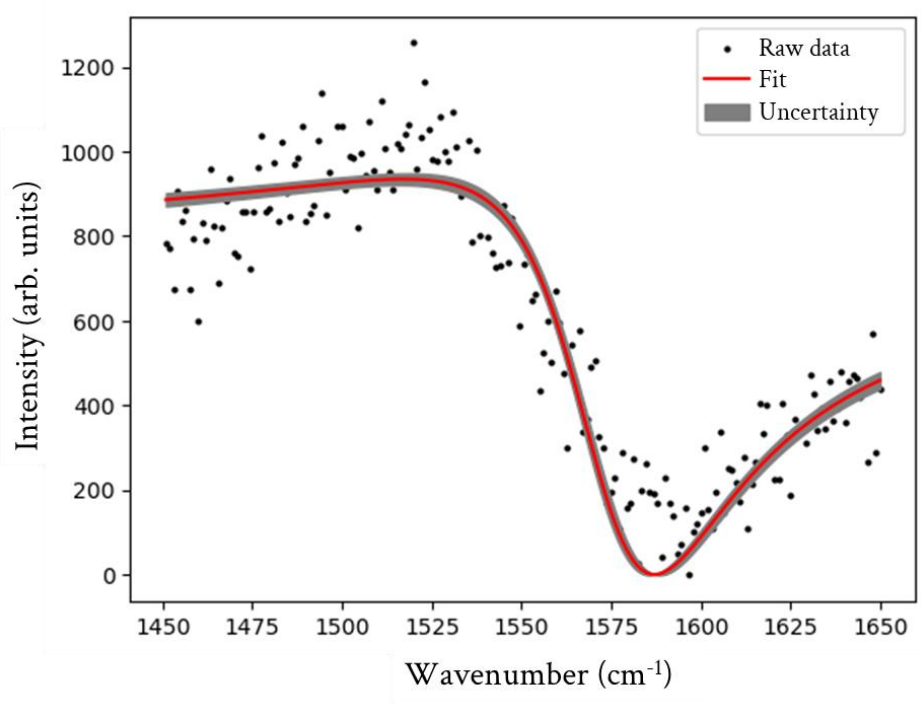


Figure 62: Example of Fano lineshape fit.

4.3 BM02 experiment

4.3.1 Experimental set-up and cell specifications

The data were acquired at the BM02-D2AM beamline from ESRF, an image of the experimental set-up is shown in **Figure 63**. A commercial cell from KOKAM® was used for this specific measurement. It is composed of 16 double-coated and two single-coated sheets of NMC811 with a coating thickness of 65 µm on 11 µm (double-coated) and 47 µm (single-coated) aluminium current collectors and 17 double-coated sheets of 80 µm graphite coated onto an 8 µm copper current collector finally separated by a polyethylene film (15 µm). This cell has a nominal capacity of 11.6 Ah. The positive electrode is composed of 85%$_{wt}$ of NMC and 15%$_{wt}$ of carbon and binder, with a loading of ~19 mg.cm^{-2} in the active material and a porosity of 31% (Hg intrusion). The negative electrode is composed of graphite (without any specification from the manufacturer), with a loading of ~12.5 mg.cm^{-2} and a porosity of 35% (Hg intrusion). The N/P ratio was estimated to be approximately 1.2. The cell specifications are given in annex (**Table A2**).

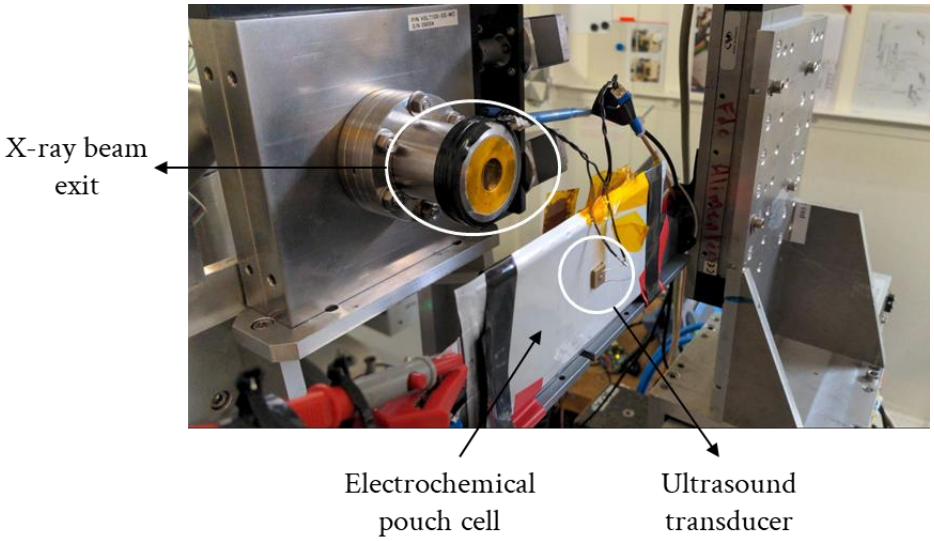


Figure 63: Image of the experimental set-up used at BM02.

The cell was cycled at the synchrotron beamline as follows: in a thermoregulated hutch at ~25 °C without a pressure appliance, the cell was first discharged and charged at the C/3 rate, followed by one cycle at the C/8 rate, and the last cycle was performed via a GITT-like protocol with a cycling rate of C/3 and then paused for 1 hour. The cut-off voltages were 2.7–4.2 *V*. The C-rate in this study was defined as a specific current of 1 C = 372 $mA.g^{-1}$ for graphite and 200 $mA.g^{-1}$ for NMC 811.

4.3.2 WAXS data acquisition and treatment

The beam energy was set to 25 keV with a beam size of 100 x 100 μm^2. The detector was a Cegitek innovation detector, with Si hybrid pixel technology and a pixel size of 130 μm^2. The detector was mounted just after the sample to measure a large *q* range. The 2D images were integrated via the pyFAI library[171] after the geometry was calibrated by using LaB_6 samples. All integrations were corrected to mitigate the effects of the flat detector geometrical distortion and incoming beam intensity.

From the raw diffraction patterns obtained, specific ranges of *q* ($Å^{-1}$) were selected to isolate the peaks of interest (1.2 to 1.45 $Å^{-1}$ for 003 NMC Bragg reflection and 1.6 to 1.95 $Å^{-1}$ for 002 graphite Bragg reflection). Each diffractogram was fitted as explained in p7**1**, and the peak position was then extracted. Other metrics, such as the FWHM and amplitude, were extracted but not relevant because of the high broadness of the peaks. Simpler metrics, such as the mass centre of the diffractograms, were extracted *via* weighted averaging of the peak mean positions.

4.3.3 Ultrasound acquisition

On the surface of the cell, piezoelectric ceramic elements (manufactured from the PIC255 material by PI Ceramic, with dimensions L x B x T of 10 mm × 10 mm × 2 mm and a resonance frequency of 1 MHz) were glued at the centres of both sides. Special care was taken to place the elements directly opposite each other. At the synchrotron, an Olympus Epoch 650 was used to excite one of the piezoceramic elements with a single pulse (500 µs duration) and read out the other element's delayed response.

5 MECHANICAL CHARACTERISATIONS

5.1 Dilatometric measurements

5.1.1 Experimental set-up

The dilatometric measurements were realised with the ECD-3-nano electrochemical dilatometer of EL-CELL®, illustrated in **Figure 64**. The electrochemical cell is composed of a T-frit separating the working and counter electrodes, a reference electrode, and a membrane that translates the variations of the working electrode thickness to the sensor. The counter electrode and the T-frit are fixed in the cell, whereas the working electrode is free to move in the sensor direction.

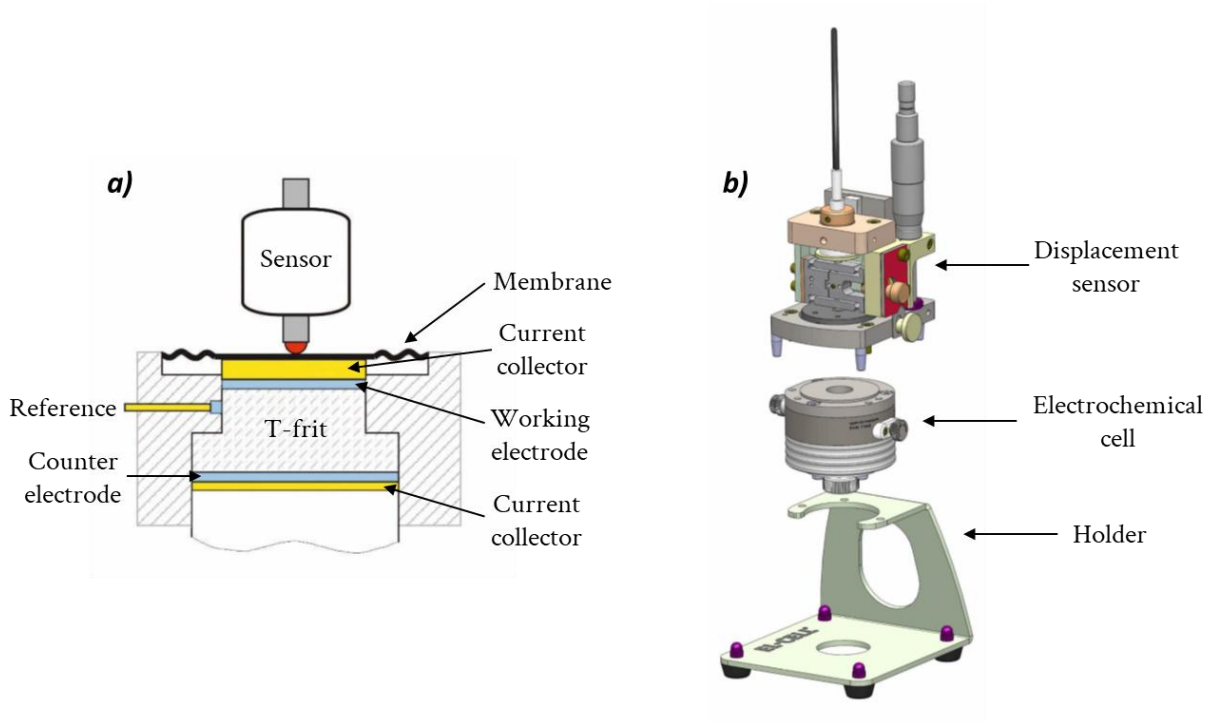


Figure 64: Illustration of the ECD-3 electrochemical nano-dilatometer from EL-CELL®. a) Schematic of the electrochemical cell. b) Schematic of the dilatometer assembly. Adapted from the ECD-3-nano manual of EL-CELL®.

5.1.2 Electrochemical cell assembly

The electrochemical cell was assembled in an Ar-filled glovebox. The cell components were dried before the assembly at 80°C overnight, the electrodes were dried in dynamic vacuum at different temperatures depending on the active material. The T-frit and the Whatman separators were dried at 180°C under dynamic vacuum overnight. The assembly consists in a counter electrode of 12 mm of diameter, and a working electrode of 10 mm. An additional Whatman separator of 12 mm diameter was added between the counter electrode and the T-frit based on the recommendations of the cell supplier, and the separators were soaked by ~400 µl of electrolyte up to the saturation of T-frit. To ensure a good thickness between the T-frit and the membrane, a stainless-steel spacer of 2.1 mm was added. Because of issues with the cell air-tightness, sealing gaskets of 38 x 33.3 x 1.8 mm were bought, and each gasket was used only one time to seal the cell. After each experiment, the electrochemical cell was dismounted and washed using ethanol. The T-frits were washed in a nitric acid solution overnight, then washed with ethanol and dried in an oven at 80°C.

5.1.3 Cycling conditions

The electrochemical cell was fixed on the holder unit, and the displacement sensor unit was screwed on the electrochemical cell. The positioning of the sensor unit was done with a micrometric screw, and with the help of a light indicating the good contact between the sensor and the membrane. The dilatometer was cycled in a thermoregulated oven (IPP30, Memmert®) at 25°C. Because of the high resistance generated by the large T-frit separator, a cycling rate of C/40 was always used as recommended by EL-CELL. An OCV period of at least 20 hours prior the cycling was always performed to ensure the stabilisation of the cell voltage as well as the displacement of the electrode.

5.1.4 Reproducibility issues

If the experimental concept is rather simple, the use of this nano-dilatometer was not. Indeed, a major issue of reproducibility was observed with a lot of failures upon cycling. Most of the time, these failures were linked to air-tightness issues or to loss in the contact between the electrode and the probe. In the end, an approximative success rate of 1/5 functional dilatometer was obtained. Despite these issues, some tests were conclusive and are presented in this manuscript.

6 ^{6}LI-ISOTOPE

6.1 ^{6}Li-enriched electrolyte

6.1.1 Electrolyte preparation

A home-made ^{6}Li-enriched LP30 (^{6}LP30) was prepared using $^{6}LiPF_6$ (Sigma Aldrich, > 95% isotopic purity) as salt and EC:DMC (1/1 $\%_v$) as solvents. After reception, each $^{6}LiPF_6$ salt was placed in an Ar-filled glovebox, introduced in a Büchi, and dried under dynamic vacuum at 100°C for 24h. In parallel, a solution of EC:DMC (1/1$\%_v$) was prepared in glovebox and dried using molecular sieves (themselves preliminarily dried at 180°C under dynamic vacuum). The molecular sieves were introduced in the solution (~1/3 of the solution volume) and let for 24h under static conditions. The solution was collected using a syringe with a filter to remove the dust created by the sieves. The drying procedure was realised twice for a cumulated drying time of at least 48h.

The ^{6}LP30 solution was prepared by introducing the $^{6}LiPF_6$ salt (targeting a concentration of 1 M) in a graduated flask of 2 or 5 mL, and adding the EC/DMC solution up to the gauge line. The solution was then analysed by ^{19}F Nuclear Magnetic Resonance (NMR) and Induced Coupled Plasma-Mass Spectrometry (ICP-MS) to measure the salt concentration and the isotopic purity.

6.1.2 Electrolyte characterisation

To measure the salt concentration, a direct measurement of the lithium content using ^{6}Li NMR was not possible with our NMR apparatus. Indeed, the gyromagnetic moment of ^{6}Li is very near from deuterium and their respective Larmor frequency are very close (58.90 MHz vs. 61.43 MHz respectively)[177]. For this reason, the NMR apparatus disabled the tuning of the probe at such frequency using pass-band filters. Using ICP-MS, the measurement of ^{6}Li isotope concentration was also not possible because it requires a specific column to avoid cross contaminations. For these reasons, the measurement of salt concentration was realised by measuring the counter-anion concentration using ^{19}F NMR. The fluorine concentration quantification was done using an internal standard, introduced at 1 M in the ^{6}LP30 solution. Two internal standards were used: 1,1,2,2-tetrafluoroethyl 2,2,3,3-tetrafluoropropyl ether (TCI, > 95% purity) named TFETFPe, and fluoroethylene carbonate FEC (Sigma Aldrich, > 99% purity). Both internal standards were selected because of their respective fluorine NMR shift that do not overlap with the PF_6^- signal, and because of their good solubility in the carbonate-based solutions. Practically, an NMR tube was prepared by introducing a 300 µL solution composed of ^{6}LP30 and the internal standard (1 M). **Table 5** gives the volumes of each component in the NMR tubes to obtain a concentration of 1 M in internal standard and the dilution factor. An insert containing deuterated-DMSO ($(CD_3)_2SO$) was introduced to enable the NMR apparatus locking.

Table 5: Specification of the internal standards and ^{6}LP30 volumes in the NMR tests.

Internal standard	Internal standard volume (µL)	^{6}LP30 volume (µL)	Dilution factor
TFETFPe	45	255	0.85
FEC	22	278	0.927

Several batches of $^{6}LiPF_6$ salt were tested because of purity issues. The tests are reported here, with a description of the method to determine the concentration in counter-anion of the ^{6}LP30 solutions.

Prior using this method on ^{6}LP30 solutions, the reliability of the method was evaluated using a commercial LP30 solution. The same procedure was used as described above for the NMR tube preparation. The obtained ^{19}F NMR spectra are given in **Figure 65**, the PF_6^- signal appears in the form of a doublet at -75 ppm (each peak integrating for three fluorine atoms), the TFETFPe signals (**Figure 65a**) are spread from -93 ppm to -140 ppm (each one integrating for two fluorine atoms), and the FEC signal (**Figure 65b**) is located at -124 ppm for one fluorine atom of integration.

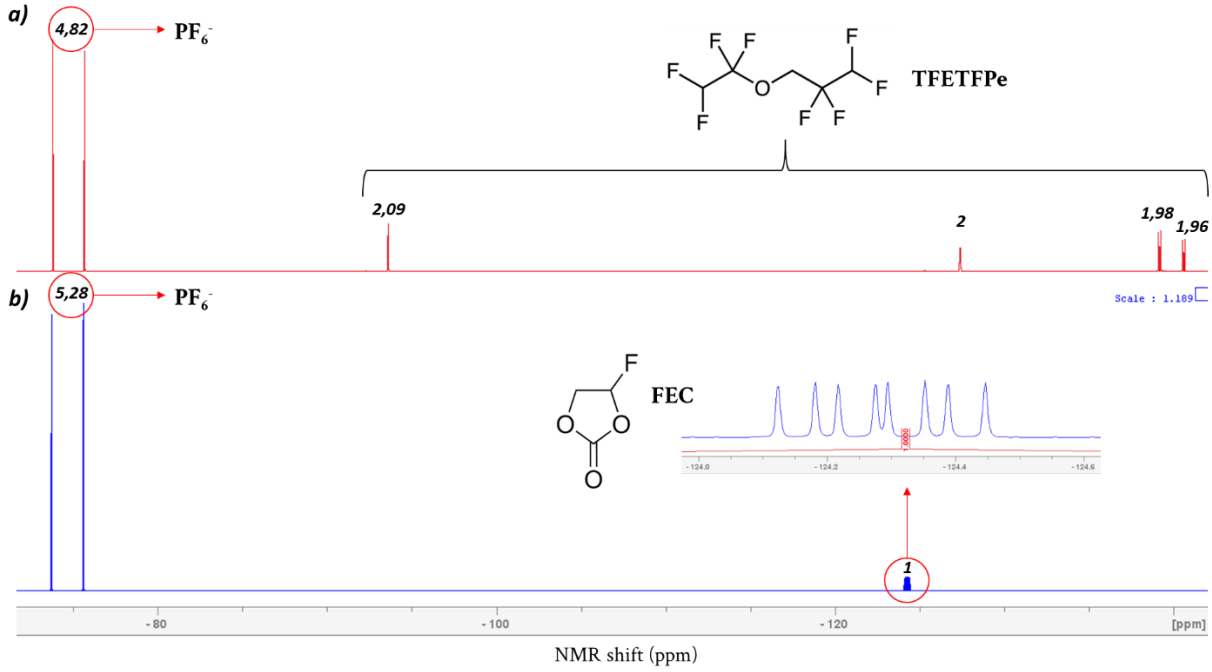


Figure 65: ^{19}F NMR spectra of LP30 + internal standards solutions with deuterated-DMSO insert. a) With TFETFPe as internal standard. b) With FEC as internal standard.

Since the internal standards were introduced at 1 M, the quantification of the PF_6^- concentration in the NMR tube can be assessed through its integrated signal (sum of the two peaks). Taking the example of the NMR spectra with TFETFPe as internal standard (**Figure 65a**), the PF_6^- signal

integrates for 4.82 whereas its theoretical integration accounts for 6 fluorine atoms. This leads to a concentration of PF_6^- in the NMR tube of 4.82 / 6 = 0.8 M, and considering the dilution factor (0.85), the PF_6^- concentration in the initial LP30 solution is estimated at 0.8 / 0.85 = 0.95 M. The obtained value is in the error bar of ^{19}F NMR experiments for the measurement of concentrations (±5%) with a target concentration in PF_6^- of 1 M for LP30. The same method was used for the experiment using FEC as internal standard, and a concentration of 0.95 M was also obtained.

The methodology was tested in a commercial LP30 and it demonstrated its reliability in the measurement of PF_6^- anion concentration. Then, the prepared ^{6}LP30 solutions were characterised using the same method and internal standards. The first $^6LiPF_6$ salt received was used to prepare a 1 M $^6LiPF_6$ in EC/DMC (1:1%$_v$) solution. The obtained ^{19}F NMR spectra are plotted in **Figure 66**. Impurities are observed around -85 ppm and probably correspond to OPF_2OH degradation products (~2% of concentration) coming from hydrolysis of the PF_6^- anion[178].

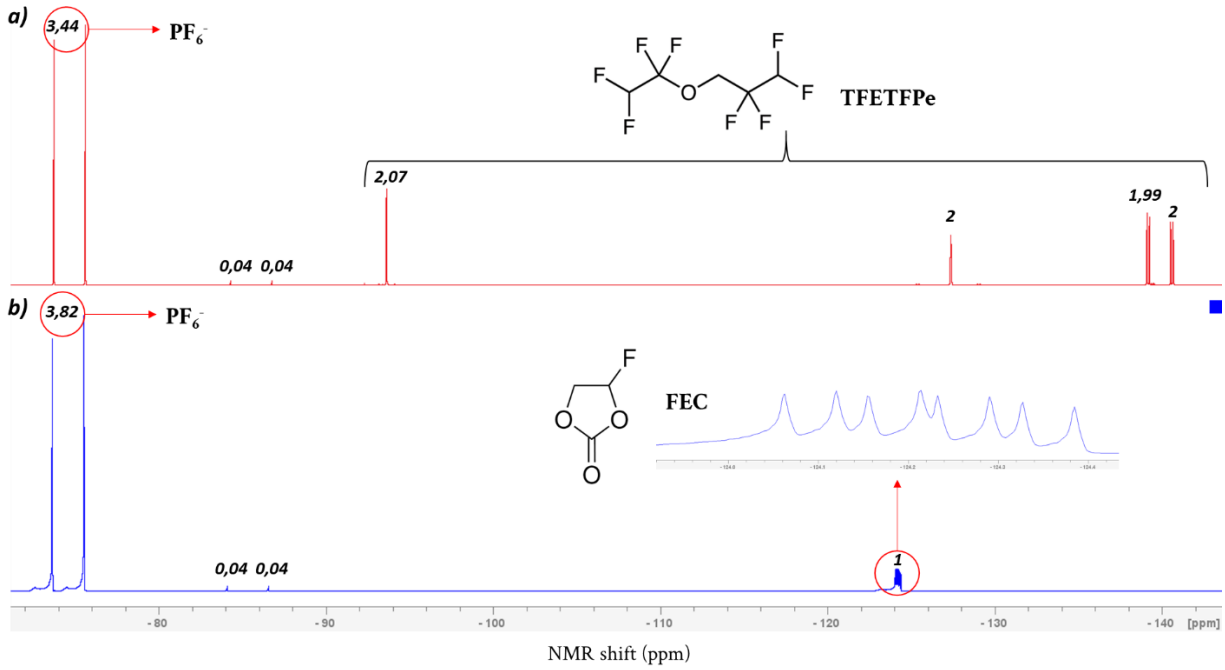


Figure 66: ^{19}F NMR spectra of ^{6}LP30 + internal standards solution with deuterated-DMSO insert. a) With TFETFPe as internal standard. b) With FEC as internal standard.

The quantification of the PF_6^- concentration in the initial ^{6}LP30 solution was estimated to 0.67 and 0.69 M using the two internal standards. This result has important implications for the study because it implies an issue of purity in the $^6LiPF_6$ salt bought.

Due to this salt impurity, other $^6LiPF_6$ batches were tested, and the results of PF_6^- concentration and the targeted concentrations are given in **Table 6**. The three tested batches of $^6LiPF_6$ displayed a rather white powder colour (as every lithium salt used in battery field). Each of them was measured with PF_6^- concentrations lower than the expected concentration of $^6LiPF_6$ salt. The best

batch obtained was the third one with a targeted concentration of 1.5 M, and an obtained one at 1.26 M (±5%). This third batch was kept for the following of the study and the ^{6}LP30 solution was diluted to 1 M (concentration of the PF_6^- salt).

Table 6: Concentration of PF_6^- anions in the several ^{6}LP30 solution prepared.

$^6LIPF_6$ batch number	**Targeted concentration of $^6LiPF_6$ in EC/DMC (in mol.L^{-1})**	**Concentration of PF_6^- (in mol.L^{-1})**
1	1	~ 0.68
2	1	~ 0.25
3	1.5	~ 1.26

6.1.3 Coin cell assembly

The metal lithium electrode was substituted with ^{6}Li from Sigma-Aldrich (> 95% ^{6}Li enrichment). In an Ar-filled glovebox, the ^{6}Li chunks were removed from the mineral oil and washed using hexane or heptane. The chunks were hammered to shape them into a foil of roughly 100 – 200 µm, and a razor blade was used to remove the black native layer of oxides. Then, the coin cell assembly was realised as described in p**60** with 130 µL of ^{6}LP30 as electrolyte and ^{6}Li as negative electrode.

CHAPTER III

THIN ELECTRODE CHARACTERISATION

This third chapter is dedicated to the investigation of graphite electrodes in thin-film-like configuration (2D). By combining electrochemical and structural characterisations, the lithiation of graphite is discussed under quasi-thermodynamic conditions. In a first part, electrochemical investigations are discussed to understanding the kinetic properties associated to the lithium diffusion in graphite. Then, *operando* experiments using X-ray diffraction and Raman spectroscopy are discussing the mechanism of graphite lithiation. Part of the results are taken from the following publication:

- Understanding Fast Charging Ability Limitation in Graphite Electrode for Li-ion Batteries: Quasi-thermodynamic Approach and Methodology, C. Renais, M. Mirolo, M. Servajon, J. Drnec, F. Alloin and C. Villevieille, *Chemistry of materials*, 2025, 37, 5647-5657 [179].

1 ELECTROCHEMICAL CHARACTERISATION OF THIN GRAPHITE ELECTRODES

Graphite electrodes as thin as possible are the optimal configurations for investigating a system without any electronic/ionic limitations. Indeed, with very low electrode thicknesses/low loadings (few micrometres), the ionic species transport in liquid phase is very fast, as well as the electronic transport because of the short-distances to travel for the charge species. Thin* graphite electrodes were prepared as described in p**59**. **Figure 67** shows an electrode cross-section image obtained by SEM, and the estimated thickness was around ~6.5 µm. Porosity was estimated to be around 70%, providing an optimal wetting once soaked by the electrolyte. As a reminder, the thin electrodes were composed of 90%$_{wt}$ of SFG 6L graphite and 10%$_{wt}$ of PVDF as binder to provide mechanical strength. No carbon additives were voluntarily added to supress as much as possible secondary processes upon dis/charging such as adsorption on the carbon nano-particles, with this the electrode answer only depends on the studied graphite particles which is the electroactive material.

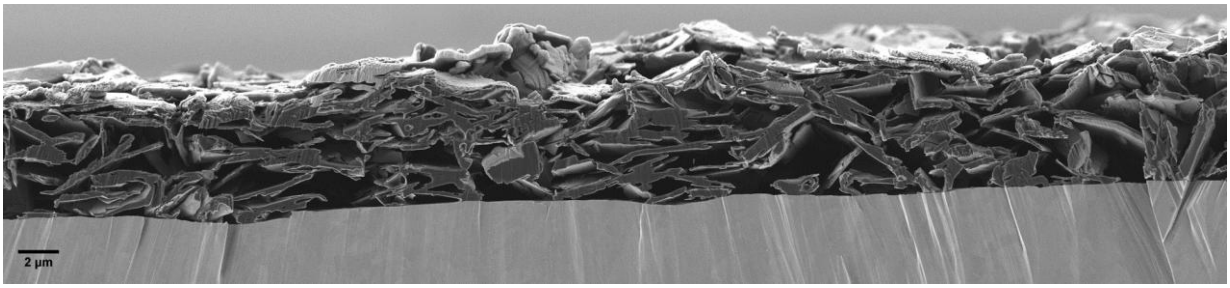


Figure 67: SEM cross-sectional image of a thin graphite electrode. The current collector is at the bottom of the image.

1.1 Cycling profiles and rate capability tests

The electrochemical characterisation of the thin electrodes was performed in half-cells with lithium metal as counter electrode (CE), cycled between 1.2 V and 0.01 V, with LP30 electrolyte (1M $LiPF_6$ in ethylene carbonate (EC)/dimethyl carbonate (DMC) 1:1%$_v$). A typical voltage profile of such cell is displayed in **Figure 68**. The capacity estimation in (mAh.g^{-1}) is rather difficult in such systems because of the high uncertainty in the weighting of the thin electrode. Instead, cell capacity is always normalised between 0 and 1 at C/20 cycling rate, referring to the cell state of charge (SoC). In addition, as graphite is investigated in half cell, using metallic lithium as negative electrode, the insertion of lithium in graphite under reductive conditions will be attributed to the discharge of the cell, and the charge corresponds to the removal of lithium ions from graphite

* The thin electrodes refer to a thin-film like configuration with an electrode thickness of few micrometres.

under oxidative conditions. To avoid any confusion, these processes will be referred as lithiation and delithiation of the graphite electrode.

1.1.1 Hysteresis

As discussed in the state-of-the-art, first-order transitions are associated to a hysteresis between charge and discharge[180]. This hysteresis can originate from an activation energy barrier associated to the nucleation of the phase that is formed[181]. A very good example is the water freezing and its melting point that can be different under static conditions. Indeed, by decreasing the temperature, the water freezing can occur at negative temperatures (up to -40°C, known as supercooling) if no nucleation point is initiated by water crystallisation[182]. The same applies for the ice melting that can occur at higher temperature than 0°C (supermelting). These phenomena illustrate the hysteresis coming from the short-history of first-order transitions, in this case, the biphasic transition temperature depends on if the temperature increases of decreases. The same applies for solid-state first-order transitions such as in two-phase transition electrode materials as LFP or graphite. As explained by Jahn *et al.*, the equilibrium potential (also called OCV profile) of materials highly depends on the short-term history of the applied current[183]. The hysteresis induces a lower potential in lithiation and a higher potential in delithiation, and can be interpreted as the result of different activation energy barriers for the nucleation of the two solid phases ($LiFePO_4$ and $FePO_4$ as an example). In the case of LFP, an hysteresis of ~20 mV is reported[184–186] whereas for graphite, the voltage difference is around 10 mV[187] but also depends on the phase transition.

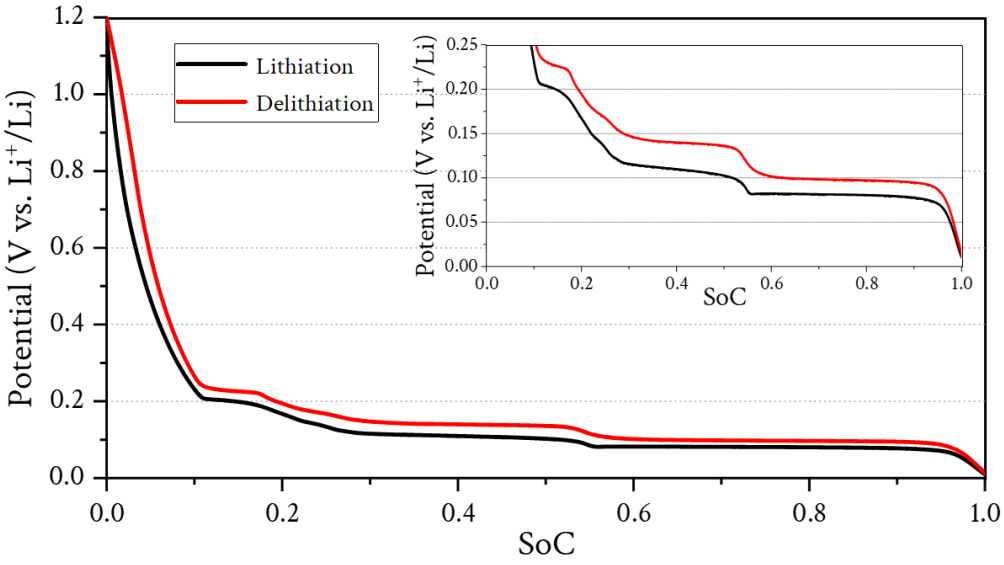


Figure 68: Potential of a thin graphite electrode cycled at C/20 rate in half cell at 25°C with LP30 electrolyte. Inset corresponds to a zoom of the main plot to better see the potential plateaus.

In **Figure 68**, the hysteresis of potential between charge and discharge is clearly observed, as expected for first-order transitions[84]. To go further in the analysis of the potential profile, a DCA was performed that allowed the localisation of the several potential plateaus (**Figure 69**). In **Figure 69**, three principal peaks (a, d and e) were attributed to the three main potential plateaus visible in **Figure 68**. With this representation, an easiest estimation of the several potential plateaus is possible, and the hysteresis between lithiation and delithiation was expressed by the peak-to-peak shift. The peaks correspond, according to literature (see p**38**), to the following hypothetic Reaction VIII - Reaction XII:

$$(a)\ LiC_{72} + Li^+ + e^- \rightleftharpoons 2\ LiC_{36} \qquad \textit{Reaction VIII}$$

$$(b) 3\ LiC_{36} + Li^+ + e^- \rightleftharpoons 4\ LiC_{27} \qquad \textit{Reaction IX}$$

$$(c)\ 2\ LiC_{27} + Li^+ + e^- \rightleftharpoons 3\ LiC_{18} \qquad \textit{Reaction X}$$

$$(d)\ 2\ LiC_{18} + Li^+ + e^- \rightleftharpoons 3\ LiC_{12} \qquad \textit{Reaction XI}$$

$$(e)\ LiC_{12} + Li^+ + e^- \rightleftharpoons 2\ LiC_6 \qquad \textit{Reaction XII}$$

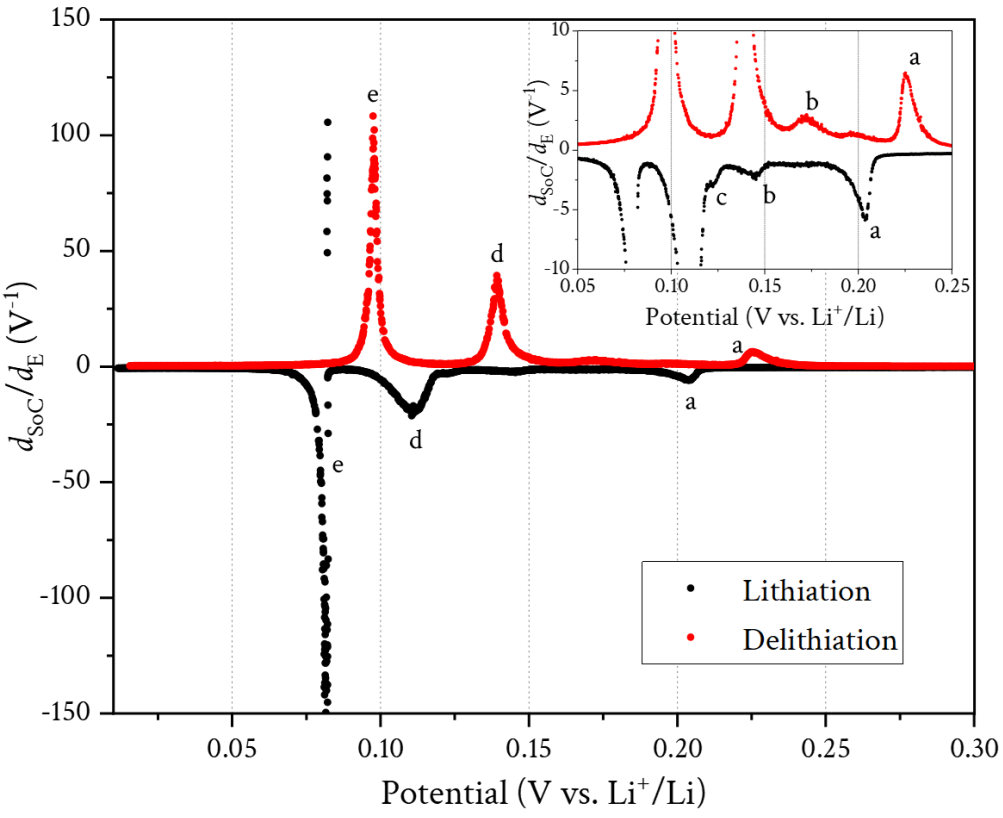


Figure 69: DCA of a thin graphite electrode cycled at C/20 in half cell at 25°C with LP30 electrolyte. Inset corresponds to a zoom on the main plot that shows better the different features.

Table 7 summarises the peak potential of the several phase transitions in lithiation and delithiation. A lower hysteresis can be seen for the last potential plateau ('e' peak), whereas the 'd' peak displays the higher hysteresis. To understand this, some authors studied the open-circuit voltage (OCV, or equilibrium voltage) of graphite electrode as a function of temperature. Mercer *et al.* demonstrated a higher temperature dependence for stage I' to stage IV ('a' peak) and stage II-L to stage II ('d' peak) transitions, whereas the transition from stage II to stage I ('e' peak) was not temperature dependent. According to the authors, the higher hysteresis attributed to the 'd' peak would originate from different structural paths in lithiation and delithiation. DFT calculations demonstrated that metastable phases of stage II-L exist in delithiation but not in lithiation, supporting different chemical potentials in lithiation and delithiation[187]. The non-dependence to temperature changes is typical from first-order transitions, and these results highlight an ambiguity in the lithium insertion mechanism for the stage I' to stage IV ('a' peak) and the stage II-L to stage II transitions ('d' peak), probably not corresponding to a classic biphasic process.

Table 7: Potential in lithiation, delithiation and hysteresis for the several peaks observed in DCA obtained at C/20 cycling rate.

Peak	Potential in lithiation (mV)	Potential in delithiation (mV)	Hysteresis (mV)
a	203.8	225.0	21.2
b	145.2	172.1	26.9
c	122.5	-	-
d	111.0	139.1	28.1
e	82.2	97.4	15.2

1.1.2 Voltage profile during rate capability

To investigate the kinetic properties of the several stages of graphite, a thin graphite electrode was investigated with a rate capability test protocol. The electrode was tested from C/20 to 5 C rate, corresponding to current densities from ~ 9 $\mu A.cm^{-2}$ to ~ 0.9 $mA.cm^{-2}$. An important point to discuss is the current density with respect to the lithium metal electrode. High critical current densities (15 - 18 $mA.cm^{-2}$) can be reached with solid-state electrolytes[188], but, in liquid electrolyte, the limit current densities are observed in the range of 0.5 – 1.5 $mA.cm^{-2}$ [189]. This implies that for too high current densities, lithium plating/stripping reactions start to limit the cell performance, generating high overpotentials because of non-uniform lithium deposition on the surface of the lithium. In this rate capability test, only very high rates (3 C – 5 C) could be influenced by the lithium electrode.

The voltage profiles obtained upon this rate capability test are plotted in **Figure 70**. A shift toward a lower potential is observed by increasing the cycling rate in lithiation and toward higher potential in delithiation. In addition, the increase of cycling rate induces a gradual loss of the

typical potential plateaus, with less marked potential steps (*e.g.*, at the phase transition around 0.5 SoC). The potential shifts can originate from i) an increase of the ohmic contribution that cannot be avoided (ohmic law) and/or ii) the appearance of overpotentials. For the latter, they can have several origins; in the case of a thin electrode, one can assume that electronic transport and ionic transport (in liquid phase) do not limit the system. Then, the thin electrode response is probably controlled by the solid-state transport of lithium and/or the charge transfer step (corresponding to the insertion step and associated to a mechanical opening of the graphite plane).

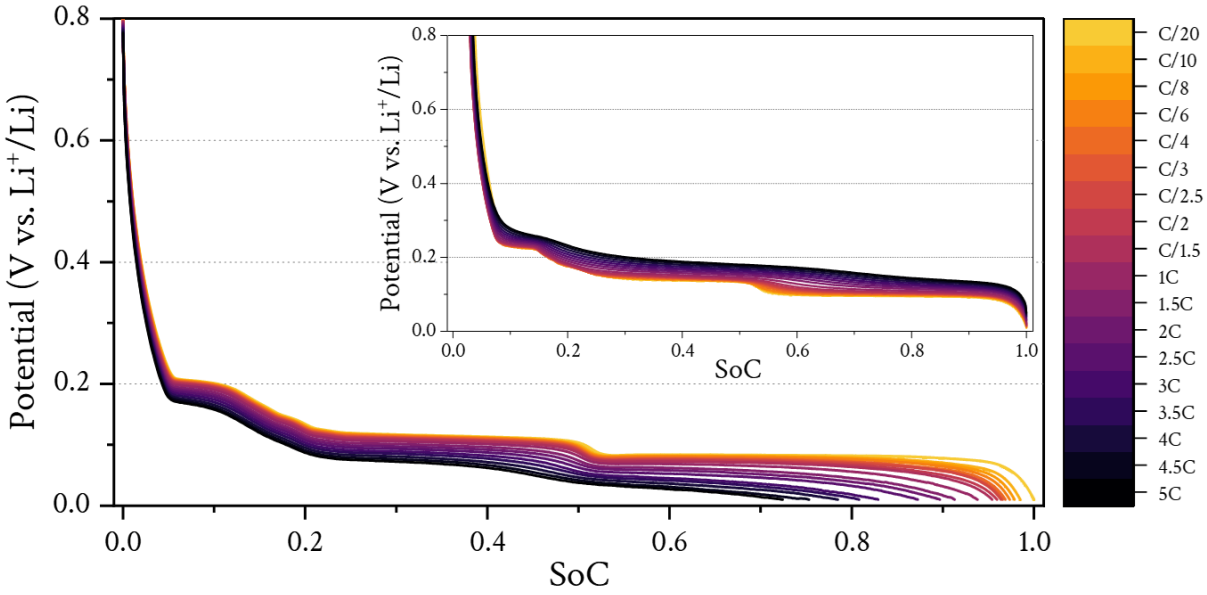


Figure 70: Galvanostatic profile as a function of SoC for a thin graphite electrode cycled from C/20 to 5 C rate in half cell at 25°C with LP30 as electrolyte. The main plot window corresponds to the lithiation and the inset corresponds to the delithiation.

Using DCA, the potential of each plateau was determined as a function of the cycling rate. **Figure 71a, c** shows the DCA profiles obtained upon the rate capability test in lithiation and delithiation, respectively. To highlight the impact of the C-rates, the insets in **Figure 71a, c** shows the evolution of the stage I' to stage IV transition ('a' peak) in charge and discharge. A gradual shift toward lower potential in lithiation, and toward higher potential in delithiation is observed. In parallel to these shifts, a decrease of the peak intensity is seen associated to a peak broadening. Quantitatively, these shifts were analysed by following the peak position as a function of the applied specific current, for the several features ('a' to 'e' peaks). For each cycling rate, the ohmic drop was estimated by ΔV value when the current was reversed between lithiation and delithiation. The ohmic drop contribution was removed from the calculated peak potential either by adding the ohmic drop to the peak potential in lithiation and by subtracting it in delithiation. The results are plotted in **Figure 71b, d**. For the lithiation process (**Figure 71b**), the decrease of peak potential as a function of specific current can be observed with two different regimes: i) a first period, rather linear for some peaks and non-linear for others, is observed from C/20 (18.6

mA.g^{-1}) to C/3 (124 mA.g^{-1}), whereas ii) a second linear period is observed from C/2 (186 mA.g^{-1}) to 5 C (1860 mA.g^{-1}).

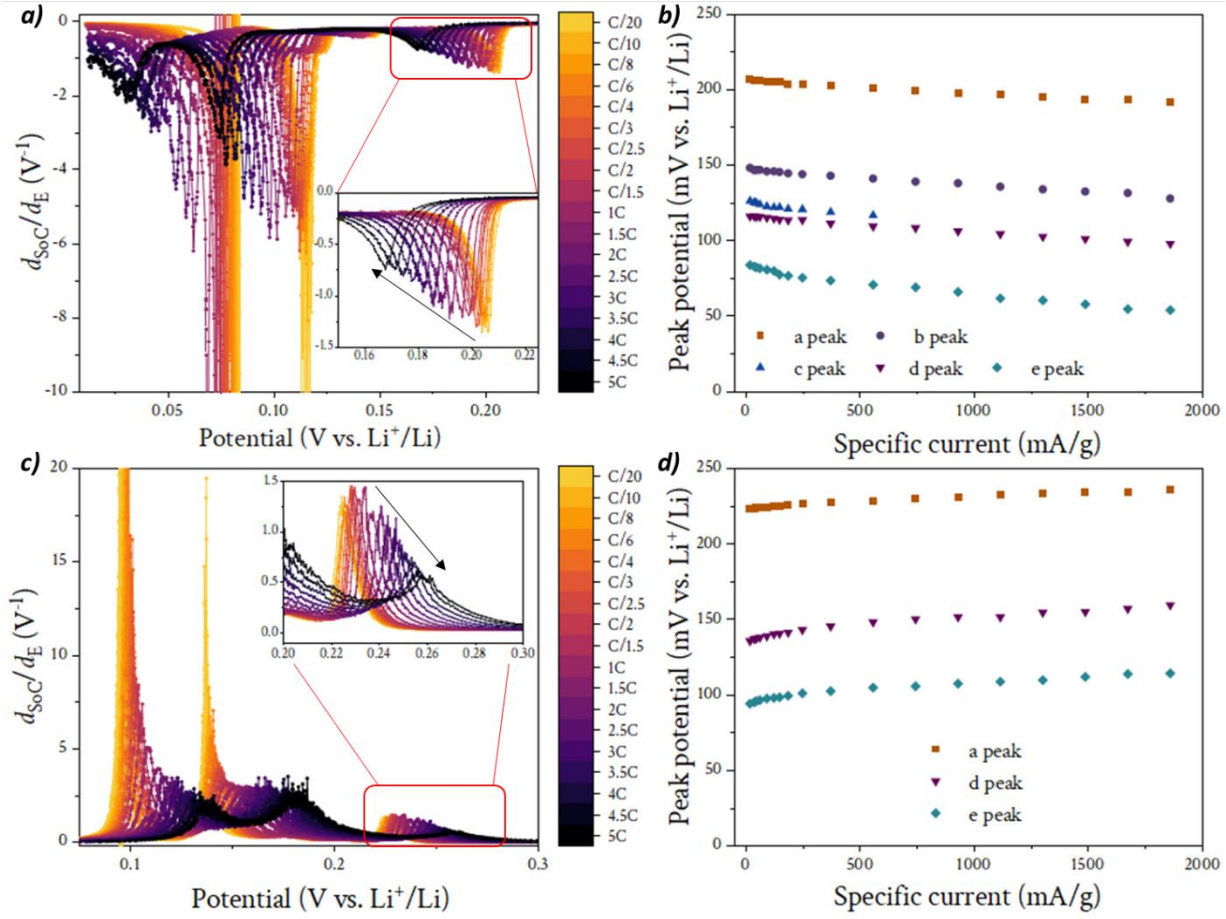


Figure 71: Differential capacity analysis (DCA) in lithiation (a) and delithiation (c) of a thin graphite electrode cycled from C/20 to 5 C in half cell at 25°C with LP30 as electrolyte. Insets show the 'a' peak evolution with increasing C-rate. Peak potential of the several features as a function of the specific current in (b) lithiation and (d) delithiation.

Linear regressions were performed on the second specific current period (> 186 mA.g^{-1}) and the results are summarised in **Table 8**. In lithiation, the 'a' peak displays the lowest slope, 'b' and 'd' peaks display very similar intermediate slopes, indicating that the potential shift occurs with the same intensity for these phase transitions (*i.e.* stage IV to stage III and stage II-L to stage II, respectively). For the stage II to stage I phase transition, ('e' peak) the highest slope is observed. These results, in lithiation, indicate that the last phase transition ('e' peak) displays higher overpotentials associated to solid-state lithium transport and/or charge transfer by increasing the specific current. Whereas the phase transition stage I' to stage IV (peak 'a') displays the lowest overpotentials. Concerning the delithiation process, the same two regimes of peak potential evolution were observed (non-linear from 18.6 to 124 mA.g^{-1} and linear from 186 to 1860 mA.g^{-1}). Only the 'a', 'd' and 'e' peaks were analysed because of the difficulty of estimating the peak potential for other features. As for the evolution in lithiation, the slope attributed to the stage I' to stage IV

phase transition ('a' peak) is the lower one, whereas the stage II-L to stage II phase transition ('d' peak) and stage II to stage I ('e' peak) showed similar slopes. In delithiation, it seems that the overpotentials associated to the specific current increase are not larger for the last plateau ('e' peak), in contrast to the lithiation process.

Table 8: Slopes obtained from linear regressions fitting the peak potential evolution in Figure 71b, d.

Peak	Slopes from linear regressions (in $mV.mA^{-1}.g$)	
	Lithiation > 186 $mA.g^{-1}$	**Delithiation > 186 $mA.g^{-1}$**
a	-7.3 ± 2.10^{-1}	5.8 ± 2.10^{-1}
b	-9.4 ± 3.10^{-1}	-
d	-9.5 ± 2.10^{-1}	9.7 ± 6.10^{-1}
e	-14.1 ± 4.10^{-1}	8.5 ± 4.10^{-1}

One hypothesis to support these observations relies on the mechanical aspect of lithium de/insertion, which is significantly different in lithiation and delithiation. If during lithiation the opening of the graphite layers occurs to allow lithium insertion, the delithiation is associated to the removal of lithium from the opened-layers. This mechanical difference makes the insertion process more difficult and energy-intensive compared to delithiation. Based on this, larger overpotentials can be expected upon lithium insertion, which is the case for the stage I' to stage IV ('a' peak) and stage II to stage I ('e' peak) phase transitions. Because the lithiation and delithiation phenomenon do not follow the same pathway for the stage II-L to stage II transition ('d' peak), one cannot expect the same trend.

1.1.3 Specific charges

The specific capacity was also analysed to determine the power capability of the thin graphite electrode. The CC-CV protocol consisted of a CC period that lasted between 0.8 and 0.01 V vs. Li^+/Li, and the CV lasted 30 minutes in both charge and discharge. **Figure 72a** shows the specific capacity obtained in charge and discharge, as well as the coulombic efficiency (CE) as a function of the cycling rate. Stable specific capacities were obtained in delithiation, whereas a specific capacity higher than the theoretical capacity of graphite was observed for the first cycles at C/20 and C/10 rates. This phenomenon could be attributed to an excess of charge in lithiation caused by the SEI formation (~ 10 cycles), which irreversibly consumes charges. In the following, a coulombic efficiency around 100% was obtained until 5 C cycling rate. The galvanostatic and potentiostatic contribution to the total charge were decomposed in **Figure 72b**, and one can observe the stable capacity obtained during the CC period in delithiation. As a contrast, the specific capacity obtained in lithiation during the CC period starts to decrease around C/1.5

cycling rate, and the charge obtained during CV step increases as a consequence. At this cycling rate, in the lithiation process, the galvanostatic period ends-up, due to the cut-off voltage (0.01 V), before reaching the maximal specific capacity, indicating a power limitation even in thin electrode. In the end, the galvanostatic contribution (CC) reaches ~70% of the total charge at 5 C for the lithiation process.

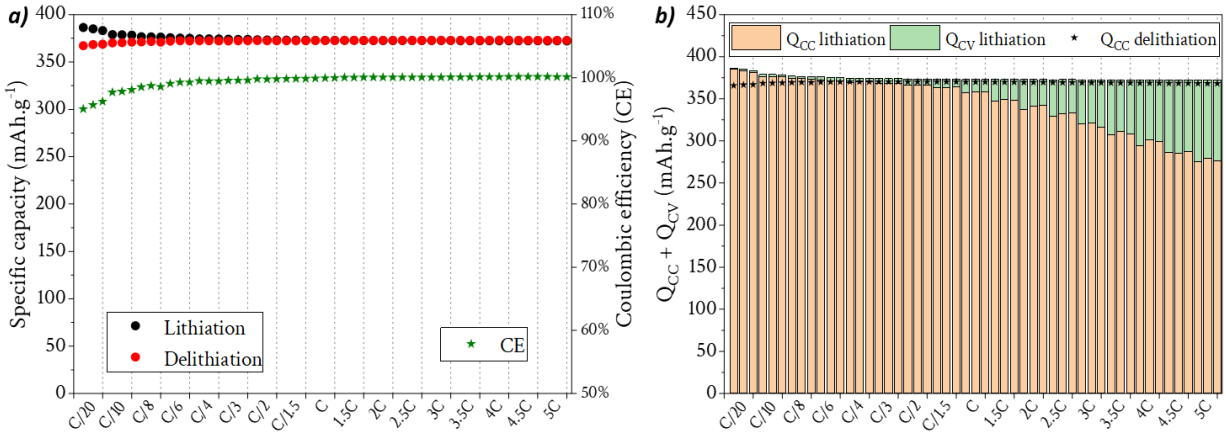


Figure 72: a) Specific capacity and coulombic efficiency in lithiation and delithiation as a function of the cycling rate for a thin graphite electrode at 25°C with LP30 as electrolyte. b) Specific capacity of the CC and CV periods in lithiation and CC contribution from delithiation.

This rate capability test highlights the difference in power capability between lithiation and delithiation for graphite material, with higher kinetic of delithiation than lithiation.

1.2 Diffusion coefficient measurement

In the previous section, the rate capability and the kinetic properties of the several stages of graphite were discussed. It was suggested that upon lithiation, the last plateau of potential displays the lower kinetic of insertion compared to that of other phase transitions. Unfortunately, the experimental conditions disabled the understanding of the origin of this kinetic limitation, *i.e.* solid-state transport of lithium and/or charge transfer.

To assess the solid-state transport of lithium, several techniques have been used in the literature such as GITT, PITT, EIS and CV. These techniques are all based on the measurement of characteristic diffusion times[190] (Eq. 21):

$$\tau = L^2/D \qquad \text{Eq. 21}$$

Where L is the characteristic diffusion length (m), and D is the diffusion coefficient ($m^2.s^{-1}$).

The experimental conditions are a crucial point in the measurement of diffusion coefficient. To ensure that the response signal depends on the solid-state transport of lithium, the system should be investigated with the lowest achievable loading to ensure that there is no mass transport limitation in the liquid phase, or electronic transport limitation.

Derived from the Fick's second law, all these methods are based on models that can, under specific conditions, estimate the diffusion coefficient of lithium in intercalation compounds. However, the assumptions made for some models imply specific conditions that are not fulfilled for every active material. This is the case of the GITT, which is assuming a linearity between the potential variation and the lithium concentration in the particles of active material. Then, only materials involving a single phase (solid solutions) upon de/lithiation are eligible, such as NMC. However, for materials such as graphite or LFP, the biphasic domains do not fulfil the conditions for such an assumption[191]. This is also the case for a more recent technique, the Intermittent Current Interruption[192] which cannot be used in the case of first-order transitions. On the other hand, PITT, CV and EIS can be applied for first-order transition materials. Here, PITT was used with the methodology described in p**62**.

The diffusion coefficients obtained are given in **Figure 73** as a function of the potential. In the case of biphasic systems, the diffusion coefficient depends on the two solid domains that coexist, and the extracted value is considered as binary. The evolution of diffusion coefficient with potential is specific for graphite compared to other materials such as NMC that shows less dependence on potential[193].

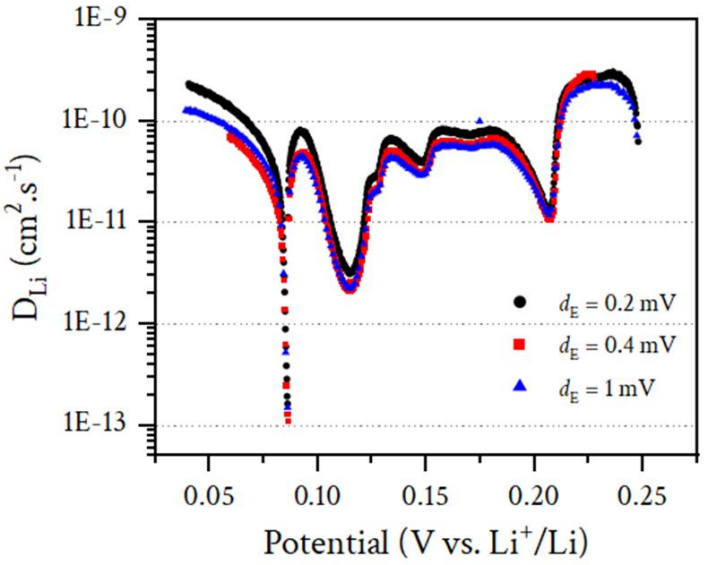


Figure 73: Diffusion coefficient as a function of potential obtained from PITT measurement in lithiation for a thin graphite electrode cycled at 25°C with LP30 as electrolyte.

This behaviour is strongly correlated to the lithium intercalation mechanism in graphite. Indeed, for regions involving a single phase (solid solutions) such as between 0.25 and 0.21 V vs. Li^+/Li, a quasi-constant diffusion coefficient is observed around 10^{-9} – 10^{-10} $cm^2.s^{-1}$, whereas lower diffusion coefficients are observed in biphasic regions. As an example, the transition from stage I' to stage IV ('a' peak in **Figure 69**) reaches a diffusion coefficient of 10^{-11} $cm^2.s^{-1}$. To make the link with the previous discussion, a lower diffusion coefficient can be seen for the stage II to stage I phase

transition compared to the others. This agrees with the observation made above, suggesting that this last first-order transition is the most kinetically limited. Compared to the literature, good agreement was noticed for the diffusion coefficient of the stage II to stage I transition around 10^{-13} – 10^{-14} $cm^2.s^{-1}$ [194]. Similarly, values in the range 10^{-10} – 10^{-11} $cm^2.s^{-1}$ were obtained for early lithiation (up to ~0.15 V)[195].

To understand this evolution of lithium diffusion kinetic, one should refer to the Daumas-Hérold[116] or localised-domain[118] models for graphite, in which defects and deformation of the carbon planes exist. These defects introduce additional strain along the carbon layers that are no longer flat, slowing down the lithium diffusion. As a consequence, the diffusion coefficients are low upon first-order transitions, and this effect is even more pronounced during the last stage II to stage I transition. Indeed, as illustrated in **Figure 74**, the transition from stage II to stage I implies the conversion of "deformed" carbon layers into plane layers. This is associated to a higher strain compared to other stage transition, which do not imply such a conversion of arrangement. In contrast, for regions of solid solution phase, lithium ions can diffuse "freely" in the host matrix and the associated diffusion coefficient is rather high. Interestingly, the magnitude order in solid solution regions for graphite (~ 10^{-9} – 10^{-10} $cm^2.s^{-1}$) is the same as that of NMC material that only involves solid solutions[193].

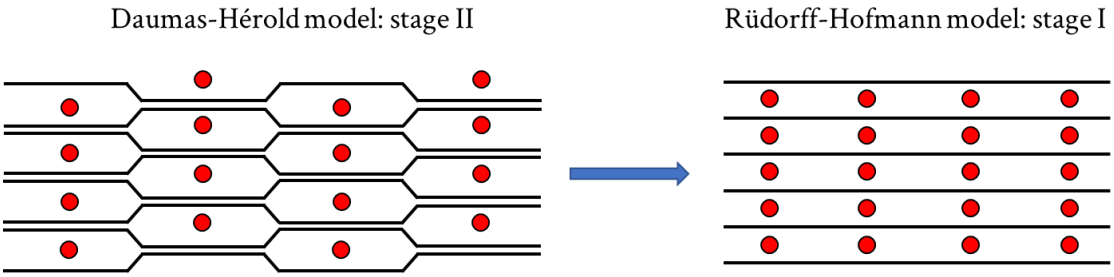


Figure 74: Illustration of the stage II and stage I arrangement following model from Daumas-Hérold and Rüdorff-Hofmann.

In this section, the lithiation and delithiation signatures of a thin graphite electrode were investigated. It was evidenced that the delithiation process is significantly faster than the lithiation, which suffers from higher kinetic limitations. On the basis of this, most of the experiments will discuss only the lithiation of graphite in half-cells. The investigation of the diffusion coefficient also highlighted the low diffusion rate of lithium in the stage II to stage I phase transition.

2 STRUCTURAL CHARACTERISATION OF THIN ELECTRODES

Electrochemistry is a powerful tool for the characterisation of electrodes from batteries, but it is important to combine it to other characterisation to achieve an in-depth understanding of reaction mechanism and limiting parameters. Graphite is a very atypical material with a characteristic structural organisation, which makes it an ideal case for structural investigations. In this part, the discussion is focused on the structural characterisation of graphite upon lithiation.

2.1 Operando XRD

2.1.1 Experimental considerations

As introduced in the state of the art, diffraction experiments are well adapted to the characterisation of the several stages of Li_xC_6, and their evolution upon cycling. To characterise the thin electrode, an XRD experiment was realised at the ID31 beamline from the European Synchrotron Radiation Facility (ESRF), the data acquisition is summarised in p**71**. This beamline is dedicated to X-ray diffraction experiments using either Wide-Angle or Small-Angle X-ray Scattering (WAXS / SAXS), and displays very high temporal and spatial resolutions. Because the SAXS technique is sensitive to nano-scaled materials, only WAXS was adapted to the investigation of graphite lithiation. The high temporal resolution allowed the acquisition of diffraction patterns in few seconds, leading to the characterisation of graphite lithiation *in operando* with ~500 diffraction patterns for a cycling carried out at C/10 (0.2% SoC variation between each acquisition).

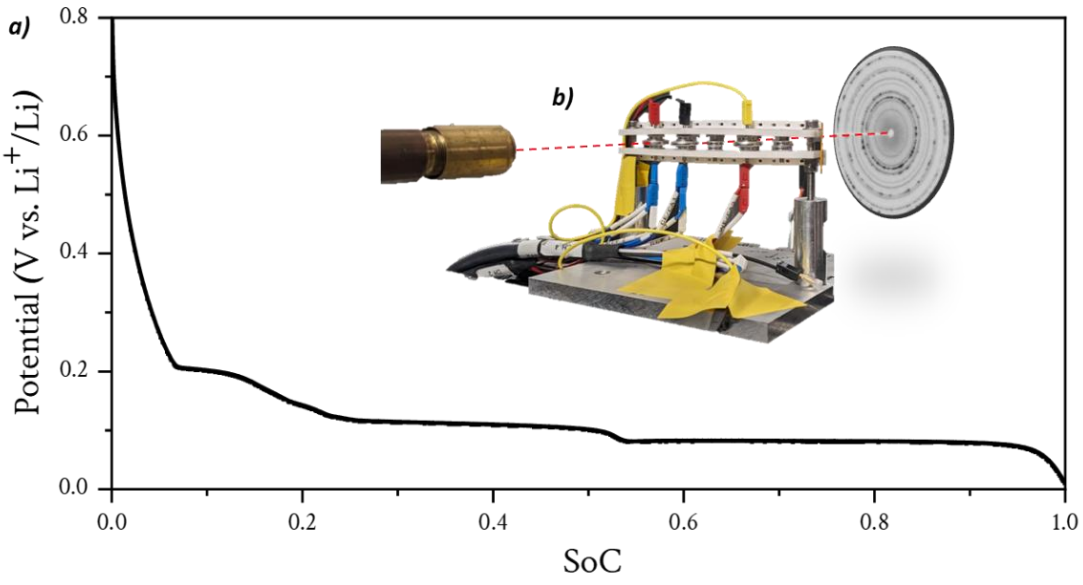


Figure 75: a) Cell potential of the thin electrode as a function of the state of charge. b) Experimental set-up at the ID31 beamline, ESRF.

The experimental set-up is represented in **Figure 75b**, which shows that the coin cell was probed parallel to the beam direction to ensure that the entire electrode diameter was probed by the X-ray beam. This beam was roughly 5 µm thick whereas the thin electrode was approximatively 6.5 µm, under these conditions almost the whole electrode thickness was in the field of view of the X-rays. The cell was cycled at C/10 under galvanostatic conditions, at 25°C with LP30 as electrolyte and the potential profile of the cell is shown in **Figure 75a**. Before the beamline experiment, the cell was preliminary cycled at C/20 in the laboratory to form the SEI. During lithiation, the cell accumulated ~0.2 mAh which was consistent with the maximum specific capacity obtained in the laboratory without beam exposure. According to the shape of the electrochemical curve, the low cut-off voltage achieved, and the accumulated charge, the graphite electrode reached its maximal state of charge.

Regarding the diffraction patterns, the q scattering vector was used instead of the diffraction angle (2θ) usually used in XRD with Eq. 22:

$$q = \frac{4\pi}{\lambda}\sin\left(\frac{2\theta}{2}\right) \qquad \textit{Eq. 22}$$

Where λ is the wavelength (Å) and θ is the diffraction angle.

Note that the q scattering vector does not depend on the beam wavelength, enabling direct comparison of diffraction patterns between different experiments with potentially different wavelengths.

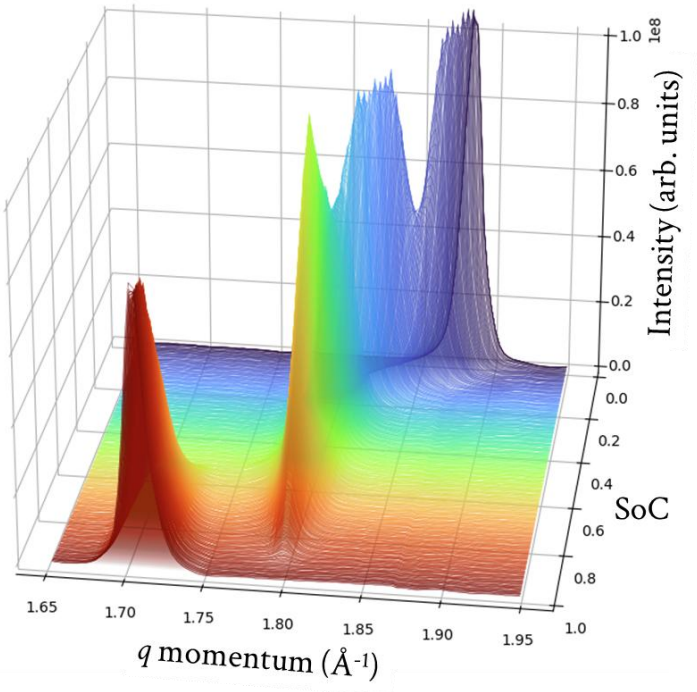


Figure 76: 3D representation of the diffraction patterns obtained upon lithiation of a thin graphite electrode obtained at ID31 beamline.

The diffraction patterns obtained during the experiment are plotted in **Figure 76**, because the graphite lithiation induces an increase in layer spacing (*d*-spacing), a shift of the (002) Bragg reflection is observed upon lithiation and occurs from ~1.88 $Å^{-1}$ (SoC = 0) to ~1.70 $Å^{-1}$ (SoC = 1). Here, the investigated *q* range only contains the (002) Bragg reflection, and one can follow the peak evolution upon lithiation with this 3D representation. The (002) Bragg reflection of graphite shifts toward lower angle (lower *q* scattering vector) while keeping the same peak intensity in a first part, corresponding to a solid solution process, whereas a biphasic region is visible for SoC > 0.6. In the end of lithiation, the Bragg reflection at ~1.78 $Å^{-1}$ totally disappeared, and only one Bragg reflection localised at ~1.70 $Å^{-1}$ is present. This supports the disappearance of the two-phase coexistence attributed to stage II to stage I transition before the end of charge, this will be discussed later.

The structural and electrochemical data were correlated in **Figure 77** and the phase transitions were identified based on the potential plateaus of the electrochemical profile.

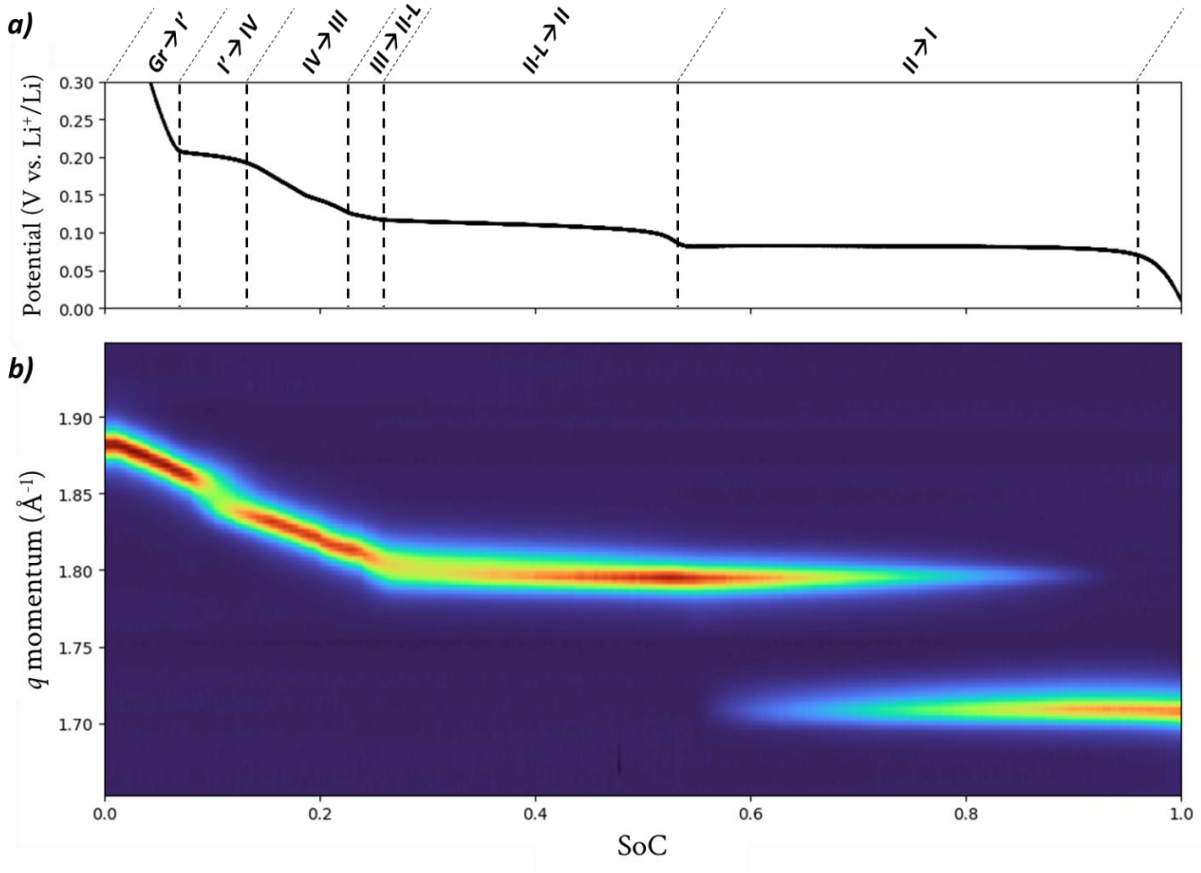


Figure 77: a) Evolution of the thin graphite electrode potential with respect to the SoC for a half cell cycled at C/10 rate at 25°C with LP30 as electrolyte. b) Contour plot representation of the diffraction patterns, the (002) Bragg reflections, obtained upon operando measurement of the thin graphite electrode.

Briefly, in the first region of potential drop (**Figure** 77**a,** transition from graphite to stage I'), a shift toward lower angles (**Figure** 77**b**) is observed, which is correlated with the solid solution process as discussed above. Entering the first potential plateau, a decrease in intensity of the peak (seen in the contour plot signal) is noticed and correlates with the appearance of a second phase (stage IV) that increases in intensity.

2.1.2 Peak fitting procedure

2.1.2.a Method

To analyse these data, Rietveld refinements are usually performed. However, this procedure is time-consuming, cannot be properly performed on huge amount of diffraction patterns when multiphases are present and can include biased results because i) *via* XRD, the thermal agitation parameter is too important and generates uncertainty on the lithium occupancy, and as Li is the lightest solid element, it is barely exploitable. ii) *Via* neutron powder diffraction, the signals are acquired on powders at the gram scale (thus very difficult to obtain suitable electrochemical data), averaging graphite particles that would be at the thermodynamic equilibrium for excessively low C-rates (*e.g.* C/500), making impossible such *operando* experiments in reasonable timeframe. For these reasons, the data analysis was performed using peak fitting with either one contribution for solid solution or two contributions for biphasic processes. In XRD, the peaks are usually fitted using a PseudoVoigt function[176] that is a linear combination of Gaussian and Lorentzian contributions (see the methodology in p7**1**). As a consequence, four parameters characterise a PseudoVoigt (pV) function: i) the peak position or centre (μ), ii) the peak amplitude or area under the curve (A), iii) a width at half maxima parameter (σ), note that because of the PseudoVoigt function symmetry, the full width at half maxima corresponds to 2σ, and iv) the peak fraction (α) corresponding to the fraction of Lorentzian contribution and (1- α) the fraction of Gaussian component. To ensure consistency in the performed fitting procedure, the diffraction patterns were fitted along the cycling direction (from SoC = 0 to SoC = 1) using a dynamic approach, *i.e.* the n^{th}+1 diffraction pattern was fitted using initial guess parameters from the results obtained for the n^{th} diffractogram. The number of contributions was selected based on the electrochemical signal, then, for an expected solid solution region, only one pV contribution was selected, whereas for biphasic regions, two contributions were implemented.

In the case of the stage III to stage II-L transition, XRD experiments already observed very difficult deconvolution of the two phases because of the lack of resolution[100]. For this reason, the diffraction pattern was fitted using one contribution accounting for the two-phase contribution. To take into account the peak asymmetry generated by the presence of two phases, the PseudoVoigt function was modified into a SplitPseudoVoigt (spV) function (see the methodology in p7**1**).

2.1.2.b Results – Analysis of the through-plane order via (00l) reflection

To better visualise and separate the electrochemical processes that appear in the voltage profile (**Figure 77a**), a differential representation of the data was used. First, the evolution of state of charge of the cell was derived with respect to the cell voltage (differential capacity analysis, DCA). This derivative was then expressed with respect to the cell state of charge instead of the cell voltage ($d_{SoC}/d_E = f(SoC)$, **Figure 78a**). With this representation, the peaks obtained by DCA are translated into waves that correspond to the different potential plateaus and the identification of each electrochemical process with respect to cell SoC is facilitated (note here that the curve displayed in **Figure 78a** is zoomed and the wave attributed to the stage I formation is cropped). A description of this methodology is given in p**65**.

The fitting results are plotted with respect to the cell SoC, and the evolution of the peak centre (**Figure 78b**), the peak FWHM (**Figure 78c)** and the peak amplitude (**Figure 78d**) can be seen. The graph was separated in seven regions based on the electrochemical signature ($d_{SoC}/d_E = f(SoC)$).

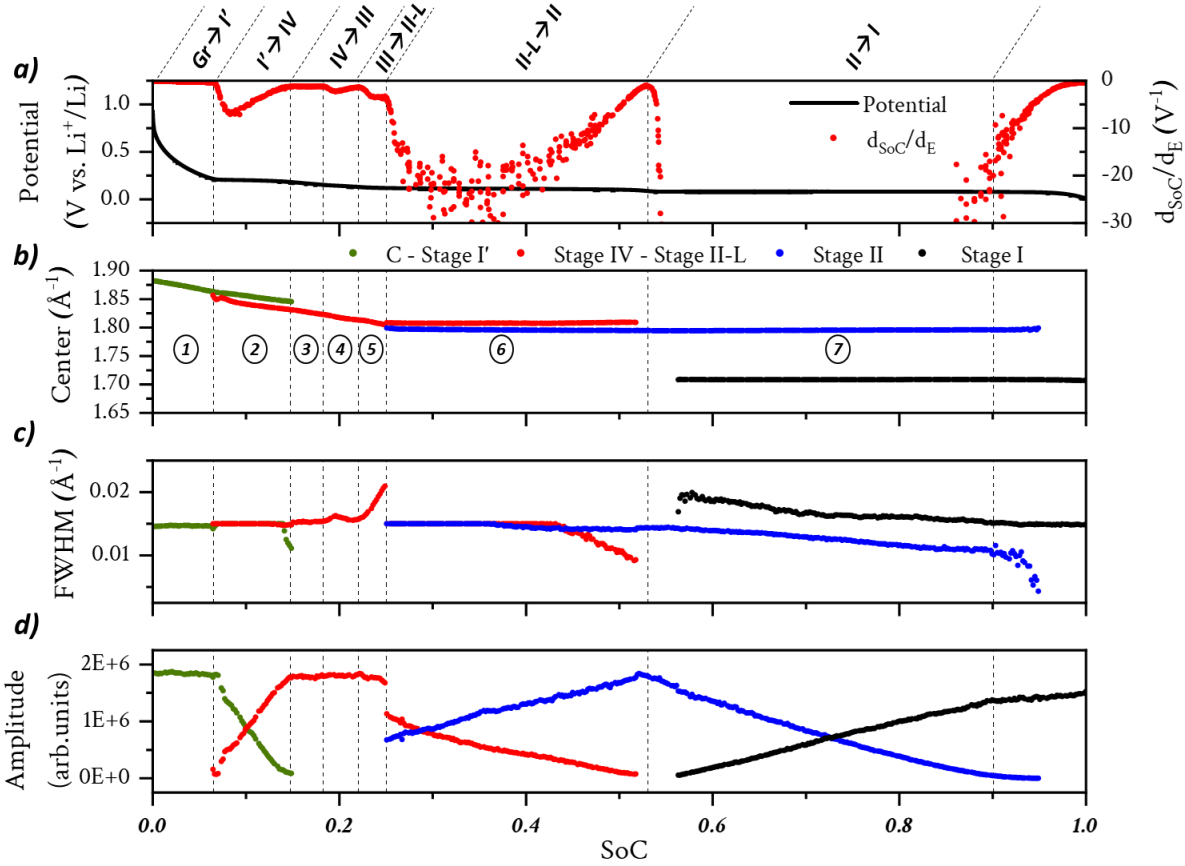


Figure 78: Results of fitting procedure obtained using either one or two (Split)PseudoVoigt contributions, depending on the investigated region. a) Evolution of graphite electrode potential (vs. Li^+/Li) on the left y-axis and d_{SoC}/d_E on the right y-axis with respect to the cell state of charge, b) peak centre evolution, c) FWHM evolution, and d) amplitude evolution.

In regions 1, 2, 3, 6 and 7, the phases were fitted using PseudoVoigt functions with a restrained FWHM around ~0.015 $Å^{-1}$ to ensure consistency in the fitting (note that only stage I was fitted with a slightly larger FWHM due to the volume change). In contrast, the phases deconvolution in regions 4 and 5 was not possible due to overlap of the peaks that led to peak broadening. In those regions, a SplitPseudoVoigt function was used.

Following the graphite lithiation mechanism, region 1 is ascribed to a solid solution mechanism from graphite (C_6) to stage I' (LiC_{72}). A focus on this first region is provided in **Figure 79**. A shift of the peak centre toward smaller *q* scattering vector can be seen in **Figure 79a**, indicating an expansion of the *c*-axis (since the Bragg reflection is the (002)). The peak shifts non-linearly from 1.882 $Å^{-1}$ to 1.863 $Å^{-1}$ as can be seen in **Figure 79b** with stable FWHM (**Figure 78c**) and amplitude (**Figure 78d**) during the full process, coherent with a solid solution mechanism. To compare with data from the literature, authors generally assume a linear shift of the diffraction peaks as a function of the SoC for solid solutions[152,154]. Here, it demonstrates that this assumption is not fully correct and highlights the need to characterise each electrochemical process *in operando* with high temporal resolution. The non-linearity observed can come from a competition between insertion of lithium and secondary reactions, such as adsorption and/or SEI formation, that do not influence the structural state of graphite.

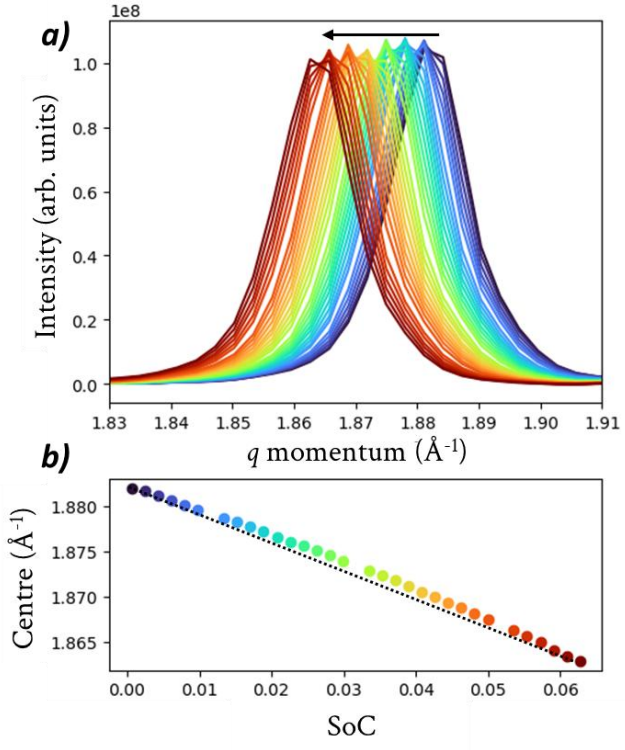


Figure 79: Evolution of the (002) Bragg reflection in region 1 (graphite to stage I' phase transition). a) X-ray diffraction patterns. b) Peak centre evolution obtained from the fit.

For region 2 (**Figure 78**), generally ascribed to the first biphasic mechanism of graphite lithiation from stage I' to stage IV (LiC_{72} to LiC_{36} respectively), a relative exchange in amplitude can be observed between the two phases (stage I' disappears while stage IV appears, **Figure 78d**). This amplitude exchange is typical for a biphasic mechanism. However, a continuous shift of both peaks towards lower q values can be seen (stage I' contribution shifts from 1.863 $Å^{-1}$ to 1.845 $Å^{-1}$ and stage IV contribution shifts from 1.844 $Å^{-1}$ to 1.831 $Å^{-1}$, **Figure 78b**), this behaviour being typical of a solid solution mechanism, as in region 1. From this, an ambiguous interpretation of the mechanism responsible for the formation of stage IV from stage I' can be noticed, which is achieved *in fine* through biphasic and solid solutions mechanisms running in parallel. Electrochemically, the observed signature also correlates with a mechanism involving several processes:

- The potential is not perfectly constant with the increase of SoC (if the mechanism involved a biphasic transition, a constant potential of intercalation should be observed).
- An asymmetry in the $d_{SoC}/d_E = f(SoC)$ curve is observed, indicative of a mechanism of intercalation that evolves during this step.

The transition from stage IV to stage III is divided into two regions (3 and 4), with region 4 being fitted using a SplitPseudoVoigt (sPV) function to take into account the peak asymmetry. In region 3, the flat signature observed in the $d_{SoC}/d_E = f(SoC)$ curve (**Figure 78a**) supports a solid solution mechanism. Indeed, a single peak in the (002) Bragg reflection is observed with a shift toward lower angles, which is associated to a stable FWHM and amplitude evolutions (**Figure 78c, d**).

According to the literature, region 4 could correspond to the formation of phases in the range LiC_{30} – LiC_{24}[106,112,196]. Here again, the mechanism is not purely biphasic, since electrochemically, a very small wave is observed on the $d_{SoC}/d_E = f(SoC)$ curve (**Figure 78a**), indicative of graphite potential tending to form a "potential plateau" but still varying with SoC. Structurally, an increase of the FWHM (**Figure 78c**) is observed, correlating with the appearance of a second peak due to the biphasic contribution. Then, the disappearance of the initial phase induces a decrease of FWHM. Based on the electrochemical signature, an estimation of the lithium content was possible for the stages involved in region 4. Taking into account the stoichiometries reported in literature for stage IV ($Li_{0.166}C_6$) and stage III ($Li_{0.25}C_6$), a ratio of lithium content was calculated between the two phases (0.25/0.166 = 1.5). Using the localisation in SoC of the two phases within the experiment, a charge ratio of (0.214/0.147 = 1.46) was estimated. The very close value obtained (1.46 vs. 1.5) proves the agreement between the literature data and their corresponding signature in the experiment. Using the same reasoning, the stoichiometry attributed to the intermediate stage formed at the end of region 3 (**Figure 78a**) was estimated. A ratio of SoC between this

intermediate stage and stage IV of (0.182/0.147 = 1.24) was found, corresponding to a stoichiometry of ~$Li_{0.2}C_6$ (LiC_{30}) for the intermediate stage. Similarly, a ratio of SoC was estimated between the intermediate stage and stage III signature of (0.214/0.182 = 1.18), corresponding to a stoichiometry of ~$Li_{0.21}C_6$ (LiC_{28}) for the intermediate stage. The results are in good agreement and comparable to the literature stoichiometries found to be in the range LiC_{30}-LiC_{27}.

To summarise the formation of stage III:

Stage IV is first transformed into an intermediate stoichiometry in the range LiC_{30} – LiC_{27} through a solid solution process (region 3).

$$LiC_{36} \rightarrow LiC_{30-27}\ (solid\ solution\ mechanism)$$

From the $LiC_{30\text{-}27}$ stoichiometry, stage III is formed by a solid solution process coupled to a biphasic one, ending in a stoichiometry probably corresponding to LiC_{24} (region 4).

$$LiC_{30-27} \rightarrow LiC_{24}\ (solid\ solution + biphasic\ mechanism)$$

In line with region 5, the signal was also fitted using a spV function to account for asymmetry. The lithiation process is associated to the formation of liquid-like structures, named stage II-L (LiC_{18} stoichiometry[106,112]). Structurally, the FWHM (**Figure 78c**) increases and reaches a maximum once stage II-L is formed. Some literature tried to explain this observation. Didier et al. refined the neutron diffraction peak attributed to stage II-L and evidenced a large grain size broadening[105]. According to the authors, this may be explained by a high-strain disorder associated to the coexistence of several domains. This observation is corroborated by Weng et al. that characterised graphite stage II-L (attributed to stage III in their study) by cryo-TEM[118]. From their study, stage II-L was microscopically composed of stage III and stage II domains (localised-domain model). Again, this coexistence of domains generates high strain, responsible for peak broadening.

The last two regions, 6 and 7 in **Figure 78**, involve the formation of LiC_{12} and LiC_6 phases according to the literature, the latter being the phase where the maximum amount of Li can be inserted in graphite particles. For region 6, **Figure 80** plots the evolution of peak centre and amplitude as a function of graphite potential corresponding to the formation of stage II (LiC_{12}) with respect to the SoC.

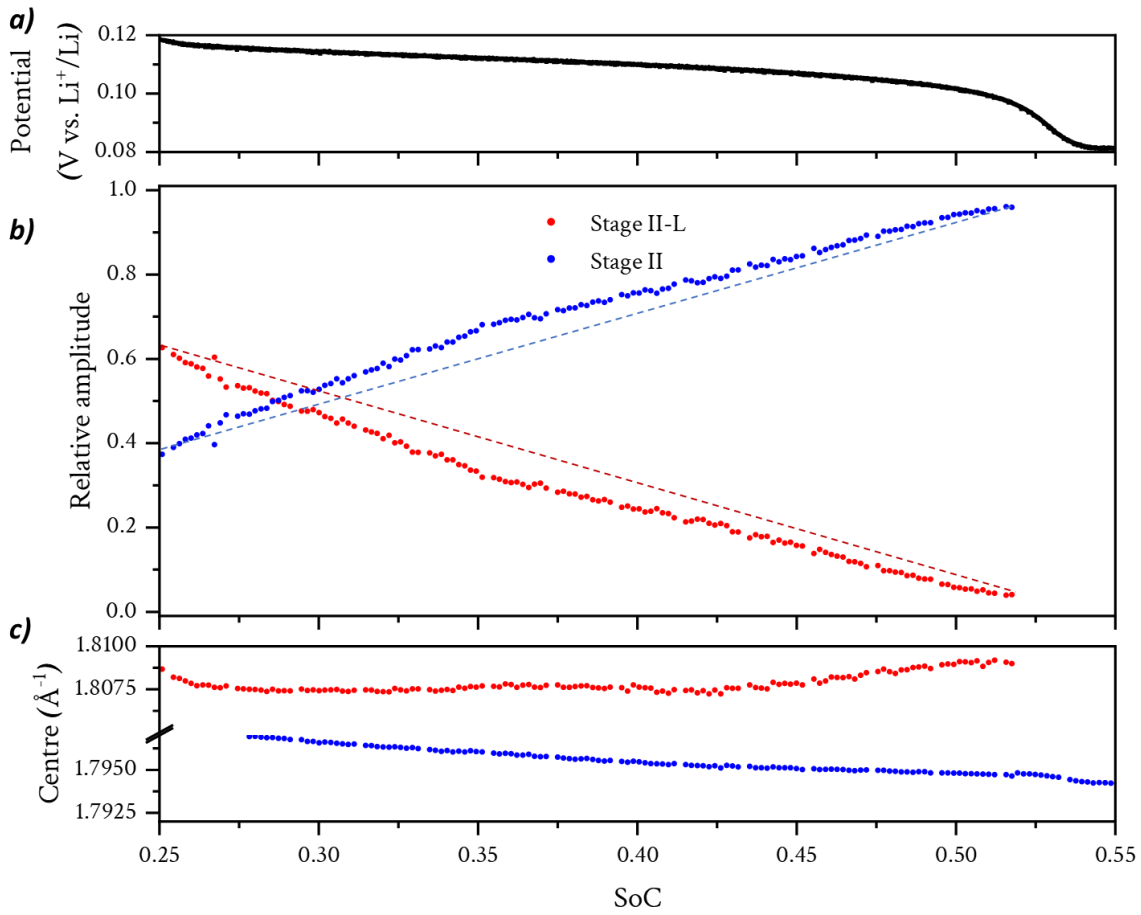


Figure 80: Evolution of structural parameters and potential of the cell with respect to the SoC for stage II formation (region 6) for the (002) Bragg reflection. a) Potential of the thin graphite electrode. b) Relative amplitude exchange between stage II-L and stage II. c) Peak centre of the two stages.

As can be seen in **Figure 80a**, the potential evolution does not strictly follow a plateau (discussed latter). Structurally, this transition is characterised by a relative amplitude exchange (**Figure 80b**) between stage II-L and stage II that is not linear with the cell state of charge, demonstrating that the latter is not a first-order transition. In the peak centre evolution (**Figure 80c**), one should be careful that the convolution of the two peaks is too important and can bias the physical meaning behind the fitting results. For this reason, this transition (region 6) will be discussed by analysing the lithium in-plane order through the (*hk0*) and (*h*00) Bragg reflections in few paragraphs.

For region 7 in **Figure 78**, that involves the formation of stage I, usually attributed to the formation of LiC_6, **Figure 81** shows the evolution of the relative amplitude exchange between the two phases, correlated to graphite potential and peak centre evolution of both phases.

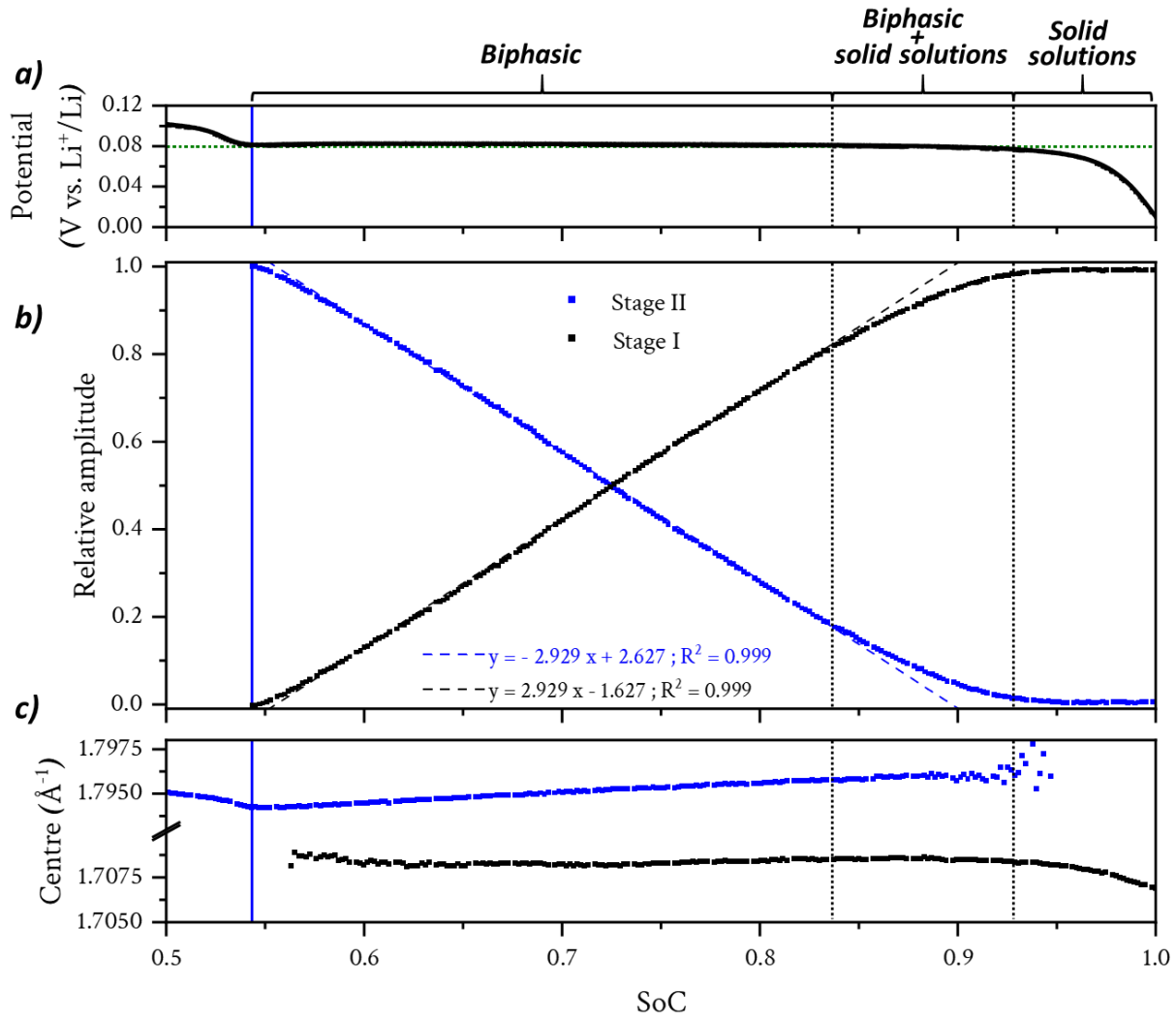


Figure 81: Evolution of relative amplitude exchange between stage II and stage I for the (002) Bragg reflections. Linear regressions were performed between 56% and 83% SoC and are plotted in dashed lines. The vertical blue line corresponds to beginning of stage I formation estimated from the electrochemical signature.

A linear period of relative amplitude exchange is observed (**Figure 81b**) and is characteristic of lithium insertion fully driven by biphasic mechanism, responsible for the constant potential of graphite observed in **Figure 81a**. A slowdown in amplitude exchange rate is observed at SoC equal to 0.84, and can be interpreted as a dual mechanism involving both biphasic and solid solution processes. Then, for state of charge higher than 0.93, a monophasic period is observed, associated to a shift of stage I peak toward lower angles (increase of *d*-spacing, **Figure 81c**).

In this last region, a solid solution is indeed observed as suggested by several authors such as Heß and Novák[119], or Mercer *et al.*[187]. Indeed, it was demonstrated by Filhol *et al.* that the configuration entropy prevails over the enthalpic contribution at the terminals of a biphasic state[197]. This implies that biphasic domains are always bounded by monophasic domains for entropic reasons, and that the last biphasic transition (stage II to stage I) is necessarily bounded by solid-solutions. From this observation, a better understanding of the stage I formation is possible. Since the maximal

stoichiometry of lithiated graphite is LiC_6 and this phase is only formed at the end of the graphite lithiation *via* solid solution mechanism, this implies that the first-order transition observed from 54% - 84% SoC forms a lithiated phase of graphite with a stoichiometry probably in the range $Li_{0.85}C_6$ - $Li_{0.95}C_6$, according to the experimental cell SoC. To corroborate this hypothesis, Schweidler *et al.* denoted from XRD refinement that the fully lithiated graphite phase was only composed of stage I and that a monophasic period was observed from $x = 0.85$ to $x = 0.95$ in Li_xC_6[198]. In addition, Boulet-Roblin *et al.* refined (*via* neutron diffraction) the pattern attributed to stage I during the biphasic process and the best fit provided a stoichiometry of ~$Li_{0.9}C_6$[199].

To summarise, our findings reveal that:

- From 54 – 84% SoC, a biphasic mechanism forms stage I (~ $Li_{0.9}C_6$) from stage II (LiC_{12}).
- From 84 – 93% SoC, some regions of graphite particles start to enrich and form an enriched stage I (solid solution) while others are still in a biphasic mechanism, this could be explained by the coexistence of several microscopic domains as suggested by Weng *et al*[118].
- From 93 – 100% SoC, stage I is enriched by additional Li insertion and a solid solution process led to the final LiC_6 stoichiometry.

This last solid solution will be further discussed *via* the analysis of lithium in-plane ordering and *via operando* Raman spectroscopy.

2.1.2.c Results – Analysis of the in-plane order through (hk0) and (h00) reflections

Following the through-plane ordering *via* the (002) Bragg reflections is the best way to characterise the lithium insertion in graphite because the inter-layer *d*-spacing is directly impacted. However, the transition from stage II-L to stage II (region 6) was problematic due to the very low difference of *d*-spacing between the two phases. For this reason, the interpretation of the fitting results can probably be biased. To bypass this problem, the in-plane ordering of Li_xC_6 compounds was followed, appearing in superlattice cells as discussed in the p**36**.

The in-plane superlattice peaks were analysed by following the (110) and (300) Bragg reflections in the range 2.8 – 3.0 $Å^{-1}$. In **Figure 82**, the correlation between the thin graphite electrode potential and the (110) Bragg reflection is shown as a function of the cell SoC.

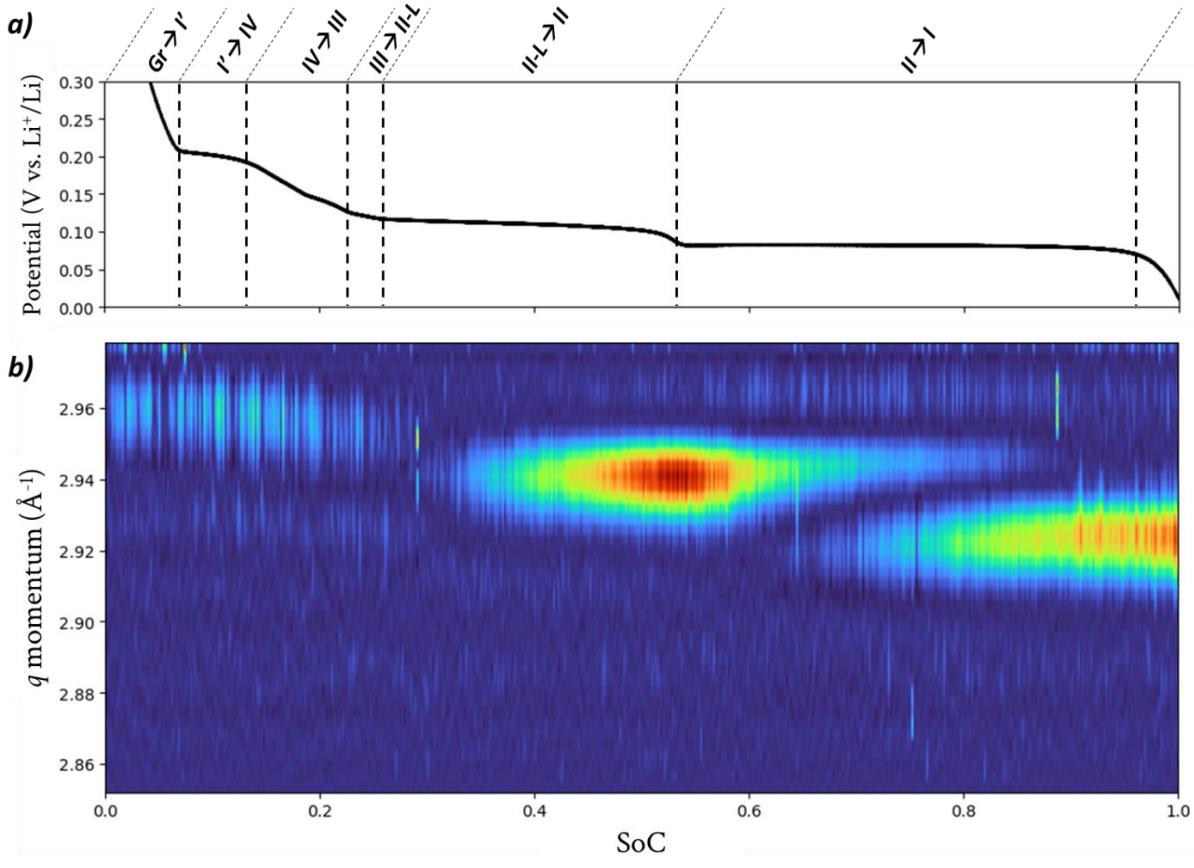


Figure 82: a) Evolution of the thin graphite electrode potential with respect to the SoC for a half cell cycled at C/10 rate @25°C with LP30. b) Contour plot representation of the diffraction patterns, the (110) Bragg reflections, obtained upon operando measurement of the thin graphite electrode.

A small signal is noticed around 2.96 $Å^{-1}$ from SoC = 0 to SoC = 0.25, corresponding to a LiC_9-type $P(3 \times 3)\ R\ 0°$ supercell (300) as observed in the literature[110,112]. The disappearance of the superlattice peak correlates with the beginning of the stage II-L to stage II transition (previously discussed region 6).

Pursuing the lithiation, a superlattice peak appears around 2.94 $Å^{-1}$ at ~ SoC = 0.25 – 0.3 and corresponds to a LiC_6-type $P(\sqrt{3} \times \sqrt{3})\ R\ 30°$ supercell (110). This peak is in agreement with the stage II superlattice peak observed in the literature[110,112], and an increase of intensity is observed during this stage II-L to stage II transition. To resume, upon the stage II-L to stage II transition, no LiC_9-type $P(3 \times 3)\ R\ 0°$ superlattice peak is observed supporting a stage II-L that evolves in solid solutions. In contrast, a LiC_6-type $P(\sqrt{3} \times \sqrt{3})\ R\ 30°$ superlattice peak is observed supporting a "pure" stage II with in-plane order.

For SoC > 0.5, the superlattice peaks were fitted using two PseudoVoigt functions, and the results are given in **Figure 83**. A noisier relative amplitude exchange (**Figure 83b**) than for the (002) Bragg reflection was observed, leading to poor interpretation. However, the disappearance of the

stage II signal at ~ 88% SoC (**Figure 83c**) can still be seen. This observation correlates with the above-mentioned mechanism, demonstrating that the end of lithiation is ensured through a solid solution. The end of biphasic state around 0.9 SoC is consistent with the $Li_{0.9}C_6$ stoichiometry of stage I.

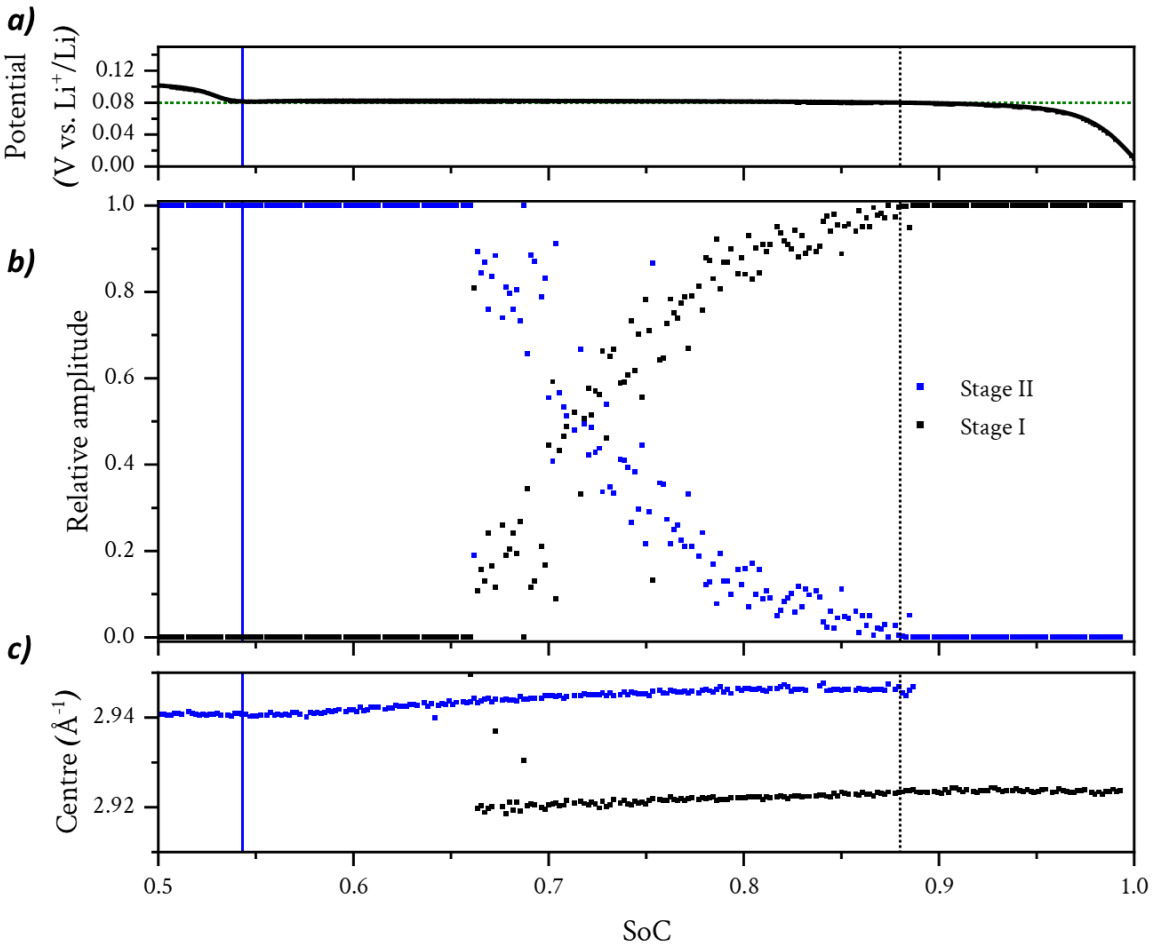


Figure 83: Evolution of relative amplitude exchange between stage II and stage I for the (110) Bragg reflections. The vertical blue line corresponds to beginning of stage I formation estimated from the electrochemical signature.

With this structural investigation, better insights into the lithium insertion mechanism were highlighted. It was demonstrated that the stage I' to stage IV and stage II-L to stage II transitions cannot be considered as solely a first-order transition. In the case of the stage II-L to stage II transition, it was suggested that the stage II-L did not display any lithium in-plane order, whereas stage II displayed in-plane order with an intense (110) Bragg reflection. Thus, this transition involves the coexistence of a solid solution (stage II-L) and a pure stage II phase.

This structural investigation was not only performed to investigate the lithiation mechanism of graphite, but also to use the results as a calibration profile for the estimation of structural state of charge in thick electrodes presented in the next chapter.

2.1.3 Method development for the determination of lithium content in Li_xC_6 phases upon lithiation

To avoid the problems encountered with data refinement (time-consuming, not adapted to a huge amount of data), a method was developed based on the calculation of one parameter to characterise the diffraction pattern obtained upon lithiation of graphite. With this method, a gain in time is expected by analysing only one variable extracted from the diffractogram.

A mass centre (or gravimetric centre) was extracted from each diffraction pattern focused on the (002) reflection; the calculation is explained in p**73**. Because the structural state of charge of graphite directly impacts the peak position, one can expect the mass centre to be representative of the graphite state. However, the mass centre evolution cannot distinguish a solid solution mechanism from a biphasic one, as illustrated by the following examples. **Figure 84** illustrates the dynamic of lithium insertion in terms of diffraction pattern, the associated mass centre, and the amplitude (area under the curve) of the Bragg reflections in the case of a solid solution mechanism (**Figure 84a - c**) and for a biphasic mechanism (**Figure 84d - f**).

Figure 84a represents the evolution of (002) Bragg reflection of graphite in the case of a solid solution mechanism for early lithiation stage from 0 to 6% SoC, associated to the mass centre calculated in **Figure 84b**. As expected, a shift of the peak position toward lower q momentum is observed, and is associated to an increase of the interlayer *d*-spacing upon lithium insertion. This shift is joint to a stable amplitude (**Figure 84c**). In terms of mass centre evolution, it results in a decrease toward lower *q* momentum.

Concerning the biphasic mechanism, **Figure 84d** and **Figure 84e** show the dynamic of the (002) Bragg reflection of graphite associated to the mass centre calculated from 56% to 85% SoC, containing the stage I formation from stage II, respectively. In this case, the exchange of amplitude between the two phases (**Figure 84f**) is linear with the increase of cell state of charge, and it results in a linear decrease of mass centre from the position of the disappearing phase (stage II ~ 1.795 $Å^{-1}$) to the position of the appearing one (stage I ~ 1.708 $Å^{-1}$). With these two examples, one can more easily understand the link between the mass centre that is discussed here and the physical meaning behind, in terms of diffraction patterns and cell state of charge.

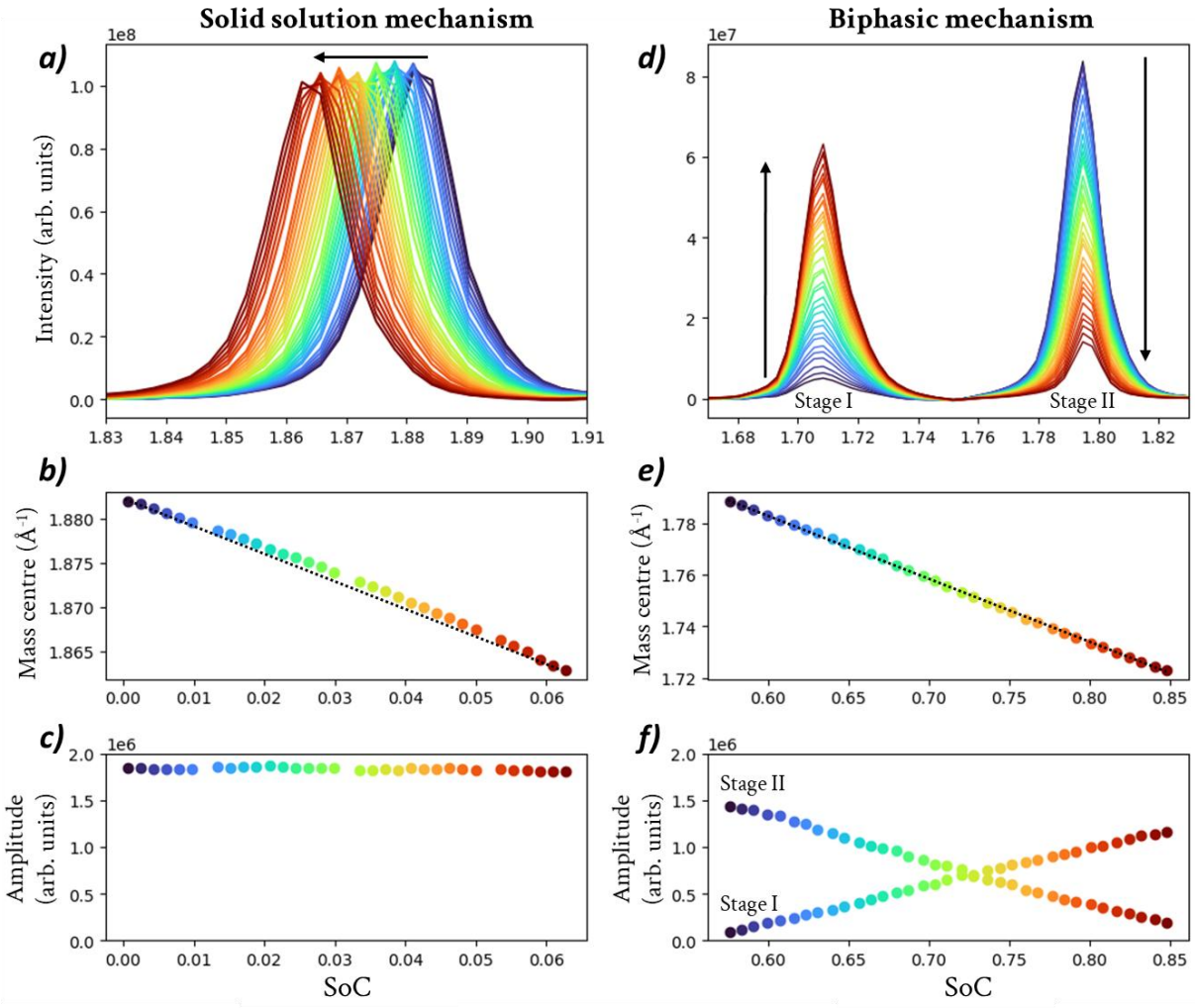


Figure 84: Dynamic of the (002) Bragg reflection of graphite upon lithiation with respect to the SoC (from blue to red). a) Evolution of diffraction patterns for a solid solution mechanism, b) Associated mass centre evolution as a function of SoC and c) amplitude of the phase. d) Evolution of diffraction patterns for a biphasic mechanism, e) Associated mass centre evolution as a function of SoC and f) amplitude of the two phases.

The analysis of the mass centre evolution as a function of the cell state of charge is presented in annex (p**I**). As a summary, a very good sensitivity of the mass centre is observed with the variation of cell state of charge, demonstrating the interest of using this indicator for the estimation of structural state of charge of graphite upon lithiation. In **Table 9** are summarised the advantages and drawbacks of proceeding with both refinement (fitting) and mass centre calculation.

Table 9: Advantages and drawbacks of estimating structural state of charge of graphite using mass centre calculations and fitting analysis.

Method	Mass centre	Fitting (refinement)
Time spent	**Very fast** – few seconds for hundreds of XRD patterns	**Slow** – can take several hours to have consistent fits
Batch processing	**Very easy** – simple mathematical calculations	Possible – but imposes verifications from the experimenter to ensure consistency
Sensitivity to structural changes	Similar – depends on the detector resolution	
Determination of lithium content	**Need of a calibration sample** that correlates the mass centre evolution as a function of electrode SoC	**Feasible** by Rietveld refinement (with neutron diffraction data)
Inputs	**None**	**Require a structural model** to refine a structure
Bias	**None**	**Bias can be introduced** by the experimenter
Requirements	**Require same quality of XRD** pattern between reference and sample to analyse	**None**

In this part, it was demonstrated that the mass centre of a diffraction pattern was a good indicator of the graphite structural state of charge. Based on this, the mass centre evolution as a function of the cell SoC obtained in **Figure A1b** will serve as a calibration profile to estimate the structural state of charge of graphite (x in Li_xC_6) for a given diffraction pattern in other experiments. This procedure is illustrated in **Figure 85** and makes the link between the results obtained from the thin graphite electrode and the thick electrodes presented in **Chapter IV**. The thin electrode, probed under quasi-thermodynamic conditions, provided a calibration curve in output results correlating the mass centre of the (002) Bragg reflection to the amount of lithium in the graphite particles (x in Li_xC_6). For the thick electrodes, probed under kinetic limitations at cycling rates from C/4 to C/1, the evolution of mass centre with the cell state of charge will be analysed as a function of the electrode depth, and with the calibration profile as input, the structural state of charge (x in Li_xC_6) will be determined.

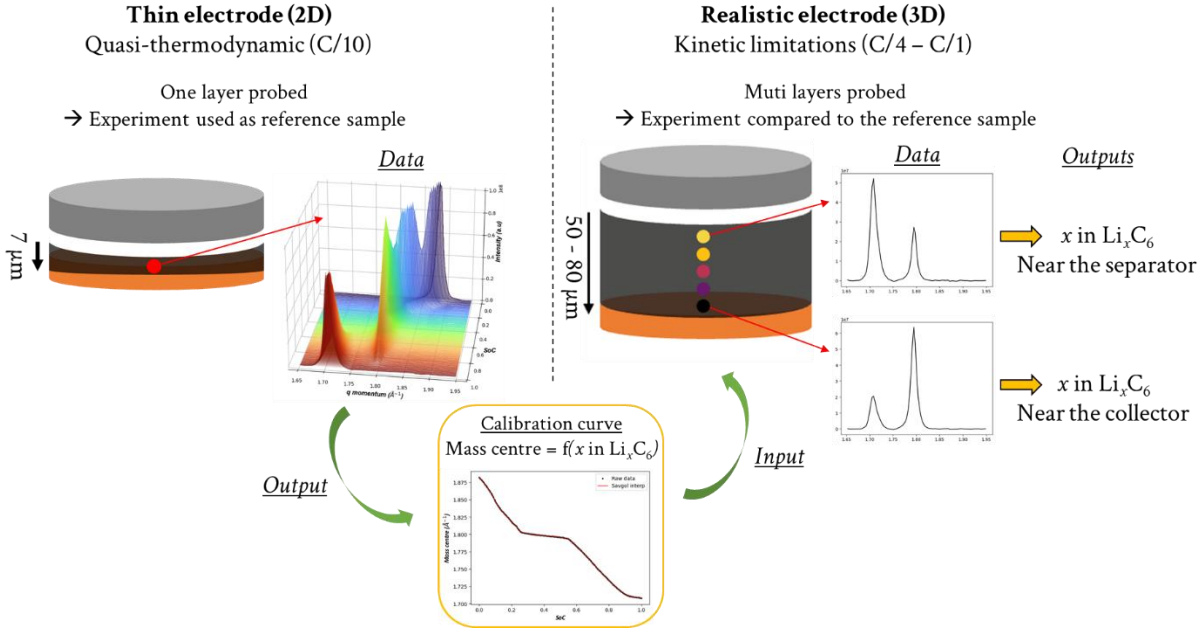


Figure 85: Illustration of the procedure used to extract the structural state of charge in thick electrodes from the calibration profile obtained with the thin electrode results.

This *operando* XRD experiment evidenced important structural features such as the enrichment of the $Li_{0.9}C_6$ phase through solid solutions processes to the well-known LiC_6 phase. This last point is rather new in the literature and has not been properly discussed to date. For this reason, it deserves additional characterisations. On this purpose, Raman spectroscopy is sensitive to the lithium insertion in graphite as discussed in p**48**, and this bulk sensitive technique (few micrometres of penetration depth) can provide additional insights about the last solid solution.

2.2 Raman spectroscopy investigation of graphite lithiation

An *operando* Raman spectroscopy experiment was realised using the same thin graphite electrode. As described in the state of the art, graphite and carbonaceous materials were often investigated by Raman spectroscopy because of their strong resonance activity, especially due to the C-C sp^2 hybridisations.

The method for the spectra treatment (such as background removal) and the cell assembly are given in p**75**. The graphite was lithiated at C/35 rate using LP30 as electrolyte and cycled at 20°C between 1.2 V and 0.01 V, then 1 h of CV and 30 min of OCV succeeded the CC period. For the delithiation, and knowing that there is less kinetics limitation, the rate was increased to C/17. The electrochemical profile is plotted in **Figure 86a**, one can observe the characteristic potential plateaus of graphite. The Raman spectra obtained during graphite lithiation are plotted in **Figure 86b** in a contour plot representation. The characteristic G-band at ~1580 cm^{-1} is visible at the beginning of the lithiation, and a splitting of the band in two signals in regions 2 and 3 is visible. The seven delimited regions are the same as in the XRD experiment presented above. The G-band

disappears at ~SoC = 0.5, meaning that one cannot characterise the stage II to stage I transition (region 7) through this peak. In parallel to this, a band at ~1850 cm^{-1} appears upon lithiation with a significant intensity at the end of charge. This band was already observed in the literature and will be discussed later (p**119**).

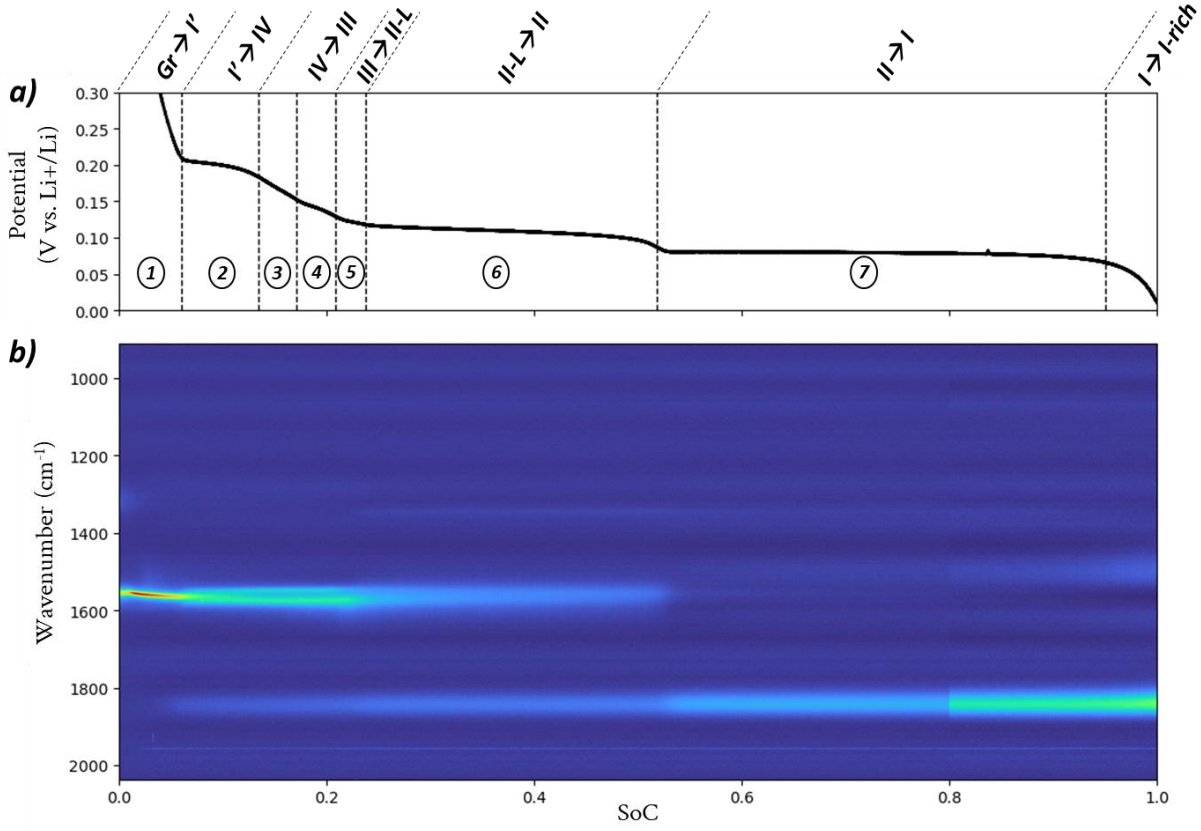


Figure 86: Evolution of Raman spectra upon lithiation of a thin graphite electrode cycled at C/35 with LP30 at 20°C. a) Potential of the graphite electrode with respect to the cell SoC. b) Contour plot of the Raman spectra evolution with respect to the cell SoC.

2.2.1 G-band analysis

The G-band is a common signature from sp^2 hybridised carbonaceous materials attributed to the C-C in-plane bond vibration (E_{2g})[146]. Because the Fermi level of graphite is modified by the lithium insertion, the C-C in-plane resonance changes upon dis/charge and the G-band varies with the cell SoC. To follow the G-band upon lithiation, a peak fitting analysis was realised based on the same procedure as in the XRD experiment. PseudoVoigt functions were used, and either one or two contributions were implemented depending on the cell SoC. The fitting results are given in **Figure 87** in the range 0 – 53% SoC (region 1 – 6), and correlated to the potential profile in **Figure 87a** and the $d_{SoC}/d_E = f(SoC)$ representation on the right axis. In region 1, a shift of the G-band from ~1580 cm^{-1} to 1590 cm^{-1} is observed (**Figure 87c**) but only starts at ~1% SoC (corresponding to a graphite potential of ~0.6 V vs. Li^+/Li). This suggests that the lithium insertion probably

starts at 0.6 V (this depends on the applied C-rate, C/35 here), and that the accumulated charge prior this potential is only coming from adsorption on graphite particles surface. This increase in cm^{-1} is related to an increase of the force constant of the in-plane C-C bonds. The peak shifts with a slope of -27 $cm^{-1}.V^{-1}$, in agreement with the literature reports[146,147].

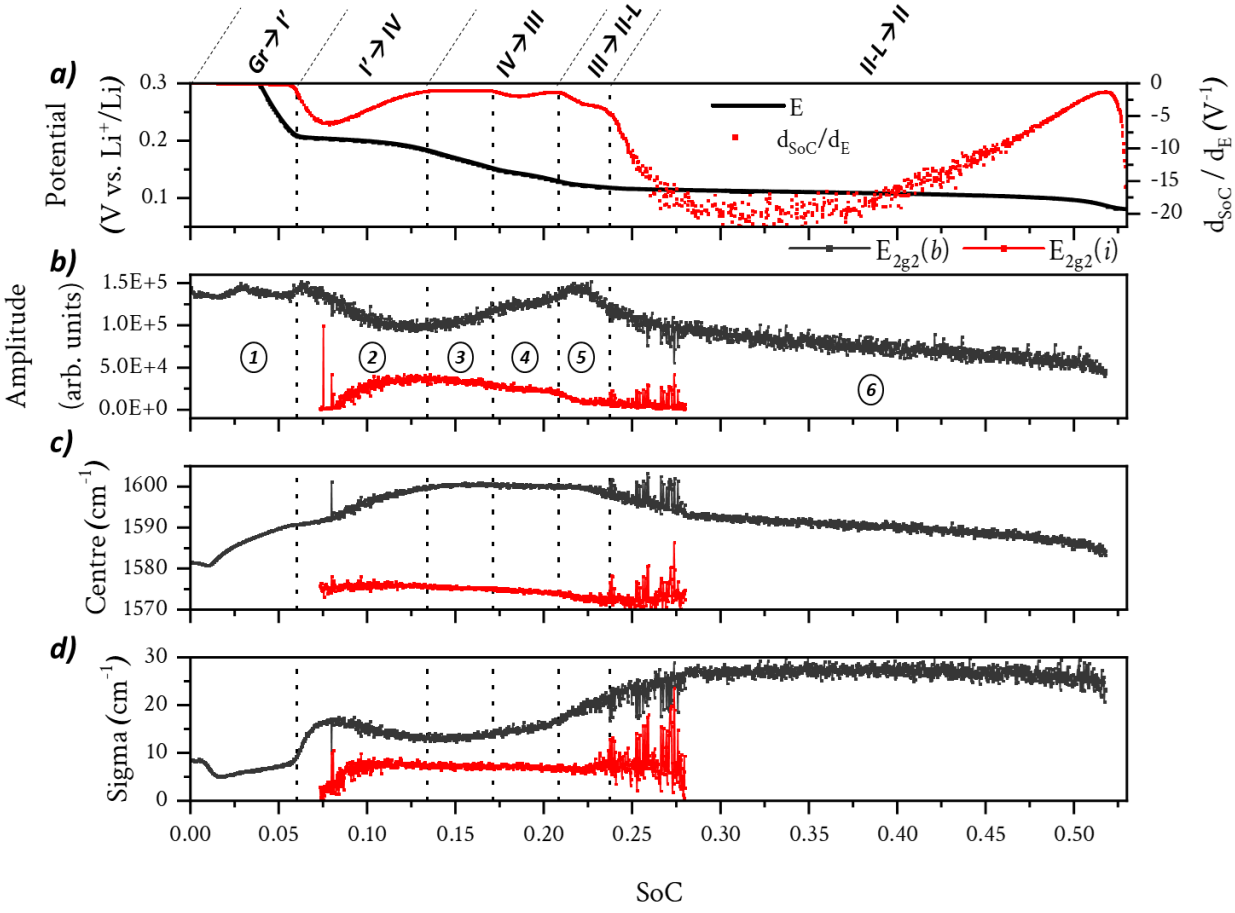


Figure 87: Analysis of G-band peak fitting. a) Potential profile on the left axis and d_{SoC}/d_E curve on the right axis. b) Peak amplitude. c) Peak centre. d) Sigma parameter (FWHM/2).

Entering the stage I' to stage IV transition (region 2), a split is observed in two vibration modes of the G-band. The former one (1600 cm^{-1}) is attributed to the E_{2g2} (*b*) vibration mode due to the bounding C-C vibration from carbon planes adjacent to lithium intercalant layers as illustrated in **Figure 88 (right)**, and the latter at lower energy (1575 cm^{-1}) is attributed to a E_{2g2} (*i*) vibration mode coming from the interior C-C vibration from carbon planes not-adjacent to Li-intercalated layers as illustrated in **Figure 88 (left)**.

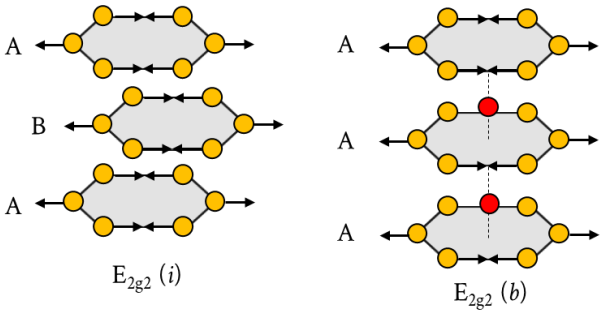


Figure 88: Illustration of the E_{2g2} vibration mode. Left: E_{2g2} (i) vibration mode attributed to the carbon planes without intercalated lithium. Right: E_{2g2} (b) vibration mode attributed to the carbon planes with intercalated lithium. The arrows represent the C-C vibration. Inspired from ref. [200].

Pursuing with regions 3 to 5, the coexistence of the two vibration modes is still observed. However, for the stage II-L to stage II transition (region 6), a large uncertainty can be observed in the peak centre **(Figure 87c)** and peak sigma parameter (**Figure 87d**) for the E_{2g2} (*b*) band and the disappearance of this band for the rest of region 6. This observation is in agreement with previous investigations in the literature[150,201,202].The remaining band in region 6, shifts toward lower energies, which could be attributed to the increase of charge transfer between the 2s lithium orbital and the π^* carbon orbitals, decreasing the C-C bond strength[203]. In parallel, the peak amplitude (**Figure 87b**) decreases because of the increase in electrical conductivity of graphite upon lithium insertion. As a consequence, the optical penetration depth decreases, and a lower scattering intensity is observed[148].

For higher cell SoC (> 0.55), the high electrical conductivity decreases too much the penetration depth of the laser, and the C-C bond vibration signal is hidden in the scattering background. A solution to this issue is to use Kerr-gated Raman, to remove the scattering background signal and observe the C-C vibration. Neale *et al.* succeeded to probe the graphite lithiation until 100% SoC and observed a linear shift of the G-band (from 1590 to 1564 cm^{-1}) in the end of lithiation[202]. In the case of "classic" Raman spectroscopy, a Fano effect takes place in the end of lithiation and can be used to describe the last phase transitions of graphite lithiation.

2.2.2 Fano effect

A Fano effect occurs in the end of graphite lithiation and is responsible for the generation of an asymmetric peak at a position similar to that of the G-band (~1550 cm^{-1}). The evolution of the Raman spectra between 50% - 100% SoC is given in **Figure 89**. One can observe the presence of the G-band at 50% SoC, that progressively disappears whereas a Fano lineshape appears in the end of charge.

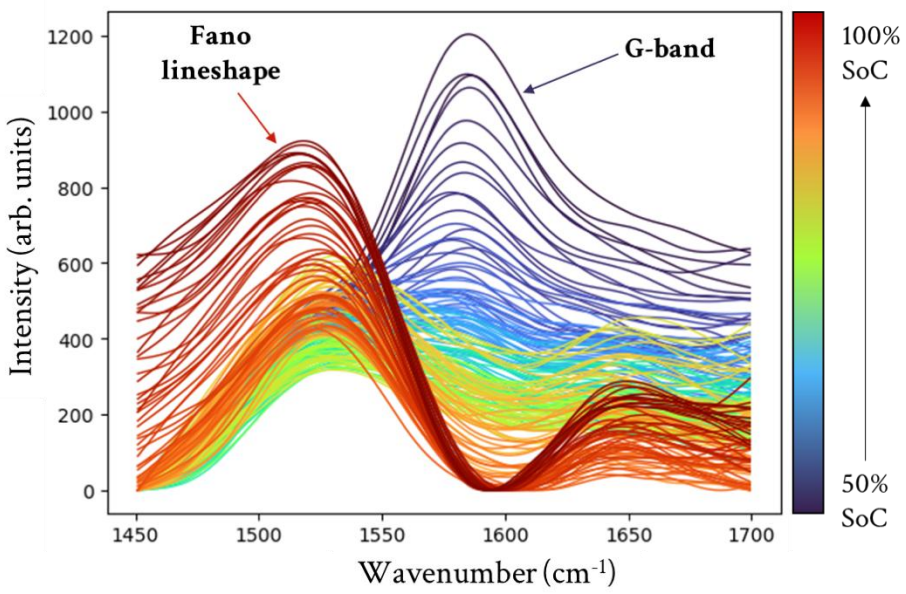


Figure 89: Raman spectra obtained from 50% to 100% SoC in lithiation.

In 1961, Fano[204] described the "Fano effect" as the result of the coupling between a discrete vibrational term and an electronic continuum term. The vibrational contribution corresponds to a normal Raman scattering signal, responsible for a sharp, intense, and symmetric band with a Lorentzian-type profile; whereas the electronic contribution originates from a continuum of electronic excitations, commonly observed in the case of metallic materials. This so-called Fano interference generates an asymmetric line shape and is defined by the following Eq. 23 [205]:

$$I(\omega) = \frac{\left(q + \frac{\omega - \omega_0}{\Gamma}\right)^2}{1 + \left(\frac{\omega - \omega_0}{\Gamma}\right)^2} = \frac{(q+\varepsilon)^2}{1+\varepsilon^2} \; with \; \varepsilon = \frac{\omega - \omega_0}{\Gamma} \qquad \textit{Eq. 23}$$

Where q is an asymmetry factor, ω is the wavenumber, ω_0 is the centroid wavenumber, and Γ is the linewidth (FWHM).

In its scaled form, the equation turns into Eq. 24 [206,207]:

$$I(\omega) = I_0 \frac{\left(1 + \frac{\varepsilon}{q}\right)^2}{1+\varepsilon^2} \qquad \textit{Eq. 24}$$

With I_0, the centroid intensity.

By implementing this function in a python script, a fitting of the Fano profiles was realised. However, fitting analysis was more difficult than in the case of symmetric line shapes (such as Lorentzian or Gaussian profiles) because of a continuum of scattering signal coming from the set-up (Sapphire window, electrolyte, Whatman separator). This background signal interferes with

the global band, and the deconvolution of the background and Fano contributions was practically impossible without biasing the data. An example of the Fano lineshape fitting is described in p**76**. Still, the fitting results were analysed, so that one could appreciate the kind of value that the asymmetry factor *q* can take for eventual other Raman experiments.

The fitting results of the *q* asymmetry factor are given in **Figure 90a** only for the end of lithiation, where a successful fit was obtained. The data are separated in three regions, with the end of constant current period (95 – 100% SoC, CC), the constant voltage (CV) and the OCV period. Concerning the *q* asymmetry factor, large values ($\pm\infty$) lead to a symmetric lineshape similar to a Lorentzian profile, whereas the asymmetry lineshape intensifies when *q* tends toward zero. The sign of *q* impacts the asymmetry direction. Here, the negative values are coherent with the Fano lineshape that displays an asymmetry with higher intensity on the left hand of the lineshape. An increase of the asymmetry factor (*q*) from -1.5 to -0.8 is observed in the end of the CC period. This can be attributed to an intensification of the coupling between the vibrational and electronic contributions because of the increase in metallicity of the graphite sample upon lithium insertion. In the CV and OCV periods, a rather stable asymmetry factor (still slightly increasing) is observed and correlates with a stabilisation of the metallicity. Indeed, because the thin electrode was charged at low C-rate (C/35), the maximal content of lithium was reached at the end of the constant current period and a non-significative increase of charge was observed in the CV period (2 µAh compared to 0.35 mAh of CC capacity), as a consequence no gain in metallicity occurred in the CV and OCV periods.

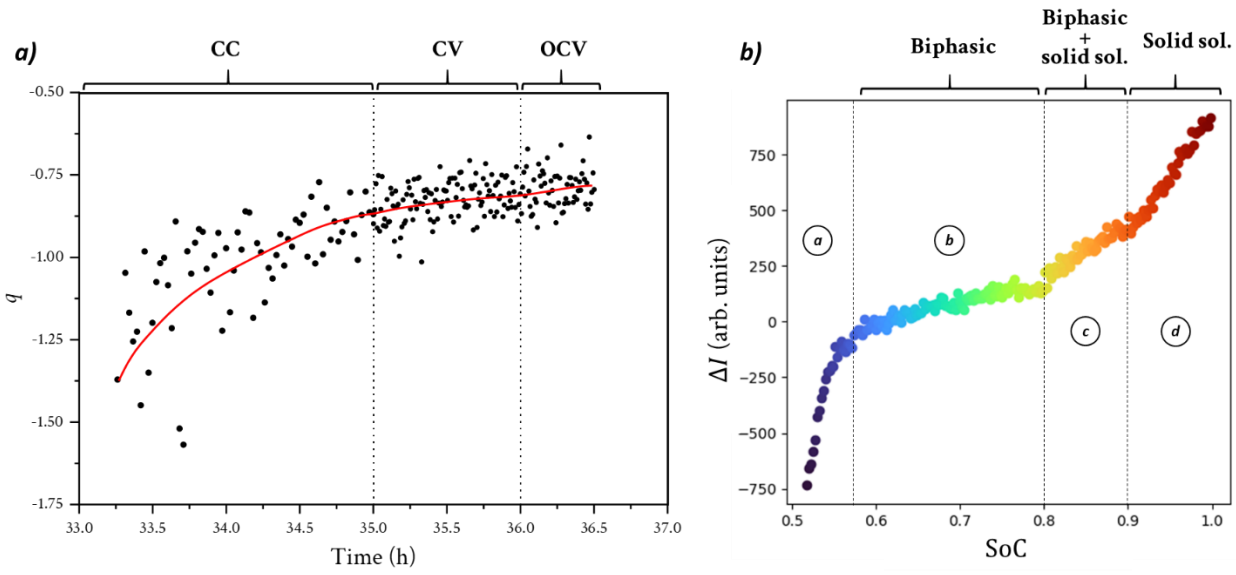


Figure 90: Analysis of the Fano lineshape asymmetry. a) Evolution of the fitted q asymmetry factor as a function of time in CC, CV and OCV periods. b) Evolution of the intensity difference between 1535 and 1600 cm^{-1} wavenumbers as a function of the cell SoC during the CC period.

Due to the difficulty to fit the Fano lineshape, another method was used to estimate the peak asymmetry. The lineshape maxima and minima, located at 1535 and 1600 cm^{-1}, were subtracted to quantify the intensity difference which is a way to characterise the lineshape asymmetry, as illustrated in **Figure A3**. This rough estimation is given in **Figure 90b**, and the plot is divided into four regions of interest. In region "a", the negative delta of intensity stands for the presence of the G-band, still present in the end of the stage II-L to stage II transition (50 – 55% SoC). Then, the G-band disappears and an intensity delta around ~0 is observed in the beginning of the region "b". Upon the stage II to stage I transition (region "b"), a very slight increase in delta intensity is observed, supporting a slight increase of asymmetry in the Raman band. Entering region "c", a slope failure is observed with an intensification of the peak asymmetry. This change in peak asymmetry dynamic correlates with the XRD observation in **Figure 81**, indeed, at ~0.8 SoC it was suggested that solid solutions appear in a biphasic medium. Similarly, entering region "d", another slope failure is observed and correlate with the last solid solution state of graphite upon lithiation. One can notice the very good agreement between the SoC range of this region "d" (0.9 – 1 SoC) and the $Li_{0.9}C_6$ stoichiometry reported from literature and the XRD characterisation.

To summarise, the analysis of the Fano lineshape asymmetry revealed a dependency between the *q* factor and the lithium storage mechanism. The analysis of the Fano lineshape asymmetry evidenced different dynamics of lithium insertion mechanism, correlating with the evolution observed by XRD. In the end of lithiation, the appearance of solid solution domains in the graphite particles is responsible for a significative increase of metallicity, increasing the coupling between vibrational end electronic contributions in the Raman signal. The origin behind this intensification of electronic and vibrational coupling with the appearance of solid solutions is still unknown and remains an open question.

2.2.3 1850 cm^{-1} band analysis

Surprisingly, during the *operando* measurement, a new band at 1850 cm^{-1} appears, a band still debated in the literature. Panitz *et al.* analysed this band evolution upon de/lithiation and observed a shift toward lower energies upon lithiation, and a mirror evolution was noticed in delithiation (reversible band)[149]. The authors attributed this band to complexes formed between lithium ions and electrolyte degradation products lying in the graphite SEI. Later, this signal was assigned to the lithium-acetylide (Li_2C_2) signature, and Schmitz *et al.* attributed it to a SEI component[208]. Recent papers still try to figure out the origin of this band[209], it seems that the nature of the band is commonly accepted as Li_2C_2, but its origin (degradation of solvent, salt, or others) is still unclear.

Using the same procedure as for the G-band analysis, **Figure 91** shows the fitting results for the Li_2C_2 band analysis. In region 1, no coherent fit was obtained because of the poor signal/noise ratio. Instead, the appearance of this band was analysed by curve integration between 1800 and

1900 cm^{-1}, and the signal was detected at ~1% - 2% SoC (corresponding to a potential of 0.6 – 0.45 V vs. Li^+/Li). The appearance of this band correlates with the start of lithium insertion in graphite. For the region 2, a fixed peak position is observed at 1860 cm^{-1} in **Figure 91c** (see the red guidelines), associated to a rather stable amplitude (**Figure 91b**). In regions 3 to 5, a shift towards lower energies (from 1860 to 1858 cm^{-1}) is observed and the peak amplitude increases. Pursuing with the stage II-L to stage II transition (region 6), a stabilisation of the peak position at ca. 1857 – 1858 cm^{-1} is observed with a stable amplitude. During the transition from region 6 to region 7, the amplitude of the peak drastically increases and a slight decrease of the peak centre is observed. Again, a stable band position is visible for the stage II to stage I transition (region 7) at 1855 – 1856 cm^{-1}, associated to constant amplitude (note that the sharp increase of amplitude at 80% SoC was generated by a manual change in the optical focus on the cell). Then, when the potential plateau ends (stage I to enriched-stage I), a shift towards lower energies is observed with a peak position reaching 1853 cm^{-1} at 100% SoC and an increase of amplitude follows.

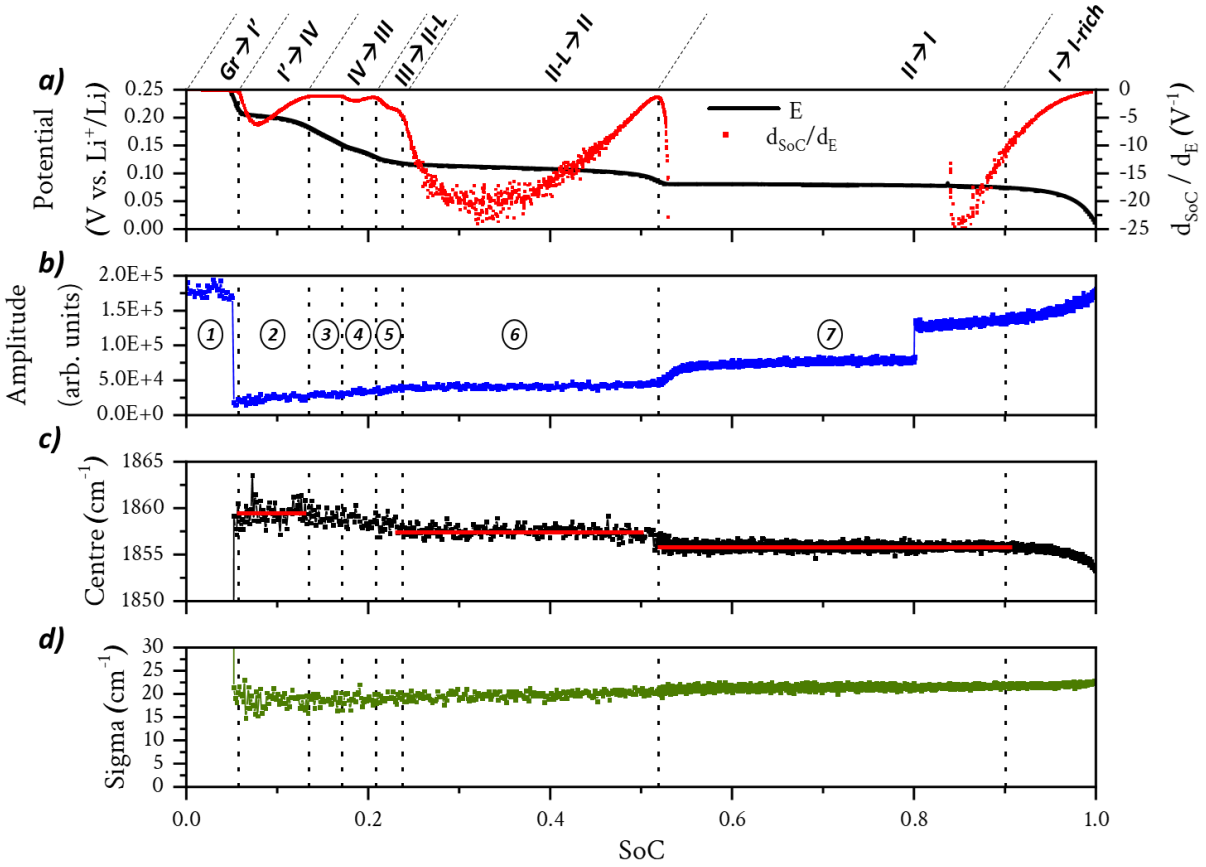


Figure 91: Li_2C_2-band peak fitting analysis upon lithiation. a) Potential profile on the left axis and d_{SoC}/d_E curve on the right axis. b) Peak amplitude. c) Peak centre. d) Sigma parameter (FWHM/2). The red lines are added as visual guidelines.

These observations suggest that the supposed Li_2C_2 is strongly correlated to the evolution of graphite potential. Indeed, for regions of rather stable potential (region 2, 6 and 7), a constant

band position with stable amplitude was observed. In contrast, as soon as the graphite potential changes, the band shifts and changes in amplitude. One can suppose that the electric field evolution is responsible for the changes in the C≡C band strength.

The delithiation was also investigated but at a higher C-rate (~C/17) and the fitting results are plotted in **Figure 92.** Briefly, a reversible evolution of the Li_2C_2 was observed, with a stable peak position (**Figure 92c**) during the potential plateaus at 1856 cm^{-1} (stage I to stage II transition), 1858 – 1859 cm^{-1} (stage II to stage II-L transition) and 1862 cm^{-1} (stage IV to stage I' transition). From this, a slight hysteresis in peak position is observed between lithiation and delithiation but could be attributed to the different C-rate used. On the amplitude side (**Figure 92b**), even if the constant regions were less marked, the same trend can still be observed as in lithiation. It is important to notice that at 0% SoC (pristine graphite state), the Li_2C_2 band is still present.

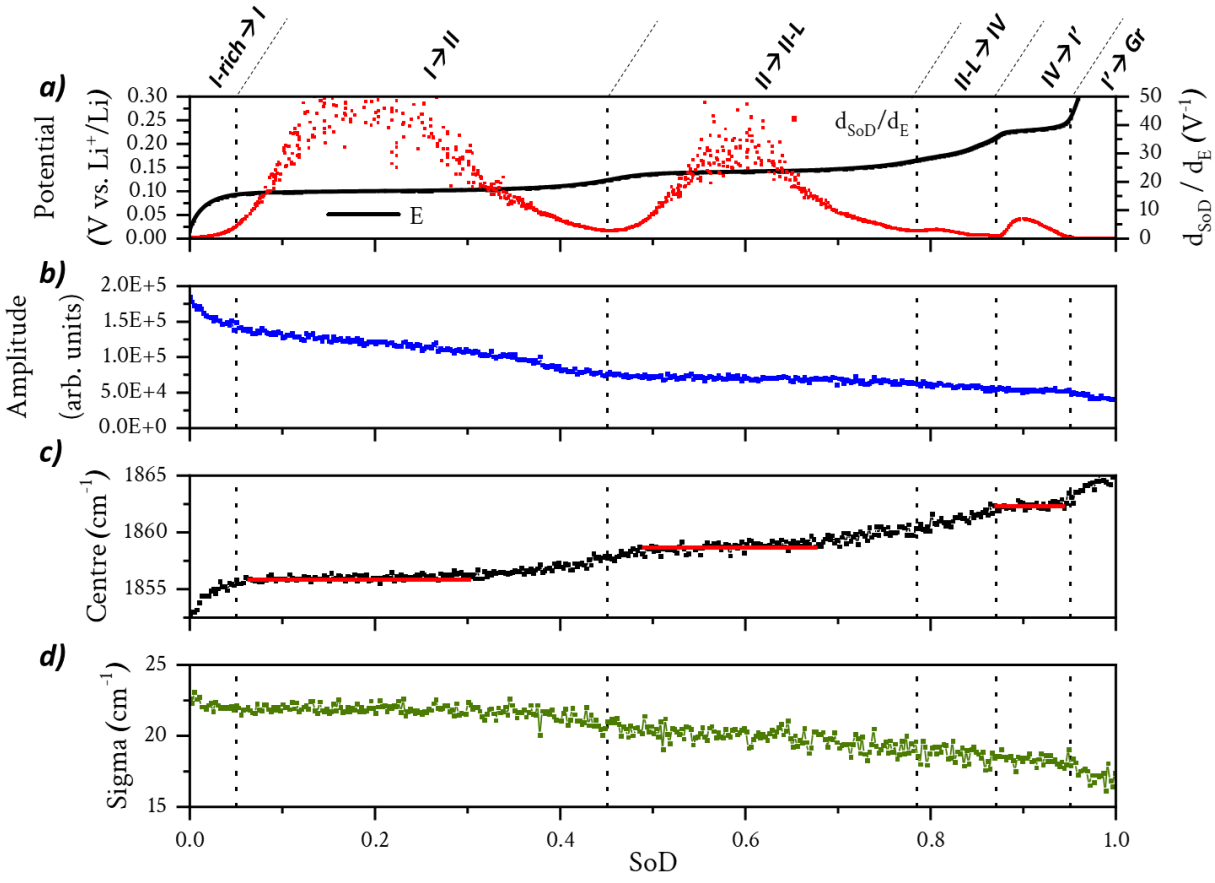


Figure 92: Analysis of Li_2C_2-band peak fitting upon delithiation. a) Potential profile on the left axis and d_{SoD}/d_E curve on the right axis. b) Peak amplitude. c) Peak centre. d) Sigma parameter (FWHM/2). The red lines are added as visual guidelines.

2.2.4 Controversial Li_2C_2

The presence of Li_2C_2 in the Raman analysis is still often debated in the literature, since this phase can only be obtained in specific synthesis condition. Drüe *et al.* investigated the thermodynamic stability of Li_2C_2 and demonstrated that LiC_6 phase was not stable above 330°C and disproportionate into graphite and Li_2C_2 by a de-intercalation mechanism[210]. Furthermore, during the synthesis of LiC_6 by reaction of lithium vapor on graphite, a significative proportion of Li_2C_2 was observed above 400°C by Basu *et al.*[211]. This suggests that the Li_2C_2 phase can originate from the reaction between lithium ions and graphite under specific conditions (high temperature). Thus, it is surprising to obtain a metastable phase at room temperature during cycling. Also, some authors suggested that it comes from a degradation product but Li_2C_2 species was never detected to date by X-ray Photoelectron Spectroscopy (XPS), or other surface characterisation techniques. Finally, if the Li_2C_2 species originated from degradation products in the SEI, the lithium acetylide band should be observed at 0% SoC in this experiment since the SEI was mainly formed in a preliminary cycle, and this is not the case.

We suggest that the Li_2C_2 phase can originate from an *in-situ* synthesis induced by the local laser heating in combination with the electric field applied upon lithiation and delithiation. As a result, this Li_2C_2 phase would lie on the graphite surface and be electrically connected to the graphite electrode. This can explain the high correlation between the electrode potential and the signature of the band upon cycling. A suggestion of experiment to verify this hypothesis would be to probe a lithiated graphite electrode with a very low laser power and time exposure to decrease as much as possible the local heating. Then, probing graphite electrode as a mapping can also be performed to reduce the dose. If the Li_2C_2 band appears with the increase of laser power, and disappears by changing the region of electrode probed, it would demonstrate that the lithium acetylide band originate from the laser heating and not from degradation products lying in the SEI.

3 CONCLUSION – CHAPTER 3

This chapter was dedicated to the understanding of the lithium insertion mechanism in graphite. The investigations were conducted on thin graphite electrodes to avoid eventual limitations from the transport of electrons and ions through the porous matrix. Electrochemical characterisations were performed to study the kinetic properties of graphite de/lithiation as a function of the several stages of intercalation. Higher kinetic of delithiation were measured, justifying the lower energies required to extract lithium from graphite particles compare to their intercalation. Concerning the lithiation, different kinetic of lithium insertion were identified with respect to the type of lithiation mechanism. On the basis of mechanical aspects, it was suggested that the formation of the graphite stage I was more difficult, and a lower diffusion coefficient of lithium in graphite particles was measured.

CONCLUSION – CHAPTER 3

The lithiation mechanism was also investigated by means of *operando* XRD and Raman experiments. The end of lithiation mechanism was revisited, demonstrating the existence of a solid solution following the stage I phase. It is suggested that the stage I corresponds to a $Li_{0.9}C_6$ stoichiometry, and the last solid solution ends-up to an enriched-stage I corresponding to the well-known LiC_6 phase. This succession of first-order transition and solid solution was confirmed by Raman spectroscopy with the analysis of the Fano effect appearing in the end of lithiation. To date, the analysis of this band dynamic in the lithiation of graphite was not reported in the literature.

Aside the understanding of the graphite lithiation, a method for the determination of the structural state of charge of graphite using XRD was developed. By analysing the mass centre of the (002) Bragg reflections evolution upon graphite lithiation, a good sensitivity of this indicator was observed with the cell state of charge. The results obtained within this experiment will serve as input data for the estimation of the structural state of charge in thick graphite electrodes in the next chapter.

CHAPTER IV

GRAPHITE ELECTRODE ENGINEERING

This fourth chapter is dedicated to the graphite electrode engineering, with the idea of understanding the origin of the power limitation in realistic electrodes. By combining electrochemical, morphological and structural characterisations, thick graphite electrodes are investigated by varying their porosity and the electrolyte's salt concentration. The results discussed are part of an under-writing publication:

- Understanding fast charging limitation in graphite electrode for Li-ion batteries. Heterogeneities of lithiation in conventional electrodes[212].

1 CONTEXT

In the State of the art, an overview of the graphite electrode engineering and the impact on the cells power capabilities was discussed. Multiple ways are available to improve the rate capability of graphite electrodes, but at the expense of the energy density. During this thesis, graphite electrodes were investigated with high loading known to suffer from poor power densities. Graphite electrodes of ~6 – 7 mg.cm^{-2} were prepared using the methodology given in p**59**. In this chapter, the microstructure of graphite electrodes with different porosities were investigated by means of X-ray holotomography measurement showing impact of the tortuosity onto rate capability measurement. Furthermore, *operando* structural characterisations using XRD were carried out to understand the impact of the electrode microstructure on the electrochemical performance and limitation of the electrode engineering.

2 ELECTROCHEMICAL CHARACTERISATION

Literature studies reveal that power capabilities for graphite electrode of 45-50% porosity with graphite flakes below 20 µm are optimal. Based on this, it was chosen to investigate the impact of the electrode porosity by studying graphite electrodes of 50% and 30%, on 6 µm diameter graphite particles (SFG 6L, Imerys®). This choice was driven by selecting a theoretical optimal porosity (50%) and comparing it with an electrode with an excessive compaction. This investigation was first axed on the characterisation of the electrochemical performance for both electrode porosity.

2.1 Rate capability measurement

2.1.1 Impact of the loading

To highlight the importance of the electrode loading on the power capabilities, the rate capability of the thin electrode (presented in p**87**) was compared with the thick electrode of 50% porosity. A large thickness difference exists between the thin (2D) and thick (3D) electrodes (~7 µm vs. ~80 µm), drastically impacting the electronic and ionic transport. These two electrode architectures were cycled from C/20 to 4C – 5C with a CC-CV protocol. **Figure 93** compares the rate capabilities of the two electrodes, with the total specific capacities obtained (Q_{CC} + Q_{CV}) and the coulombic efficiencies as a function of the applied C-rate. The 2D electrode always reaches the theoretical specific capacity of graphite (372 mAh.g^{-1}), whereas the 3D electrode does not reach this value above C/3. **Figure 93c,d** provides additional information by giving the charge proportions achieved through the CC and CV periods (Q_{CC} and Q_{CV}) for the 2D and 3D electrodes, respectively. For the thin electrode (2D), the maximal specific capacity is reached only with the CC period until C/3 – C/2 rate, whereas for higher C-rates the CV period compensate the missing

charges. For the thick electrode (3D), already from C/8 rate, the CC period cannot reach the maximal capacity by itself and the CV compensate the lacking charges.

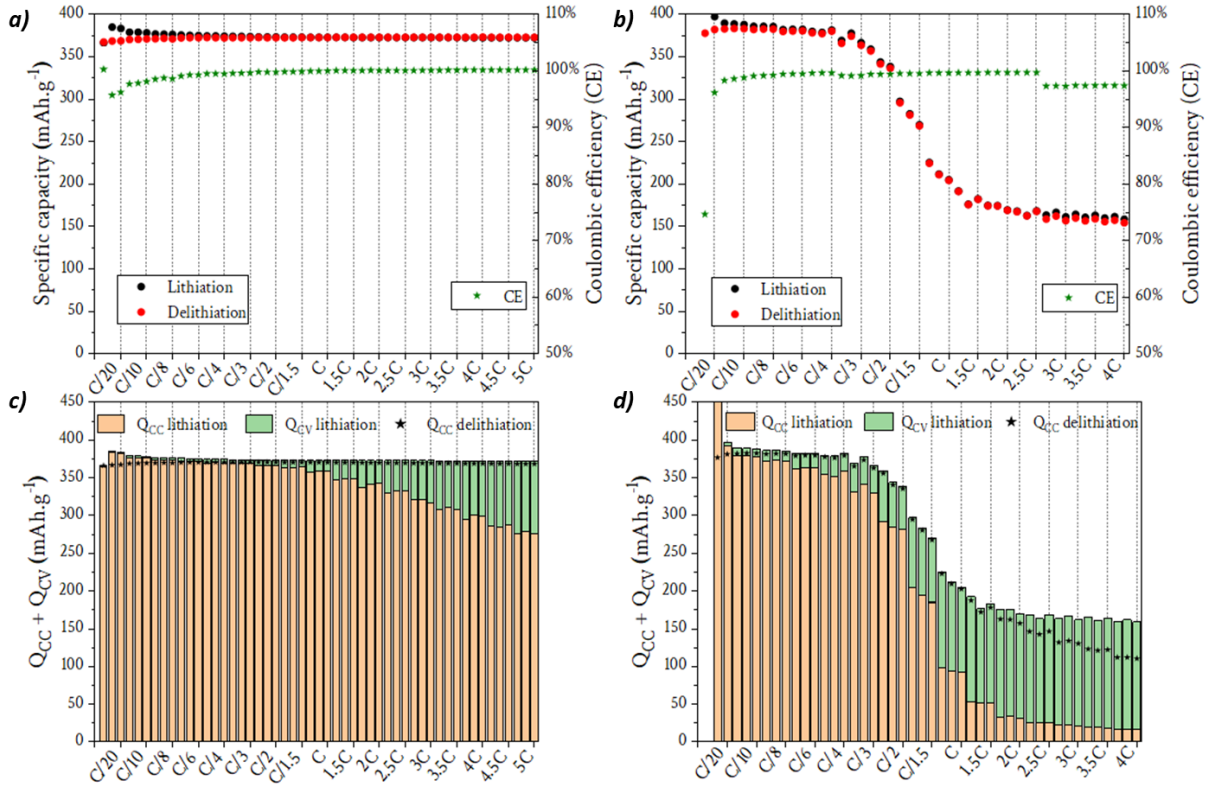


Figure 93: Specific capacities obtained in charge and discharge using a Constant Current (CC) and Constant Voltage (CV – 30 min long) protocol as a function of the C-rate applied. a) Specific capacities and coulombic efficiencies (CE) obtained for the thin electrode (2D). b) Specific capacities and coulombic efficiencies (CE) obtained for the thick electrode of 50% porosity (3D). c) Specific capacities of CC and CV periods in charge and specific capacities of CC in discharge for the thin electrode (2D). d) Specific capacities of CC and CV periods in charge and specific capacities of CC in discharge for the thick electrode of 50% porosity (3D).

The potential profiles obtained at a C/4 rate for each electrode are compared in **Figure 94**. At C/4 cycling rate, the thin electrode delivers ~370 mAh.g^{-1} and the potential plateaus are clearly separated. This demonstrates that the thin configuration provides a very good power capability. For the thick electrode, the potential profile is much more polarised with potential plateaus that are less marked and at lower potentials. As an example, the potential step localised at ~200 mAh.g^{-1}, which is very visible for the thin electrode, is almost not observed for the thick electrode. The DCA profile (inset of **Figure 94**) shows the difference in the potential plateaus shape. The peaks of the thick electrode are always shifted by ~30 mV to lower potentials, and systematically reach lower intensity with larger width because of potential plateaus that are less flat. This analysis demonstrates that higher overpotentials are associated to the lithiation of the thick electrode at C/4 cycling rate. In addition, a significative difference for the first plateau of potential is observed between the two electrode thicknesses. The first plateau starts at ~20 mAh.g^{-1} for the thin electrode, whereas it starts at ~34 mAh.g^{-1} for the thick one. This difference of capacity is

attributed to the effect of the carbon additive, at 10%$_{wt}$ in the thick electrode while the thin electrode does not contain Super C65 particles. As a result, a larger adsorption capacity is observed and shifts the potential drop toward higher capacity for the thick electrode.

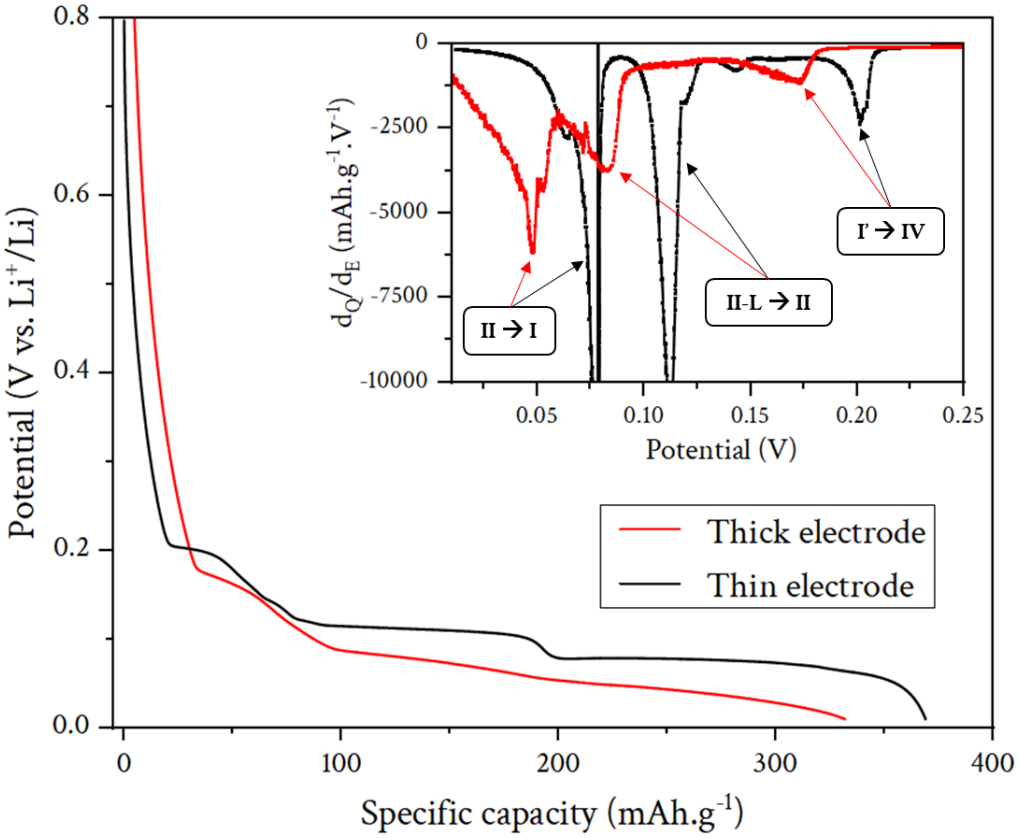


Figure 94: Lithiation potential as a function of the cell state of charge at C/4 cycling rate for a thin (black) electrode and a 50% porosity thick (red) electrode. The inset shows the DCA analysis of the two potential profiles.

With this comparison, one can easily notice the better power capability of the 2D electrode. While the thin electrode does not display any kinetic limitation up to C/2 rate, the thick electrode is limited starting from C/8 rate. The higher kinetic limitation of the thick electrode can be attributed to transport limitation through the microstructure. This limitation can originate from the electronic transport or the ionic transport, yet impossible to answer.

2.1.2 Effect of the electrode porosity

To understand the limitation, the ionic pathways and electronic percolation were tuned by modifying the electrode compactness. By reducing the electrode porosity from 50% to 30%, one can expect an improvement of the electronic percolation by bringing closer carbon particles (that are not such good conductors as discussed in p**13)**, but also a degradation of the ionic transport due to an increase of tortuosity linked to the microstructure. Depending on which effect is the most dominant, the power capability can be improved or degraded.

The two electrode porosities were investigated by means of a rate capability measurement with LP30 as electrolyte at 25°C. **Figure 95** shows the rate capability test results for the lithiation with the evolution of the galvanostatic charge fraction over the total charge obtained during the CC-CV discharge*. The inset shows the specific galvanostatic capacities for each cycle, for both electrode porosities. For low cycling rates (C/20 – C/6), stable specific galvanostatic capacities are obtained (slightly decreasing from 383 $mAh.g^{-1}$ to 358 $mAh.g^{-1}$) for both porosities. The obtained specific capacities are higher than the theoretical specific capacity of graphite (372 $mAh.g^{-1}$) because of at least three side reactions. First, the C65 carbon nanoparticles can provide additional capacities. On this purpose, an electrode composed of C65 (90%$_{wt}$) and PVDF (10%$_{wt}$) was prepared and cycled against a metal lithium counter-electrode to probe the specific capacity of the carbon additive. The charge and discharge profiles are given in **Figure A4**, the first lithiation containing the SEI formation (not displayed) delivered a specific capacity of ~550 $mAh.g^{-1}$. For the following cycles, a reversible specific capacity of ~150 $mAh.g^{-1}$ is observed, with a potential profile similar to a hard-carbon cycling (with two distinguishable slopes). This high specific capacity is rather surprising since C65 is sold as carbon additive without hard-carbon properties. The C65 used probably display graphitic domains providing intercalation capacity, and a large surface area providing high capacitive capacity. Considering a theoretical specific capacity of 150 $mAh.g^{-1}$ for the C65, the carbon additive should contribute to ~5% (20 $mAh.g^{-1}$) of the specific capacity in a composite electrode composed of graphite (80%$_{wt}$) and C65 (10%$_{wt}$). This additional capacity is rather coherent with the excess of specific capacity obtained in these composite electrodes (~10 – 15 $mAh.g^{-1}$). In addition to the carbon additive effect, the SEI formation could increase the specific capacity, as well as the corrosion of the coin cell casing. However, these side reactions should contribute to a lower extent then the C65 additional charges.

Coming back to the analysis of **Figure 95**, a difference appears at C/4 with a specific galvanostatic capacity lower for a porosity of 30%, that decreases the galvanostatic charge fraction (Q_{cc} / (Q_{cc} + Q_{cv})). By increasing the cycling rate to 2C, this difference increases. The highest difference is obtained at C/1.5 with a galvanostatic specific capacity of 230 $mAh.g^{-1}$ for 30% porosity, whereas 273 $mAh.g^{-1}$ is achieved for 50% porosity. For higher cycling rates (2C – 4C), a stabilisation of the specific galvanostatic capacities is observed, representing less than 20% of the total specific capacities for both porosities. In this range, the graphite particles probably deliver a very little capacity (few $mAh.g^{-1}$) and the capacity stabilisation around 20 $mAh.g^{-1}$ is explained by super capacitive effects coming from the high rate capability of the C65 additive. In addition, the lithium counter electrode can take the lead in terms of kinetic limitation. Indeed, a specific rate of 2.5C is equivalent to current densities around 0.8 $mA.cm^{-2}$, corresponding to critical current densities of

* Note that the total specific capacities of both electrode porosity were normalised by the specific capacity obtained at C/20 (assuming that the maximal specific capacity is reached at this low cycling rate).

lithium plating and stripping as reported in the literature[213]. Based on the literature, the rate capability tests suggest that a decrease of porosity from 50% to 30% is responsible for a change in the electrode microstructure, most probably linked to a higher tortuosity.

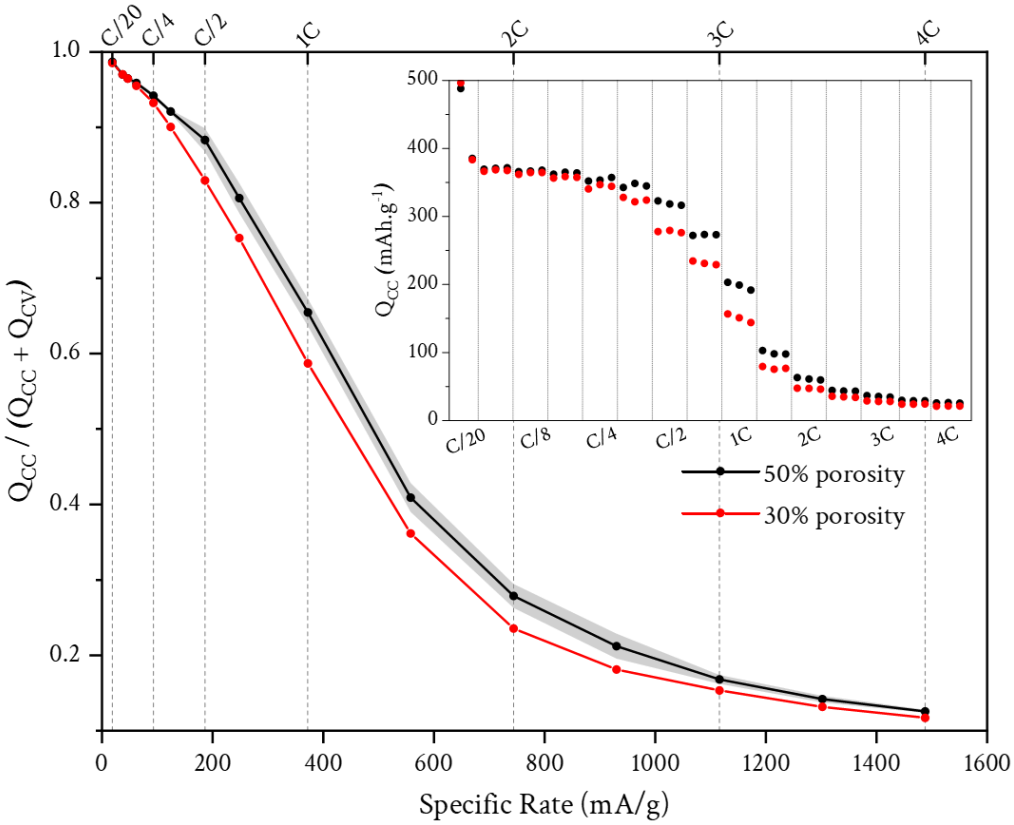


Figure 95: Rate capability test of graphite electrode (50% and 30% porosity) cycled in half-cell with LP30 at 25°C, in lithiation. Main plot shows the fraction of galvanostatic charge over the total specific capacity obtained by CC-CV with a CV period of 30 min, as a function of the C-rate applied. The standard deviations are represented by the grey and red shadows. The inset gives the galvanostatic specific capacity obtained for both electrode porosity.

To further characterise the electrochemical behaviour of the two electrodes, the lithiation profiles obtained at C/4 cycling rate were investigated. **Figure 96a** shows the lithiation profiles of both electrode porosity, normalised between zero and one to compare the potential plateaus. One can observe a similar starting potential for each potential plateau, but with a potential variation much tilted for the electrode with 30% porosity. This is more visible in the plot inset showing the stage II-L to stage II transition, starting and ending potentials are similar but a flatter plateau is observed for the electrode with 50% porosity. The DCA (**Figure 96b**) provides a better visualisation of the difference between the two electrode porosities. The peaks reach higher intensity and are sharper (because of flatter plateaus) in the case of the electrode with 50% porosity. All these features highlight higher limitations in the graphite electrode lithiation for 30% porosity.

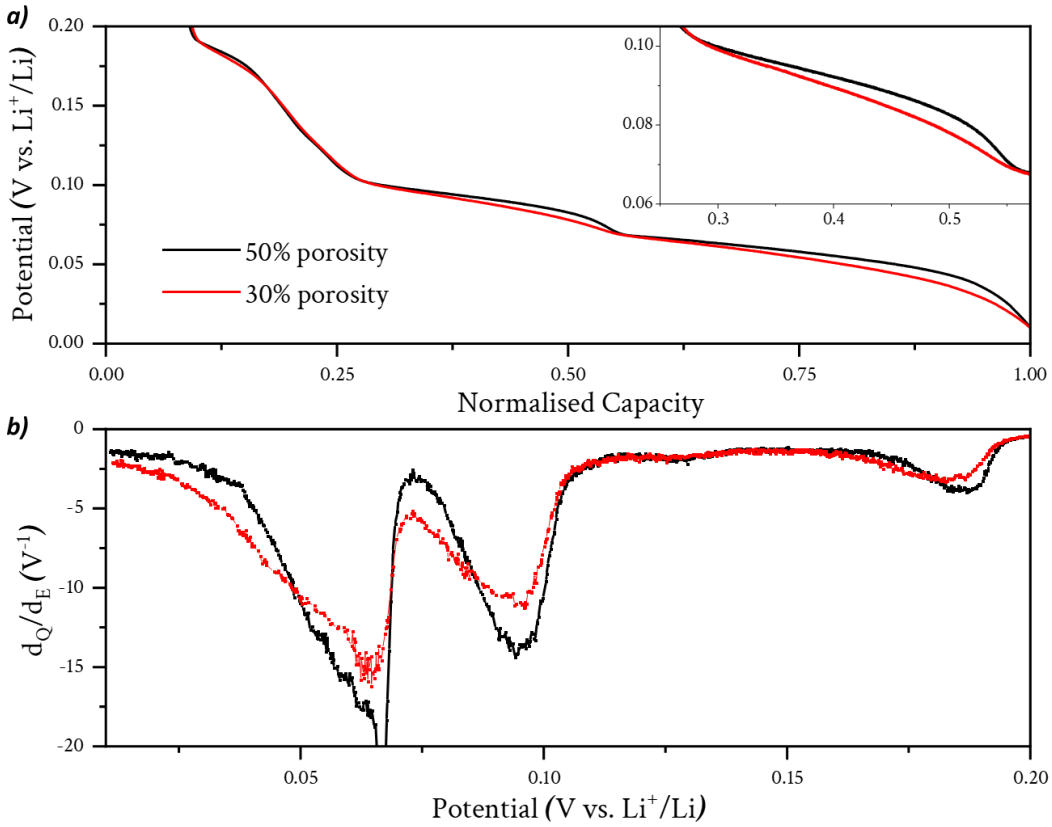


Figure 96: a) Lithiation profiles obtained at C/4 rate for each electrode porosity. The inset is the zoom on the second potential plateau. b) Differential Capacity Analysis of the lithiation profile obtained at C/4 rate for each electrode porosity.

To understand whether the power is limited by electronic or ionic transport, the electrolyte salt concentration was varied from 1 M in $LiPF_6$ to 0.7 and 0.35 M. By decreasing the salt concentration, a degradation of the ionic transport is expected because of a lower ionic conductivity, lower lithiation kinetics, and because the consumption of Li^+ has a higher impact on the conductivity for low concentrations. To emphasize the effect of salt concentration, the electrode of 30% porosity suffering from lower power capability was selected. The cells with different salt concentrations were studied using rate capability tests and the results are shown in **Figure 97**. Two features can be noticed: i) a decrease of galvanostatic specific capacity is observed by decreasing the salt concentration from C/10 to 2.5 C (inset window), and ii) the fractional charge coming from galvanostatic period decreases faster for lower salt concentration by increasing the charging rate (principal window). Again, above 2.5 C, the lithium counter-electrode plays a key role in the electrochemical response.

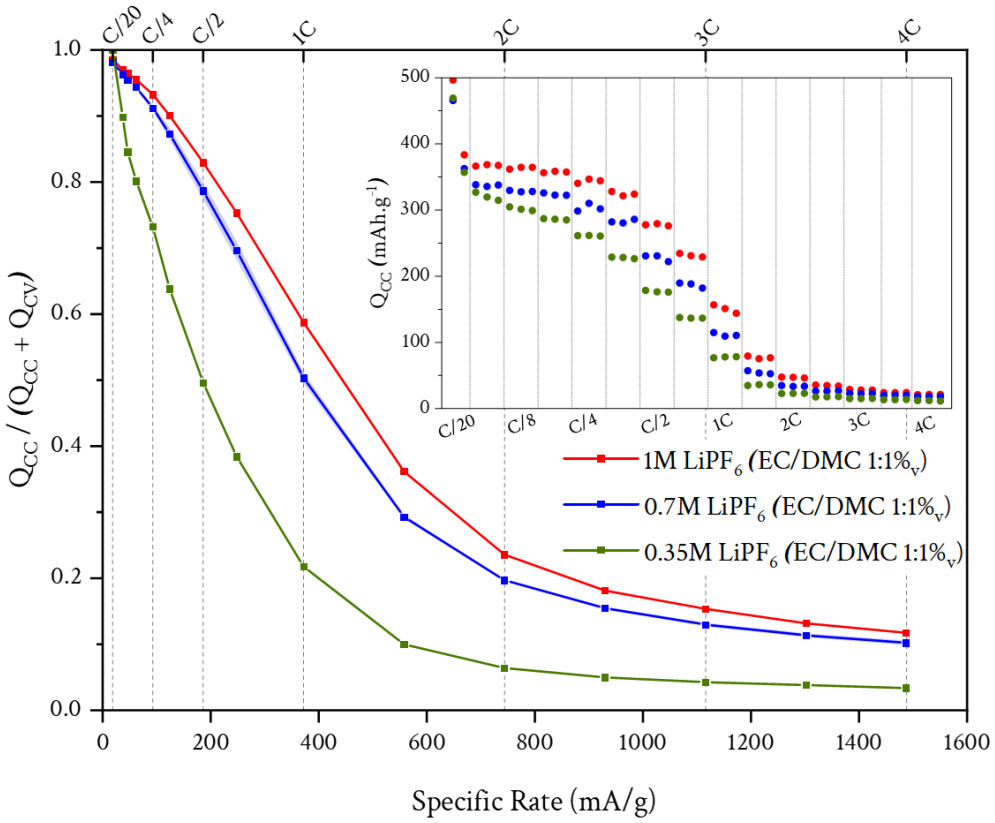


Figure 97: Rate capability test of 30% porosity graphite electrode cycled in half-cell with 1 M, 0.7 M and 0.35 M $LiPF_6$ in EC/DMC(1:1%$_v$) at 25°C, in lithiation. Main plot shows the fraction of galvanostatic charge over the total specific capacity obtained by CC-CV with a CV period of 30 min, as a function of the C-rate applied. The inset gives the galvanostatic specific capacity obtained for both electrode porosity.

In **Figure 98a**, the lithiation profiles are displayed as function of salt concentration at C/4 cycling rate. Decreasing the salt concentration leads to less "marked" potential profiles with the loss of the typical potential plateau-shape of graphite staging process, and the specific capacity obtained during the CC period is lowered. On the DCA representation (**Figure 98b**), this is expressed by i) a shift of the peaks towards lower potentials (materialised by the horizontal arrows), and ii) a lower peak intensity by decreasing the salt concentration (materialised by the vertical arrows). The former is probably due to an increase of overpotential because of the lower salt concentration and/or due to lower kinetics of lithiation, whereas the latter is probably linked to more "dispersed" processes of lithiation in the electrode volume. The effect of salt concentration supports the hypothesis of an ionic limitation in the electrode causing higher depletions of lithium ions in some part of the electrode volume.

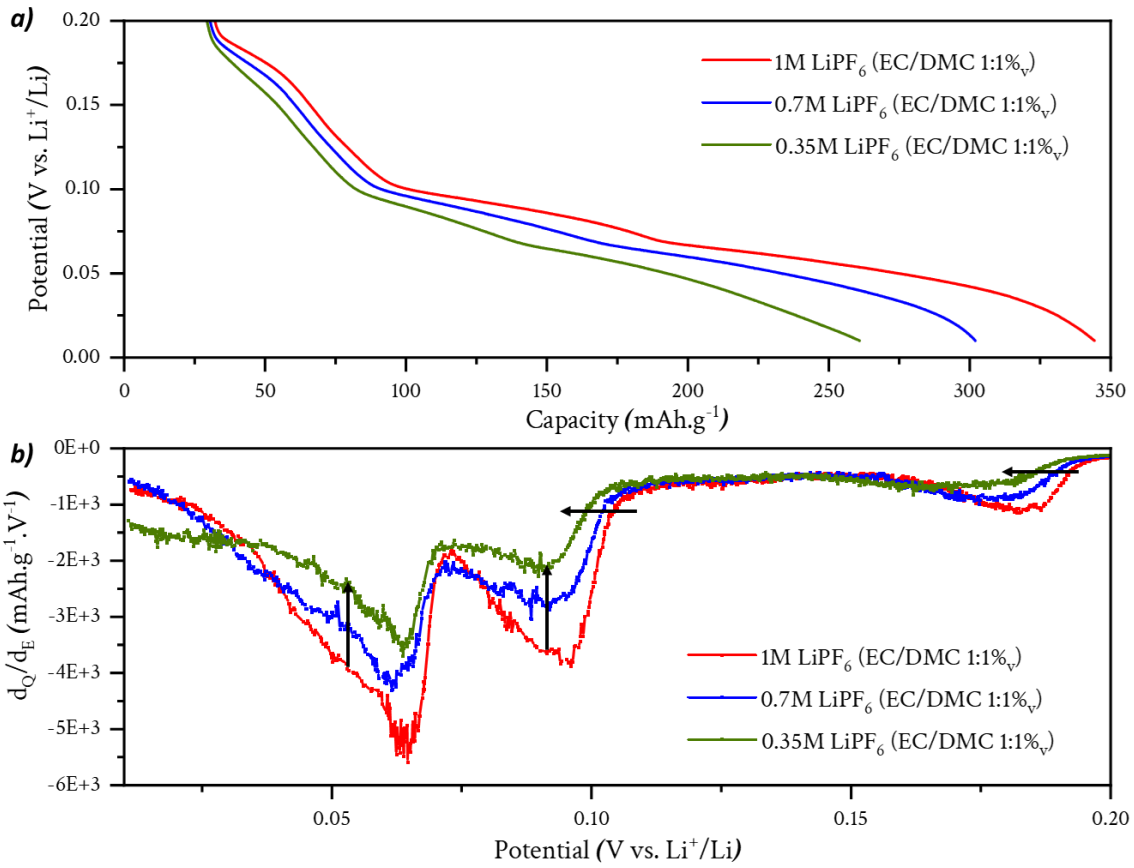


Figure 98: a) Lithiation profiles obtained at C/4 rate for a 30% porosity graphite electrode with 1 M, 0.7 M and 0.35 M $LiPF_6$ in EC/DMC (1:1%$_v$). b) Differential Capacity Analysis of the lithiation profile obtained at C/4 rate for each salt concentration.

The rate capability tests demonstrated that lithium diffusion in the electrolyte is the limiting factor regarding the power capability of graphite electrodes. This result is in agreement with similar studies from the literature that highlighted a limitation by the ionic transport, as discussed in the state of the art. A decrease of the electrode porosity is known to increase the tortuosity associated with the ionic pathway* that is responsible for higher diffusion times of lithium ions through the electrode microstructure for a given distance. Based on this, the measurement of ionic tortuosity was realised using both electrochemical and high-resolution imaging techniques.

By electrochemistry, the tortuosity was measured by EIS in symmetric cells composed of pristine graphite electrodes of identical porosities and a Whatman® separator soaked by the electrolyte. The measurement consists in fitting the impedance diagram using a Transmission Line Model (TLM), described in p**66**. The measurement was realised using 0.35 M $LiPF_6$ in EC/DMC (1:1%$_v$) as electrolyte to enable a proper deconvolution between the diffusion regime at medium frequency and the capacitive region at low frequency. Indeed, with classical LP30, the ionic conductivity is too high and the deconvolution between both phenomena is difficult. The tortuosity was

* The tortuosity associated with the ionic pathway is latter referred as ionic tortuosity.

measured for non-calendered graphite electrodes (~70% porosity), 50% and 30% porosity electrodes. The Nyquist impedance diagrams of each electrode porosity are given in **Figure 99**. From these diagrams, the ionic tortuosity was estimated, and results are given in **Table 10**. A relationship can be seen between calendaring and increase of tortuosity. The obtained tortuosity are in the upper range of reported values for graphite electrodes with similar porosities and particle morphologies[130,161,214–216].

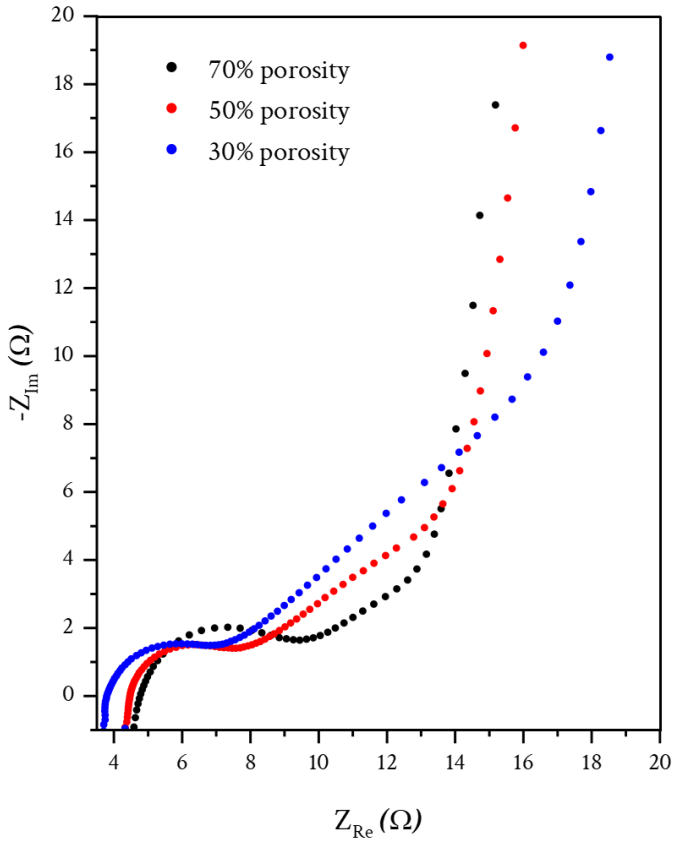


Figure 99: EIS response (Nyquist plot) from symmetric cells composed of 70%, 50% and 30% graphite electrodes with 0.35 M $LiPF_6$ in EC/DMC (1:1%$_v$).

Table 10: Ionic tortuosity estimated by EIS for different graphite electrode porosities (SFG 6L particles).

Porosity	Tortuosity
70%	4.5 ± 0.5
50%	7.1 ± 0.2
30%	9.4 ± 0.7

These results demonstrate the impact of the electrode densification, generating more tortuous ionic diffusion pathways and increasing the diffusion times in the liquid phase. To further characterise the porosity reduction and its impact on the electrode, a morphological study was realised combining SEM and X-ray holo-tomography.

3 MORPHOLOGICAL CHARACTERISATION

3.1 SEM images

To characterise the microstructure of the porous electrodes, cross-sections using ion-milling were realised as described in p**68**. The corresponding SEM images are provided in **Figure 100**. The electrode with 50% porosity (**Figure 100a**) displays a thickness of ~80 µm, deposited on a copper current collector of 10 µm. A rather homogeneous distribution of binder agglomerates (lighter particles) is observed, testifying a good electrode elaboration. At the top of the image, redeposition of materials that were vaporised by the ion-flux can be seen which is not representative of the initial electrode microstructure.

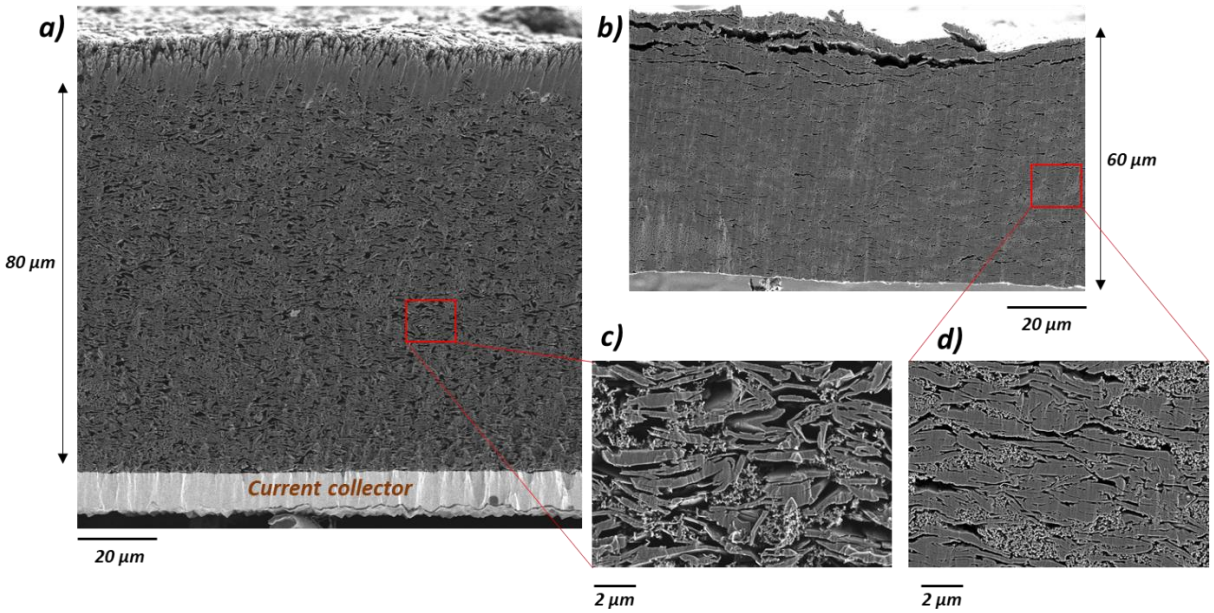


Figure 100: SEM cross-sectional images of the porous graphite electrodes. a-b) Large views of the 50% and 30% electrode porosities, respectively, with the current collector side on the bottom. c-d) Zoom on the two large view images.

On the zoom of this image (**Figure 100c**), the graphite particles are nicely visible. The particles are flakes-shaped with an average thickness lower than 1 µm, whereas the particle length is more difficult to estimate because most of the flakes are folded on themselves. The electrode with 30% porosity (**Figure 100b**) is 60 µm thick and the current collector was removed during the electrode preparation because it partially detached from the copper. A rather homogenous microstructure is also observed, despite the large fracture seen on the top of the electrode. The cause of this fracture is unknow to date, since it could originate from the electrode handling or from the electrode calendaring. By zooming on this image (**Figure 100d)**, the difference in porosity between the two electrodes in easily noticed. An evident less tortuous porosity network is observed for the electrode of 50% porosity, with larger pores. The distinction between the different graphite flakes is also more difficult in the case of the 30% porosity electrode, which

demonstrates that the calendering should increase the electronic percolation, but also increase the tortuous path for the electrolyte.

These images give 2D information about the electrode microstructures, and provide first insight on the impact of the calendering. However, the electrode microstructures are established on 3D volumes that are not accessible using conventional SEM imaging. To assess the morphology of electrodes, several techniques are used and display different advantages and limitations. FIB-SEM is a useful technique combining focused ion-milling and SEM imaging[217,218]. The reachable resolution (nm-scale) is one of the best for imaging techniques, however the probed volumes are low and cannot be representative of the full electrode thickness. In addition, the realisation is time-consuming and possible artefacts such as redeposition as observed in SEM can be observed. In a similar spirit, X-ray tomography measurements can provide 3D information on the full electrode thickness, without generating physical artefacts. However, a limited resolution (µm-scale) is obtained in laboratory experiments. To improve the resolution (up to 50 nm), an X-ray holotomography experiment was performed on the electrodes using a synchrotron radiation.

3.2 ID16b holo-tomography experiment

The electrode microstructures were assessed using X-ray holotomography at ID16b beamline, ESRF with the help of Dr. Victor Vanpeen (CEA). The working principle of the holotomography is given in p**69**, as well as the method used for the data acquisition and treatment. The electrodes of 50% and 30% porosity (SFG 6L as graphite particle) were probed and the reconstructed volumes were analysed. Based on random forest algorithm, each phase of the composites electrodes was segmented using three phases, the graphite phase, the carbon binder domain (CBD) and the porosity.

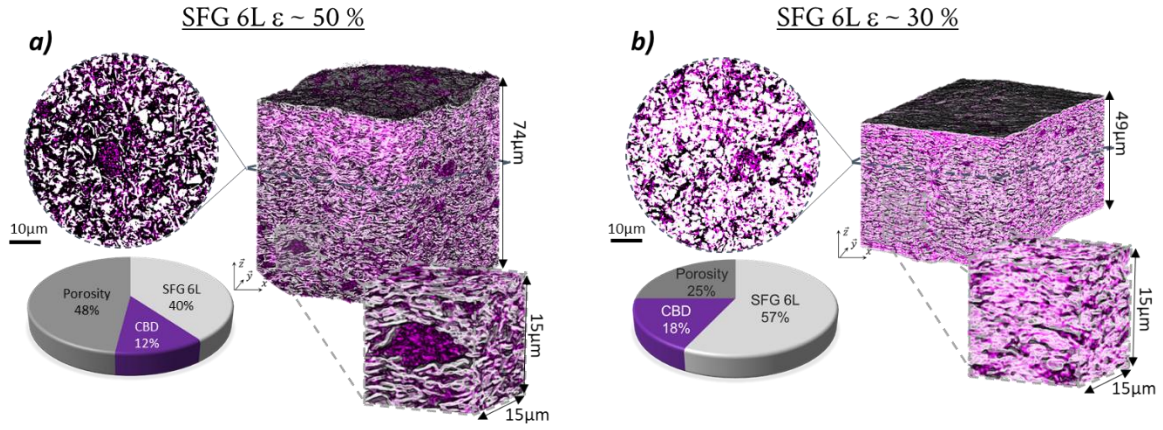


Figure 101: X-ray holo-tomographs obtained at ID16b beamline at ESRF. a) Segmented image and volume of the 50% porosity graphite electrode, with the volume fraction of each phase. b) Segmented image and volume of the 30% porosity graphite electrode, with the volume fraction of each phase.

The segmented volumes of each electrode porosity are given in **Figure 101**, the whole electrode thicknesses were probed (74 µm and 49 µm) on a field of view of 102 x 102 µm² in the electrode plane. Each segmented phase was characterised by its volume fraction and mean thickness, and the results are given in **Table 11**.

Table 11: Results obtained from the segmentation of the X-ray holo-tomography experiments for 50% and 30% porosity graphite electrodes.

Electrode	Graphite		CBD		Porosity		CBD median local thickness	Pores median local thickness	Pores intra-connectivity
	$\%V_{theo}$	$\%V_{exp}$	$\%V_{theo}$	$\%V_{exp}$	$\%V_{theo}$	$\%V_{exp}$			
50%	37%	40%	13%	12%	50%	48%	195 nm	510 nm	100%
30%	53%	57%	17%	18%	30%	25%	240 nm	370 nm	97%

First, a good agreement is observed between the theoretical volume fraction of each phase (estimated from the components weight and density) and the experimental one. This highlights the segmentations effectivity, providing representative information on the electrode microstructures. Due to the achieved resolution (voxel size of 50^3 nm), a small fraction of the pores was probably not segmented and attributed to graphite phase, this can explain the slight underestimation of the porosity volume fraction and the slight overestimation of the graphite one. On the calendering effect, CBD domains of similar thicknesses were estimated (195 vs. 240 nm for 50% and 30% porosities, respectively), in the range of the experimental resolution. As expected, the pores size decreases when the porosity of the electrode is decreased (from 510 nm to 370 nm), supporting the SEM observations. From the porosity phase, the pores intra-connectivity was evaluated and excellent values were found (100% and 97%, for 50% and 30% porosity respectively), ensuring a proper wettability of the electrode once the electrolyte will be added. As expected, the calendering slightly decreases the intra-connectivity, probably because of the closing of some pores that could hindered ionic transport.

The pore size distribution was also analysed along the electrode thickness for both porosities in **Figure 102**. The calendering enabled a homogenisation of the pore size along the electrode thickness (**Figure 102a**). At 50% porosity a higher distribution was observed with larger pore size at the separator/electrode interface reaching 60% porosity, which can be explained by the "free" surface volume allowing relaxation after calendaring (memory effect type). Concerning the isolated pores (**Figure 102b**), an increase of the volume was observed by decreasing the porosity, and the distribution along the electrode thickness was rather homogeneous. This confirms that calendering the electrode induces the closing of some pores, leading to "dead" porosity.

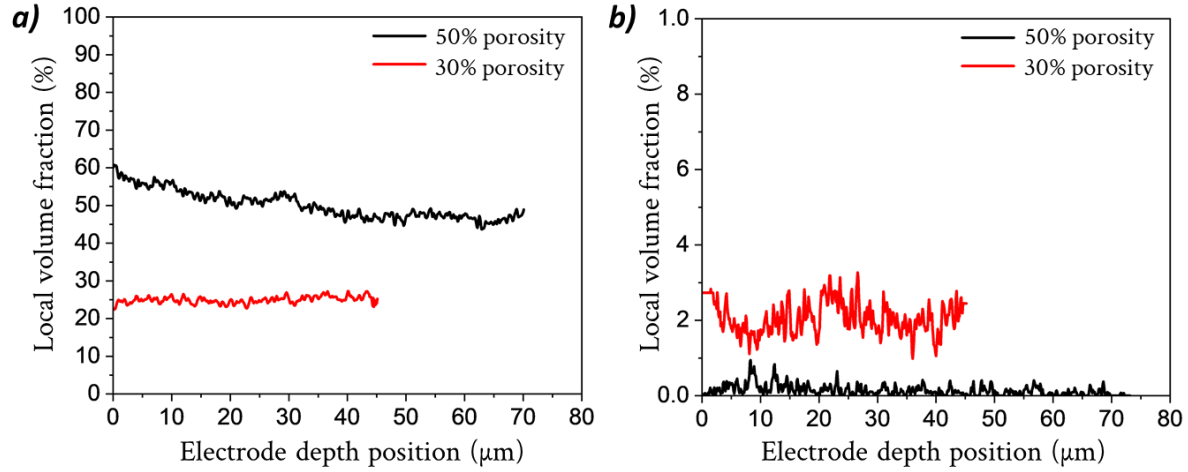


Figure 102: Spatial distribution of a) the global porosity and b) the isolated pores along the electrode thickness. Note that 0 µm corresponds to the separator/electrode interface.

Based on these microstructures, the geometric tortuosity was estimated through the geodesic/euclidean distances along the through- and in-plane directions (**Figure 103**). The in-plane and through-plane tortuosity are given in **Figure 103b, d** for the two electrode porosities. A similar in-plane tortuosity was observed for both electrode porosity (1.13 vs. 1.33), whereas the through-plane tortuosity (from where the calendaring is effective) was increased by the calendering step (1.4 vs. 2.0, for 50% and 30% porosity respectively). The estimated values are in agreement with literature studies[219]. A thinner distribution for the in-plane direction than for the through-plane direction is observed which supports a more heterogeneous pore size distribution along the electrode thickness compared to the electrode plane direction. These observations correlate with the flakes-shape of graphite particles, that are naturally oriented with their basal plane parallel to the current collector plane, generating more tortuous pathways in the through-plane direction. The results are also in agreement with the tortuosity estimated via EIS, demonstrating the detrimental effect of decreasing the porosity from 50% to 30% by calendering. However, the difference of tortuosity between the electrochemical and the geometric measurement is large because the two techniques are not sensitive to the same physical phenomena (*via* EIS, migration effects as well as the impact of the lithium solvation sphere is accounted, but not by geometric determination)

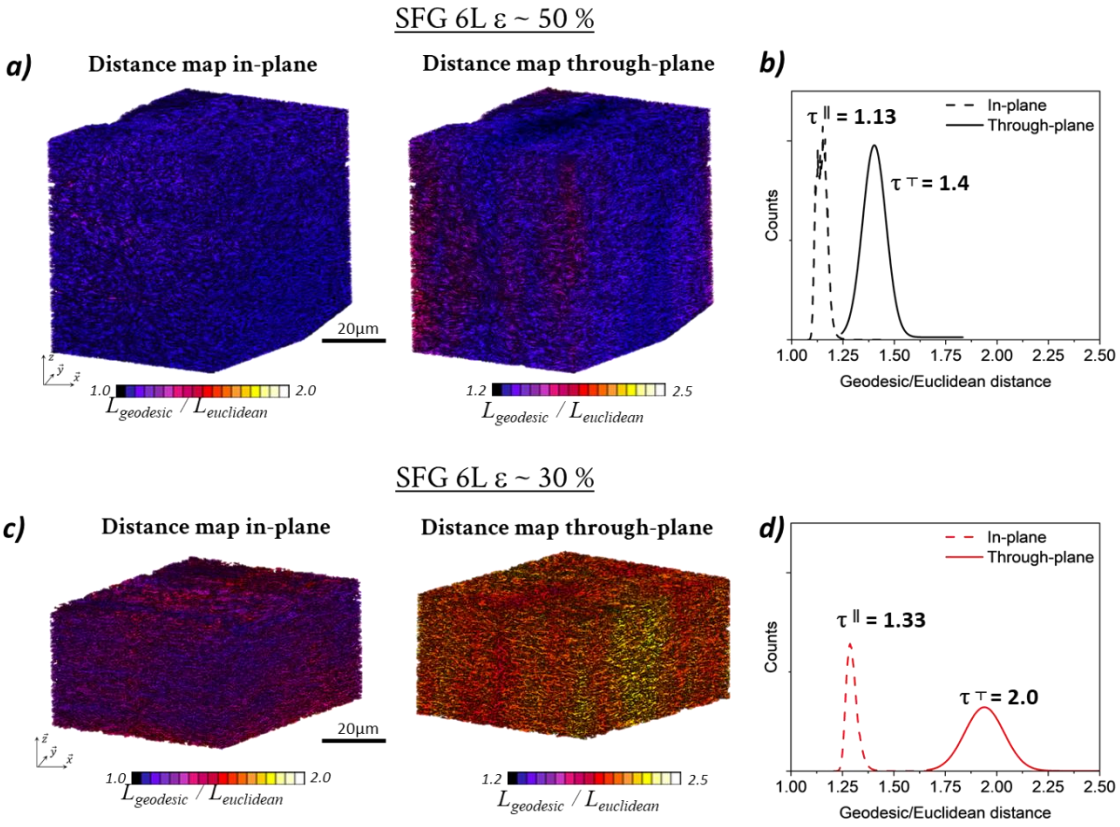


Figure 103: Geodesic distance maps along the in-plane and through-plane directions for the 50% (a) and 30% (c) porosity graphite electrodes. Populations of geodesic/euclidean distances for the 50% (b) and 30% (d) graphite electrode porosities.

Based on these electrochemical and morphological investigations, the electrode calendering induces an increase in tortuosity of the ionic pathway in the electrode thickness. As a consequence, heterogeneities of lithiation are expected to appear along the electrode thickness upon cycling, that should be more pronounced for a porosity of 30%. To characterise this, a structural investigation was realised with the idea of probing the structural state of charge of graphite as a function of the electrode depth.

4 STRUCTURAL CHARACTERISATION

4.1 Structural state of charge determination

The structural investigation was carried out at ID31 beamline (ESRF) similarly to the thin graphite electrode probed in p**97**. The graphite electrodes (50% and 30% porosity) were probed in coin cells (30% porosity) and Swagelok cells (50% porosity) with a *z*-profiling procedure as schematised in **Figure 104**. To ensure that no significative effect of the cell architecture was present, the lithiation profile at C/10 rate of both cells (50% and 30% porosity) are shown in **Figure A5**. Very similar potential profiles were observed (same potential plateaus), supporting a similar pressure inside

the Swagelok and coin cells. The 50% and 30% porosity electrodes were probed at 5 positions and 9 positions in their thickness (see p**73**).

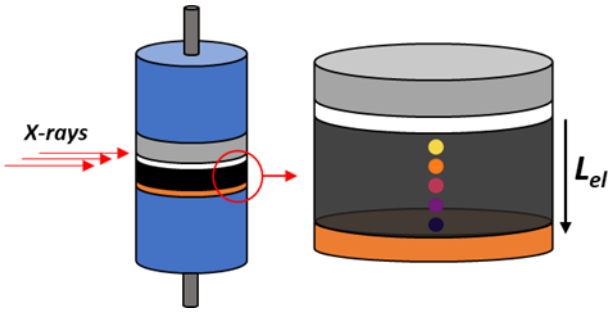


Figure 104: Schematic illustration of the Swagelok cell probed with a z-profiling procedure at ID31.

The two graphite electrodes were preliminarily cycled in the lab at C/20 to properly form the SEI, and then brought to the beamline at the discharged state. The two graphite electrodes were cycled from C/4 to 1C cycling rates and probed with the *z*-profiling protocol *in operando*, with LP30 electrolyte and cycled at 25°C. The electrochemical profiles obtained during the experiment are given in **Figure 105**. The capacities reached at each cycling rate were normalised to the capacities obtained at C/20 after the formation cycle (considered as the maximal capacity of the cells). The *x*-axis corresponds to the cell state of charge (SoC_{cell}).

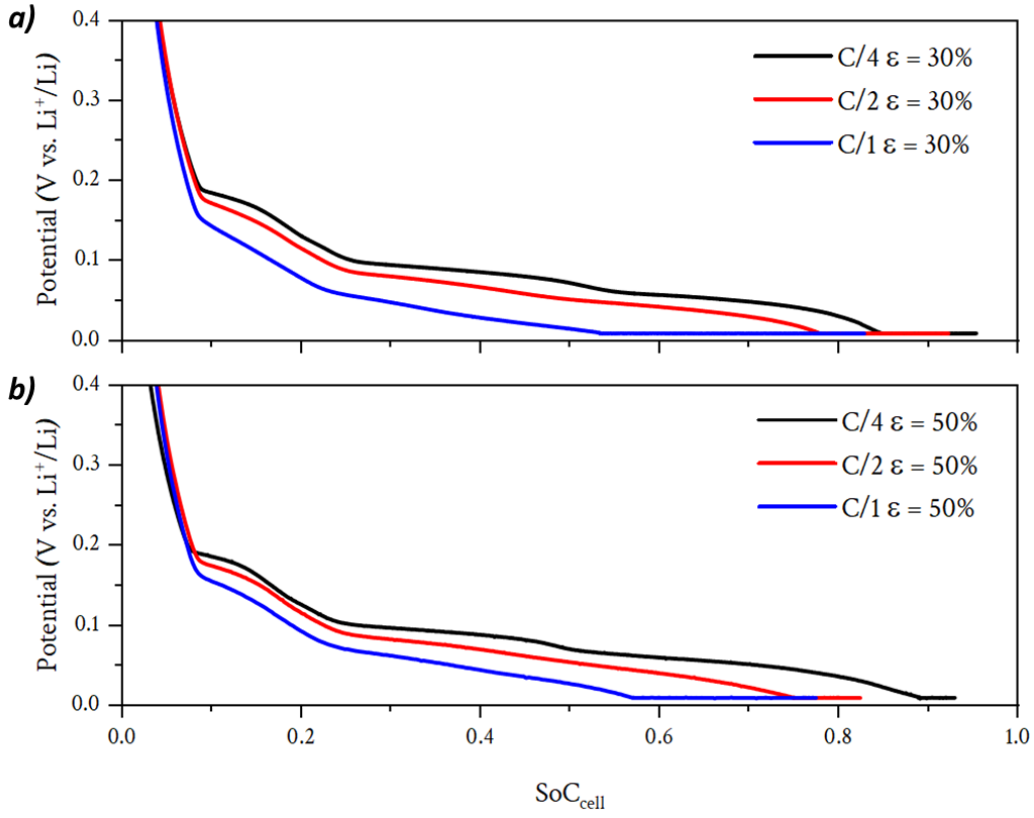


Figure 105: Lithiation profiles of the (a) 30% and (b) 50% porosity graphite electrodes cycled from C/4 to 1C rate obtained during the ID31 experiment.

For the diffraction patterns, the background was removed as mentioned in p**71**, and the (002) Bragg reflections can be followed in **Figure 106** where the 0.1 L (close to separator) and 0.9 L (close to current collector) positions of the 50% porosity graphite electrode upon lithiation at C/4 are displayed. By following the (002) Bragg reflection at ~1.69 $Å^{-1}$ corresponding to the stage I phase, a delay in the appearance of this peak for the 0.9 L position was observed. As well, in the end of charge, the presence of the (002) Bragg reflection at ~1.78 $Å^{-1}$ corresponding to the stage II phase at the 0.9 L position is still observed, whereas no peak is visible for the 0.1 L position. These observations suggest that the 0.9 L position is delayed in the lithiation process, leading to a lower structural state of charge at the end of the C/4 discharge. Physically, this means that the graphite particles near the current collector/electrode interface are delayed in the lithiation process compared to the separator/electrode interface.

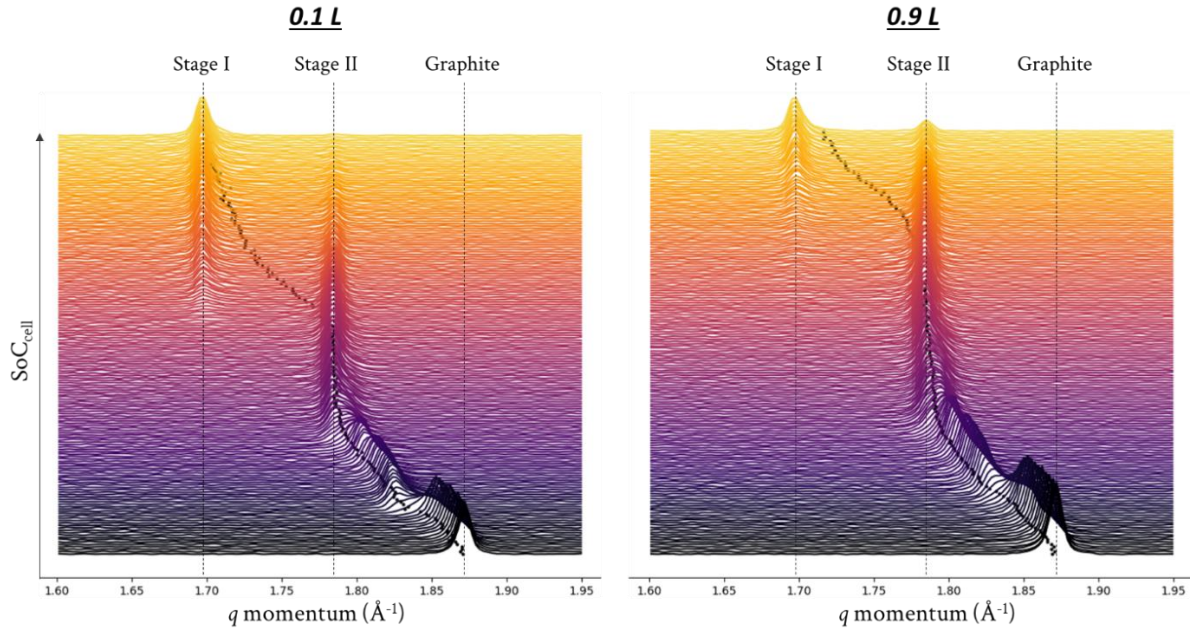


Figure 106: Diffraction patterns evolution for the graphite electrode of 50% porosity upon discharge at C/4 near the separator (0.1 L) and near the current collector (0.9 L). The black dotes under the diffraction patterns gives the mass centre.

To go further in the data analysis, the mass centre of each diffraction pattern was calculated as mentioned in p**73**, using the methodology developed in the Chapter 3. The mass centre for each *z*-position of the two graphite electrodes is given in **Figure 107**. Because the lithiation of graphite induces a shift of the (002) Bragg reflection towards lower *q* momentum, a decrease of the mass centre is expected. Based on this, a delay of the mass centre shift is observed as function of the electrode depth in at least two regions. From 0.05 to 0.15 SoC_{cell} (insets of **Figure 107**), and 0.5 to 0.9 SoC_{cell}. In both cases, a gradient is observed with mass centres that are shifting earlier for the position near the separator/electrode interface (0.1 L). These observations confirm the hypothesis that the graphite electrodes are limited by the lithium diffusion in the electrode porosity,

generating a gradient of lithiation established from the separator towards the current collector. Similar qualitative observations can be made for both electrode porosities.

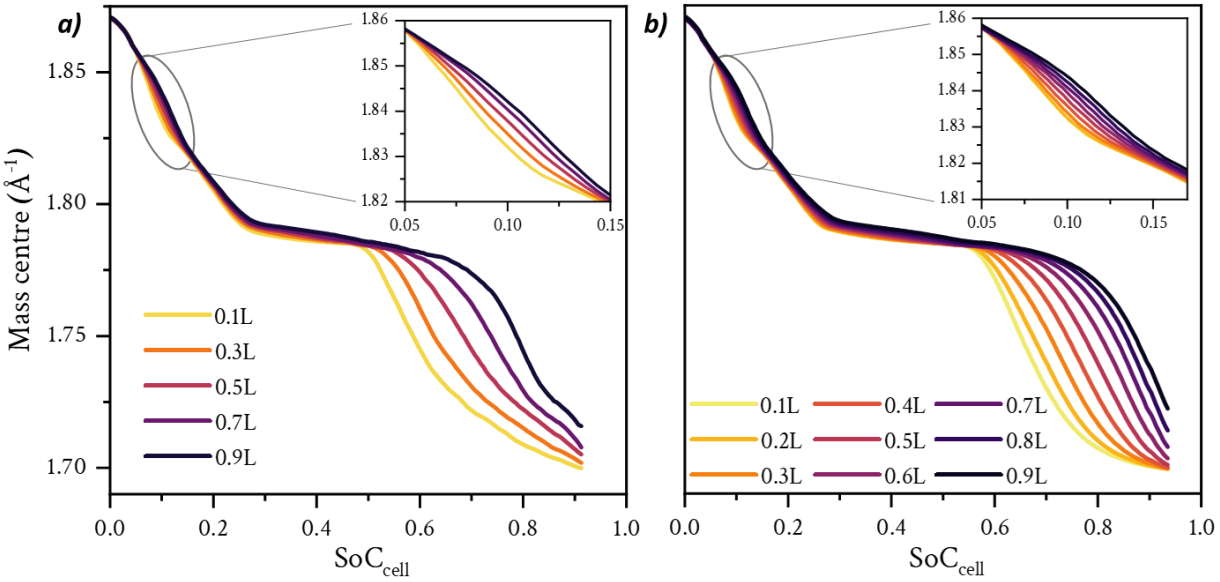


Figure 107: Mass centre evolution at the different z-positions probed for the 50% (a) and 30% (b) porosity graphite electrodes at C/4 rate as a function of SoC_{cell}. Insets are a zoom on the principal plot.

By using the "model" curve obtained with the thin graphite electrode, providing the evolution of the diffraction pattern mass centre as a function of the cell state of charge (**Figure A1**), the structural state of charge of graphite can be determined. Then, the mass centre profiles obtained in **Figure 107** were translated to the structural state of charge of graphite (x in Li_xC_6) in (**Figure 108**). A constant shift between the diffraction patterns of the thin electrode and the thick electrodes (50% and 30% porosity) was observed. To correct this shift (~ 0.011 $Å^{-1}$), the diffraction patterns were aligned based on specific peak positions such as pristine graphite, stage II and stage I. The lithiation of both electrode porosity are given in **Figure 108a, b** and correlated to the structural state of charge of graphite (x in Li_xC_6) as a function of the SoC_{cell} in **Figure 108c, d**. A x = y straight line is given as an indication and corresponds to the ideal match between structural state of charge and SoC_{cell}, meaning that each electron is injected in the conduction band of graphite increasing the structural state of charge. If the electron distribution was homogeneous in the electrode thickness, one would expect a homogeneous evolution of structural state of charge (x in Li_xC_6) following the x = y line for each z-position. A gradient of lithiation appears in at least two regions of SoC_{cell} for the two electrode porosities. From 0.25 to 0.5 SoC_{cell} (stage II-L to stage II transition) and from 0.5 to 0.9 SoC_{cell} (stage II to stage I transition), a distribution of the structural state of charge around the x = y straight line is noticed, with z-positions near the separator (0.1 L) passing above the line. Here, because of a heterogeneous distribution of current, a distribution of x in Li_xC_6 is observed along the electrode thickness. Physically, this means that the positions near the separator (0.1 L) are favoured and evolve faster in structural state of charge

than the one near the collector (0.9 L). This is again the visualisation of a limitation coming from the penetration of lithium ions through the electrode microstructure.

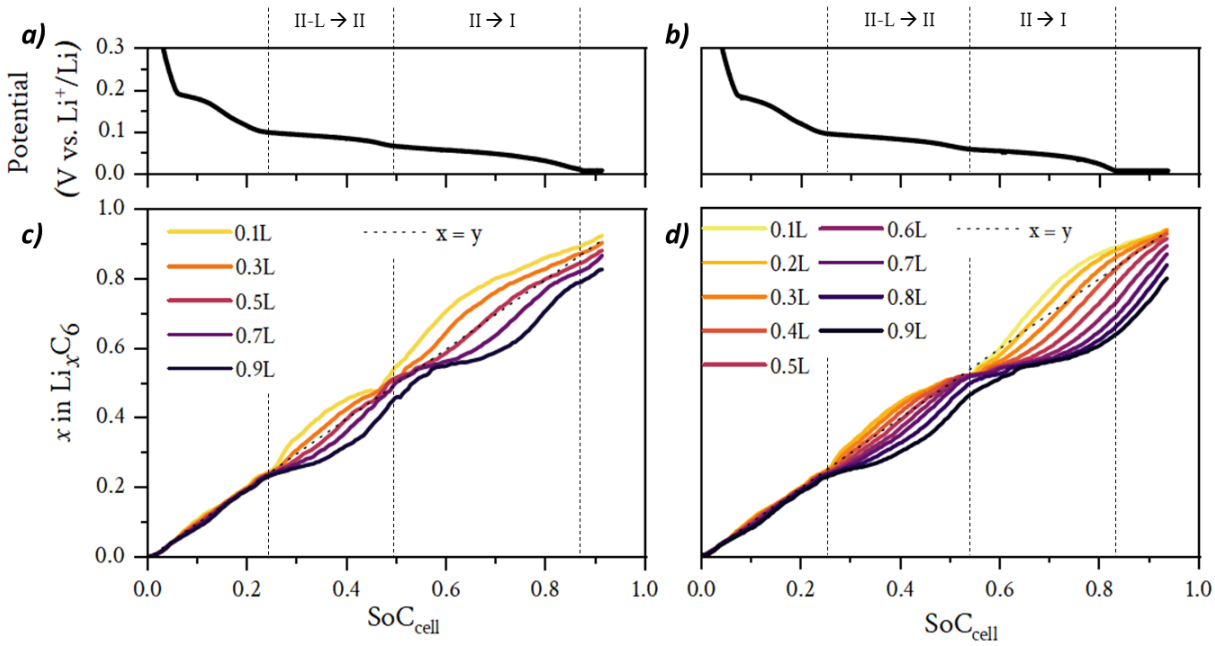


Figure 108: Evolution of structural state of charge (x in Li_xC_6) for both porosities upon lithiation at C/4 rate. a, b) Graphite potential evolution as a function of SoC_{cell}, respectively for 50% and 30% porosity electrodes. c, d) Structural state of charge (x in Li_xC_6) evolution as a function of SoC_{cell}, respectively for 50% and 30% porosity electrodes.

To ensure that there is no artefact in data treatment, another method was employed to determine the graphite state of charge (x in Li_xC_6). The signal of stage II and stage I (or stage I-enriched) peaks was integrated to obtain the number of X-photons scattered by each phase. Similarly to the method using the mass centre determination, the data from the thin graphite electrode were taken as reference to plot the quasi-thermodynamic evolution of the proportion of stage I (or stage I-enriched) phase on the total integral as a function of x in Li_xC_6 (**Figure A6**). The results are plotted in **Figure 109** comparing the mean structural state of charge (mean x_{Li}) obtained through the two methods (method 1: from the mass centre, method 2: from the stage I and stage II integration). In **Figure 109a**, consistency between the two methods is observed on the graphite electrode with 50% porosity. Additionally, a very good agreement is observed between the mean structural state of charge and the x = y straight line, even if a slight deviation is noticed around 0.85 SoC_{cell} which correlates with the holding potential period (CV).

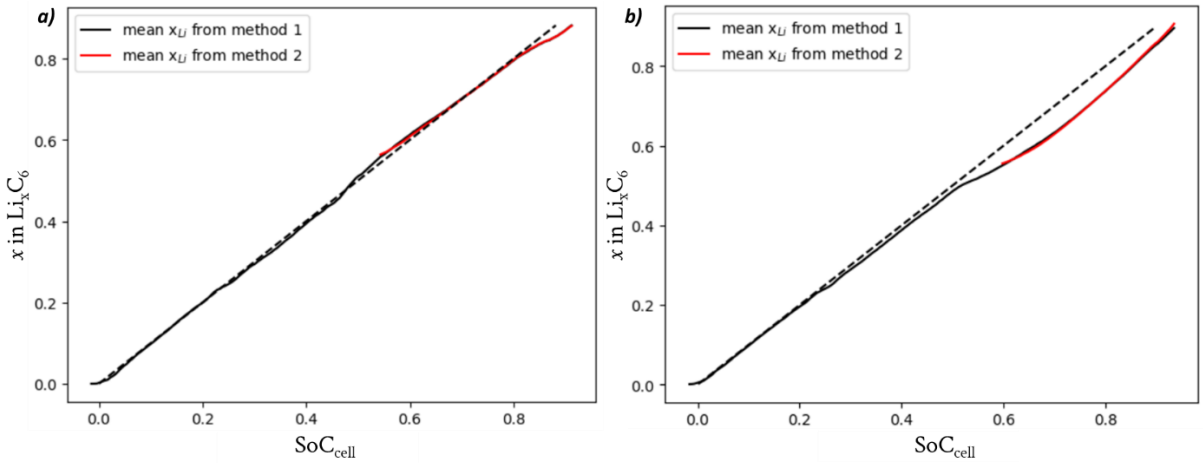


Figure 109: Comparison of the mean structural state of charge (x in Li_xC_6) determined using the mass centre method (method 1) and the integration method (method 2). a) For the 50% porosity electrode cycled at C/4 rate and b) for the 30% porosity electrode cycled at C/4 rate. The dashed line corresponds to x = y.

For the electrode with 30% porosity (**Figure 109b**), a good consistency between both methods is also observed demonstrating that no artefacts are introduced by the mass centre method. A good matching between the mean structural state of charge and the x = y straight line is observed until 0.5 SoC_{cell}, above, a deviation reaching 7% appears with the structural state of charge evolving slower than the electrochemical one. Here are listed hypothesis to explain the deviation observed with the 30% porosity electrode:

- Upon cycling, graphite particles undergo volumetric changes reaching + 14% at the end of lithiation[198], translated into a unidirectional expansion increasing the electrode thickness. As a consequence, the *z*-positions that were probed by the X-ray beam at the beginning of the lithiation are not exactly the same as at the end. Since the electrode thickness expansion is unidirectional and oriented toward the separator, the z-positions probed near the current collector do not significantly change upon lithiation, but near the separator the initially probed graphite particles are not anymore in the field of view as schematised in **Figure 110**. With rough calculation for the electrode porosity of 30%, it was estimated that the 0.1 L position initially localised 5 µm near the separator should be localised at 12 µm from the separator in the end of lithiation (~0.2 L). Therefore, the volume probed at the end of lithiation might be slightly less representative of the mean structural state of charge (x in Li_xC_6). To justify the difference between the two electrode porosities, it is suspected that a large porosity (50%) is more likely to buffer the electrode thickness expansion. Indeed, with a larger fraction of pores, a higher volume is available to accommodate the volume changes, reducing the total thickness expansion upon lithiation.

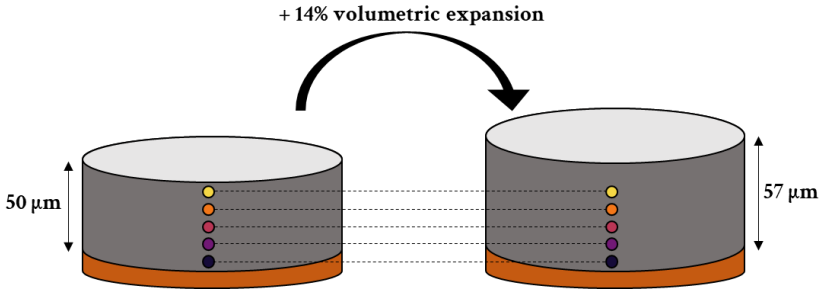


Figure 110: Scheme showing the 30% porosity graphite electrode expansion upon lithiation. The coloured points represent the z-positions probed by the X-ray beam, before and after cycling to show the impact of uniaxial volume changes.

- Another hypothesis relies on the consumption of charges by parasitic reactions such as SEI and/or adsorption. As an example, upon lithiation, because of the volume expansion, new "fresh" surfaces of graphite particles are exposed to the electrolyte and the solvents reduction can proceed. This would imply the consumption of charges without modifying the structural state of charge, which can contribute to the slight deviation observed. However, since it does not correspond to the formation cycle, no significative amount of charges consumed for this SEI formation are expected. This cannot explain solely the observed deviation.

4.2 Heterogeneities of lithiation

Based on the structural state of charge of each *z*-position for the two electrode porosities, a quantitative analysis of the lithiation heterogeneity was realised. As discussed in the state of the art, Gu introduced the concept of Normalised Absolute Average Deviation (NAAD) on Zn/NiOOH cells[220]. This indicator was used to evaluate the distribution of current in the entire electrode. Tardif *et al.* [154] and Dufour *et al.* [221] also used this indicator to quantify the heterogeneity of state of charge along the electrode thickness of graphite electrodes. Inspired by the NAAD, an Absolute Average Deviation (AAD) was used instead, as expressed in Eq. 25.

$$AAD(SoC_{cell}) = \frac{1}{L}\int_{z=0}^{z=L} |x(z) - \langle x \rangle_z| \, dz \qquad \text{Eq. 25}$$

Where L is the electrode thickness, x(z) is the structural state of charge at the corresponding z-position and $\langle x \rangle_z$ *is the mean structural state of charge along the electrode thickness.*

The NAAD parameter has a sensitivity depending on the region of x in Li_xC_6, with a higher sensitivity near x = 0. On the contrary, the AAD parameter expresses the absolute deviation in x in Li_xC_6 with the same sensitivity on the overall lithiation range, bringing the possibility to compare its evolution from x = 0 – 1 quantitatively.

The evolution of the AAD indicator as a function of the SoC_{cell} was first analysed for the electrode with 50% porosity upon lithiation at C/4 cycling rate in **Figure 111b**. The data are correlated to the graphite electrode potential in **Figure 111a**, and on the right y-axis, to the evolution of $d_{SoC}/d_E = f(SoC_{cell})$. Low values of AAD are obtained for the regions 1 and 3 involving the transitions graphite to LiC_{72} (stage I') and LiC_{36} to LiC_{24} (stage IV → stage III), transitions driven by solid solution mechanisms. To contrast, a bell-shaped curve is observed for the AAD parameter in correlation with the peaks observed on the d_{SoC}/d_E representation, with each peak is linked to a (quasi-)potential plateau.

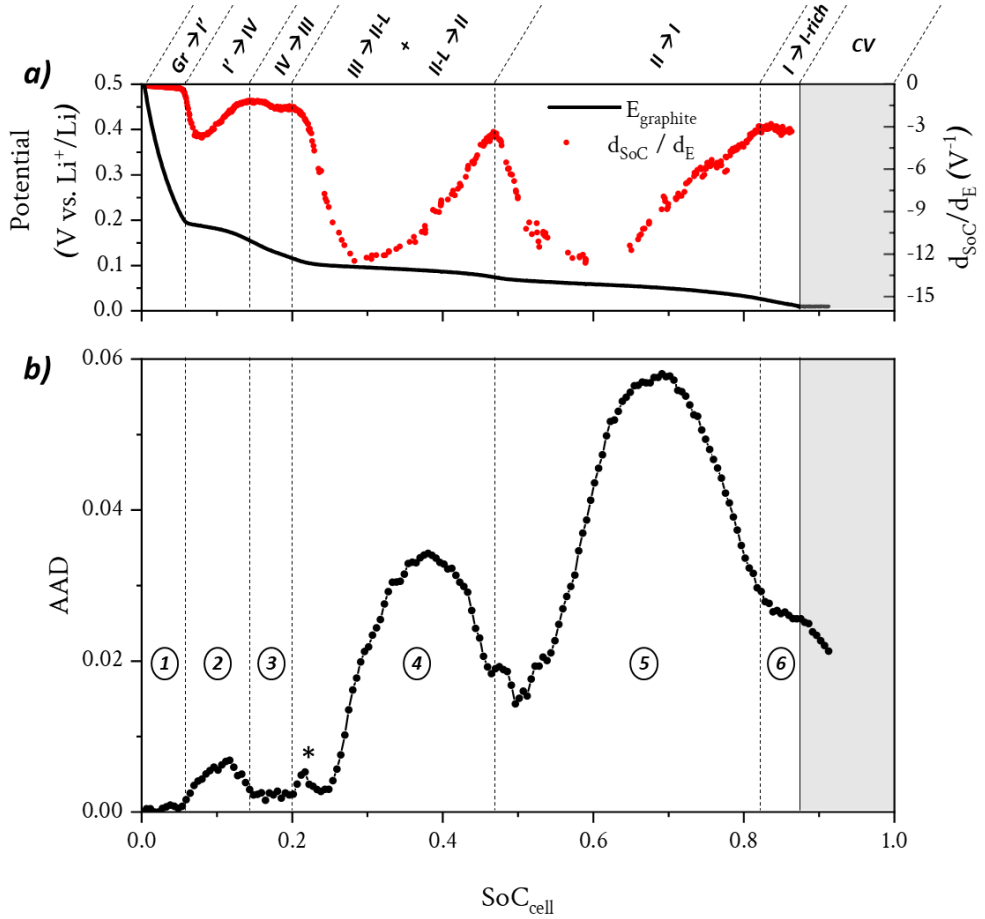


Figure 111: Correlation between the AAD parameter and the electrochemical signature obtained at C/4 rate for the graphite electrode with 50% porosity. a) Evolution of the graphite potential on the left axis and d_{SoC}/d_E on the right axis, as a function of SoC_{cell}. b) Evolution of the AAD parameter as a function of the SoC_{cell}.

The origin of the bell-shaped curve is linked to the nature of lithiation mechanism, the example of region 2 which is associated to the stage I' to stage IV transition is schematised in **Figure 112**:

i) When graphite electrode reaches stage I' (LiC_{72} stoichiometry, **Figure 112a**), no heterogeneity is observed, meaning that graphite enters the first quasi-potential plateau homogeneously in the electrode volume. Because of the rather flat potential evolution during this transition, the chemical potential associated to lithium

intercalation is rather constant and homogeneous along the electrode thickness. Then, the consumption rate of lithium ions is only controlled by the local concentration of salt in the electrolyte, which becomes more and more heterogeneous along the electrode thickness upon discharging, due to the tortuous microstructure. This is responsible for the generation of a salt concentration gradient with depletions in the current collector direction; the consequence is the appearance of heterogeneities of state of charge (increase of the AAD parameter, increasing part of the bell-shaped) with favoured lithiation at the separator/electrode interface.

ii) This biphasic transition ends earlier for graphite particles near the separator side, implying that their chemical potential starts to change by entering in the solid solution domain (**Figure 112b**). The latter acts as an activation barrier energy and limits the intercalation of lithium ions. In these conditions, the rate of lithium ions consumption is not only controlled by the salt concentration but also by the chemical potential that increases the energy barrier for lithium intercalation. It results in a favourable lithiation of the graphite particles that are still in the quasi-potential plateau, *i.e.* near the current collector side, and a homogenisation of structural state of charge (x in Li_xC_6) is observed (decrease of the AAD parameter leading to the decreasing part of the bell-shaped curve).

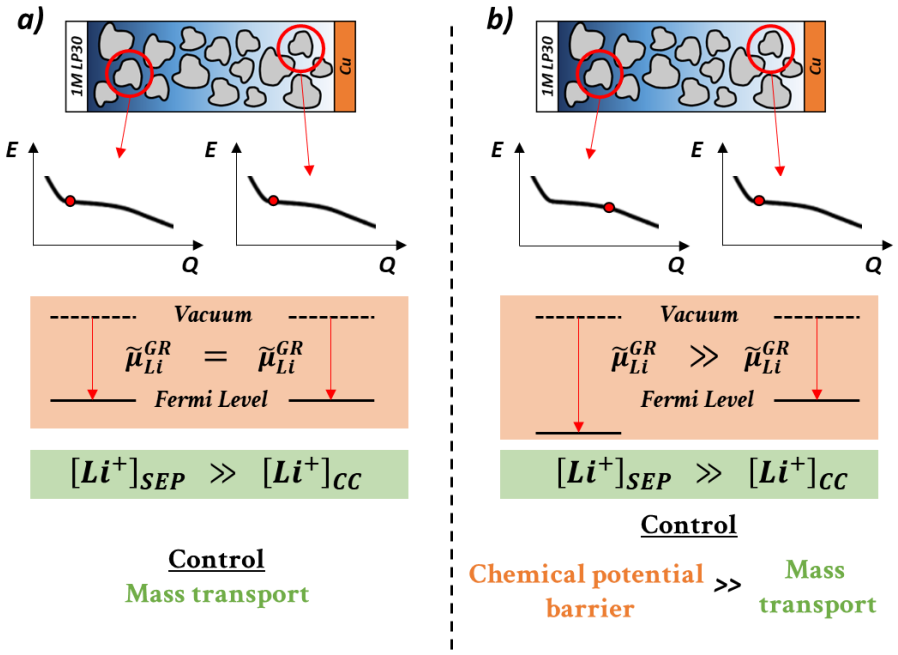


Figure 112: Scheme explaining the AAD bell-shaped evolution. a) Graphite particles display similar lithium chemical potentials ($\tilde{\mu}_{Li}^{GR}$), meaning that the lithiation is favoured near the separator. b) A chemical potential barrier limits the lithiation near the separator, the lithiation becomes favourable near the current collector. $[Li^+]_{sep}$ and $[Li^+]_{cc}$ correspond to the lithium concentration in the electrode porosity near the separator or near the current collector.

Pursuing our investigation with the region 4 (**Figure 111**), a slight increase of dispersion in *x* is visible between 0.2 and 0.25 SoC_{cell} materialised by the asterisk (**Figure 112b**) which can be due to the transition between stage III to stage II-L (LiC_{24} to LiC_{18}) that is partially driven by biphasic mechanism as discussed in chapter 3 and in our paper [222]. Entering the stage II formation at 0.25 SoC_{cell}, a large increase of dispersion in *x* (second largest bell-shaped) is observed. The larger heterogeneity compared to the first bell-shaped (stage IV formation) is related to the higher number of exchanged coulombs on this second potential plateau. At the end of the stage II formation, the dispersion in *x* did not disappear totally, meaning that the re-homogenisation of state of charge was partial, despite the potential drop between the two-last potential plateaus. Therefore, the dispersion in *x* observed in region 5 during the biphasic transition between stage II to stage I (LiC_{12} to ~$Li_{0.9}C_6$) is even more pronounced. Between 0.83 and 0.88 SoC_{cell} (region 6), a rather stable AAD evolution is noticed and correlates with the transition between stage I and the enriched-stage I, materialised by the stable period on the d_{SoC}/d_E representation. This specific feature is like the trend observed for the transitions involving solid solutions (Gr → stage I' and stage IV → stage III, region 1 and 3 respectively), it supports the existence of solid solutions during the enrichment of stage I to form the LiC_6 phase as discussed previously [222].

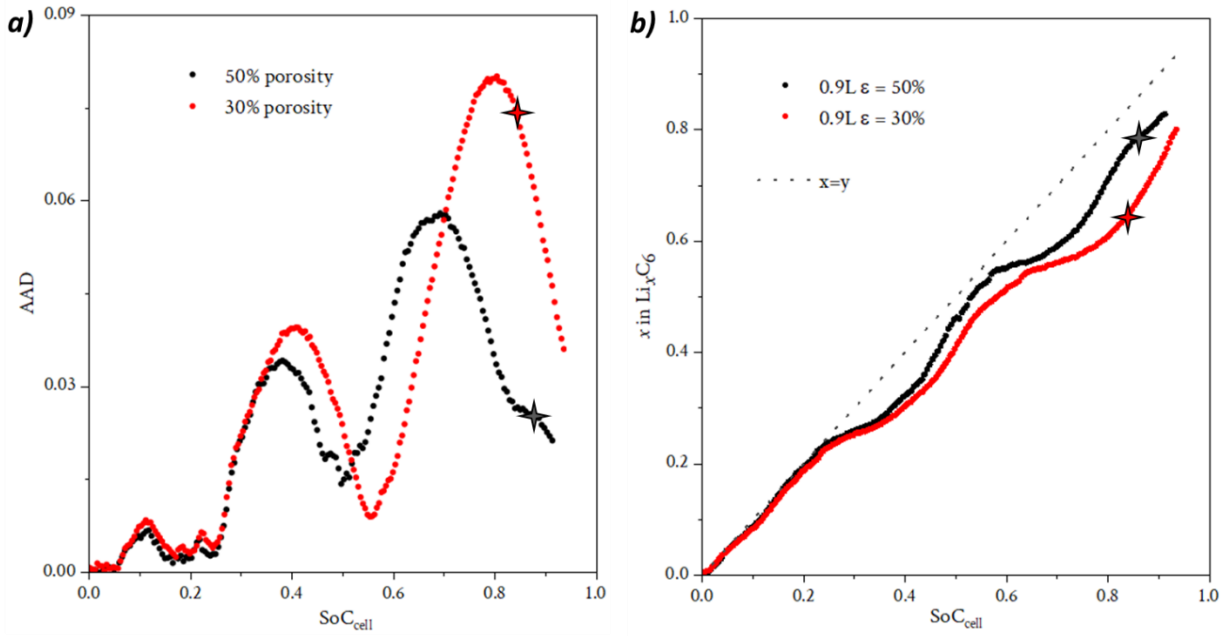


Figure 113: Comparison of the lithiation heterogeneity for the 50% and 30% electrode porosity. a) Evolution of the AAD parameter as a function of the SoC_{cell} for both porosities. b) Evolution of the structural state of charge at 0.9 L for the two electrode porosities depending on the SoC_{cell}. The red and black stars represent the switch between CC and CV periods.

The impact of the porosity on the AAD parameter can be seen in **Figure 113a**. A similar evolution is noticed until 0.25 SoC_{cell} meaning that the distribution in *x* is similar in both cases, whatever the electrode microstructure. On the contrary, a larger heterogeneity in *x* is observed for the

second bell-shaped (associated to stage II formation) with the porosity of 30%. The latter is highlighted in **Figure 113b** where the structural state of charge near the current collector side (0.9 L) is plotted for both porosities. Starting from 0.25 SoC_{cell}, the 0.9 L position for 30% porosity is more delayed in terms of structural state of charge evolution (below the x=y line). This is directly linked to the so-called penetration depth that is lower for this electrode porosity (higher tortuosity) meaning that the kinetics of lithiation at an equivalent relative depth (0.9 L) is lower. Pursuing with the last bell-shaped, the dispersion in x is even larger for 30% porosity. Additionally, at the end of the galvanostatic part (materialised by a star on both AAD curves), the electrode with 30% porosity is way more heterogeneous in structural state of charge along its thickness, demonstrating the limitation for power applications.

4.3 Cycling rate and current distribution

The rate capability measurement for the 50% porosity graphite electrode at C/4, C/2 and C/1 is discussed in **Figure 114a**. For very low SoC_{cell}, a similar AAD is observed which is consistent with a cell that is not limited by any transport phenomena. However, pursuing the lithiation, larger heterogeneities are observed by increasing the cycling rate, with higher AAD values at the maxima of the bell-shapes. Additionally, in the regions where the structural state is re-homogenised (such as at SoC_{cell} = 0.5), one can notice the higher AAD values by increasing the C-rate, which reflects the difficulty to homogenise the lithium content along the electrode thickness. The increase in the AAD parameter as a function of the rate is larger for the second bell-shaped (materialised by the black arrow) than the last one (materialised by the red arrow), meaning that the graphite electrode power ability seems to be more C-rate dependent from 0.25 – 0.6 SoC_{cell} than above. The evolution of x in Li_xC_6 at the 0.9 L position (near the current collector) is shown in **Figure 114b** as a function of the applied C-rate. By increasing the cycling rate, the structural state of charge is more and more delayed by deviating from the straight line in the region 0.25 – 0.6 cell SoC_{cell} (this is true for C/4 and C/2 rates that are in CC mode, whereas at C/1 rate the cell entered the CV mode at ~0.55 SoC_{cell}). Surprisingly, when the structural state of charge is above x = 0.55 (near the potential step between stage II formation and stage I formation), no additional delay is observed by increasing the C-rate. This highlights the lower dependence to C-rate increase in this region of SoC_{cell} (x > 0.55). For the electrode with 30% porosity, the data are given in **Figure A7** and a very similar behaviour was observed as for the electrode with 50% porosity.

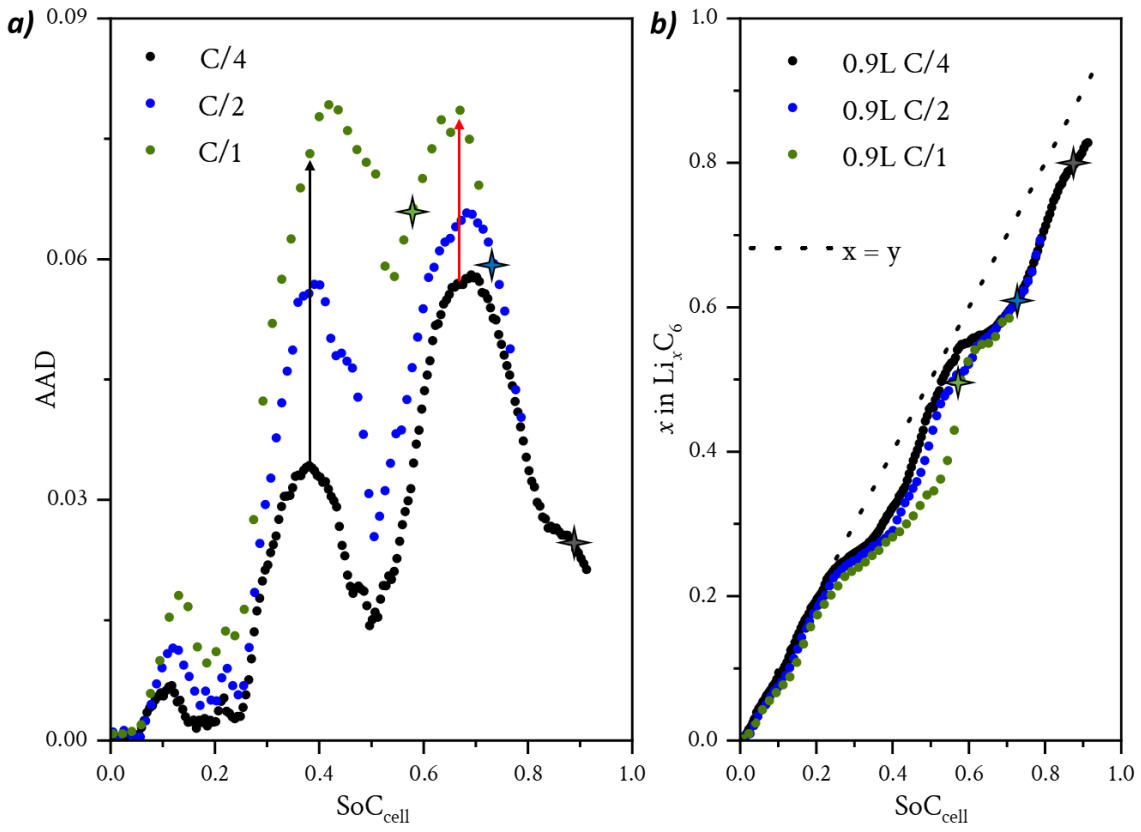


Figure 114: Evolution of structural state of charge dispersion for 50% porosity graphite electrode at different cycling rates. a) Evolution of the AAD parameter as a function of SoC$_{cell}$ for different cycling rates. b) Structural state of charge evolution as a function of the SoC$_{cell}$ at the 0.9 L position (near the current collector) for different cycling rates. The black, blue and green stars represent the switch between CC and CV periods.

The comparison between 50% and 30% porosity demonstrated the detrimental impact of the high ionic tortuosity in the through-plane direction of graphite electrodes with flakes particle-shape, despite having almost 100% of interconnected porosity, meaning no problem of wetting in the electrode depth. The limited penetration depth of lithium ions through the electrode microstructure during fast lithiation probably generates depletions of salt concentration which implies a current distribution that should be heterogeneous along the electrode thickness, consequently.

In electrochemical cells, a real challenge is the determination of current distribution that would provide direct information on the kinetic of reactions in the electrode volume. In practice, this could be achieved using micro-reference electrodes inserted along the electrode thickness by micro-indentation. However, this approach is so difficult that no publication was found. Instead, the current distribution is inferred from structural and morphological observations such as in this reference[223] or computed based on simulations[224]. Here, the current distribution was inferred based on the evolution of structural state of charge. By plotting the differential evolution of x in Li_xC_6 as a function of the electrochemical SoC$_{cell}$ for each z-position (**Figure 108c, d**), the equivalent local

current of lithiation (effective C-rate) along the electrode thickness was determined. However, this is an estimation of the local current only responsible for lithium intercalation, and does not consider eventual secondary reactions such as SEI formation or adsorption phenomenon. In **Figure 115b**, the distribution of effective C-rate along the electrode depth is given for the electrode with 30% porosity and correlated to the electrochemical signature (**Figure 115a**) obtained upon lithiation at C/4. During the first quasi-potential plateau (0.08 SoC_{cell}), a higher effective C-rate is observed near the separator (0.1 L) with a decrease toward the current collector (0.9 L). Overall, an exchange of current distribution along the whole lithiation is observed, with sometimes higher local C-rates near the separator or the reverse situation at other SoC_{cell}.

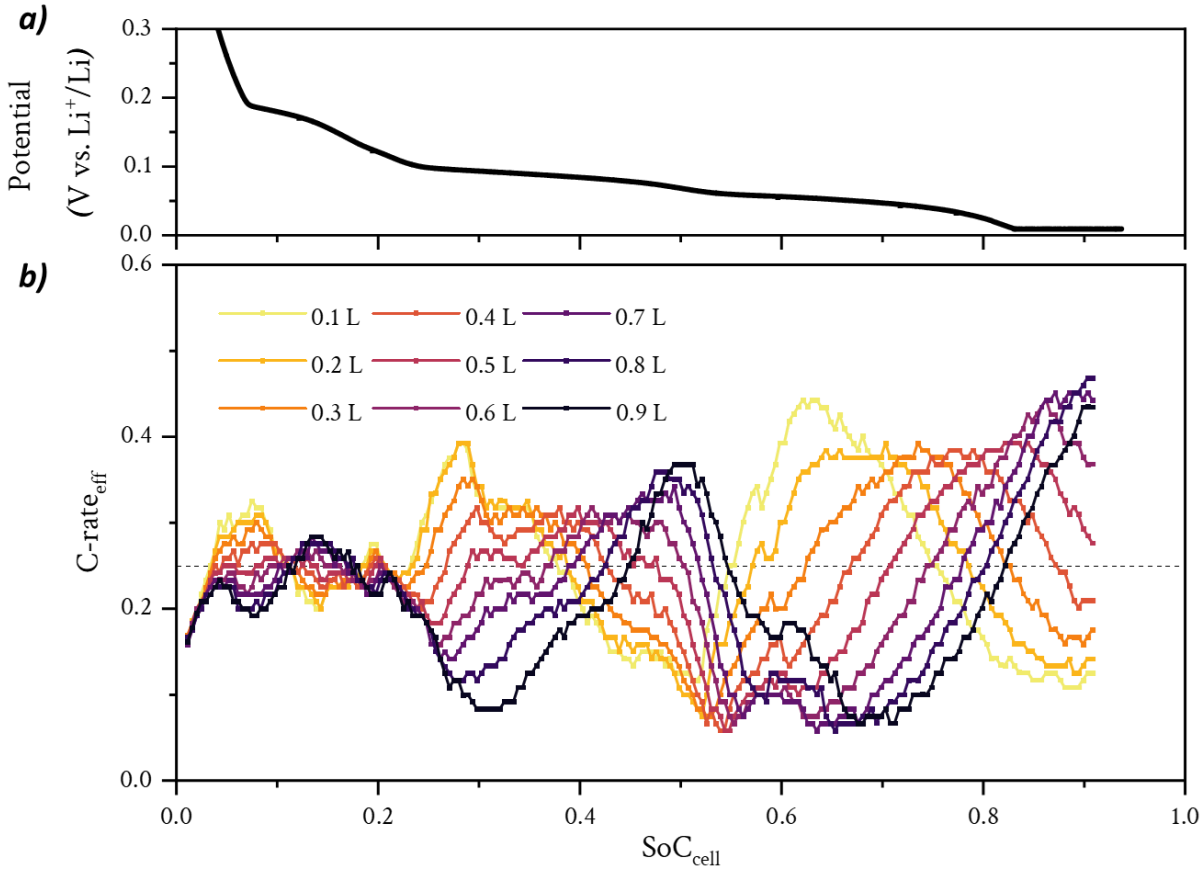


Figure 115: Distribution of effective C-rate along the 30% porosity graphite electrode thickness for the lithiation obtained at C/4. a) Evolution of the graphite potential as a function of SoC_{cell}. b) Evolution of the effective C-rate in the electrode depth as a function of the SoC_{cell}. The dashed line corresponds to the applied C-rate of C/4.

To better visualise this current distribution, the effectives C-rates for the positions near the separator (0.1 L) and the current collector (0.9 L) are compared in **Figure 116** for the different applied C-rates. Looking at **Figure 116a** around 0.1 SoC_{cell}, the 0.1 L position is in higher-regime of lithiation exceeding the applied C-rate (0.25, C/4) while the 0.9 L position displays a lower-regime of lithiation. This situation with higher local current near the separator is materialised by the black arrows at three regions, correlating with the three main quasi-potential plateaus. For

the 0.9 L position, the local effective current also reach important values but slightly lower with a large delay compared to the 0.1 L position. It seems that these two extreme positions (nearest from separator and collector) display the highest local effective current compared to intermediate positions as observed in **Figure 115b**. This is due to the lowest time of lithium replenishment for the 0.1 L position, providing high current densities when the electrode is on a quasi-plateau of potential. Regarding the 0.9 L position, this is probably because the position is the latest to insert lithium, and when other positions are in quasi-stationary regime, the latter receives high current densities. The maximal effective C-rate reached is around two times higher than the applied C-rate, regardless of the cycling rate. The same trend was observed for the graphite electrode with 50% porosity, with similar maximal effective C-rates given in **Figure A8**.

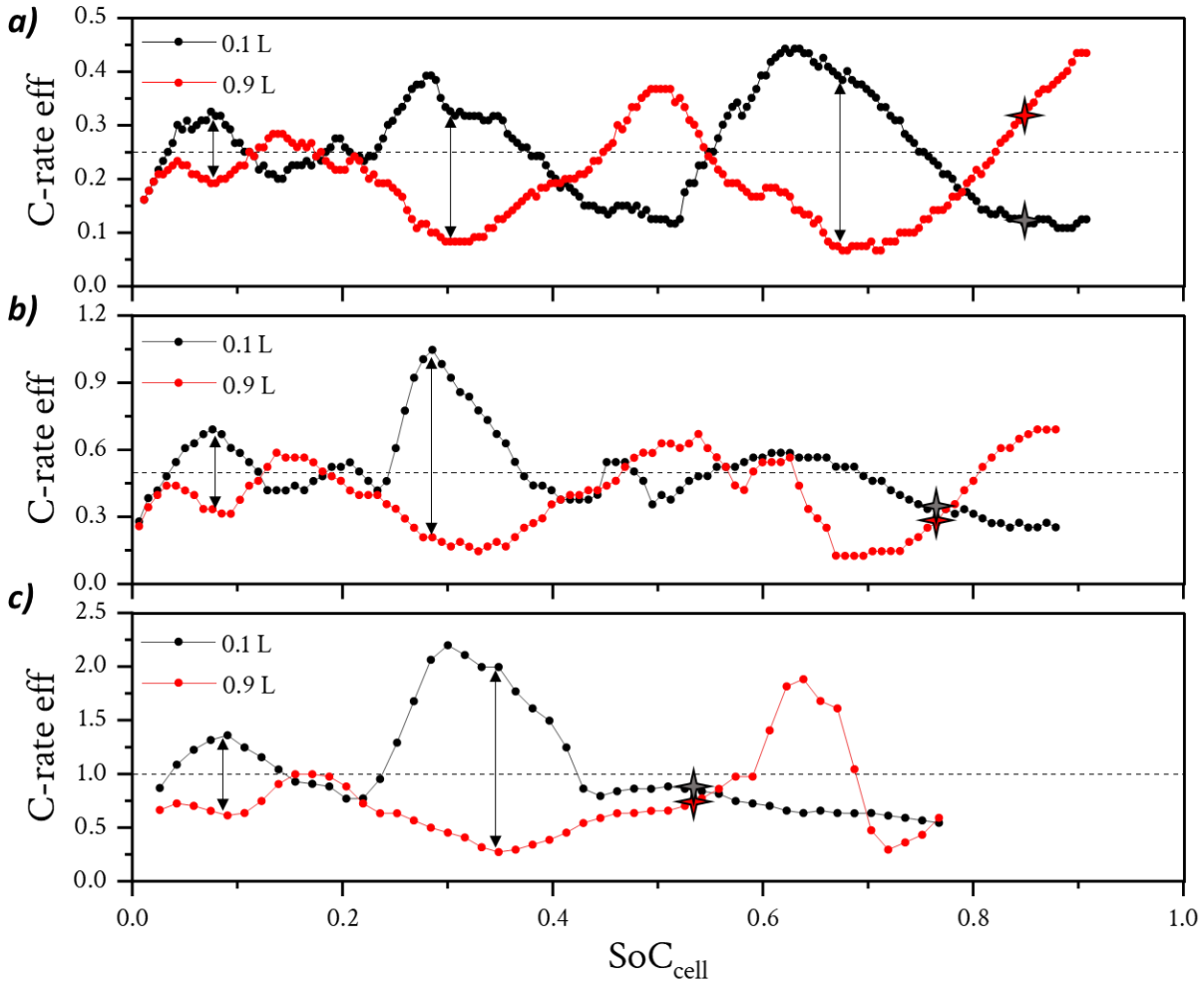


Figure 116: Evolution of effective C-rates as a function of SoC_{cell} at the positions 0.1 L and 0.9 L for the graphite electrode with 30% porosity. a) Cycling rate of C/4, the dashed line at 0.25 corresponds to the applied C-rate at the cell level. b) Cycling rate of C/2. c) Cycling rate of C/1. The double arrows highlight the regions where current is distributed in priority near the separator/electrode interface. The switch between CC and CV periods are illustrated by the red and black stars.

With these evolutions of current distribution, the mean effective C-rate "received" by each position in the electrode depth was estimated for the whole cell lithiation. This metric relates to the average current passed through the graphite particles and was normalised with the applied C-rate (C/4, C/2 and C/1) in **Figure 117**.

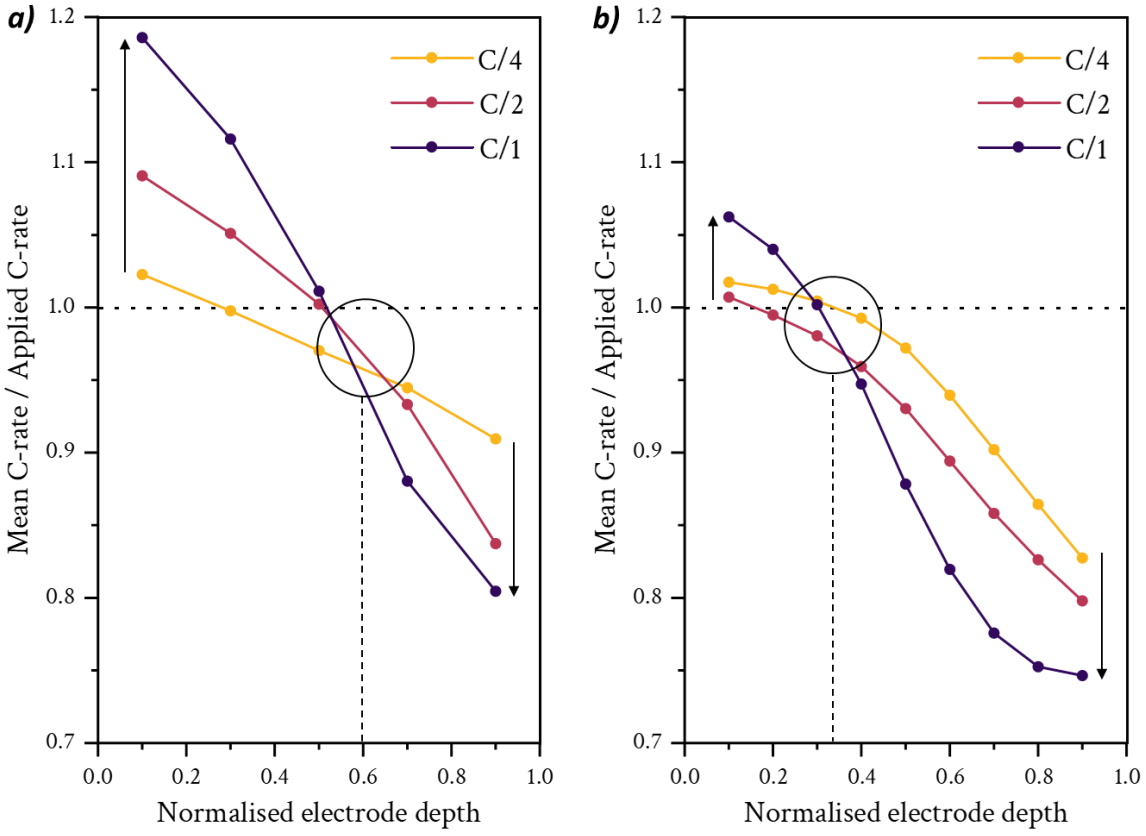


Figure 117: Mean effective C-rate normalised by the applied C-rate as a function of the electrode depth, for C/4, C/2 and C/1 cycling rates. during the CC periods a) Graphite electrode with 50% porosity. b) Graphite electrode with 30% porosity. Separator/electrode interface = 0 and electrode/current collector = 1.

With this C-rate factor (mean C-rate/applied C-rate), a value > 1 means an average current of lithiation that was higher than the one applied at the cell level, whereas a value < 1 corresponds to an average under-regime of lithiation. For the electrode with 50% porosity (**Figure 117a**), several features are observed:

i) C-rate factors are decreasing with the penetration in the electrode depth, for each applied C-rate. This is the image of lower kinetics of lithiation because of decreased salt concentration towards the current collector/electrode interface.

ii) By increasing the cycling rate, the C-rate factors are accentuated (materialised by the arrow) near the separator (0.1 L) reaching almost 1.2 (120% of the applied current in average), whereas the former are decreased near the current collector (0.9 L) until 0.8 (80% of the applied current). This is the sign of more heterogeneous distribution of

current along the electrode thickness when increasing the cycling rate, most probably due to higher depletions of salt towards the current collector.

iii) An invariable point is observed with similar C-rate factor regardless of the applied C-rate at the cell level. This point is localised around ~0.6 L with a C-rate factor almost equivalent to 1. At this electrode depth, the average current of lithiation is almost equivalent to the applied current, and does not vary with the increase of cycling rate.

Regarding the electrode with 30% porosity (**Figure 117b**), an increase of C-rate factors is observed by increasing the cycling rate near the separator, but to a lower extent by reaching ~105% of the applied C-rate. On the other side, an accentuated decrease was observed near the collector reaching less than 75% of the applied current. This has to be linked with the penetration depth concept discussed in the state of the art (p**29**), that is lower for higher ionic tortuosity. Indeed, the electrode with 30% porosity displays a lower penetration depth, inducing lower local current near the collector. Similarly, an invariant point is observed at the electrode depth of ~0.3 L with an average lithiation current equivalent to the applied C-rate. This peculiar position is nearer from the separator for the electrode of 30% porosity (~14 µm, 0.3 L) than for the 50% porosity (~48 µm, 0.6 L), and this is again the proof of a penetration depth that is lower for the electrode with 30% porosity.

To conclude, these local current distributions through the electrode thicknesses raise important questions about cell ageing. Higher degradation processes near the separator /electrode interface are expected for at least two reasons: i) graphite particles systematically reach higher lithium content and then undergo higher volumetric changes that can be detrimental on long term cycling; ii) higher effective C-rate of lithiation are observed near the separator, that probably can increase the local temperature and degrade the electrolyte and/or the SEI.

5 CONCLUSION – CHAPTER 4

Throughout this chapter, the engineering of thick graphite electrodes was investigated to understand the origin of their power limitation. First, electrochemical characterisations were performed on thick graphite electrodes of 50% and 30% porosities. By varying the electrolyte concentration, a better rate capability was observed for the electrode of 50% with the higher salt concentration. Morphological characterisations were performed using SEM and X-ray holotomography to investigate the impact of the electrode calendering on the electrode's microstructures. The results revealed more tortuous pathways of lithium diffusion in the electrolyte for the electrode of 30% porosity, results in agreement with electrochemical impedance measurements.

To quantify the limitation by the ionic transport, X-ray diffraction *z*-profiling experiments were performed on the two electrode porosities. Using the methodology presented in the chapter 3, the evolution of the structural state of charge of graphite in the electrode's depth was estimated upon cycling. Gradients of lithiation were observed from the separator toward the current collector, corroborating the limitation by the ionic transport. Quantitative analyses were performed to measure the lithiation gradient intensity. Using the AAD indicator, greater dispersion of state of charge were observed for the porosity of 30%, corroborating the higher ionic tortuosity measured.

The local current distribution in the electrode thicknesses was inferred from the kinetic of structural evolution. The results highlight higher effective C-rate of lithiation near the separator, reaching two-times the applied current. These observations raised serious questions about inhomogeneous ageing along the electrode thickness.

CHAPTER V

MECHANICAL ASPECTS OF GRAPHITE LITHIATION

In this fifth chapter, the discussions will focus on the mechanical aspects of the dis/charging of graphite half-cells. A first important aspect is the electrode dilatation upon cycling, measured thanks to a dilatometric apparatus. The goal is to monitor the evolution of electrode thickness upon de/lithiation and correlate it to mechanical evolutions at the material level. Then, a more realistic condition was applied with the cycling of a commercial full cell composed of graphite and NMC. Through this study, the electrochemical behaviour of the cell will be correlated to the structural evolution of both electrode materials (measured *via operando* XRD) upon cycling as well as the response to ultrasound stimuli. A part of the results from this chapter is extracted from:

- Exploring Electrochemical Dynamics in Graphite || $LiNi_{0.8}Mn_{0.1}Co_{0.1}O_2$ Cells *via* Operando Ultrasound and Multiprobe Approaches, C. Renais, B. Mercier-Guyon, D. Wasylowski, M. Sonnet, P. Dechent, M. Servajon, N. Blanc, S. Lyonnard, D. Uwe Sauer and C. Villevieille, *Nature Communications*, 2025, 16, 7774[225]

Lithium insertion induces volumetric changes at crystal lattice scale that can play a key role in the power capability of electroactive material in particular graphite. This chapter is dedicated to the investigation of the mechanical aspect of graphite's electrode upon cycling, at the material level and at the electrode level. A brief state of the art is presented, focusing on dilatation measurements and the use of ultrasound in LiBs.

1 STATE OF THE ART

Upon lithiation, the graphite particles undergo an increase of the inter-layer spacing, resulting in an expansion of the *c*-axis and an almost unidirectional volume increase of the crystal lattice. This behaviour can be seen by XRD experiment by following the evolution of the (002) Bragg reflections. Schweidler *et al.* reported the total volume change of the graphite unit cell upon lithiation in **Figure 118**[198] reaching ca. 14%. The unit cell expansion follows the staging processes, with a non-monotonic expansion. As an example, a small volume increase is noticed from 0.25 to 0.6 *x*, correlating with the stage II-L to stage II transition, that does not involve a modification of the through-plane organisation of lithium, whereas an important increase is observed for the last transition (stage II to stage I, from 0.6 to 0.9 *x*). Interestingly, a change in slope is observed around ~0.9 *x*, which correlates with the last solid solution leading to the enrichment of stage I ($Li_{0.9}C_6$) to the LiC_6 phase as discussed in p**101**.

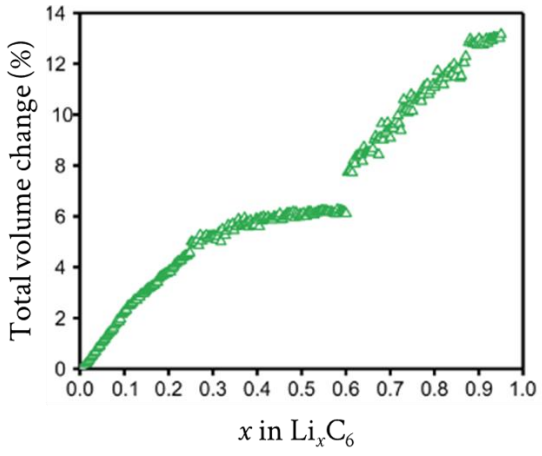


Figure 118: Total volume change of the graphite unit cell upon lithiation. Reprinted with permission from ref.[198].

This volume expansion is important to consider since a particle expansion will translate into an expansion of the electrode and results in changes of the microstructure upon charge and discharge. As demonstrated by Qi and Harris[226], the graphite particle expansion induces a deformation at the electrode level that significantly modifies the electrode porosity upon cycling*. The authors estimated that the particle expansion could reduce the electrode porosity by 15-25%. Knowing that

* In this study, deformation-strain maps were obtained by *in situ* optical measurement in coin-cells equipped with a quartz window.

the porosity reduction can induce a drastic increase of tortuosity, this effect could impact the power capability of graphite electrodes upon cycling.

A lot of studies tried to assess the mechanical properties of graphite electrodes, especially using dilatometric measurements. Hahn *et al.* investigated the lithiation of a graphite electrode in half-cell using a home-made dilatometer[227]. The obtained results agreed with the qualitative expansion of the graphite unit cell, however an expansion of 4 – 6% from the initial electrode thickness was obtained for SFG 6L and SFG 44 graphite particles. This difference with the theoretical unit cell expansion of 14% is attributed to the electrode porosity. The authors also highlighted a significative increase of electrode thickness upon SEI formation. Similarly, Michael *et al.* investigated the irreversible dilatation of a graphite electrode by *in situ* electrochemical dilatometry[228]. Their results highlighted an irreversible graphite electrode dilatation that did not return to its initial thickness upon successive charge and discharge cycles, due to electrode delamination and changes in the microstructure (corroborated by X-ray computed tomography measurements).

Probing the mechanical features of LiBs electrodes is a real challenge that is usually done in peculiar electrochemical cells, such as with a dilatometer. But most of the time, side effects of these systems can question the obtained results and their applicability in conventional and commercial cells. Thus, the use of characterising tools that can probe the LiBs in operation in their respective cell format is necessary. Ultrasound is a promising technology that is used in many fields, such as in medical[229] and nuclear[230] industries, thanks to their low cost, high technology readiness level (TRL) and non-invasiveness. Thus, researchers have used ultrasound techniques to probe the batteries upon cycling to estimate their state of charge and state of health. Robinson *et al.* probed a commercial full cell graphite/$LiCoO_2$ and highlighted a relationship between the acoustic intensity and the density of materials that change upon de/lithiation[231]. Especially, through the analysis of ultrasound time of flight (ToF), the authors demonstrated that the current collector tab inhibited the electrode dilatation upon charging. Similarly, Liu *et al.* probed a LFP/graphite cell[232]. Using ToF measurement, the authors demonstrated a high dependence of the signal evolution with the Young's modulus of materials, that evolves upon cycling. It was concluded that the graphite electrode dominated the ultrasound ToF evolution. In addition to studies trying to develop a methodology for the SoC determination using ultrasound[233], some studies such as one of Bommier *et al.* demonstrated the interest of ToF measurement to probe lithium plating on graphite electrode[234]. By correlating XRD characterisation with *operando* probing of an LCO/graphite cell, the authors successfully highlighted lithium plating induced by a fast charging rate.

2 GRAPHITE ELECTRODE DILATOMETRY

The volume variations of graphite electrodes upon cycling were assessed using a nano-dilatometer from EL-CELL® (see the methodology in p**79**). With this equipment, the changes in electrode height are monitor, and only a unidirectional evolution of the electrode dilatation is accessible. Graphite is the ideal material to probe since most of the volume variations are directed along the electrode thickness. This is due to i) a de/lithiation that induces changes in the *c*-axis at the lattice scale, and ii) because the graphite particles are mainly oriented parallel to the current collector plane. As a result, the graphite particles expansion/contraction mostly induce an increase or decrease of the electrode thickness, but almost no change in the electrode plane. The measurement of the electrode height can then be correlated to the structural changes at the lattice scale (assessed by XRD), giving assess to the volume change of the lattice, and the one at the electrode level as illustrated in **Figure 119**. However, the link between the changes at the lattice scale and at the electrode level is not straight-forward and highly depends on the electrode microstructure. At least two effects should be considered, the electrode porosity that can accommodate the graphite particles dilatations, and the binder that can buffer the volume expansion by stretching. In the end, a part of the particle's expansion should be accommodated at the electrode scale, depending on the porosity, the binder elastic properties and its weight fraction in the composite electrode.

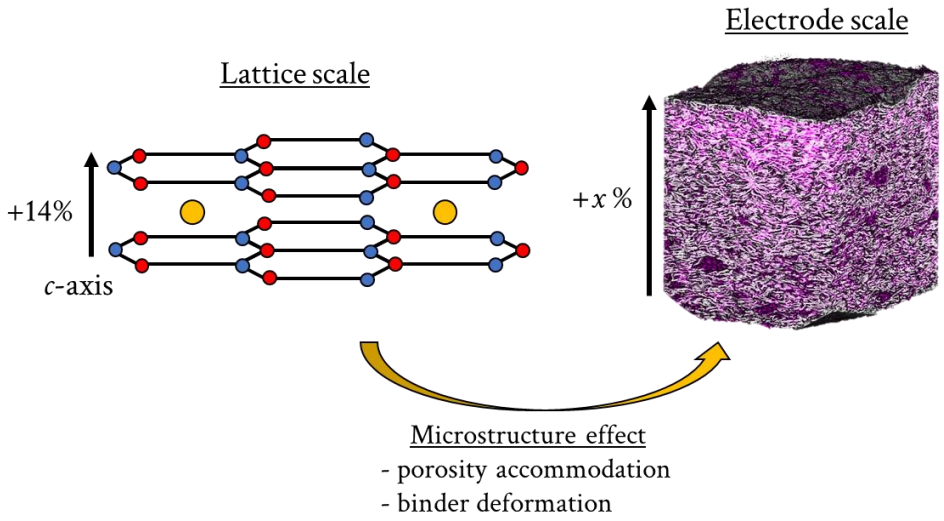


Figure 119: Illustration of the link between dilatation at the lattice scale of graphite and at the electrode level.

A graphite electrode of 70% porosity and 6 mg.cm^{-2} was probed at a cycling rate of C/40 to reduce as much as possible the resistance link to the T-frit separator. The initial electrode thickness was ~130 µm and the changes in electrode height (initialised at zero) upon cycling are given in **Figure 120**. The evolution of the graphite electrode potential is plotted on the left axis, and the formation cycle (first lithiation) can be recognised due to a potential feature at ~0.8 V, ascribe to the SEI formation. The changes in electrode height upon each lithiation and delithiation are given in

Table 12. For the first cycle, an irreversible electrode height change is observed with 10.2 µm of expansion upon lithiation and 3.5 µm of shrinkage in delithiation, corresponding to 8% of relative expansion and 2.7% of relative shrinkage. For the second and third cycles, an irreversible electrode thickness change is observed but to a lesser extent and seems to be stable.

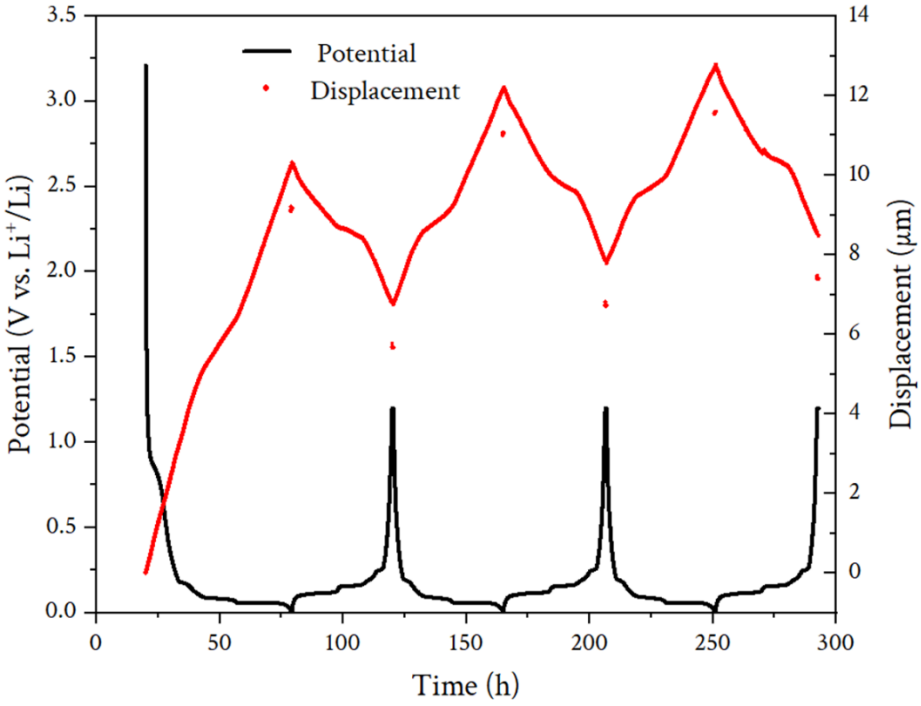


Figure 120: Dilatometric measurement of a graphite electrode with 70% porosity, cycled with LP30 as electrolyte at 25°C and C/40 rate.

Table 12: Graphite electrode expansion and shrinkage upon lithiation and delithiation for the first three cycles.

Cycle	Expansion in lithiation (µm)	Shrinkage in delithiation (µm)	Hysteresis (µm)
1st	10.2	3.5	6.7
2nd	5.3	4.4	0.9
3rd	4.9	4.2	0.7

The main difference between the first cycle and the following is probably due to the SEI formation and an irreversible deformation of the binder that significantly irreversibly increases the electrode height. This irreversible increase is highlighted with a comparison between the first lithiation and the mean behaviour of the 2nd and 3rd cycle. The first lithiation is given in **Figure 121**, with the evolution of the graphite electrode potential and the dQ/dE representation* (**Figure 121a**) correlated to the absolute electrode dilatation (**Figure 121b**). The plot is divided in height regions, each of them corresponding to a phase transition. The regions 0 and 1 contain the graphite to

* In this chapter, the dQ/dE representation is used instead of the $dSoC/dE$ as presented in the previous chapters. This choice is made to ensure the uniformity of this chapter with the graphite | NMC cell investigation.

stage I' transition and the SEI formation, the electrolyte decomposition is visible on the potential profile with a large feature around 0.8 V, and a corresponding peak in the d_Q/d_E representation. The dilatation profile was analysed with linear regressions to obtain the slope in each region expressed in µm.(mAh.g^{-1})$^{-1}$. From region 0 to region 4, a gradual decrease of the slope is observed, meaning that the dilatation rate slows down. To rationalise this evolution, the theoretical rate of expansion is estimated from the reference[198] and the values are given in **Table 13**. Theoretically, a similar evolution is noticed with a gradual decrease of dilatation rate until the stage II-L.

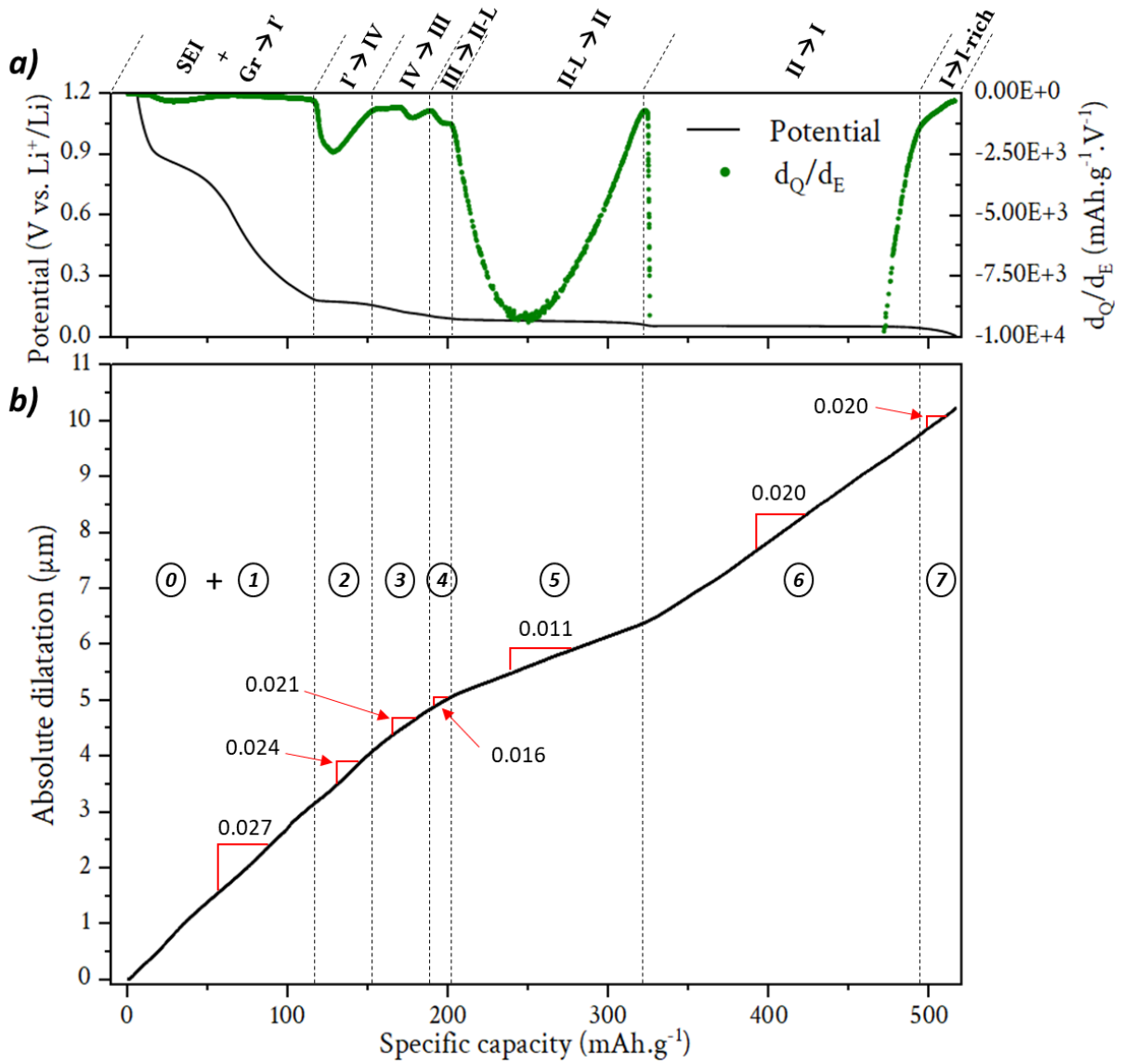


Figure 121: First lithiation of a 70% porosity graphite electrode. a) Graphite electrode potential on the left axis, and the d_Q/d_E representation on the right axis. b) Absolute electrode dilatation initialised at zero (130 µm of initial thickness).

Table 13: Dilatation rates from the graphite unit cell and from the dilatometric measurement in lithiation.

Transition	Gr → I' (1)	I' → IV (2)	IV → III (3)	III → II-L (4)	II-L → II (5)	II → I (6)	I → I-rich (7)
Theoretical dilatation* [μm.(mAh.g^{-1})$^{-1}$]	0.073	0.050	0.027		0.010	0.057	0.015
1st lithiation [μm.(mAh.g^{-1})$^{-1}$]	0.027	0.024	0.021	0.016	0.011	0.020	0.020
2nd/3rd lithiation [μm.(mAh.g^{-1})$^{-1}$]	0.018/0.015	0.021	0.014	0.009	0.005	0.016	0.017

For the region 5 (experimental data), the lowest rate of dilatation is observed and correlate with the lowest theoretical dilatation rate. During this transition, the stage II-L is already filled by lithium each two layer of graphene (LiC_{12} through-plane stoichiometry) as in the stage II. Then, almost no change in interlayer spacing results from this, justifying the lowest dilatation rate. For the regions 6 and 7, a similar slope is observed experimentally whereas a lower dilatation rate should be observed for the last transition (stage I → stage I-rich) in theory. This difference can originate from a low refinement quality for the last phase transition in the reference[198] used for the theoretical evolution.

The second and third lithiations of the cell were also analysed in terms of dilatation rate, the values are given in **Table 13** and the dilatation profiles are plotted in **Figure 122**. In region 1 (graphite to stage I' transition), a slight difference of dilatation rate is observed with a higher expansion for the second lithiation (compared to the third one). Except in this region, the dilatation rates are very similar in all the regions for the second and third lithiations. By comparing the mean values of dilatation rate in the second and third lithiation with the first lithiation (SEI formation), a larger expansion rate is systematically observed for the first cycle (**Table 13**). The latter demonstrates that the SEI is not only formed at 0.8 V vs. Li^+/Li (region 1), but along the whole potential range, and/or the irreversible deformation of the binder occurs along the whole lithiation. This observation is also corroborated by the estimation of specific capacity attributed to each phase transition for the first and second/third lithiations, given in **Table A1**. For most of the phase transitions (except in region 4 and 7), higher specific capacities are obtained during the first lithiation, demonstrating an irreversible capacity that is consumed on the whole lithiation.

The dilatation profile of the second/third lithiation were also compared to the theoretical expansion of the unit cell of graphite in **Figure 122** (black dotes). The theoretical profile was

* The theoretical dilatation was estimated with the total volume change (%) of the graphite unit cell in lithiation given in reference[198] and the absolute dilatation was calculated based on an initial electrode thickness of 130 μm.

normalised with a specific capacity of 385 mAh.g^{-1} (approximately the one obtained for the second and third lithiation) and a good agreement of dilatation profiles was obtained by multiplying the theoretical dilatation rate by a factor of 0.25. This suggests that only ¼ of the particle's dilatation (at the unit cell level) is transferred at the electrode level in terms of expansion. In other words, 75% of the particle's dilatation is buffered and accommodated by the electrode porosity and the binder deformation. Concerning the electrode porosity, the expansion of the graphite particles probably "expulses" the liquid electrolyte outside of the electrodes sandwich, and it probably induces an increase of the internal pressure. This very high accommodation level is probably linked to the high electrode porosity (70%), and the binder effect is probably low in comparison.

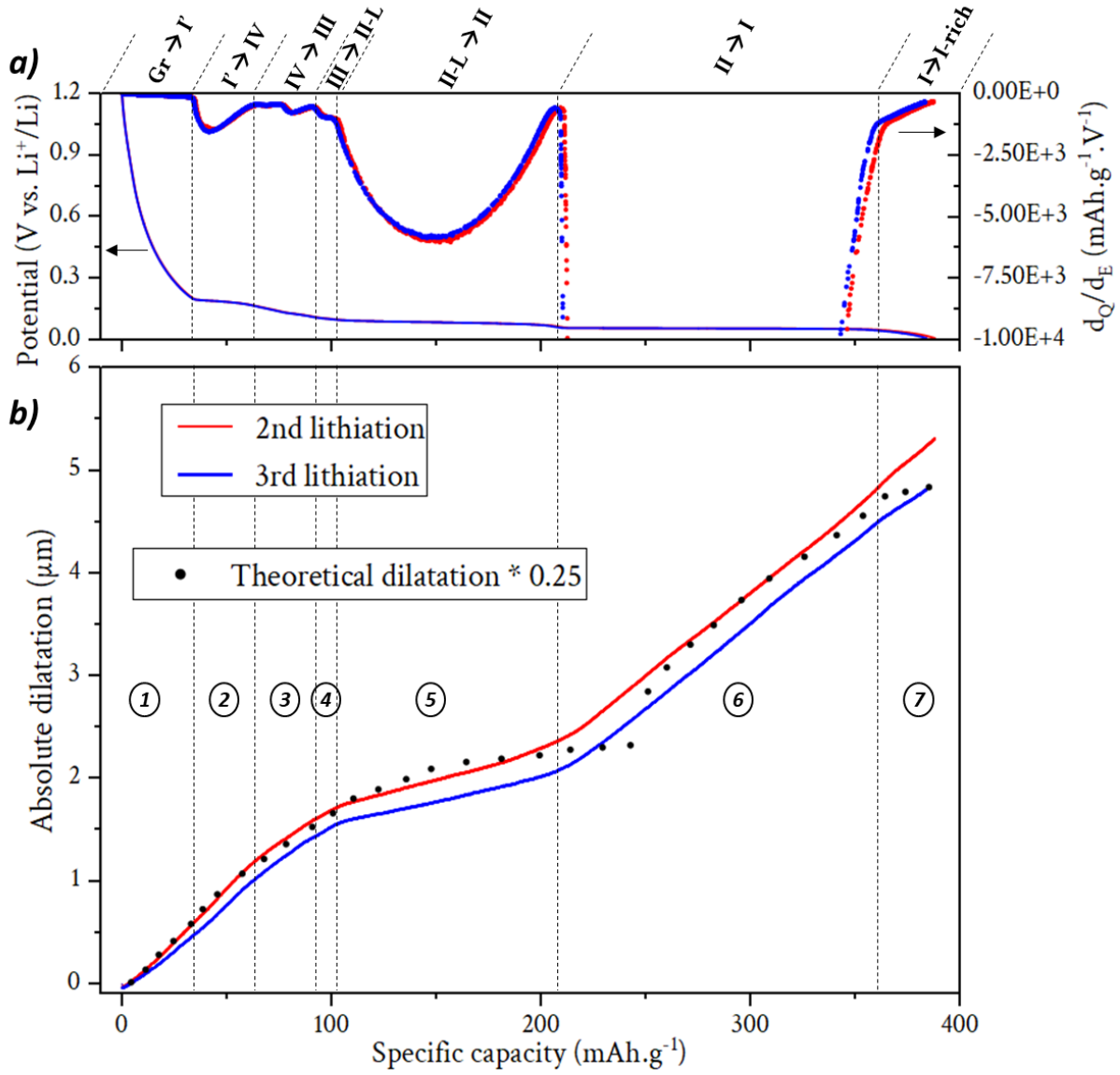


Figure 122: Second and third lithiation of a 70% porosity graphite electrode. a) Graphite electrode potential on the left axis, and the d_Q/d_E representation on the right axis. b) Absolute electrode dilatation initialised at zero (130 µm of initial thickness).

On the hysteresis between lithiation and delithiation, the second cycle was analysed and the dilatation profiles are given in **Figure 123**. To compare the two dilatation profiles, the delithiation was reversed and starts at ~360 mAh.g^{-1}. A very similar dilatation rate is observed from 0 to ~100 mAh.g^{-1} (regions 1 to 4). However, a slight difference is observed from 100 to ~200 mAh.g^{-1} (stage II-L to stage II transition, region 5) with a slower contraction rate in delithiation than the expansion rate during lithiation. This difference is even more pronounced in the range 200 – 360 mAh.g^{-1} (regions 6 and 7). This hysteresis probably comes from the PVDF stretching/shrinkage, already reported in literature since the binder ensure the electrode cohesion and can propagate the deformations. As an example, Gupta *et al.* analysed the plastic deformation of PVDF in an NMC electrode and demonstrated that the mechanical properties of the electrode were mainly controlled by the binder[235]. Based on relaxation experiments, a hysteresis between the relaxation modulus in compression and tension was observed, and a time-dependence was noticed with high hysteresis for short-times and lower one at large timescale.

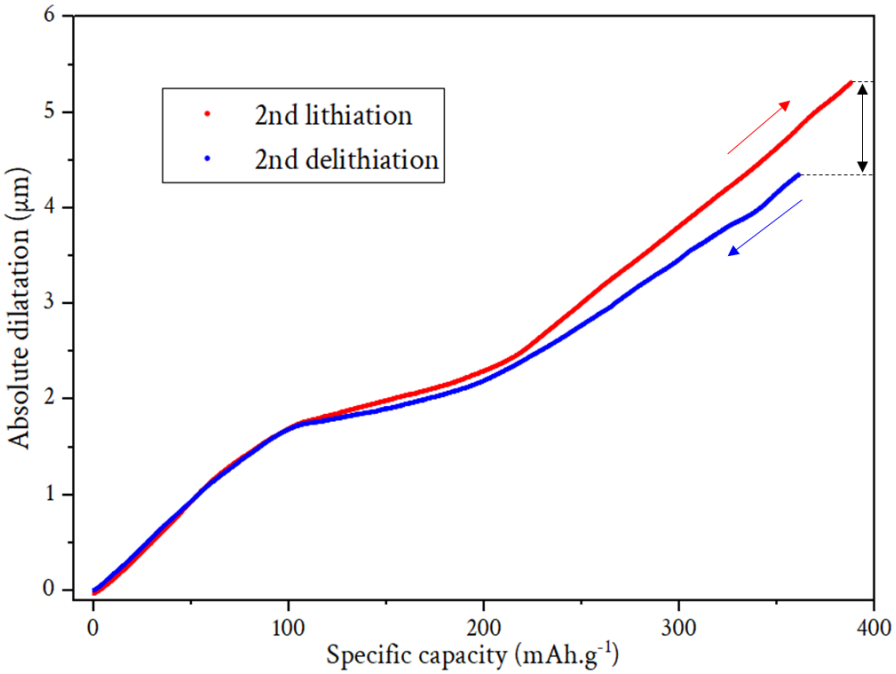


Figure 123: Second cycle of lithiation and delithiation for a 70% porosity graphite electrode. The delithiation profile was reversed on the x-axis so the delithiation started at ~360 mAh.g^{-1} to be compared with the lithiation profile.

To understand the effect of microstructure on the graphite electrode dilatometry, a graphite electrode of 50% porosity was also probed, and the dilatation profile is plotted in **Figure 124**. Unfortunately, only the first cycle was successful and provided reliable results. As for the electrode of 70% porosity, an irreversible change of electrode thickness is observed with an expansion of 8.5 µm in lithiation and a contraction of 4 µm in delithiation. With an initial electrode thickness of 95 µm, the first lithiation resulted in an increase of 9% of electrode thickness, whereas the delithiation induced a decrease of 4.2%. In comparison with the 70% porosity electrode (8% of

expansion and 2.7% of contraction), higher relative expansion and contraction are observed for the electrode of 50% porosity. This is probably the result of the lower electrode porosity that accommodate the electrode dilatation to a lesser extent upon cycling, and to a better electrode cohesion *via* the binder. Unfortunately, both electrode porosity cannot be compared for a "standard" lithiation. If one would compare the dilatation in lithiation (without SEI formation), a higher fraction of the particle's dilatation should be translated at the electrode level because of a lower buffering effect of the porosity, and the latter should exceed ¼ as observed for the electrode of 70% porosity.

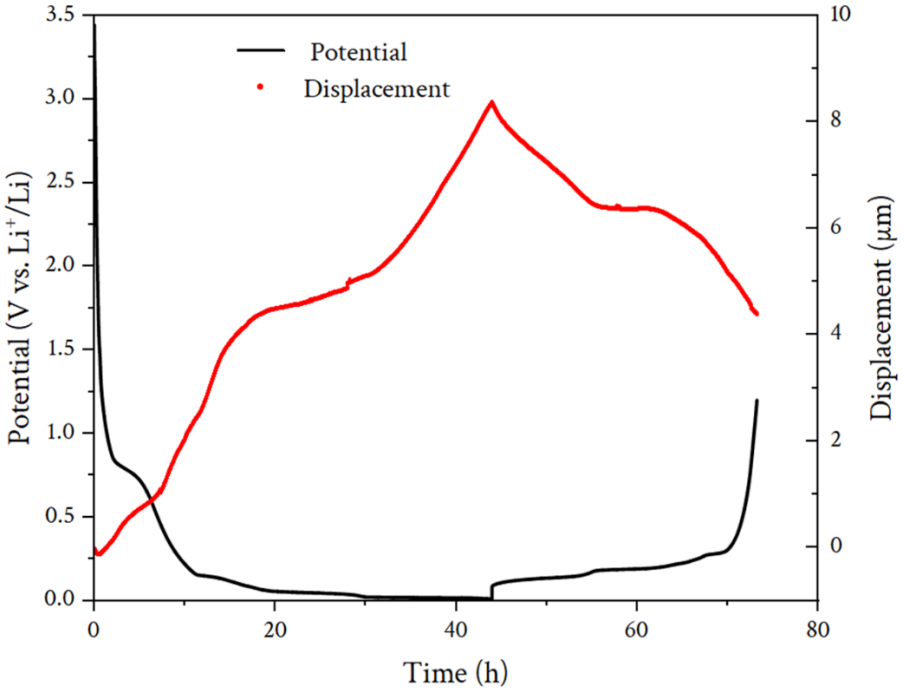


Figure 124: Dilatometric measurement of a 50% porosity graphite electrode with LP30 as electrolyte at 25°C and C/40 rate.

To conclude, the dilatometry of graphite electrodes was assessed to understand the effect of the microstructure on the electrode expansion. An irreversible expansion was observed upon cycling, to a higher extent for the first cycle due to the SEI formation and was partially attributed to the hysteresis of polymer stretching. By comparing the dilatation in lithiation with the theoretical expansion at the crystal lattice level, it was evidenced that a significative fraction of the particle's expansion (75%) was accommodated by the electrode porosity and the binder deformation. These observations demonstrate the importance of the electrode microstructure in the dilatometric evolution. Decreasing as much as possible these dilatometric evolutions is essential to reduce the ageing and the fatigue of the electrode upon cycling. The silicon negative electrode is a very good example on this purpose since it displays a volumetric change of ~300% upon lithiation, and this causes high swelling at the cell level and pressure issues[236]. To decrease the evolution of the electrode thickness, a high electrode porosity should be selected, however this would degrade the

electronic properties and the energy density. One can also play on the binder properties and increasing its fractional content in the composite electrode, but to the extent of the electrode specific energy. In the end, an optimal electrode engineering must be found to combine the better dilatometric, energy and power properties.

3 NMC|GRAPHITE COMMERCIAL CELL ULTRASOUND STUDY

Until now, the investigations were based on the graphite electrode characterisation in half-cell with metallic lithium as negative electrode. However, graphite electrodes are practically used as negative electrode in association with positive electrodes such as LFP, LCO, or NMC. Here is presented the investigation of a $LiNi_{0.8}Mn_{0.1}Co_{0.1}O_2$ (NMC811) | graphite Kokam® full cell, study led in collaboration with ISEA laboratory from Aachen University.

Ultrasound is mainly used to characterise the state of charge or state of health of full cells. However, a lack of correlation between the ultrasound features and the structural evolution of the active materials is observed. For this reason, the investigation was carried out at BM02 beamline from ESRF to probe *in operando* the structural evolution of the two electrode materials using XRD and the ultrasound transmitted signal. To this end, the full cell was cycled at C/3 rate with relaxation steps and a measurement close to quasi-thermodynamic condition was realised at C/8 rate. The experimental set-up as well as the experimental conditions are given in p77.

3.1 Basics of ultrasound in LiBs

Prior discussing the results, here are introduced some basics of ultrasound and their correlation in LiBs. Ultrasound is mechanical and elastic waves that can propagate through the full cell. In this study, the emitted signal was fixed at a frequency of 1 MHz. In transmission configuration, the emitted wave travels the entire cell, crossing the two electrodes, the electrolyte-filled separator and the cell casing, and the received signal can be characterised by two variables.

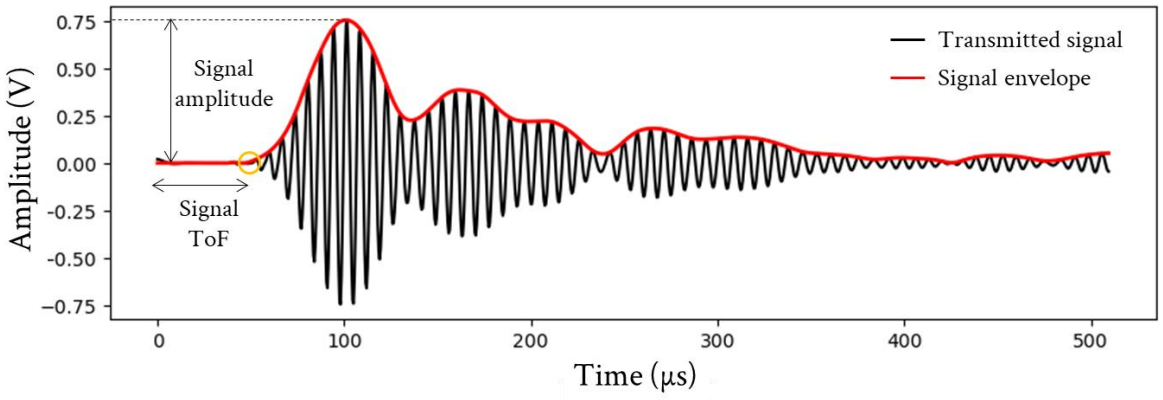


Figure 125: Example of ultrasound signal transmission.

Figure 125 is an example of received signal, a main wave packet and secondary wave packets are observed, originating from echoes generated by the several interfaces of the cell. Focusing on the main wave packet, this signal is characterised by an amplitude (maximum intensity of the wave packet) and a time of flight (ToF) corresponding to the travelling time of the ultrasound.

In solids, an ultrasound wave propagates with a velocity depending on the material properties through Eq. 26.

$$c = \sqrt{\frac{E_{eff}}{\rho}} \qquad \text{Eq. 26}$$

Where c is the wave velocity in $m.s^{-1}$, E_{eff} corresponds to the effective Young's modulus in $kg.m^{-1}.s^{-2}$ and ρ is the density in $kg.m^{-3}$.

Based on this equation, the ToF is expressed by Eq. 27.

$$ToF = \sqrt{\frac{m}{A}}\sqrt{\frac{d}{E_{eff}}} \qquad \text{Eq. 27}$$

Where m is the probed mass in kg^{1}, A represents the probed section in m^{-2}, d the thickness of the crossed medium in m.

Applying this to a full cell, the ToF of the ultrasound wave expressed in seconds, depends on the mass per surface unit (m/A in $kg.m^{-2}$) which is a constant term, and variables that change upon cycling. The thickness depends on the evolution of both electrode dilatometry upon de/lithiation, and similarly, the effective Young's modulus depends on the variation of elastic properties of both active materials. The ToF can then serve as indicator to probe the evolution of structural state of a full cell, however the variations of ToF are a convolution of both electrodes evolution that are difficult to deconvolute without additional characterisations.

The acoustic impedance Z is also characteristic of the propagation of an ultrasound wave through a medium[233] as expressed in Eq. 28, and is practically similar to the signal amplitude (or attenuation).

$$Z = \rho c \qquad \text{Eq. 28}$$

Developing this equation with Eq. 26, the following Eq. 29 is obtained and expressed as a function of the same variables as the ToF (Eq. 27).

$$Z = \sqrt{\frac{m}{A}}\sqrt{\frac{E_{eff}}{d}} \qquad \text{Eq. 29}$$

By comparing the impedance acoustic and the ToF equations, it results that both variables are linked to the mass per unit of area with Eq. 30.

$$ToF = \frac{m}{A} \cdot \frac{1}{Z} \qquad \text{Eq. 30}$$

In the end, the two variables that are commonly used to characterise LiBs (ToF and amplitude) are sensible to the same physical properties; the thickness of the medium crossed by the ultrasound wave and its elastic properties.

3.2 Correlating the ultrasound signal to the electrochemical and structural evolutions

The commercial battery (Kokam®) probed is a pouch cell composed of multiple layers of positive (NMC811) and negative (graphite) electrodes, the cell specifications are given in **Table A2**. First, the ultrasound signal was correlated to the electrochemical profile in **Figure 126**.

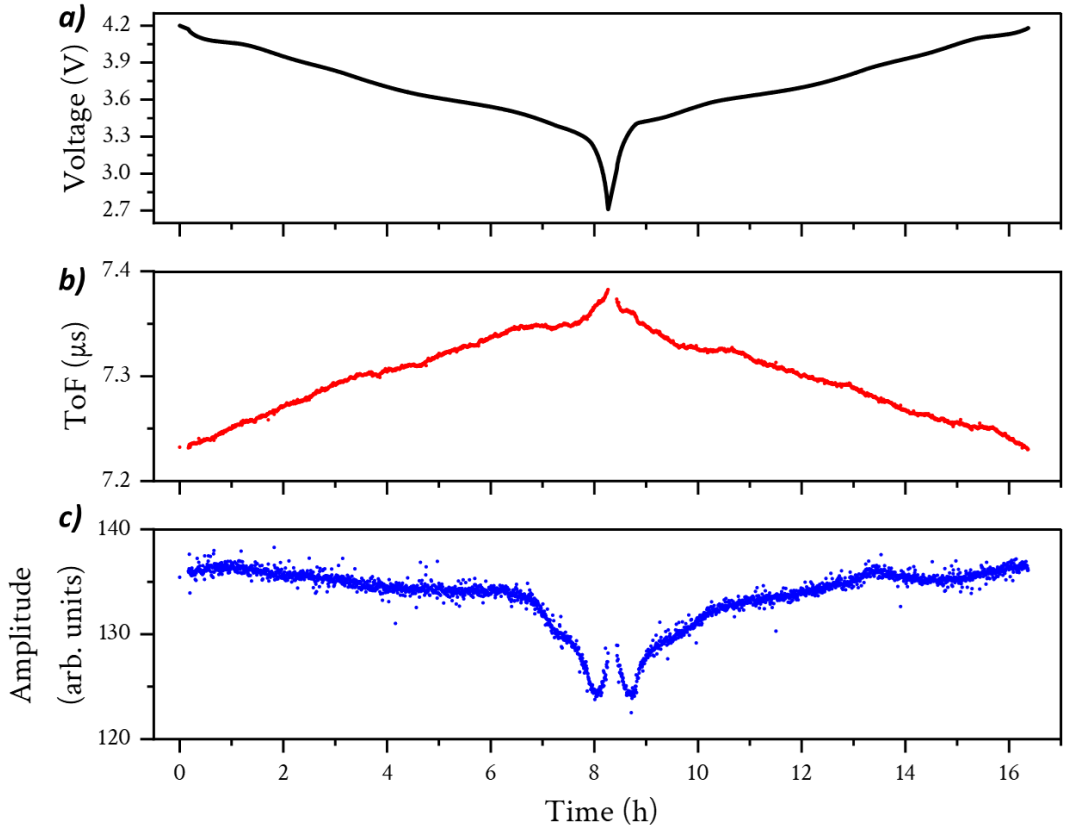


Figure 126: Ultrasound signal evolution upon discharge and charge of the Kokam cell at C/8 rate. a) Voltage of the full cell. b) ToF signal of the transmitted signal. c) Amplitude of the transmitted signal.

The voltage profile of the full cell is given in **Figure 126a**, starting by a discharge (lithiation of NMC and delithiation of graphite). The ToF (**Figure 126b**) increases upon discharge and shows a non-monotonic evolution, especially from 3.3 to 2.7 V. The evolution of amplitude (**Figure 126c**) is noisier but also displays a non-monotonic evolution upon cycling. Interestingly, the signal amplitude evolves in an inversely proportional manner with the ToF as suggested in Eq. 30. For

the following, only the ultrasound ToF was analysed due to its better signal quality upon cycling compared to the signal amplitude.

To understand the evolution of ToF signal during cycling, Eq. 27 shows that the latter evolves as a function of i) the cell thickness and ii) the effective Young's modulus of the whole cell. The interest here is then to determine which of these parameters mainly governs the evolution of ToF upon cycling. To do so, the cell thickness evolution is easily assessed using dilatometry measurements as presented in p**161**, however the assessment of the effective Young's modulus evolution is way more complicated.

3.2.1 Dilatometric behaviour of both electrode

Several papers shown that the thickness of NMC vs. graphite cells increases by several tens of micrometers during the charge[237–239] (NMC delithiation and graphite lithiation). This macroscopic thickness increase is caused by changes in the volume of the active materials at the electrode scale. Concerning the graphite particles, the evolution was already discussed in p**161** (increase of the *c*-axis upon lithiation). It results in a decrease of the thickness at the electrode level upon charge (delithiation of graphite). For the NMC particles, the evolution is slightly more complex since the particles undergo an anisotropic variation in lattice parameters along *a*-*b*-axis and *c*-axis, resulting in an overall volume contraction upon charge (this process is reversible during lithiation; *i.e.* discharge). This volume contraction is very small for a large range of lithium content ($LiNi_{0.8}Mn_{0.1}Co_{0.1}O_2$ – $Li_{0.3}Ni_{0.8}Mn_{0.1}Co_{0.1}O_2$) containing the H1 ⟷ H2 NMC phases transitions[86], while the last phase transition H2 ⟷ H3 is responsible for a higher volumetric contraction at the lattice scale. With respect to the NMC electrode scale, the volume changes are not unidirectional but result in a 3D volume contraction upon charge.

In summary, upon charge of the full cell, it is expected to observe the increase of the graphite electrode thickness, and a contraction of the NMC electrode. To verify this hypothesis, a quantitative analysis of single layers of the positive and negative electrodes dilatation was realised using the nano-dilatometric device as well as the full cell dilatation. The commercial cell was disassembled in an Ar-filled glovebox, the electrodes were washed with DMC, and one side of the double-coated negative and positive electrodes were removed and mounted in a nano-dilatometer. The electrochemical dilatometer enables a three electrodes set-up, so the positive and negative electrodes were probed as a function of a metallic lithium reference electrode (V vs. Li^+/Li) and the potential of each electrode was deconvoluted from the full cell voltage. Since only the working electrode can be probed in dilatation, two nano-dilatometers were built by inverting the full cell configuration, and both positive and negative single layers were probed in dilatation upon charge. The results are plotted in **Figure 127**, with the voltage of the full cell and the potential of the negative graphite electrode in **Figure 127a**. The dilatation of the single layers is plotted in **Figure**

127b, and compared to the full cell thickness expansion (measured with a constant pressure of 25 kPa) determined from another experiment reported in literature[237].

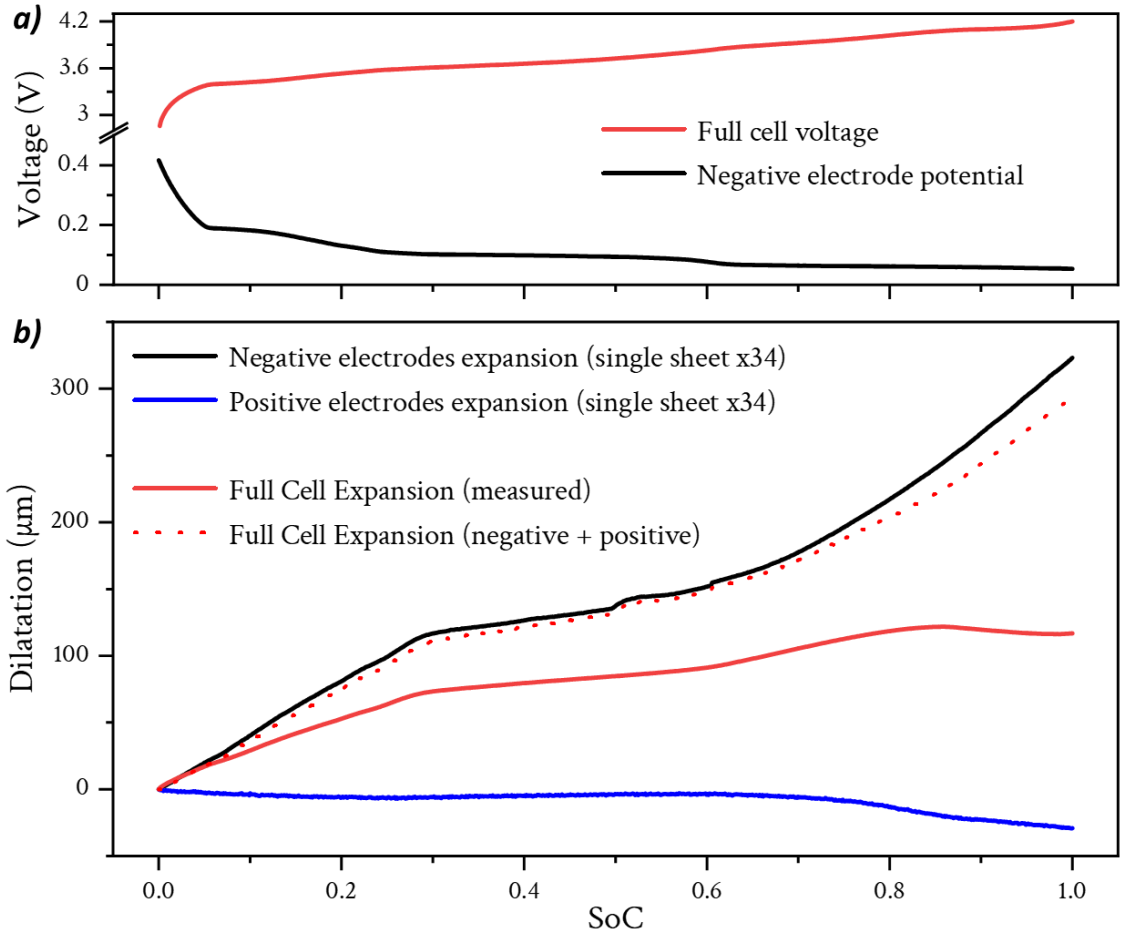


Figure 127: Swelling origin from an NMC| graphite full cell. a) Full cell voltage and negative electrode potential vs. Li^+/Li. b) Dilatation of single layers of positive and negative electrodes of the full cell, and dilatation of the full cell. The red dotes correspond to the sum of dilatation from the positive and negative electrodes.

Given that the full cell comprises 17 double-coated negative and positive electrodes, a factor of 34 was applied to the single electrode expansion measured by nano-dilatometry. The graphite electrode expansion largely exceeds the volume contraction of the NMC811 electrode. As a result, the calculated (experimental difference between the positive and negative electrode expansion, in red dots) full cell expansion strongly depends on the graphite electrode, with a slight impact of the NMC electrode that buffers the global expansion above 80% SoC. By comparing the extrapolated full cell expansion, to the dilatometric measurement with the full cell expansion measurement of the commercial cell, the impact of the cell manufacture is observed. Indeed, in the pouch cell, all the elements such as separators, casing and the void that is voluntarily introduced in the assembly by the manufacturer buffer the global expansion, and/or the internal pressure increases adding a supplementary force to limit the cell dilatation. These observations support the above-mentioned

hypothesis stating that the full cell thickness evolution upon charge mainly follows the graphite negative electrode expansion.

Based on these experiments and the ToF equation (Eq. 27), the full cell thickness expansion should lead to an increase of the time of flight upon charge of the cell, which is not the case as observed in **Figure 126**.

3.2.2 Elastic properties of both electrodes

Concerning the effective Young's modulus of the full cell, this metric is very complicated to assess *in operando* since generally the elastic modulus are acquired using bending tests. For this reason, very few papers discuss the evolution of Young's modulus of LiBs upon cycling. Experimentally, graphite, NMC and most the electroactive materials display an increase of Young's modulus upon lithiation[240–242]. Investigating a $LiCoO_2$ | graphite full cell, Davies *et al.* demonstrated more important sound velocity variations in the graphite electrode compared to the LCO[240]. This explained the larger impact of the graphite electrode on the average Young's modulus of the full cell. A reason for this statement resides in the "softness" of graphite that can deform reversibly upon de/lithiation[242] compared to lithium oxide materials such as LCO[243] or NMC[241] that easily break upon mechanical strains. Using DFT calculations, the evolution of Young's modulus at the particle's level was also investigated. For NMC and graphite, an increase of elastic modulus in lithiation, and a reversible decrease upon delithiation were observed[240,244]. Then, considering the charge of an NMC | graphite cell, the Young's modulus of graphite increases while for NMC, the latter decreases.

The point here is to determine which electrode material from graphite and NMC811 dominates the apparent Young's modulus of the full cell. Values reported from literature for both electrode materials are given in **Figure 128a**. At the discharged states ($x = 0$), a large difference of Young's modulus is observed with softer elastic properties for graphite. Upon charge, a decrease of 50% - 60% in elastic modulus of NMC is expected, whereas an increase of 240% for graphite should be observed, supporting a domination of the graphite electrode in the full cell behaviour.

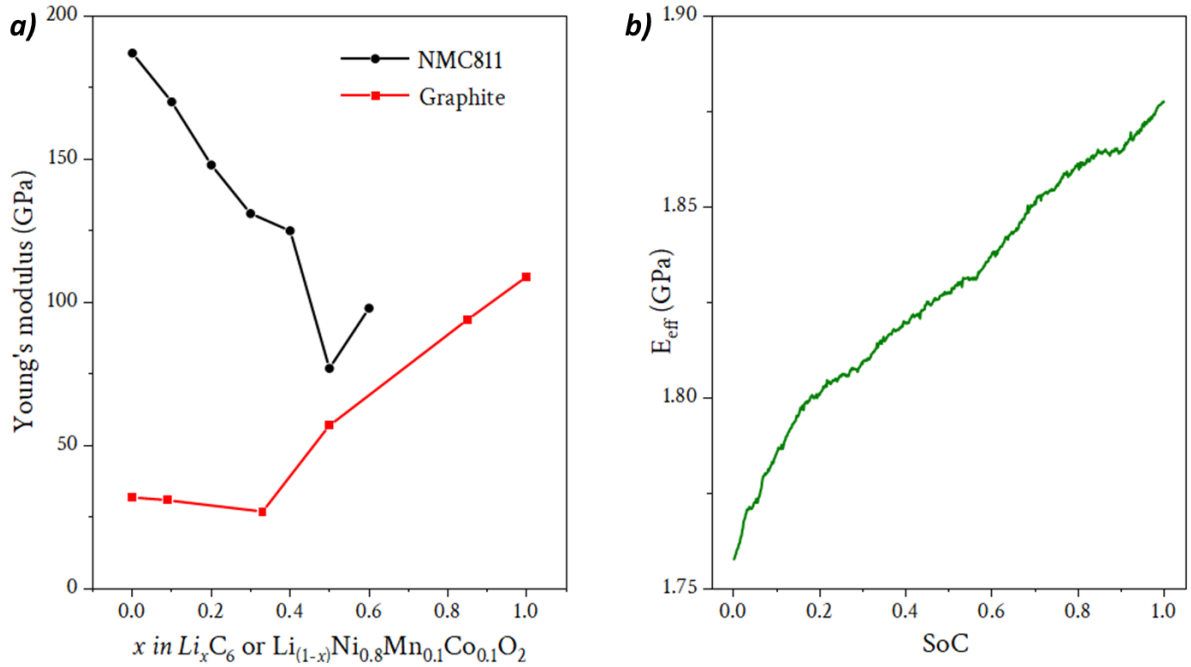


Figure 128: Young's modulus evolution upon cycling. a) Young's modulus determined by DFT calculation from ref. [244,245]. b) Effective Young's modulus numerically determined from the ultrasound ToF and the full cell thickness evolution upon charge.

To confirm this point, a numerical estimation of the average Young's modulus of the full cell was conducted, using the thickness evolution data (extracted from full cell expansion, **Figure 127b**) and the ToF signal measured (**Figure 126b**), using the Eq. 27. **Figure 128b** illustrates an increase in the average elastic modulus of the full cell during charge, as deduced above and the calculated values agree with bending tests provided in the literature for both materials[235,246]. The obtained average elastic moduli of the cell are largely lower than the Young's modulus calculated by DFT at the particle level. This is the result of the electrode microstructure and the several components of the full cell that display different elastic moduli.

In conclusion, it was demonstrated that the effective elastic modulus of the full cell is driven by the negative electrode Young's modulus. Consequently, an increase of elastic modulus during the charge is observed. Furthermore, based on the ToF equation (Eq. 27), an increase in the average Young's modulus is consistent with the observed decrease in ToF during the charging process. However, the non-monotonic evolution of ToF measurement indicates the presence of a complex correlation between the various cell components, with additional correlation between both electrode materials.

3.2.3 Understanding the electrochemical signature of the full cell

The evolution of ToF signal was understood and mainly linked to the elastic properties of the graphite electrode. However, prior to correlate the ToF evolution with the electrochemical and structural behaviours, the electrochemical signature of the full cell is investigated. Since the electrochemical dilatometer enables a three electrodes set-up, the potential (V vs. Li^+/Li) of the positive and negative electrodes were deconvoluted from the full cell signature. Three potential differences were measured:

$$V_{WE} = \frac{\mu_{Li^+}^{NMC} - \mu_{Li^+}^{Li^\circ}}{-ne} \quad \textit{Eq. 31}$$

$$V_{CE} = \frac{\mu_{Li^+}^{Gr} - \mu_{Li^+}^{Li^\circ}}{-ne} \quad \textit{Eq. 32}$$

$$V_{CELL} = V_{WE} - V_{CE} = \frac{\mu_{Li^+}^{NMC} - \mu_{Li^+}^{Gr}}{-ne} \quad \textit{Eq. 33}$$

Where μ_{Li}^{Gr} is the chemical potential of lithium in the graphite working electrode, $\mu_{Li}^{Li^\circ}$ is the chemical potential of lithium in the metallic lithium reference electrode, μ_{Li}^{NMC} is the chemical potential of lithium in the NMC counter electrode, n is the number of exchanged electrons and e represents the elementary charge.

Eq. 33 implies that the full cell voltage (V_{CELL}) variations corresponds to the sum of variations in voltage of the WE vs. Li reference (V_{WE}) and the CE vs. Li reference (V_{CE}) with respect to the full cell capacity (Q_{CELL}):

$$\frac{dV_{CELL}}{dQ_{CELL}} = \frac{dV_{WE} + dV_{CE}}{dQ_{CELL}} = \frac{\mathrm{d}(\mu_{Li^+}^{NMC} - \mu_{Li^+}^{Li^\circ})}{dQ_{CELL}} + \frac{\mathrm{d}(\mu_{Li^+}^{Gr} - \mu_{Li^+}^{Li^\circ})}{dQ_{CELL}} \quad \textit{Eq. 34}$$

Since $\mu_{Li^+}^{Li^\circ}$ is assumed to be constant during the measurement for a C-rate applied of C/40, Eq. 35 is obtained.

$$\frac{dV_{CELL}}{dQ_{CELL}} = \frac{\mathrm{d}\mu_{Li^+}^{NMC}}{dQ_{CELL}} + \frac{\mathrm{d}\mu_{Li^+}^{Gr}}{dQ_{CELL}} \quad \textit{Eq. 35}$$

To quantify the impact of the lithium chemical potential variation of one electrode (ω_{Gr} for graphite and ω_{NMC} for NMC) on the full cell voltage variation, weighting variables are introduced:

$$\omega_{Gr} = \frac{\mathrm{d}\mu_{Li^+}^{Gr}}{dQ_{CELL}} \Big/ \frac{dV_{CELL}}{dQ_{CELL}} \; and \; \omega_{NMC} = \frac{\mathrm{d}\mu_{Li^+}^{NMC}}{dQ_{CELL}} \Big/ \frac{dV_{CELL}}{dQ_{CELL}} \; with \; \omega_{Gr} + \omega_{NMC} = 1 \quad \textit{Eq. 36}$$

ω_{Gr} and ω_{NMC} are calculated using the variations of potential of the working and counter electrodes with respect to the cell capacity. To ensure consistency in the method, the sum of ω_{Gr}

and ω_{NMC} was verified to be equal to 1. Based on Eq. 36, one can mathematically separate the contribution of one electrode to another one, and thus "weight" their contribution. In practice, a weighting variable of 1 means that the voltage variation of the full cell exclusively originates from the chemical potential variation of one electrode. Those variables are plotted in **Figure 129a** as a function of the full cell voltage.

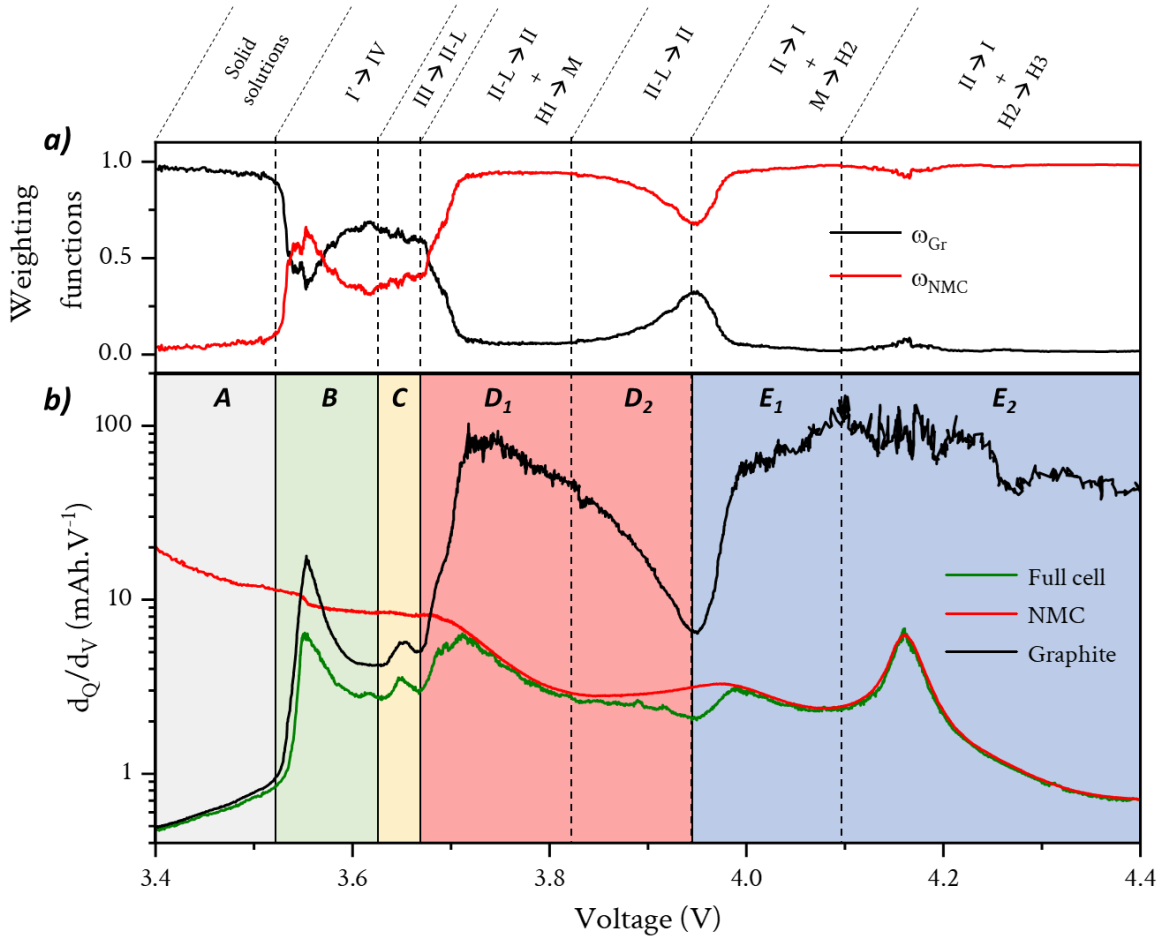


Figure 129: Identification of de/lithiation processes in the full cell NMC811 vs. graphite. a) Weighting functions of graphite and NMC electrode potential impact in the full cell voltage variation, supplemented by main phase transitions observed on top; b) dQ/dV curves of graphite, NMC, and full cell with the full cell voltage evolution.

The dQ/dV representation (DCA, **Figure 129b**) offers insight into the underlying de/lithiation mechanism. In the case of NMC811 material, lithium de/insertion occurs via a solid solution mechanism with some lattice parameter changes inducing specific variations in the dQ/dV representation. In the case of graphite, the DCA profile was already discussed in p**87.** Here, the DCA profiles were obtained by calculating the variations of cell capacity (Q_{CELL}) as a function of the NMC and graphite potentials (V_{WE} and V_{CE}). However, instead of representing these variations as a function of each electrode potential (*e.g.* $d_{Q_{CELL}}/d_{V_{WE}} = f(V_{WE})$), the DCA are plotted as a function of the full cell voltage. This explains why the DCA profile of the graphite electrode does

not display sharp peaks as observed previously but instead, wave that are distributed in potential. In this representation, the three curves are linked by Eq. 37.

$$\frac{dQ_{CELL}}{dV_{CELL}} = \frac{1}{\frac{\mathrm{d}\mu_{Li^+}^{NMC}}{dQ_{CELL}} + \frac{\mathrm{d}\mu_{Li^+}^{Gr}}{dQ_{CELL}}} \qquad \textit{Eq. 37}$$

Starting with the region A of the full cell charge, the cell voltage variations are imposed by the graphite electrode since the weighting function of graphite is near 1 (**Figure 129a**). However, no specific peak is observed on the DCA since solid solution processes of de/lithiation are occurring for both electrodes. In region B, the full cell voltage variation is attributed to both electrodes' potential variation. However, the comparable shape of the peak observed for the full cell and graphite curves in the bottom graph indicates that graphite undergoes its initial biphasic phase transition (stage I' to stage IV) while NMC811 remains delithiated through a solid solution mechanism with no phase transition. A comparable observation can be made in region C, where the apparent peak of the full cell curve is attributed to the graphite liquid-like transition. In region D, two processes are identified. The first of these (depicted as D1) involves the graphite stage II-L to stage II phase transition, while the hexagonal to monoclinic phase transition H1 → M of NMC811 occurs concurrently (a common phase transition for the NMC compounds family). The second subregion (D2) comprises the continuation of the graphite stage II formation, while the specific phase transition of NMC811 is terminated. The final region E initially exhibits a local minimum on the full cell profile (**Figure 129b**), which can be attributed to the change in biphasic mechanism of graphite from stage II to stage I. Subsequently, the NMC electrode undergoes first the monoclinic to second hexagonal phase transition M → H2 within the E1 subregion. The second characteristic peak in subregion E2 correlates with the second to third hexagonal transition H2 → H3, which involves the oxidation of Ni^{3+} and Co^{3+} to Ni^{4+} and Co^{4+}, respectively[247].

With this analysis, a better understanding of the full cell voltage evolution upon charge is possible. This enables now the correlation between the ToF signal and the structural evolution of both electrode materials assessed *via operando* XRD.

3.2.4 Correlation between ultrasound ToF, electrochemical and structural evolutions upon cycling

XRD experiment was realised in transmission mode with the X-photons crossing the pouch-cell thickness, as shown in the image given in p77. Then, the acquired diffraction patterns contained the signal of the graphite and NMC electrodes. For graphite, it was previously demonstrated that the (002) Bragg reflection was interesting to follow. Regarding the NMC electrode, the *c*-axis is also interesting to study through the (003) Bragg reflection. The Bragg reflections of both

electrodes' materials are plotted in **Figure 130** upon charge. One can follow the evolution of the (003) Bragg reflection of NMC in **Figure 130a**, the (002) Bragg reflection of graphite in **Figure 130b**.

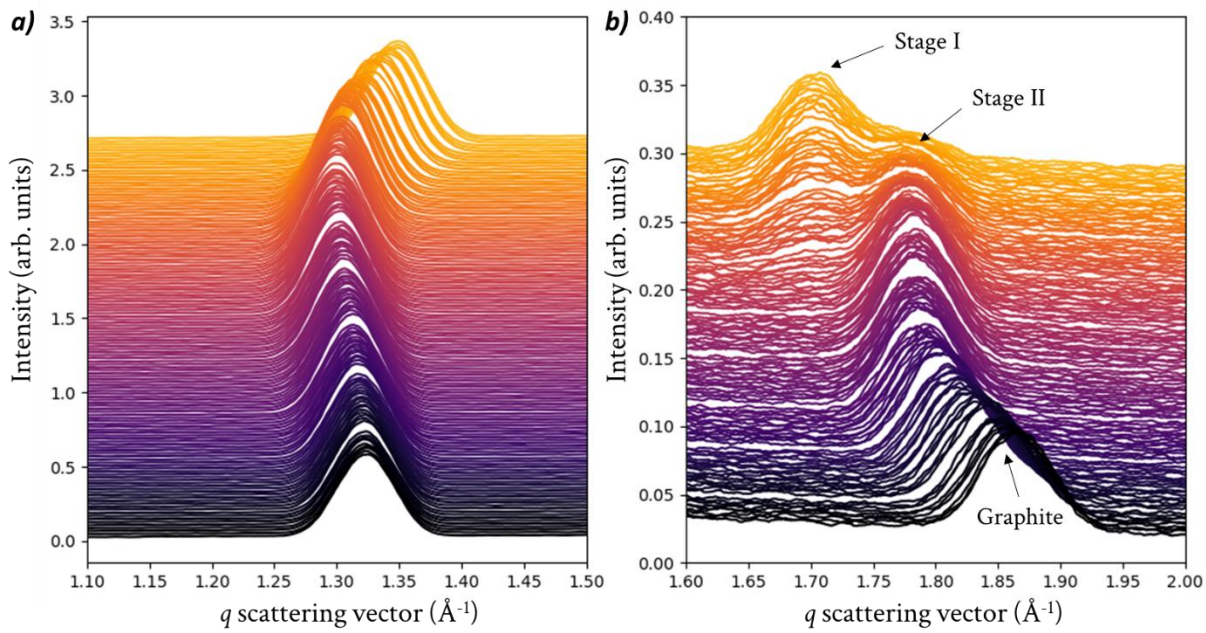


Figure 130: Waterfall representation of the diffraction patterns obtained upon charge of the cell. a) (003) Bragg reflection of NMC811. b) (002) Bragg reflection of graphite.

The Bragg reflections were fitted using PseudoVoigt functions as described in p**71**, and the structural evolution of both electrodes was studied through the peak position of the several phases. **Figure 131a, c** gives the evolution of peak position of the phases of graphite and NMC, respectively, with respect to the cell voltage (starting by a discharge). The ToF evolution is represented in **Figure 131b**, as well as the d_Q/d_V representation on the right axis. The correlated ToF-XRD data were divided by the five same regions of interest as above, beginning with the cell discharge (graphite delithiation and NMC811 lithiation). The voltage boundaries are slightly shifted between **Figure 131** and **Figure 129** due to the high separator resistance employed in the nano-dilatometric measurement.

Starting with the region E2', a significant variation in the ToF signal is observed which correlates with the peak attributed to the H3 → H2 transition of NMC811. This transition results in a clear shift of the peak position towards lower *q* value (expansion of the *c*-axis). In terms of volume change, a notable increase of the lattice volume of NMC811 estimated at 4% by Quilty *et al.*[248], which is the most important variation in volume among all the transitions of NMC811. In the remaining region E', spanning from 4.1 V – 3.8 V, a linear increase in the ToF signal is observed, which may be attributed to the disappearance of the stage I phase achieved through biphasic mechanism, associated with a decrease of the Young's modulus mitigated by the thickness decrease

of the graphite electrode. No obvious change in slope of ToF signal are noticed when NMC811 is undergoing the H2 → M phase transition (E1' subregion). A change in slope of the ToF signal is observed in the D2' region in comparison to the E1' region which correlates with the end of biphasic mechanism of graphite. It is observed that when NMC811 undergoes the M → H1 phase transition in the subregion D1', an increase in the slope intensity of the ToF signal is observed. In the third region (C'), a period of pseudo-plateau in the ToF signal correlates with the solid solutions of graphite (stage II-L → Gr). In this potential range, the exchange of charges is minimal, resulting in a negligible variation in the global Young's modulus of the cell. With regard to the B' region, again, a distinctive slope in the ToF increase is discernible, which correlates with the stage IV of graphite disappearance. For the final region of interest (A'), a plateau-like feature in the ToF signal correlates with a minimal amount of lithium stored via solid solution mechanisms in both materials.

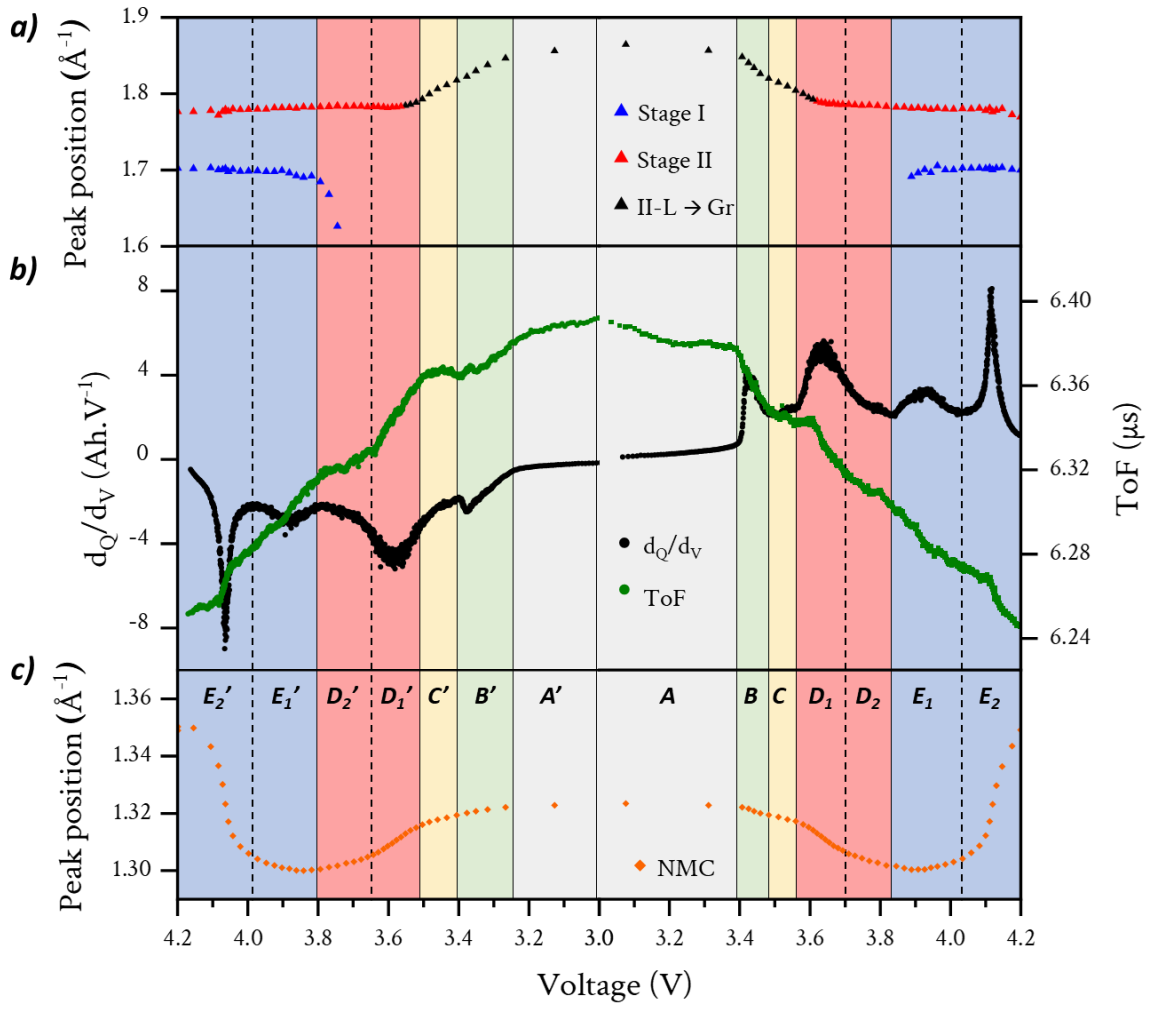


Figure 131: Correlation between structural evolution of both electrode material and the ultrasound ToF. Cycling rate of C/8 starting by a cell discharge. a) Variations in peak position of graphite. b) d_Q/d_V curve and ToF evolution with cell voltage. c) Variations in peak position of as a function of the cell voltage.

To conclude on this *operando* experiment, it was shown that the ToF signal is mainly driven by the Young's modulus evolution of graphite, leading to a decrease in ToF signal during charge of the cell and an increase during the discharge. By deconvoluting all the electrochemical processes, it was also demonstrated that most of the modulations in ToF are correlated to structural changes of the two electrode materials. It was noticed that, in general, the ToF changes linearly depend on the potential in the selected regions, with varying positive or negative slopes that might reflect a correlation between specific phase transitions and ultrasound properties. This effect could be further investigated on simplified systems to obtain a quantified relationship between ultrasound features and the electrochemical processes.

4 CONCLUSION – CHAPTER 5

In this chapter, the mechanical aspects of the graphite electrode during cycling has been discussed based on dilatometric measurements and the use of ultrasound signal. The comparison between the electrode thickness variations and the volume variations at the crystal lattice scale revealed the key role of the electrode microstructure in the accommodation of the morphological variations. These morphological variations could induce particle disconnection from the electronic network, particle fracturing, or the creation of closed porosities that are all detrimental to the electrochemical performance.

Moreover, these mechanical aspects should be captured during the operation of the batteries to enable the detection of eventual degradation processes. On this purpose, ultrasound has been used to probe a commercial battery and correlate to the structural evolution at the material level using X-ray diffraction. This study revealed the good sensitivity of ultrasound transmission signal to the structural changes of both active materials. Especially, it was demonstrated that the ultrasound time of flight is mainly driven by the variations in elastic properties of the graphite electrode in commercial cells. To push further the investigation, quantitative links between the specific variations of time of flight and the structural evolutions could be further established by performing repeated and reproducible experiments, including dedicated model systems or half-cell measurements. As prospects, monitoring the ultrasound signal transmission in commercial batteries could provide additional information for the battery management system (BMS) to improve the monitoring of the battery state of health.

CHAPTER VI

BOOSTING POWER CAPABILITY USING ^{6}LI

In this last chapter, an innovative way for improving the power capabilities of graphite and LiBs is investigated. The concept is based on the substitution of natural lithium with ^{6}Li isotope, which reduces by 14% the mass of the intercalant ion. The question is then to understand whether this substitution could serve as a booster for the kinetics of graphite lithiation. The investigations are based on the characterisation of the transport properties in graphite half-cells using ^{6}Li-enriched components.

1 CONTEXT

Power limitations in thick graphite electrodes is caused by the electrode microstructure, but this electrode microstructure is needed from an industrial point of view, where porosity should be the lowest possible to keep increasing the energy density. Lithium-ion diffusion through the porous network of the electrode microstructure is a key parameter to control, and one could envisage the enhancement of the diffusion properties of lithium in the electrolyte. Development of new electrolytes can be one solution since it can increase the transference number of Li, as well as the ionic conductivity to decrease as much as possible the diffusion time through the electrode microstructure. In the literature, all the investigations are focusing on modifying the properties linked to the lithium-hosting environments (*i.e.* the active material or the electrolyte properties) but none are considering changing the inherent properties of the lithium ion, especially using Li isotopes.

While the properties of solids can be tailored through a wide range of strategies, achieving comparable control over ions is far more challenging. *A priori*, two strategies seem feasible by playing on i) the oxidation state of the ion, and ii) the isotopic nature. A very convenient example is the case of vanadium complexes, that display multiple stable oxidation states from +3 to +5 in aqueous medium[249]. This provides a wide range of properties depending on the oxidation state, and for this reason, vanadium is used in many electrochemical fields such as redox-flow batteries[250] or Na-ion batteries[251]. The case of vanadium is very peculiar and exists because of its partially filled 3d orbitals. Since lithium is an alkaline metal, it does not display such a variety of oxidation states. Then, the only way of tuning the properties of lithium is to modify its isotopic nature.

Two isotopes display the same atomic number (*i.e.* equal number of protons and electrons) but differ in mass number (*i.e.* different number of neutron). For the lithium, ^{6}Li and ^{7}Li are the two stable isotopes present on Earth. **Table 14** provides the characteristics of the two isotopes, ^{7}Li is the most abundant with 92.5%, and the ^{6}Li is 14.3% lighter than the ^{7}Li.

Table 14: Characteristics of stable lithium isotopes.

Isotope	**^{6}Li**	**^{7}Li**
Abundance	7.5%	92.5%
Isotopic mass *(u)*	6.015	7.016

Thus, natural lithium composition LiBs is mostly ^{7}Li. The interesting questions are then the following:

Are there interests in using ^{6}Li-enriched materials and electrolytes?

Does the lower mass of ^{6}Li can serve as booster in the power capabilities of batteries?

2 STATE OF THE ART

The discovery of chemical isotopes dates back from 1922, with the Nobel prize of Francis William Aston that recorded, using a hand-built mass spectrograph, the mass difference between several stable isotopes[252]. The interest in lithium isotopes remained mostly academic in the 30 years following the Novel prize by characterising the nuclear structure of each isotope and the establishment of separation methods. The interest grown with the discovery of the nuclear properties of ^{6}Li for the development of the hydrogen bomb in the 1940 – 1950. Macklin and Banta reported the production of tritium by bombardment of ^{6}Li isotope using deuterium (^{2}D)[253]. The origin of the application for the H-bomb comes from the fission of ^{6}Li into tritium and helium when a neutron is fired on the lithium isotope[254]. An unstable ^{7}Li-like species is formed, immediately relaxes by fission, and the nuclear reaction produces 4.78 MeV of energy.

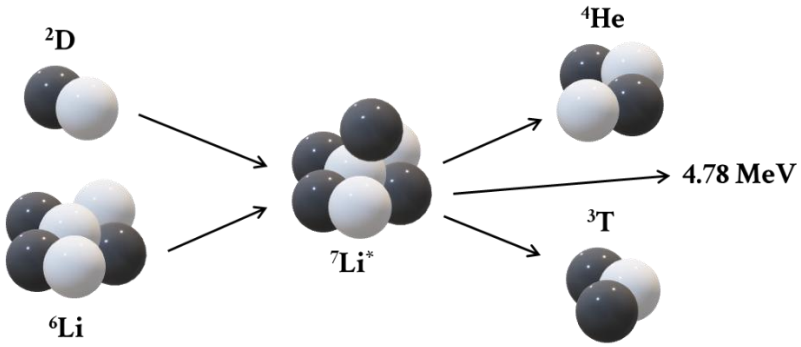


Figure 132: Illustration of the ^{6}Li bombardment with deuterium nuclear reaction.

The probability of interaction of an element with a neutron is characterised by the cross section as for X-rays. However, while the cross section increases with the atomic number of elements for X-rays[255], the absorption of neutrons does not follow a peculiar trend in the periodic table. Therefore, lithium is "transparent" to X-rays due to its very low number of electrons, regardless of the isotope nature. However, for neutrons, ^{6}Li displays 940 barns of cross section while ^{7}Li is "transparent" with 0.045 barns[256], interacting ~20,000 times less with neutrons. This important difference led to the interest of ^{6}Li isotope in the battery field, especially at the imaging beamline, as a tracer for example.

2.1 Lithium isotopes in geochemistry and electrochemistry

Aside the interest of lithium isotopes in nuclear physic, geochemistry and planetary science are the fields probably discussing the most these elements[257]. For geochemists, the study of element isotopes is very powerful and can serve as a historical tracker. Indeed, because of the difference in neutron number, the isotope mass differs and can induce a fractionation in the considered medium. This effect is referred to as mass-dependent isotope fractionation, and is related to the differences in kinetic reaction and equilibrium between isotopes[258]. This mass-dependent effect is extensively used to describe phase equilibrium in the solar system materials[259], however, mass-independent effects have also been reported. This is the case of magnetic isotope effect that drives the isotope fractionation by magnetic interaction because of differences in their respective nuclear spin[260]. A fascinating example is the oxygen isotope separation in the production of ozone (O_3). This radical reaction is driven by magnetic isotope fractionation and leads to the enrichment/depletion of ^{17}O and ^{18}O isotopes because of differences in reaction kinetics[261]. This mass-independent effect can be used to track radical reactions in the environment. If these mass-independent effects were observed, they would still be less predominant than the mass-driven fractionation.

In terms of mass-dependent isotope effect, a good example is water electrolysis. Upon electrolysis of water naturally containing H_3O^+ and D_3O^+ ions, the reduction at the cathode is favoured for the lightest isotope because of higher diffusion coefficient and lower activation energies of charge transfer. Indeed, B. E. Conway measured higher exchange current densities for hydrogen than for deuterium reduction, resulting in a higher charge transfer kinetic regardless of the metal electrode used [262]. This kinetic isotope effect depends on the zero-point energy (ZPE) defined as the minimal energy of the system at 0 K. The ZPE is inversely proportional to the system mass, meaning that deuterium imposes a lower ZPE on the system than hydrogen. It results in a higher activation barrier energy for breaking bonds involving deuterium than hydrogen, justifying the lower charge transfer kinetic of ^2D reduction[263]. The isotope mass not only affects the kinetics, but also the viscosity of D_2O or H_2O resulting in 23% higher conductivity of ions in light water (H_2O) than in heavy water (D_2O)[264]. This also results from the lower ZPE of heavy water, the bonds between deuterium and oxygen are stronger and more rigid than the H-O bonds leading to a higher viscosity of the solution.

To take advantage of the isotopic mass effects in the electrochemical field, one could hope to improve the transport processes by decreasing the atomic mass of the transported species by selecting a lighter isotope. Obviously, these mass-dependent isotope effects are more or less pronounced depending on the isotope couple. In **Table 15** are summarised some usual elements with their stable isotopes, mass and mass fraction. The mass fraction is more important for low

atomic number elements because of a higher ratio of neutron number, yielding to the highest mass fraction for hydrogen isotopes (^{1}H is 50% lighter than ^{2}D). To envisage this strategy of substitution, the selected element should be more abundant under its higher mass form, *e.g.* it is the case of helium that is abundant with more than 99% under the ^{4}He form. Then, the substitution of ^{4}He into ^{3}He would lead to a decrease of almost 25% of the element mass. Unfortunately, the use of noble gases in electrochemical systems is practically uninteresting. Concerning the battery field, one can focus on the different alkaline and alkaline-earth metals used as ion species in ion-batteries such as LiBs, Na-ion, K-ion, etc… The only interesting element is lithium with ^{7}Li being the more abundant and providing a reasonable mass fraction between the two isotopes since it is the lightest alkaline metal.

Table 15: Stable isotopes of some elements, with their respective mass and mass fraction. Values taken from refs. [265,266].

Element	Isotopes	Abundance (%)	Atomic mass *(u)*	Mass fraction (%)*
Hydrogen	^{1}H	99.99	1.008	50.0
	^{2}D	0.01	2.014	
Helium	^{3}He	0.0001	3.016	24.7
	^{4}He	99.9999	4.003	
Lithium	^{6}Li	7.5	6.015	14.3
	^{7}Li	92.5	7.016	
Sodium	^{23}Na	100	22.990	-
Magnesium	^{24}Mg	78.99	23.985	7.7
	^{25}Mg	10.00	24.986	
	^{26}Mg	11.01	25.983	
Potassium	^{39}K	93.26	38.964	4.9
	^{40}K	0.01	39.964	
	^{41}K	6.73	40.962	

2.2 Lithium isotopes in batteries

2.2.1 Uses of Li isotopes as tracer

In the battery field, ^{6}Li isotope is mostly used as a tracer to highlight diffusion mechanisms. This was the PhD thesis subject of Bertault that investigated the diffusion of ^{6}Li through the graphite and silicon SEI using time of flight secondary ion mass spectroscopy (ToF-SIMS) and NMR

* The mass fraction corresponds to the relative mass of the lightest isotope compared to the heaviest (*e.g.* $1\text{-}m_{1\text{-}H}/m_{2\text{-}D}$). For the elements with three stable isotopes, the mass fraction implies the lightest and heaviest isotopes.

techniques[267]. Similarly, Meyer developed a method to characterise the diffusion mechanism of lithium in a solid-polymer electrolyte using ToF-SIMS and solid state NMR[268]. Diehl *et al.* also investigated the diffusion of ^{6}Li isotope in a NMC622/graphite full cell composed of $^{6}LiPF_6$ as electrolyte salt with ICP-MS[269]. The authors characterised the diffusion of ^{6}Li inside the two electrodes, showing an enrichment of the NMC positive electrode upon successive cycles because of the substitution of ^{7}Li in the material structure.

Due to the high absorption cross-section of ^{6}Li for neutrons, Li-ion batteries are studied in neutron reactors with dedicated beamlines. For this purpose, Neutron Depth Profiling (NDP) experiments were developed based on the nuclear reaction described in **Figure 132**. By illuminating an electrochemical cell uniformly, most of the neutrons cross the sample without interacting, but when these neutrons interact with ^{6}Li isotopes, the nuclear reaction generates tritium and helium ions with very specific energies (2.055 and 2.727 MeV respectively). These generated atoms interact with electrons of the sample and lose energy by travelling and the energy loss can then serve to estimate the depth of the initial lithium entity[270]. As an example, Verhallen *et al.* investigated the de/lithiation of LTO vs. ^{6} lithium half-cell under successive 30 C charge/discharge cycles[271]. By illuminating a pouch-cell, the tritium emitted particles were captured by a dedicated camera, and NDP quantification was possible. In **Figure 133a** are represented the voltage profile of the LTO half-cell and the lithium content (x in $Li_xTi_5O_{12}$) for 20 successive cycles.

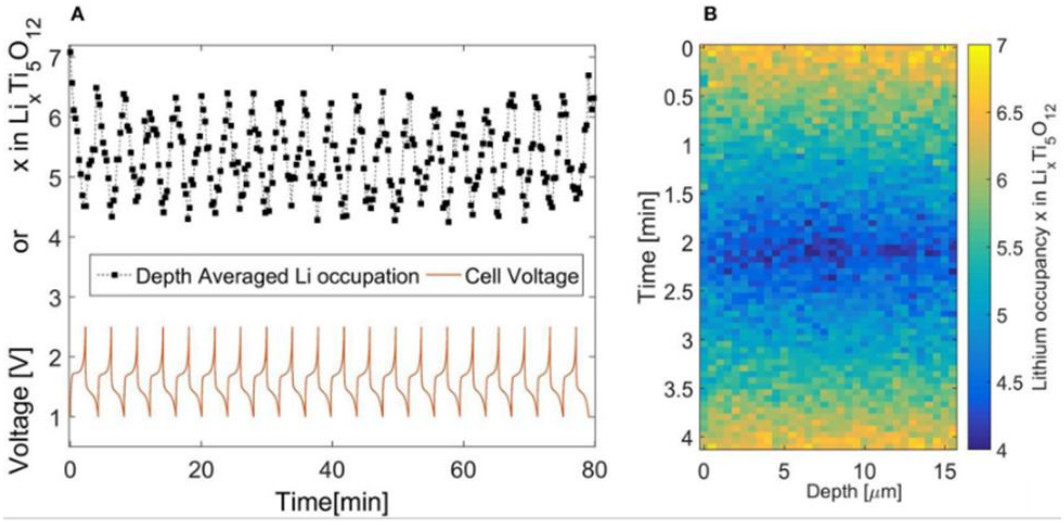


Figure 133: a) Cycling of $Li_4Ti_5O_{12}$ upon NDP experiment at 30C rate. b) Average mapping of the lithium content for the 20 cycles as a function of the electrode depth (current collector = 0 µm, separator = 15 µm). Reprinted with permission from ref. [271].

The authors claimed a good reproducibility of lithium content quantification upon charge and discharge, ranging from $Li_4Ti_5O_{12}$ to $Li_7Ti_5O_{12}$. The 20 cycles were averaged for the charge and discharge, and the lithium content as a function of the electrode depth is given in **Figure 133b**.

This investigation highlighted a homogeneous lithium distribution along the electrode depth, demonstrating the high-power capability of LTO even for an ultra-high cycling rate of 30C.

2.2.2 Uses of lithium isotopes to dope the performances

In addition to the use of lithium isotope as a tracer, some studies investigated the properties associated to ^{6}Li in batteries. It is very likely that the mass-dependent effect of isotopes governs the differences between lithium isotopes properties in batteries. It was observed for hydrogen isotopes that this mass-effect induces differences in not only the transport of the element, but also the charge transfer of redox reactions. For this reason, this effect should be effective along the whole charge and discharge processes of a battery, *i.e.* for the diffusion and migration in the electrolyte, diffusion at the solid state and for the charge transfer at the electrolyte/electrode interface.

Périé *et al.* investigated the isotopic effect on lithium migration in concentrated aqueous electrolytes[272] by electromigration. By evaluating the relative mobility between the two lithium isotopes, the authors showed higher mobility for the lightest isotope, with dependence on the concentration. The experiment was realised in ammonium nitrate and ammonium acetate solutions, until ~10 M of salt concentration. By increasing the concentration of the lithium salt, the relative mobility changed from ~0.004 (~ 1 M) to 0.015 – 0.017 at concentrations higher than 10 M. This means that ^{6}Li is 1.17% more mobile than ^{7}Li for very high concentration, whereas for very diluted solutions, the mobility difference still exists but is very low. In diluted solution the lithium isotopes are highly solvated by water molecules (4 molecules) and a very slight residual isotopic effect exists. This can be attributed i) to the slightly lower solvation sphere radius of ^{6}Li that increases its mobility ($\mu \propto 1/R$) and/or ii) to a faster migration because of the lower mass of ^{6}Li. For high concentrations, a decrease of lithium mobility was observed justified by the creation of ion pairs and aggregates, and the increase of viscosity. A new equilibrium is established between the lithium isotopes and the ion-pairs, and this is responsible for a higher contrast between the isotopic mobility because the ion-pair composed of ^{7}Li are more difficult to break. This justifies the higher difference in relative mobility between the two isotopes observed by increasing the salt concentration. To conclude, this study nicely illustrates the effect of using ^{6}Li instead of ^{7}Li to boost the mobility of the lithium ion and improve its transport in the electrolyte. However, the gain in mobility is very poor with less than 2% for very high concentration.

If this study highlighted a mass-dependent effect on lithium isotope, other experiments demonstrated counter-intuitive behaviours in molten salts. In the late 1950s, by studying the migration of cations in binary molten salts such as (Li, K)Br, Chemla discovered that the larger cation (K^{+}) can display a higher mobility than the smaller one (Li^{+}) depending on the composition range of the salt. This counter-intuitive phenomenon is a mass-independent isotopic effect and is

now known as the "Chemla effect"[273]. In general, this effect refers to molten salts in which the heavier cation exceeds the lighter cation in terms of mobility over a discrete range of composition as illustrated in **Figure 134**. These experimental observations were corroborated by calculations later in ref.[274]. This effect has important consequences for isotopes and demonstrates that mass-independent effects can provide a better mobility to heavier isotopes in specific conditions.

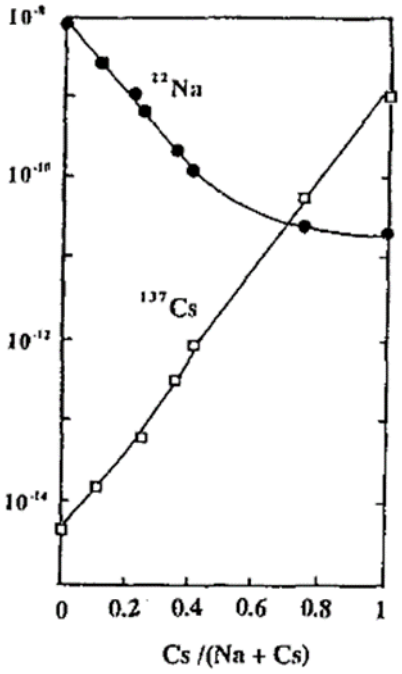


Figure 134: Chemla effect on the $(Na, Cs)_2Si_3O_7$ molten salt. The mobility (left axis) of sodium decreases whereas that of Cs increases by increasing the Cs fraction. A crossing point of equal mobility is observed. Reprinted with permission from ref. [273].

From these studies, it is very difficult to anticipate the impact of substituting natural lithium for ^{6}Li in a Li-ion battery. However, in the case of a mass-dependent effect providing a better mobility to the ^{6}Li isotope, the gain would be rather low.

To date, only few papers have discussed the impact of lithium isotope on the insertion in graphite for LiBs. Yanase *et al.* investigated the effect of lithium isotope on the intercalation in graphite[275]. By quantifying the isotopic ratio of lithium in *post-mortem* chemical analysis, the authors demonstrated a preferential intercalation of the lightest isotope, and this dependency was observed to increase with the graphite state of lithiation (x in Li_xC_6). The separation factor ranged from 1.007 to 1.025 which means that an increase of 0.7 to 2.5% in ^{6}Li was observed compared to the initial isotopic fraction. By discussing the several steps in the lithium insertion, it was claimed that the separation factor attributed to the diffusion of Li^+ in the ethylene carbonate solution ($Li^+[Ec]_4$) should reach only 1.0014. It demonstrates that the diffusion of lithium in the electrolyte cannot solely explain the separation factor obtained. Instead, it was suggested that the equilibrium

between solvated lithium in the electrolyte and intercalated lithium was at the origin of this isotopic effect, as well as the one with the SEI. However, the authors excluded the diffusion of lithium in the graphite layers as possible origin, but no clear explanation were given. Considering the lack of clear explanation and evidence, this demonstrates that the origin of this effect is not understood in the whole process of intercalation.

Modelling was also used to compute the reduced partition function ratio of lithium isotopes in graphite. Using DFT, Sato *et al.* calculated an equilibrium lithium isotope exchange constant between lithium ions solvated by EC:DMC solvents and intercalated lithium in a coronene molecule at 1.034[276]. The authors criticised the unsatisfactory agreement with the experimental results of 1.025 to the reduced size of coronene to mimic the graphite structure. Still, it demonstrates that the magnitude order of isotopic exchange in the equilibrium between solvated lithium and intercalated lithium is of few percent.

Only one paper was found with the aim of taking advantage of isotope elements in the battery field. Li *et al.* investigated the impact of isotope in Li-S batteries by substituting both lithium and sulphur elements[277]. First, the authors demonstrated that even if ^{6}Li provides the highest specific capacity of 4467 mAh.g^{-1} among metal electrodes (3860 mAh.g^{-1} for natural lithium), the impact of ^{7}Li to ^{6}Li isotope in a practical Li-S battery is limited to a gain of +1.51% in total energy density.

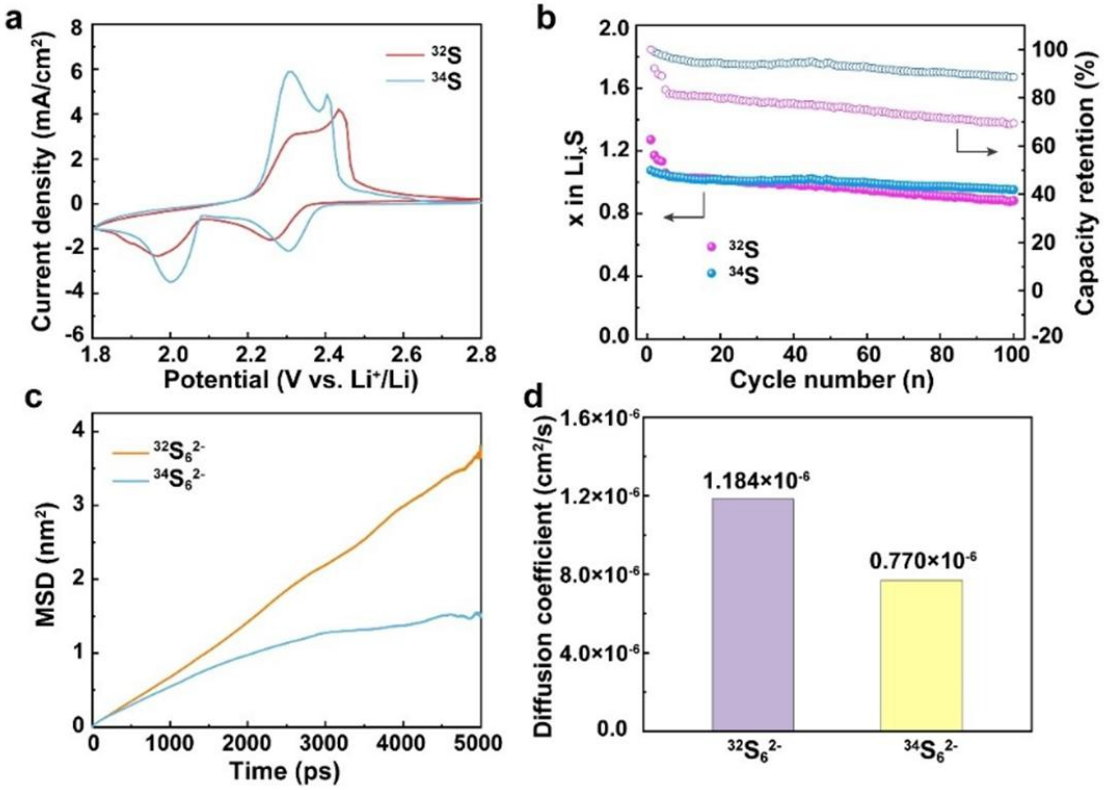


Figure 135: a) Cyclic voltammetry for the Li-^{32}S and Li-^{34}S cells. b) Capacity retention of both cells. c) Mean square displacement of $^{32}S_6^{2-}$ and $^{34}S_6^{2-}$ species by molecular dynamic. d) Calculated diffusion coefficient of both anions in $LiPF_6$ with 1,2-dimethoxy ethane as electrolyte. Reprinted with permission from ref. [277].

Then, by cycling Li-^{32}S and Li-^{34}S cells by cyclic voltammetry and galvanostatic protocol, it was evidenced in **Figure 135a, b** that a reduced polarisation and a higher capacity retention was obtained with the heavier sulphur isotope. This was attributed to a reduced shuttle-effect (diffusion of polysulphides in the electrolyte) and an improved reaction kinetic at the sulphur electrode-electrolyte interface. These hypotheses were validated by molecular dynamic calculations (**Figure 135c, d**) showing a lower diffusion coefficient for $^{34}S_6^{2-}$ anion and as a consequence, a more sluggish anion diffusion in the electrolyte. This paper is a nice example of a strategy taking the advantage of mass-dependent isotopic effects, where the higher mass of ^{34}S enables the reduction of parasitic phenomenon in Li-S batteries.

3 INVESTIGATION OF THE LITHIUM ISOTOPE EFFECT

In this state of the art, it was evidenced that lithium isotopes display different properties mainly due to mass-dependent effects and different radius of solvation spheres. This can result in better mobility and faster kinetics of transport and transfer for the lightest isotope, *i.e.* ^{6}Li, but the reported gain is of the magnitude order of few percent (1 – 2%). Based on this, this study aims to investigate the impact of substituting natural lithium with ^{6}Li isotope in graphite vs. lithium half-cells. Multiple characterisations will try to figure out the effect of ^{6}Li in the several transport processes of the battery, *i.e.* diffusion and migration in the electrolyte and diffusion at the solid-state. The interest of ^{6}Li to boost the power properties of such half-cells will be evaluated by means of rate capability tests.

3.1 Impact of Li isotope on the transport properties

To investigate the impact of lithium isotope in rate capability of graphite electrode, a ^{6}Li-enriched electrolyte was prepared as described in p**81**. The electrolyte, called ^{6}LP30, consists in a $^6LiPF_6$ salt dissolved in EC/DMC (1:1%$_v$) solvents, and the targeted concentration was 1 mol.L^{-1} to enable a proper comparison with a classical LP30 electrolyte. Unfortunately, issues with the salt purity were encountered on multiple batches of ^{6}Li-enriched salt (see p**81**). A description of the method used to quantify the salt concentration of the ^{6}LP30 electrolyte is presented in p**81**. The lithium concentration was not accessible with the available equipment, and the salt concentration was only inferred from the PF_6^- anion concentration in the ^{6}LP30 solution. ^{19}NMR tests revealed a salt impurity ranging from 20% - 80% depending on the received batch.

Two hypotheses can be envisaged, either the overall $^6LiPF_6$ salt is not pure, meaning that part of the salt mass contains impurities, or the salt is partially composed of PF_6^- anions and other non-fluorinated counter-anions (impurities). To identify whether the purity issue comes from the salt purity or from the counter-anion purity only, a quantification of the lithium concentration would have provided an answer, however the measurement was not accessible with the laboratory

apparatus. Despite the lack of information on the salt purity, a ^{6}LP30 electrolyte was prepared by targeting a concentration of 1.5 M, and the obtained anion concentration was approximatively 1.26 M (~80% of purity). The electrolyte was then diluted to 1 M in anion concentration.

3.1.1 Conductivity measurement

Before testing the ^{6}LP30 electrolyte in electrochemical cell, ionic conductivity measurements were performed to compare the migration properties of ^{6}Li isotope and natural lithium. A conductivity cell was used to measure the ionic conductivity of LP30 and ^{6}LP30 solutions at different temperatures, as mentioned in p**68**. The ionic conductivities of $LiPF_6$ and $^6LiPF_6$ at 1M and 0.7M in EC/DMC (1:1%v) are given in **Figure 136**. The two conductivity measurements were performed on two different batches of $LiPF_6$ salt, by decreasing the temperature from 20°C until -15°C and then increasing until 50°C to come back at 20°C. Concerning the experiment at 0.7M (**Figure 136b**), very similar ionic conductivities are obtained in the range of the standard deviation with a conductivity of 9 mS.cm^{-1} at 20°C. The same trend is observed for a concentration of 1M (**Figure 136ba**) with a conductivity of 10 mS.cm^{-1} at 20°C for both samples ($^6LiPF_6$ and $LiPF_6$). However, an instability was observed for the 1M $^6LiPF_6$ sample leading to a non-reversible conductivity measurement, and the glass of the conductivity cell was attacked by the salt. This issue is probably linked to the salt impurities that could generate HF by decomposition the fluorinated salt. Unfortunately, the generation of HF is known to be detrimental for the SEI stability upon cycling, and can induce overpotentials.

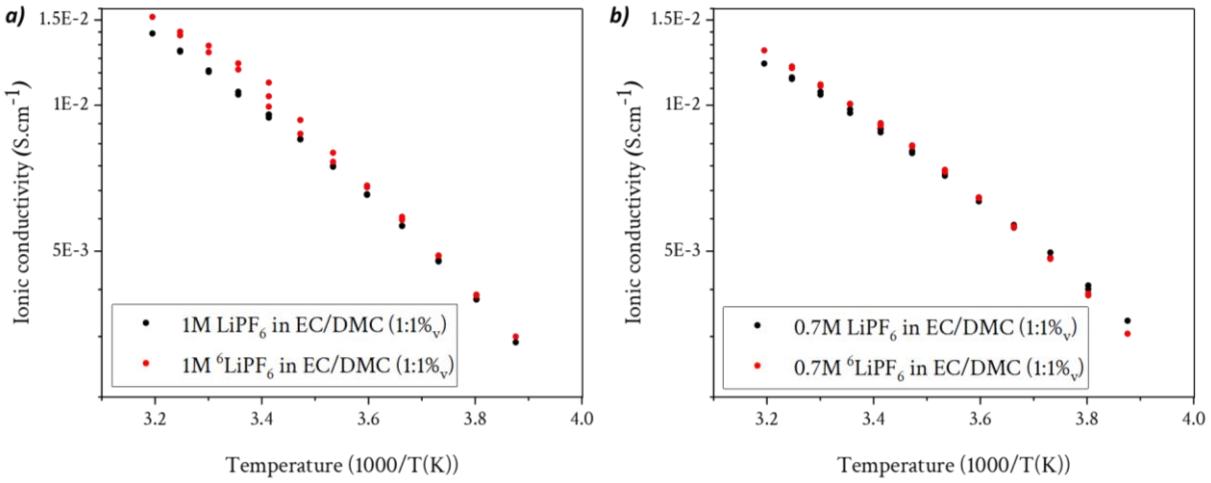


Figure 136: Ionic conductivity as a function of temperature for $LiPF_6$ and $^6LiPF_6$ salt at a) 1M and b) 0.7M in EC/DMC (1:1%v).

These conductivity measurements did not reveal any improvement of the ionic mobility by using the ^{6}Li-entiched salt, and this is rather coherent with the low transference of the cation in such electrolyte. Indeed, the Li^+ transference number is about 0.2 to 0.3 in such electrolyte, meaning that only 20-30% of the conductivity comes from the Li^+ cation. By substituting the natural Li^+

with ^{6}Li isotope, the improvement of the migration properties of the cation is not reflected in the bulk conductivity of the electrolyte.

3.1.2 Solid-state diffusion measurement

The lithium isotope can also affect the solid-state diffusion in the graphite particles. PITT experiments were realised to compare the diffusion coefficient obtained using natural lithium and ^{6}Li. The PITT experiments were realised on graphite thin-electrodes as explained in p**62**, using a potential step of 0.2 mV from 0.25 V to 0.04 V. The results for the cell involving natural lithium are taken from the experiment described in p**94**. For the ^{6}Li-enriched cell, the coin cell was composed of ^{6}LP30 as electrolyte (130 µL) with ^{6}Li counter electrode (see p**84**). The diffusion coefficients obtained from the PITT experiment are plotted in **Figure 137** as a function of the graphite electrode potential. Very similar values are obtained for the two cells with an overlap of the diffusion coefficient in most of the potential range.

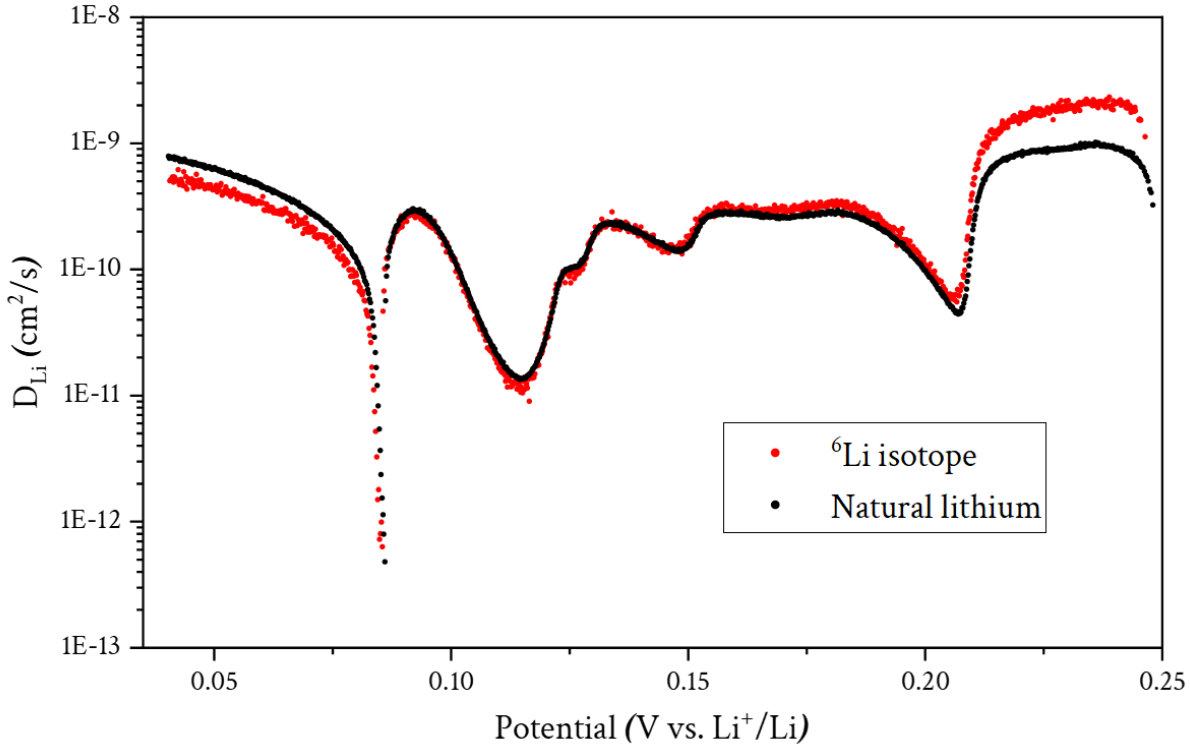


Figure 137: Diffusion coefficients as a function of the graphite potential for half-cells containing LP30 as an electrolyte with natural lithium as a counter electrode (in black), and containing ^{6}LP30 with ^{6}Li as counter electrode (in red) at 25°C.

This result shows that no difference of solid-state diffusion is measured in graphite by substituting natural lithium by ^{6}Li isotope, considering salt purity. To understand this result, one has to identify the motor of lithium diffusion in the graphite particles. Compared with transport in the electrolyte, lithium ion diffuses alone in the graphite structure, and the driving force is the concentration gradient that is established along the particle radius. At the solid-state, the diffusion

is governed by the crystal structure, the interaction between host and guest, and the diffusing ion size, but does not depend on the ion mass[278]. In this case, the interaction between lithium and carbon planes depends on the electronic density around the lithium ion and its interaction with the 2p orbitals of the graphite structure. This interaction depends on the electronic configuration of the ion, which is the same for the two isotopes. Concerning the ionic radius, it depends on the nuclear charge (number of protons) and the electronic configuration, since isotopes only differ in neutron number, their ionic radii remain identical. Then, based on the driving force in solid-state diffusion, no impact of the lithium isotope is expected, as observed in the measurement of the diffusion coefficient in graphite.

3.2 Impact of the Li isotope on the rate capability of graphite electrodes

To highlight the effect of lithium isotope on the kinetic properties of graphite electrodes, rate capability tests were realised to compare natural lithium and ^{6}Li isotope in graphite half-cells. Rate capability tests were performed on graphite electrodes of 30% porosity (the same as in the chapter IV). As for the PITT experiment, the coin cells were composed of LP30 with natural lithium as negative electrode, and ^{6}LP30 with ^{6}Li as negative electrode. First, the lithiation of both cells was analysed at C/20 under quasi-thermodynamic conditions in **Figure 138**.

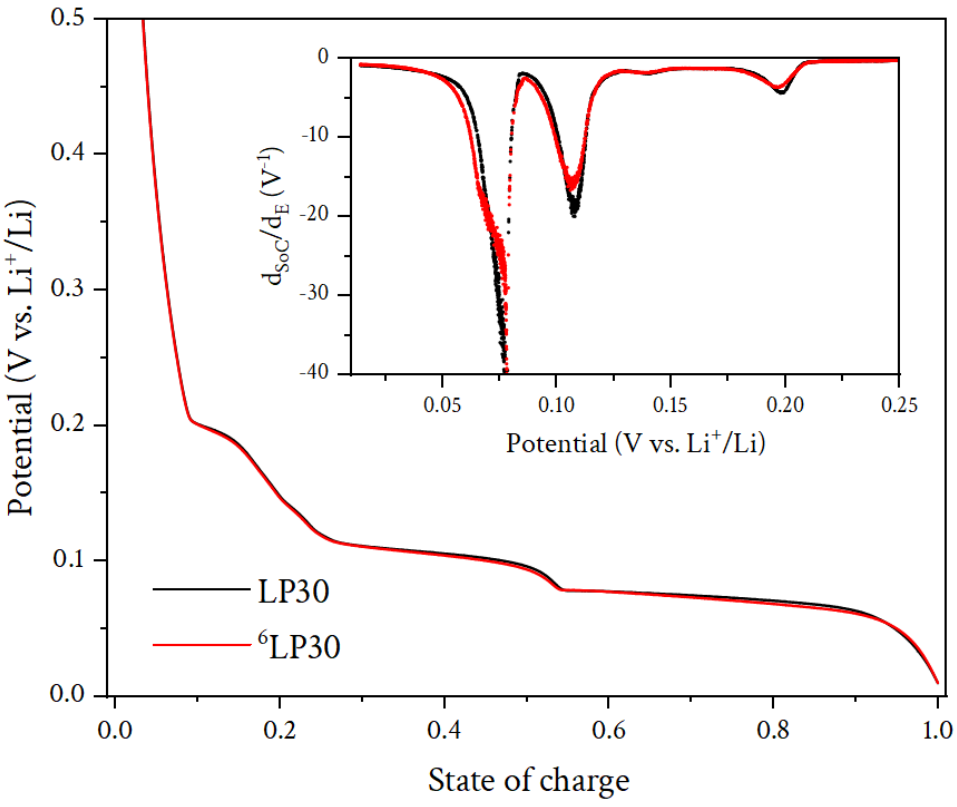


Figure 138: Graphite lithiation at C/20 rate obtained for the LP30 and ^{6}LP30-based half-cells. The inset plots the DCA analysis.

The voltage profiles are very similar for both cells with specific capacities of 391 mAh.g^{-1} (natural lithium) and 398 mAh.g^{-1} (^{6}Li isotope). The difference of specific capacity is in the standard deviation of the experiment. The voltage profiles were analysed by DCA in the inset of **Figure 138**, the peaks for the cell composed of ^{6}LP30 are slightly lower and slightly larger than for the natural lithium cell. This highlights potential plateaus a bit more polarised using the ^{6}LP30 electrolyte and ^{6}Li as counter-electrode. This effect could be attributed to the internal pressure of the coin cells that are most probably not identical. Indeed, the ^{6}Li electrode was hand-hammered leading to a thickness of probably 100 to 200 µm, whereas the natural lithium disk was 750 µm thick. This thickness difference was compensated by an additional 500 µm stainless steel spacer, however the full stack thickness was probably not identical, leading to different pressures. This higher overpotential could also be explained by the presence of HF impurities in the ^{6}LP30 electrolyte, degrading the SEI and then increasing the resistances associated to lithium diffusion.

The results of the rate capability tests are analysed in **Figure 139**. From C/20 to C/6 rates, the galvanostatic contribution over the total capacity is identical for the two cells. Similarly, the specific galvanostatic capacities obtained are very similar in this range (inset of **Figure 139**).

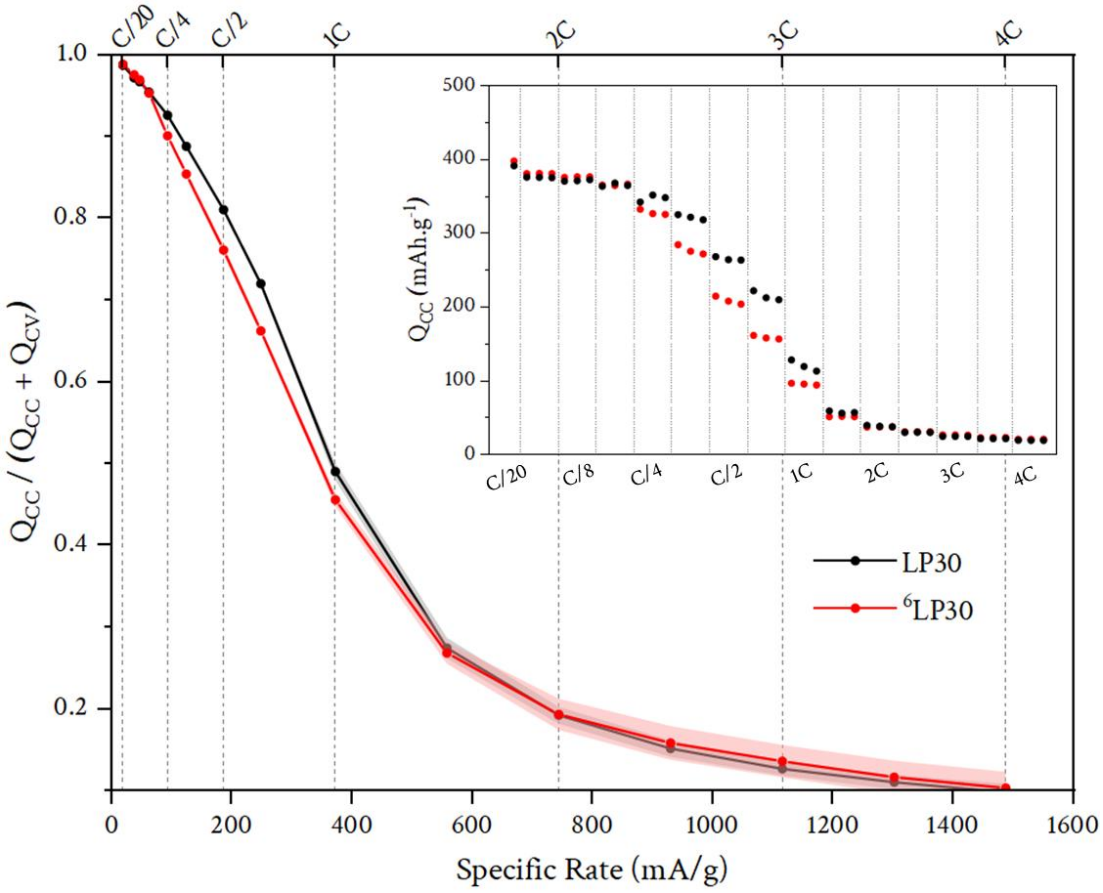


Figure 139: Rate capability of graphite half-cells composed of LP30 with natural lithium as negative electrode, and of ^{6}LP30 as electrolyte with ^{6}Li as negative electrode at 25°C. The inset plots the specific galvanostatic capacities as a function of the cycling rate. The standard deviations are represented by the black and red shadows.

By increasing the rate from C/4 to 1C, a slight difference appears with a lower galvanostatic contribution for the cell composed ^{6}Li-enriched materials. This difference of rate capability is probably generated by the HF impurities degrading the performances upon successive cycles, and/or by the difference of internal pressure of the two coin-cells. Indeed, several studies highlighted the non-negligible impact of internal pressure in coin cells and pouch cells to obtain reproductible results and on the estimated rate capability[279,280]. For higher cycling rates (> 1C) a higher standard deviation is observed and the galvanostatic capacities are similar for both cells. At such high rates, the graphite particles do not deliver any capacity and the residual capacity comes from the C65 contribution.

The lithiation profiles obtained at C/4 cycling rate are compared for both cells in **Figure 140**. The lower specific capacity of the ^{6}LP30-based cell is explained by a larger polarisation of the potential plateaus (a shift of each peak toward lower potential and larger peaks are observed on the DCA in inset of **Figure 140**). This is probably due to higher overpotentials generated by the SEI degradation caused by HF impurities and/or a higher internal pressure.

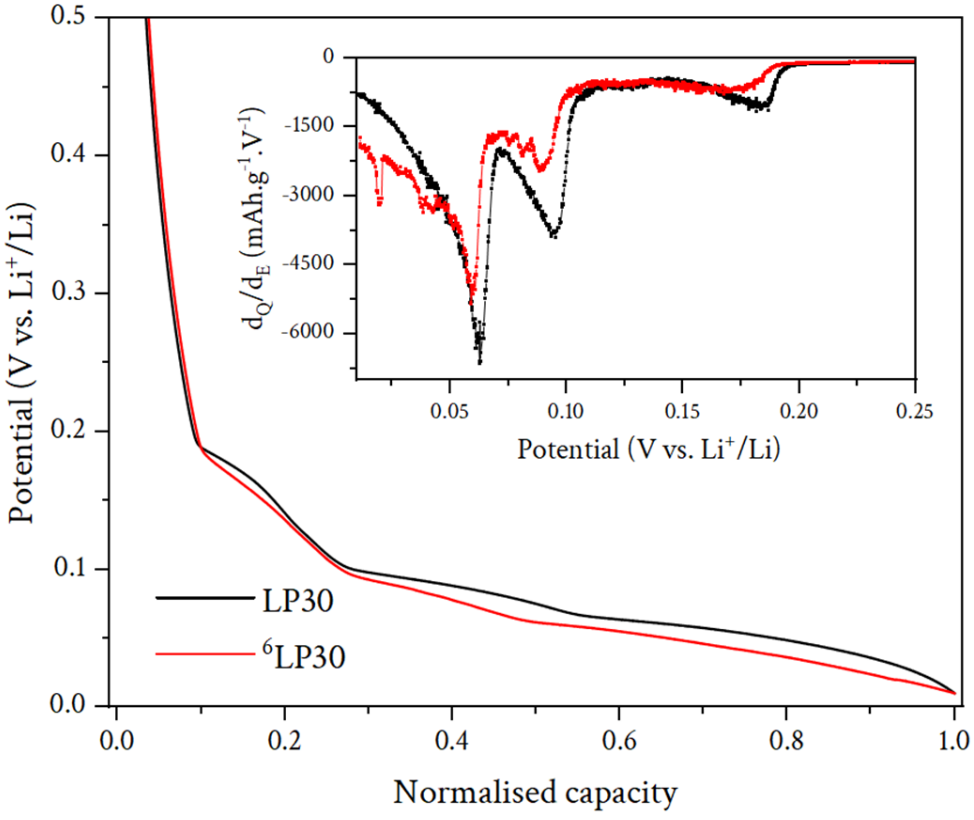


Figure 140: Graphite lithiation at C/4 rate obtained for the LP30 and ^{6}LP30-based half-cells. The inset plots the DCA analysis.

Other rate capability measurements were performed on a 0.7M $^{6}LiPF_6$ in EC/DMC (1:1%v) batch and compared with a diluted LP30 at 0.7M $LiPF_6$ in EC/DMC (1:1%v). The results are given in **Figure A9**, and similar observations can be made as for the previous rate capability test. The ^{6}Li-

enriched cell displays slightly lower rate capabilities from C/4 to 2C cycling rates. Similar hypothesis can be stated: the impurities of the $^{6}LiPF_6$ salt and/or the difference of internal pressure could be responsible for these lower performances.

To conclude, it was observed that no gain of power performance was induced by substituting natural into ^{6}Li isotope. The slight difference of rate capability observed between C/4 and 1C is probably due to the difference of stack pressure, or can be the result of the salt impurities of the $^{6}LP30$ electrolytes. Due to the high number of additional parameters that can impact the rate capability performances, it is difficult to properly conclude on the effect of the ^{6}Li isotope and its impact on the power capabilities in graphite electrodes.

4 CONCLUSION – CHAPTER VI

The impact of the substitution of natural lithium into ^{6}Li-enriched materials was investigated. The state of the art demonstrated that mass-dependent effects take place in electrochemical systems with higher mobilities for ^{6}Li isotope compared to ^{7}Li. Better kinetics of charge transfer were also reported. All these positive effects are related to the lower mass of ^{6}Li, its higher zero-point energy (ZPE) and its slightly lower solvation sphere radius. If these effects were significant under migration conditions (electromigration), they only led to ~1 – 2 % increase of lithium isotope fractionation.

The experimental investigations were focused on the characterisation of the effect of lithium isotope and the transport processes in graphite half-cells. On the mobility in the electrolyte, no effect of the lithium isotope was observed which is probably explained by the low cation transference number in LP30-type electrolytes. For the solid-state diffusion, no impact of the isotope was observed, correlating with an identical electronic cloud between both lithium isotopes. The rate capability of the graphite half-cells composed of LP30 and $^{6}LP30$ were analysed, and no gain in power performance was observed by using the ^{6}Li-enriched materials. The results of these studies should be interpreted with cautious for several reasons:

- The $^{6}LP30$ electrolyte was not ideal for the investigation because of an impurity of the counter-anion, and the suspicion of HF impurities for some batches. The PF_6^- anion was pure up to ~80% based on NMR measurements, and the effect of the unknown counter-anions could reduce the overall mobility.
- The ^{6}Li foil was thinner than the natural one, leading to probable differences of pressure inside the coin cells. This could result in a significative impact on the overpotentials and on the estimated power capabilities.

The difference in mobility of lithium isotopes is very low (< 1%) in the case of simple experiments only involving migration of lithium ions. Here, the experiments combined multiple complex and concomitant processes, and the performance of the cells do not only depend on the lithium transport properties. For this reason, the gain in mobility using ^{6}Li isotope is probably screened by other processes and it results in no difference of power performance of the graphite electrodes. Another hypothesis is also to consider that the experiments uncertainty is probably too high and would "hide" the isotopic effect.

A very crucial point arises from this study, that is the purity analysis of the commercial products that are used in the battery field. Indeed, in haste, electrolyte solutions are mostly prepared without taking care of the salt or solvents purity because of their "commercial" nature, and the results interpretation could be biased by these issues. In addition, one important aspect is the ageing of electrolyte solutions that occurs even in controlled atmospheres. Through our investigations, an important deviation of the results was observed with increasing the electrolyte age, probably because of HF generation with the contact of humidity traces and the degradation of the salt. On this purpose, it is of utmost importance to provide detailed information on the preparation of "home-made" electrolyte, as well as ensuring the use of fresh electrolyte solutions to ensure reproducibility and the truthfulness of the data interpretation.

In terms of prospects, one interesting aspect is the interaction between graphite and lithium isotopes. To highlight whether the lithium isotope has an impact on its interaction with the graphene planes, calculations using molecular dynamic or Density Functional Perturbation Theory (DFPT) could provide valuable information. Experimentally, the impact of the lithium isotope on the charge transfer between Li and C could be reflected through the phonon modes. Indeed, by substituting the lithium isotope, the vibrational modes can slightly shift because of differences in zero-point energy, and one could probe this difference by vibrational methods such as Raman spectroscopy.

Conclusion

If graphite is the oldest material studied for Li-ion batteries; challenges are still real, especially on the correlation between the electrode microstructure and the power capabilities. For this reason, investigations were carried out to answer this first question:

What are the causes of the limited power capability of graphite electrode in LiBs?

Through characterisations that combine morphological, structural and electrochemical analyses, the ionic transport of lithium was identified as the origin of lithiation heterogeneities upon cycling. The tortuosity of the ionic pathway limits the mass transport along the electrode thickness and a lithiation gradient appears creating a gradient of state of charge with favoured lithium insertion near the separator/electrode interface as illustrated in **Figure 141** at the electrode level. As a consequence, the ionic tortuosity is a key parameter to control *via* the electrode engineering, by playing on the electrode porosity and the graphite particle shape for example. However, this phenomenon has drastic consequences at the industrial scale since the porosity of the electrode should be as low as possible to maximise the energy density.

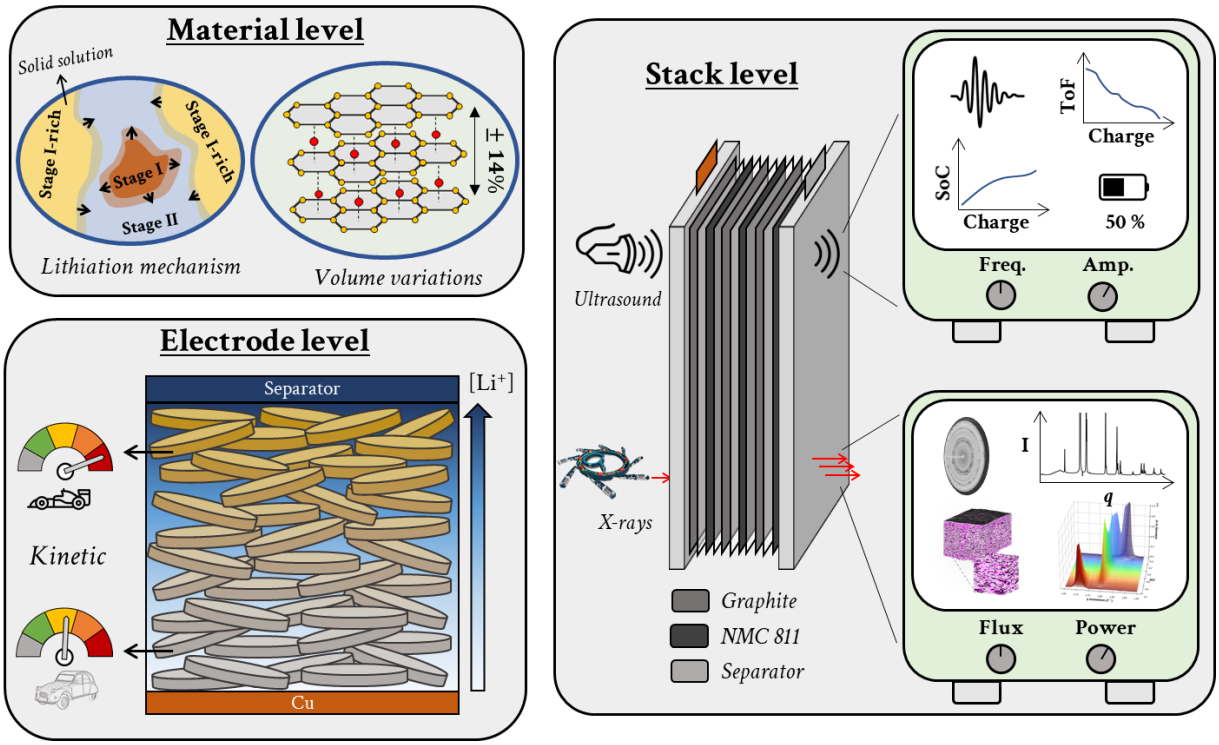


Figure 141: Illustration of the key research in the thesis.

The quantification of lithiation heterogeneities along the electrode thicknesses revealed a peculiar dynamism following the several lithium insertion mechanisms. Consequently, higher lithiation kinetics was observed at the separator/electrode interface raising important questions about the

ageing of graphite electrodes. These investigations demonstrated the importance of working on the electrode engineering to master microstructure of the graphite electrodes to find a good balance between power capabilities, energy density and long-term cycling.

Another important parameter when it comes to power capability and ageing is the mechanical evolution of the electrode upon cycling. Subject to volume expansion and shrinkage at the crystal lattice scale, the graphite electrodes display significative anisotropic thickness evolutions up to 14% along the *c*-axis. By means of dilatometric measurements, mechanical aspects were investigated to understand the impact of the electrode microstructure on the volume changes induced at the particle level. The results highlighted the important accommodation of the volume changes by the electrode porosity, and by the binder deformation. It demonstrated the importance of the elastic properties of the polymer to accommodate the electrode dilatation and contraction upon cycling. The investigation of mechanical parameters upon cycling was pushed further by studying a graphite | NMC811 commercial cell with ultrasound technique. However, to date, it remains unclear what the ultrasound can really probe, that is why, a structural investigation was performed on the commercial cell to correlate both signals. It was evidenced that the time of flight of the ultrasound wave is mainly driven by the variations of elastic properties of the graphite electrode. This investigation highlighted the potential of ultrasound to be implemented in battery management systems to monitor the structural changes of the electroactive materials upon cycling.

As changing the electrode microstructure is always difficult and requires tremendous work, an innovative approach was investigated by substituting the natural lithium salt with a ^{6}Li-enriched salt. Despite the rather poor literature on the impact of lithium isotopes in Li-ion batteries, mass-dependent effects were observed, leading to an improvement of the migration of lithium and the lithiation kinetic of few percent. The investigation of the transport properties of lithium isotope revealed no impact on the diffusion coefficient at the solid-state, nor on the ionic conductivity of electrolyte. Rate capability measurements were performed but it is very difficult to draw a proper conclusion on the effect of the ^{6}Li isotope because of the inference of parameters such as the internal cell pressure and the salt purity.

Based on the acquired knowledge, several research directions can be given for the future. The limiting factor in the lithiation of graphite electrodes is the diffusion of lithium ions inside the porous microstructure, and a very important point is the measurement of the penetration depth defined as the point where the salt concentration reaches zero. Unfortunately, by using X-ray sources the lithium element is transparent and the local lithium concentration inside the electrolyte cannot be assessed. This is feasible using neutron sources thanks to the high absorption factor of ^{6}Li isotope. For this purpose, an experiment was realised at the NeXT beamline from Institute-Laue Langevin (ILL) to acquire neutron radiographs of graphite half-cells upon charge

and discharge. By probing Swagelok cells composed ^{6}Li-based materials and electrolyte **(Figure 142b**), a gradient of lithium concentration could be observed inside the graphite electrode and the separator. Such quantitative analysis would provide a direct visualisation of the penetration depth of lithium inside the electrode microstructure. However, a real challenge is to optimise the cell composition to obtain clear contrasts between each element of the cell and to avoid causing the detector saturation to enable quantitative analysis.

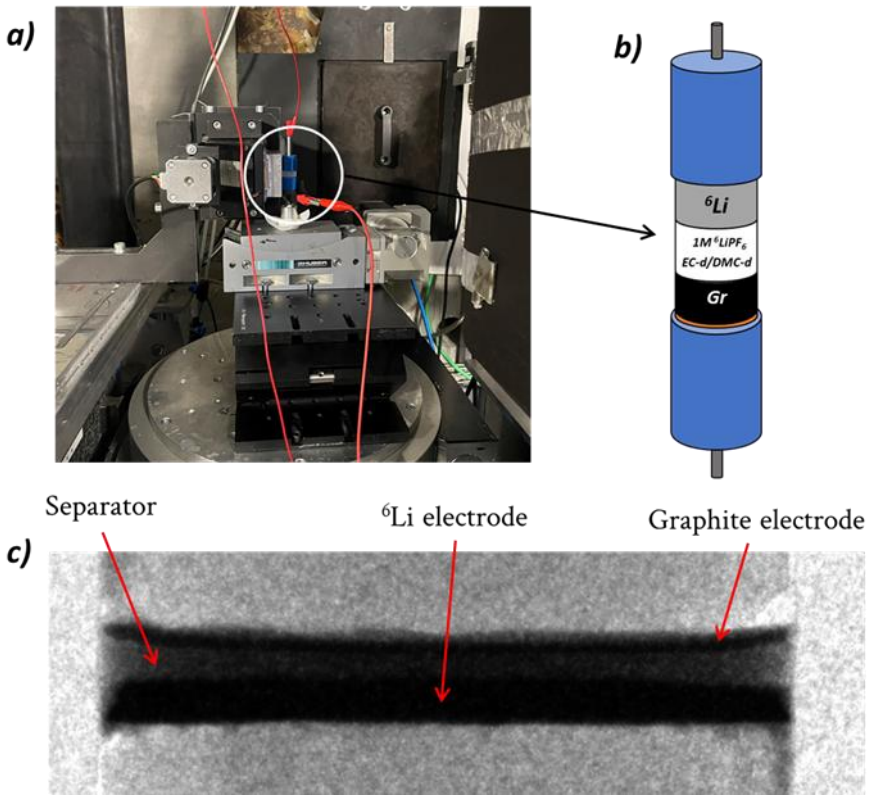


Figure 142: Neutron radiography experiment at NeXT beamline (ILL, Grenoble). a) Photograph of the experimental set-up. b) Illustration of the Swagelok cell probed. c) Radiograph of the electrochemical cell.

Pursuing the mechanical investigation, all reports in the literature investigate full cells, in which the signature of each electrode is convoluted in the global ultrasound signal. However, the signature of each electrode should be independently investigated to better understand the evolution of ultrasound signal. For this purpose, preliminary experiments were realised to characterise the charge and discharge of graphite half-cells using ultrasound transmission experiment as represented in **Figure 143a**.

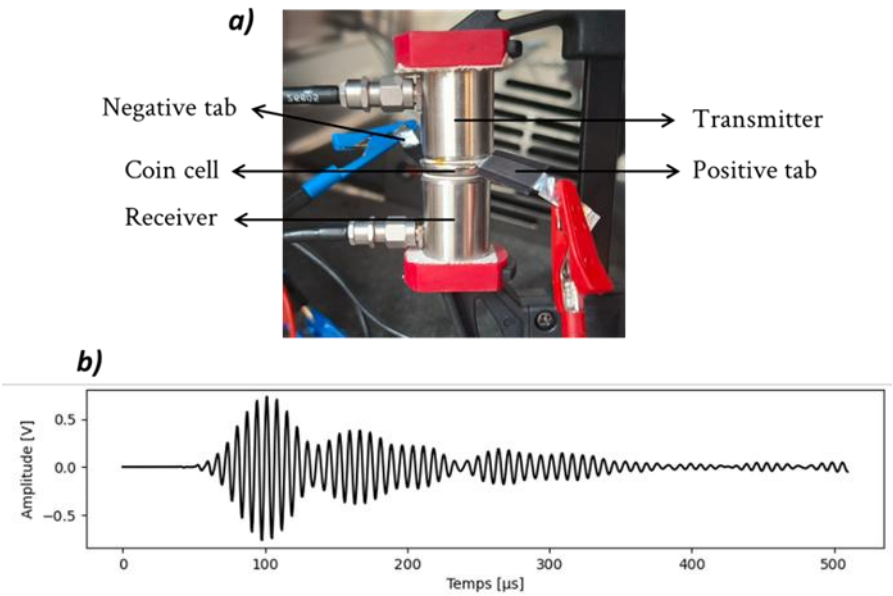


Figure 143: Ultrasound transmission experiment on a graphite half-cell in coin cell configuration. a) Photograph of the experimental set-up. b) Transmitted ultrasound signal.

The challenges of such experiments are related to the optimisation of the experimental set-up to probe, in a reproducible way, the response of the graphite electrode solely. The analysis of the ultrasound time of flight or its amplitude could enable the determination of parameters such as the elastic modulus of graphite electrodes *in operando* with a non-invasive approach and could serve as input in mechanical simulations.

APPENDICES

1 CHAPTER III

1.1 Mass centre analysis

To verify whether the mass centre is a good indicator of the structural state of graphite upon lithiation, the mass centres of each diffraction pattern acquired upon the aforementioned experiment were calculated. The data were correlated to the electrochemical signature in **Figure A1** and the same seven regions of interest were delimited as in **Figure 78**.

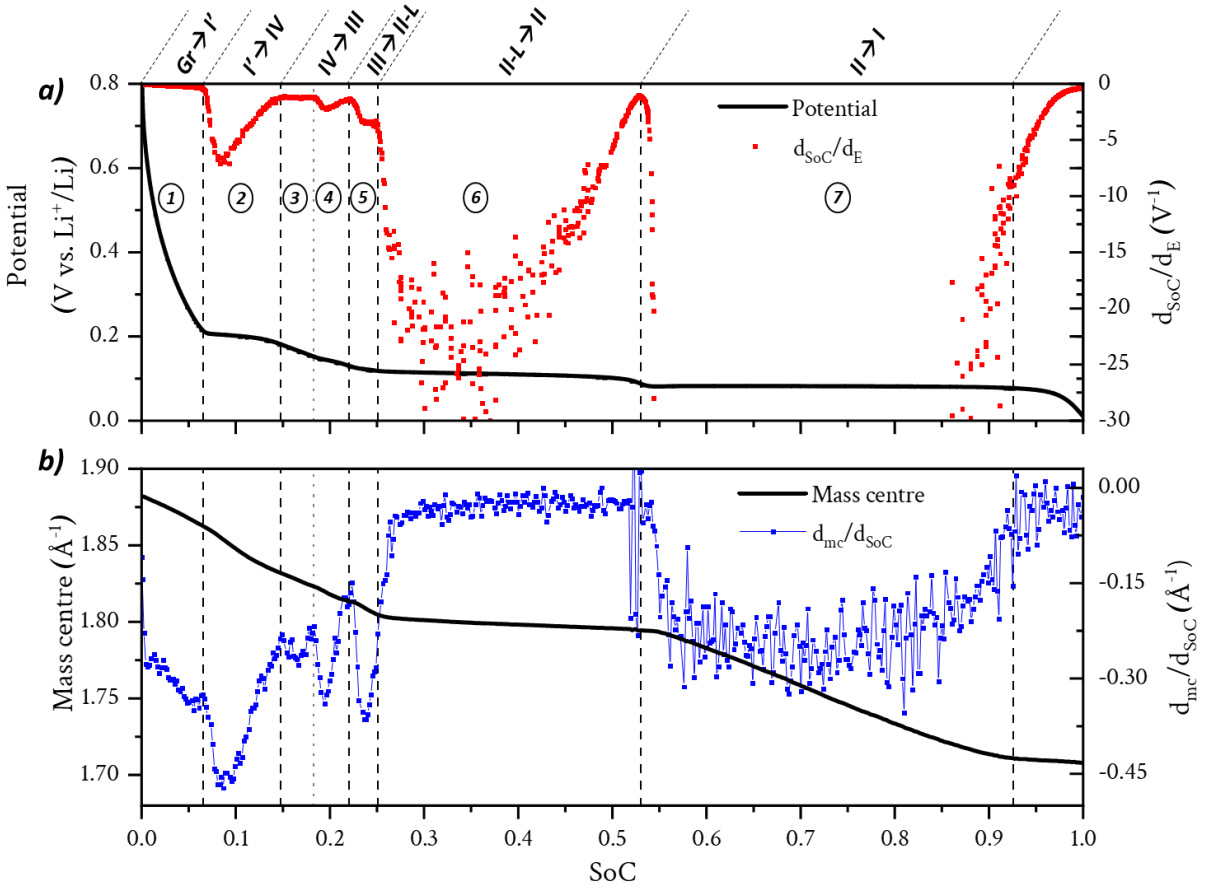


Figure A1: a) Evolution of graphite electrode potential (vs. Li^+/Li) on the left y-axis and d_{SoC}/d_E on the right y-axis with respect to the cell SoC (note here that the right y-axis is voluntarily zoomed), b) Evolution of the mass centre on the left y-axis and its derivative (on the right y-axis) with respect to the SoC.

In region 1, a shift of the mass centre correlates with the first solid solution mechanism. A non-linear evolution of the mass centre is observed through its derivative form ($d_{mc}/d_{SoC} = f(SoC)$, **Figure A1b**), implying that a solid solution process does not necessarily implies a linear shift of *d*-spacing. For region 2, it was suggested earlier that a dual mechanism transform the stage I' to stage

IV, with both biphasic and solid solution contributions. Indeed, no linear evolution of mass centre is observed as expected for a biphasic transition (no plateau is observed on the $d_{mc}/d_{SoC} = f(SoC)$ curve). Notice that the asymmetry observed on the $d_{SoC}/d_E = f(SoC)$ representation correlates with the asymmetry observed on the mass centre derivative. Supporting a good sensitivity of the mass centre to the electrochemical processes.

A rather linear shift of mass centre is observed for region 3, correlating with a solid solution process. For region 4 and 5, a local minimum on the mass centre derivative curve can be observed in agreement with a local minimum on the $d_{SoC}/d_E = f(SoC)$ representation. In region 6, attributed to the stage II formation from stage II-L, a very low variation of mass centre is observed because of the very close *d*-spacing for the two phases (1.792 $Å^{-1}$ and 1.784 $Å^{-1}$ for LiC_{18} and LiC_{12} respectively[198]). Therefore, the uncertainty in the relationship between mass centre and graphite structural SoC is the highest for this region. For the last region 7, the mass centre becomes noisier due to the higher spacing between each diffraction peak (1.71 $Å^{-1}$ and 1.80 $Å^{-1}$), but still one can observe a rather linear evolution of mass centre between 55% - 80% SoC. From 80 – 85% to 100% SoC, the mass centre evolution is no longer linear, and correlates with the appearance of solid solutions domain, leading to the enrichment of stage I as discussed above.

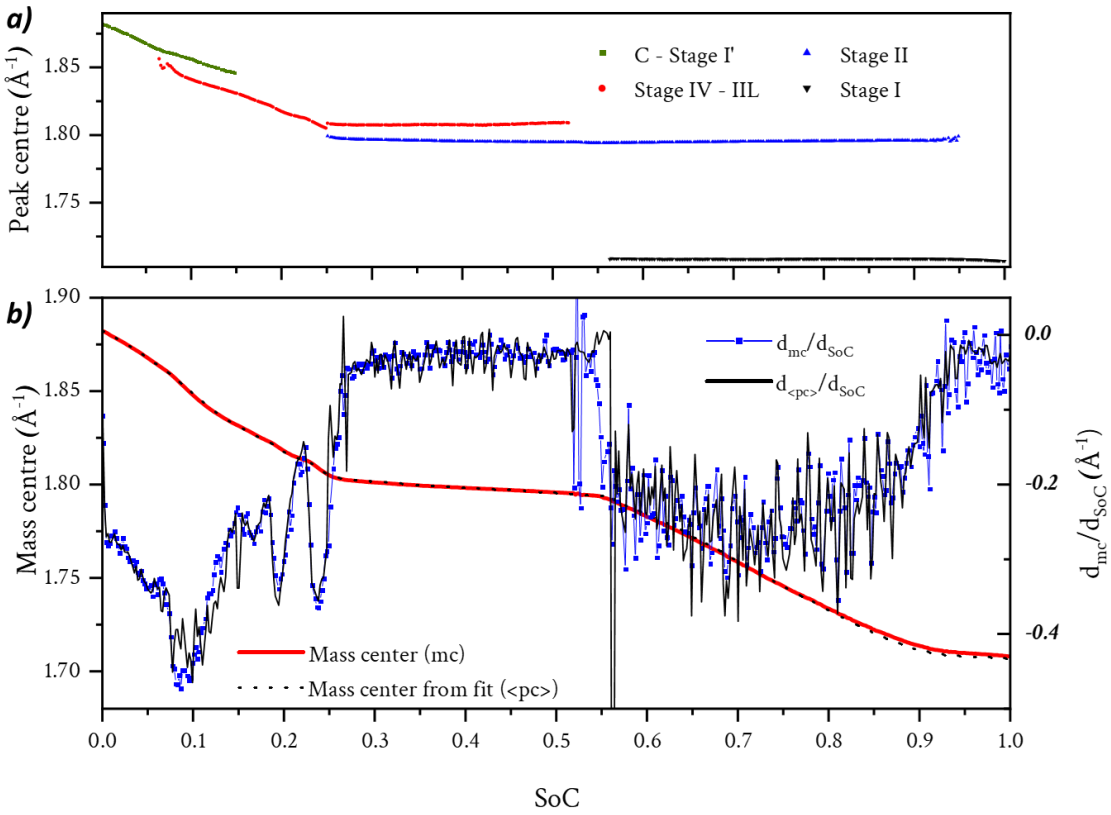


Figure A2: Qualitative comparison of peak centre evolution obtained by fitting and mass centre calculated from the raw diffractograms. a) Evolution of peak centre of the deconvoluted phases. b) Mass centre evolution calculated from the raw diffraction patterns (mc) and mass centre determined from the fitting results (<pc>) on the left axis. Derivative of the two mass centres with respect to the SoC (right axis).

To further prove that the mass centre of a diffraction pattern is representative of the structural state of graphite, the mass centres obtained from the raw diffraction patterns were compared with the fitting results and the mean peak centre (<pc>) in **Figure A2b**. One can observe the very good agreement between the mass centre and mean peak centre. It supports the idea that proceeding with mass centre calculation directly on the raw diffraction patterns provides as much sensitivity to the structural state of charge of graphite as proceeding with peak fitting.

1.2 Fano lineshape asymmetry quantification

As illustrated in **Figure A3**, the lineshape is asymmetric with a larger intensity at low frequency. To mathematically quantify this asymmetry, a subtraction of the maxima (located at 1535 cm^{-1}) and minima (located at 1600 cm^{-1}) of the lineshape was calculated.

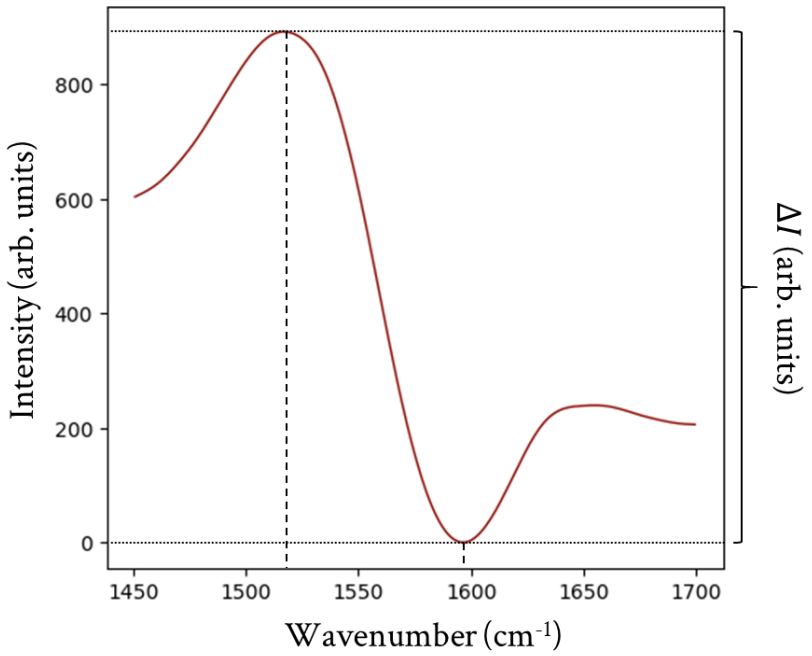


Figure A3: Illustration of the method used to quantify the Fano lineshape asymmetry.

2 CHAPTER IV

2.1 Cycling of a C65 / PVDF electrode

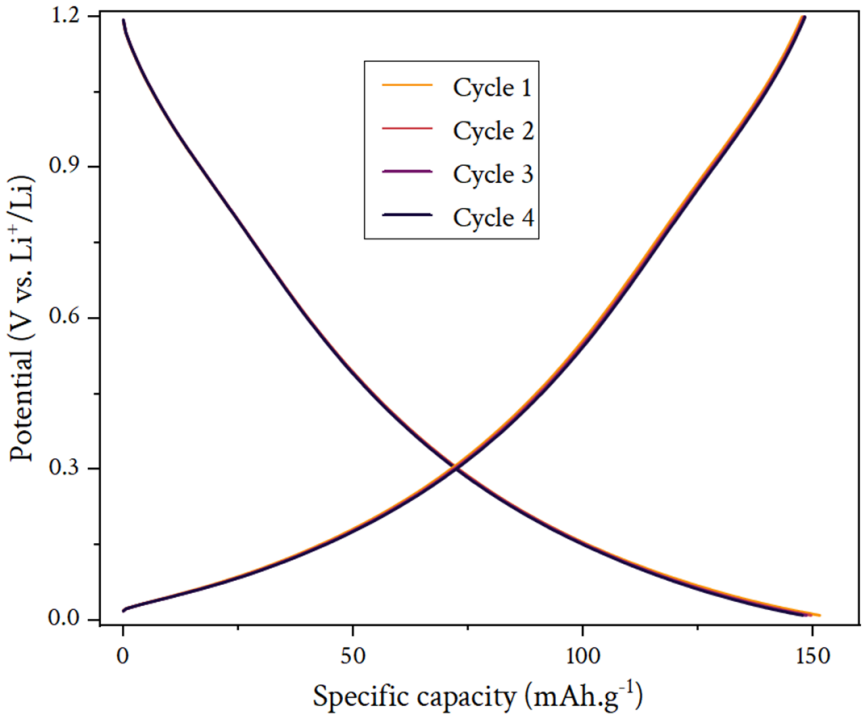


Figure A4: Charge and discharge profiles of a C65 electrode under CC condition at C/10 rate.

2.2 WAXS experiment at ID31

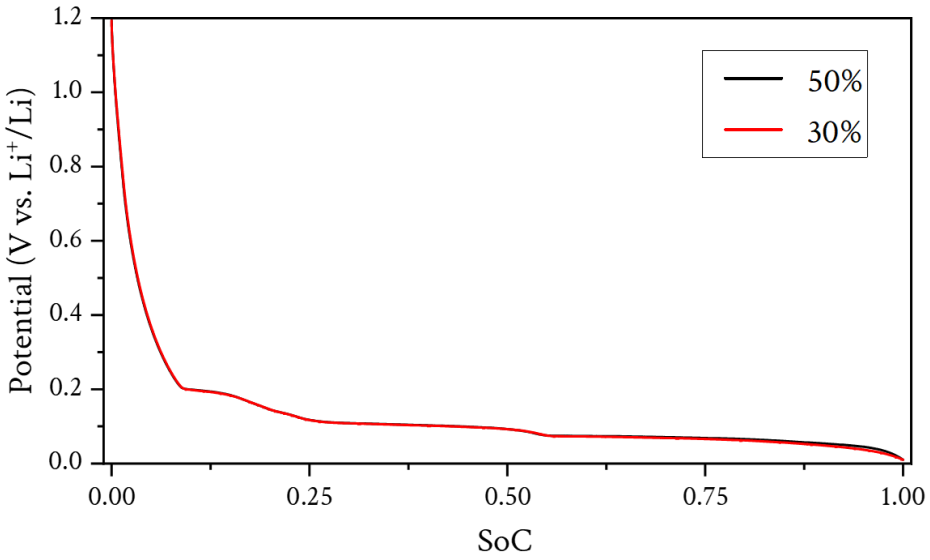


Figure A5: Lithiation profile of the 50% and 30% porosity graphite electrodes obtained at C/10 at 25°C.

Figure A6a shows the evolution of the fractional content of stage I over the total integral as a function of the structural state of charge from the thin graphite electrode. Using this model profile

and the calculation procedure on the two electrode porosities of 50 and 30% (an example is given in **Figure A6b** that plots the evolution of fractional content of stage I phase over the total integral for each *z*-position of the electrode with 30% porosity), the structural state of charge was determined with the second method (method 2). However, this method is only valid for the stage II to stage I transition, and thus in the range ~0.5 – 1 SoC_{cell}.

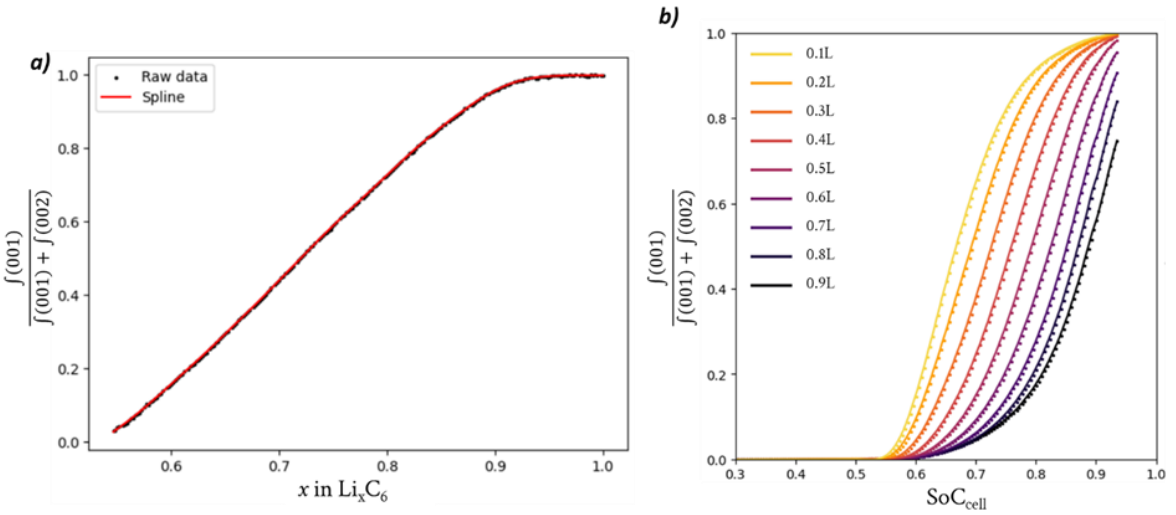


Figure A6: Fractional content of stage I (or stage I-enriched) phase over the total integral of X-photons. a) Model profile obtained with the thin graphite electrode. b) Results obtained with the thick electrode of 30% porosity cycled at C/4 rate for all the probed z-positions.

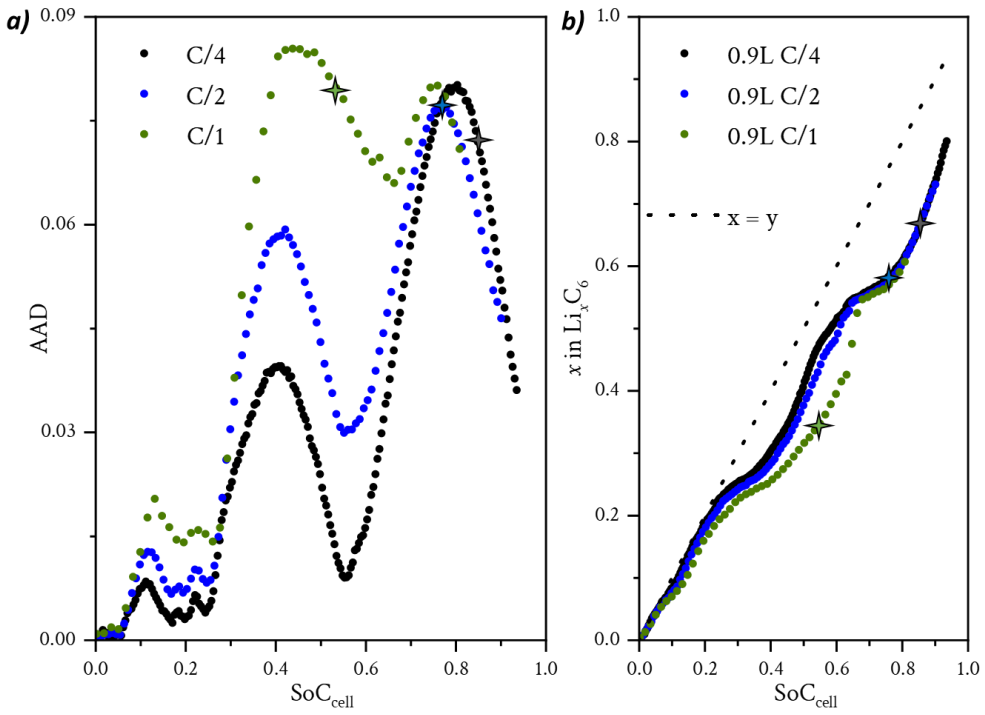


Figure A7: Evolution of structural state of charge dispersion for 30% porosity graphite electrode at different cycling rates. a) Evolution of the AAD parameter as a function of SoC_{cell} for different cycling rates. b) Structural state of charge evolution as a function of the SoC_{cell} at the 0.9 L position (near the current collector) for different cycling rates.

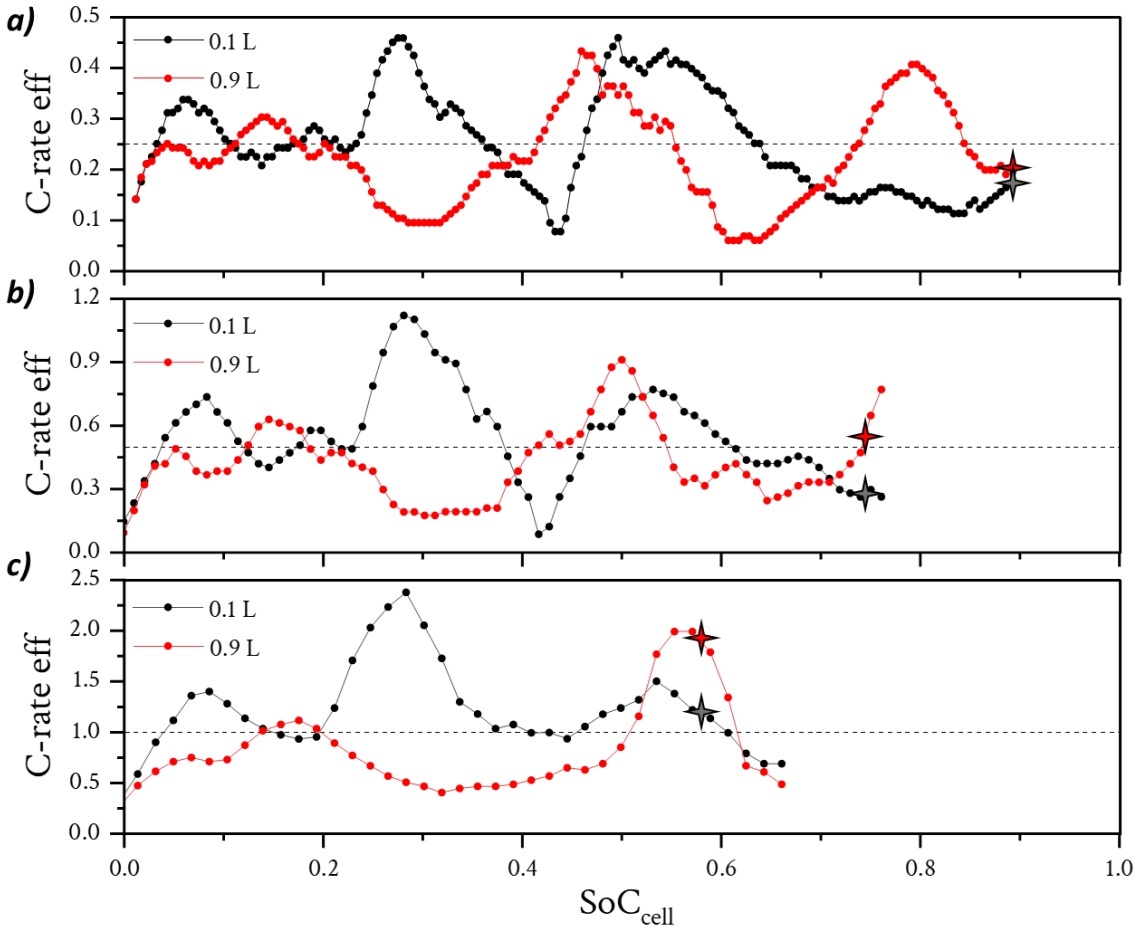


Figure A8: Evolution of effective C-rates as a function of SoC_{cell} at the positions 0.1 L and 0.9 L for the graphite electrode with 50% porosity. a) Cycling rate of C/4, the dashed line at 0.25 corresponds to the applied C-rate at the cell level. b) Cycling rate of C/2. c) Cycling rate of C/1. The switch between CC and CV periods is represented by the black and red stars.

3 CHAPTER V

3.1 Dilatometry measurement

Table A1: Specific capacity of each phase transition for the first and second/third lithiations of a 70% porosity graphite electrode.

Transition	Gr → I' (1)	I' → IV (2)	IV → III (3)	III → II-L (4)	II-L → II (5)	II → I (6)	I → I-rich (7)
1st lithiation [mAh.g^{-1}]	117	39	34	12	122	172	20
2nd & 3rd lithiation [mAh.g^{-1}]	34	29	29	11	107	153	22

3.2 Kokam® specifications sheet

Table A2: Cell specification of the Kokam pouch cell (SLPB065070180) taken from ref. [237].

Cell specification		
Nominal capacity	11.6 Ah	
Cell dimension (LxWxT)	185 mm × 84 mm × 6.6 mm	
Nominal voltage	3.65 V	
Voltage limits	2.7–4.2 V	
Cont. current limits	Charge 11.6 A (1C) @25 °C Discharge 23.2 A (2C) @25 °C	
	Separator	
Material	PE (TGA)	
Thickness	15 µm	
Folding	Z-folding	
Porosity	57% (Hg-intrusion)	
	Positive electrode	**Negative electrode**
Active material	NMC (ratio 85:5:10)	Graphite
Porosity	31% (Hg-intrusion)	35% (Hg-intrusion)
Number of sheets	16 (double coated)	17 (double coated)
	2 (single coated)	
Dimension (LxWxT)	160.8 mm × 66.2 mm × 0.14 mm (double coated)	165.5 mm × 66.5 mm × 0.17 mm (double coated)
	160.8 mm × 66.2 mm × 0.11 mm (single coated)	
Thickness of current collector	11 µm (Aluminium, double coated)	8.25 µm (Copper)
	47 µm (Aluminium, single coated)	

4 CHAPTER VI

4.1 Rate capability measurement

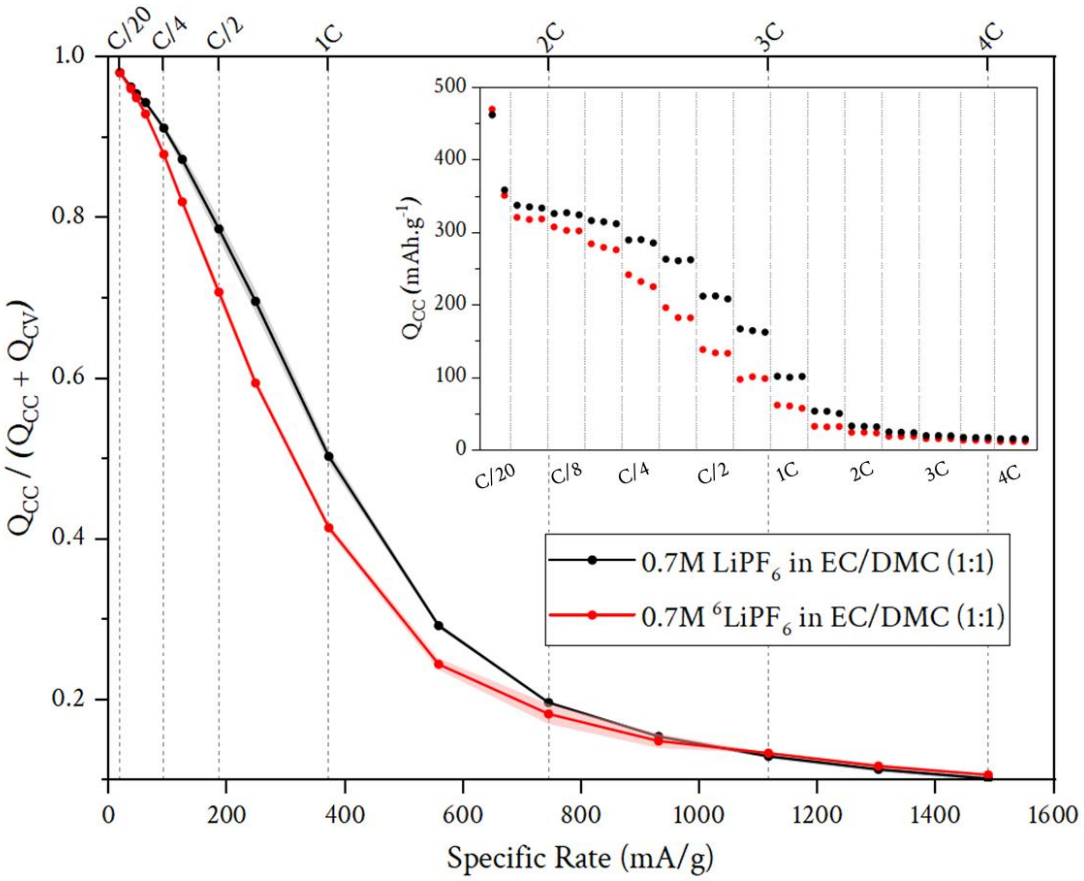


Figure A9: Rate capability of graphite half-cells composed of 0.7M $LiPF_6$ in EC/DMC (1:1%v) with natural lithium as negative electrode, and of 0.7M $^6LiPF_6$ in EC/DMC (1:1%v) as electrolyte with ^6Li as negative electrode at 25°C. The inset plots the specific galvanostatic capacities as a function of the cycling rate. The standard deviations are represented by the black and red shadows.

REFERENCES

1. Volta, A. XVII. On the electricity excited by the mere contact of conducting substances of different kinds. *Philos. Trans. R. Soc. Lond.* **90**, 403–431 (1800).

2. Samueli, J.-J. & Boudenot, J.-C. L'invention de la pile électrochimique par Volta. *BibNum* https://doi.org/10.4000/bibnum.719 (2008) doi:10.4000/bibnum.719.

3. Manwell, J. F. & McGowan, J. G. Lead acid battery storage model for hybrid energy systems. *Sol. Energy* **50**, 399–405 (1993).

4. Tarascon, J.-M. *L'énergie : stockage électrochimique et développement durable*. (Collège de France, Fayard, Paris, Paris, 2011). doi:10.4000/books.cdf.399.

5. Reddy, M. V., Mauger, A., Julien, C. M., Paolella, A. & Zaghib, K. Brief History of Early Lithium-Battery Development. *Materials* **13**, 1884 (2020).

6. Calvin, K. *et al. IPCC, 2023: Climate Change 2023: Synthesis Report. Contribution of Working Groups I, II and III to the Sixth Assessment Report of the Intergovernmental Panel on Climate Change [Core Writing Team, H. Lee and J. Romero (Eds.)]. IPCC, Geneva, Switzerland.* https://www.ipcc.ch/report/ar6/syr/ (2023) doi:10.59327/IPCC/AR6-9789291691647.

7. Wang, Y., Zhang, X., Li, K., Zhao, G. & Chen, Z. Perspectives and challenges for future lithium-ion battery control and management. *eTransportation* **18**, 100260 (2023).

8. Chen, C., Wei, Z. & Knoll, A. C. Charging Optimization for Li-Ion Battery in Electric Vehicles: A Review. *IEEE Trans. Transp. Electrification* **8**, 3068–3089 (2022).

9. De Rosa, M., Afanaseva, O., Fedyukhin, A. V. & Bianco, V. Prospects and characteristics of thermal and electrochemical energy storage systems. *J. Energy Storage* **44**, 103443 (2021).

10. Olabi, A. G. *et al.* Critical review of energy storage systems. *Energy* **214**, 118987 (2021).

11. Arévalo-Cid, P., Dias, P., Mendes, A. & Azevedo, J. Redox flow batteries: a new frontier on energy storage. *Sustain. Energy Fuels* **5**, 5366–5419 (2021).

12. Han, C. *et al.* Recent Progress on Two-Dimensional Carbon Materials for Emerging Post-Lithium (Na+, K+, Zn2+) Hybrid Supercapacitors. *Polymers* **13**, 2137 (2021).

13. Lin, Z., Taberna, P.-L. & Simon, P. Electrochemical double layer capacitors: What is next beyond the corner? *Curr. Opin. Electrochem.* **6**, 115–119 (2017).

14. Sagadevan, S. *et al.* Fundamental electrochemical energy storage systems. in *Advances in Supercapacitor and Supercapattery* 27–43 (Elsevier, 2021). doi:10.1016/B978-0-12-819897-1.00001-X.

15. *The IUPAC Compendium of Chemical Terminology: The Gold Book*. (International Union of Pure and Applied Chemistry (IUPAC), Research Triangle Park, NC, 2025). doi:10.1351/goldbook.

16. Xin, S. *et al.* Roadmap for rechargeable batteries: present and beyond. *Sci. China Chem.* **67**, 13–42 (2024).

17. Ragupathy, P., Bhat, S. D. & Kalaiselvi, N. Electrochemical energy storage and conversion: An overview. *WIREs Energy Environ.* **12**, e464 (2023).

18. Aravindan, V., Gnanaraj, J., Lee, Y.-S. & Madhavi, S. Insertion-Type Electrodes for Nonaqueous Li-Ion Capacitors. *Chem. Rev.* **114**, 11619–11635 (2014).

19. Huang, Q. & Wang, Q. Next-Generation, High-Energy-Density Redox Flow Batteries. *ChemPlusChem* **80**, 312–322 (2015).

20. Ma, J. *et al.* The 2021 battery technology roadmap. *J. Phys. Appl. Phys.* **54**, 183001 (2021).

21. Ma, Y. *et al.* A practical high-energy lithium-ion capacitor enabled by multiple conducting bridges triggered electrode current reallocation. *Energy Storage Mater.* **62**, 102946 (2023).

22. Doublet, M.-L. Batteries Li-ion - Conception théorique. *Chim. Verte* https://doi.org/10.51257/a-v1-af6612 (2009) doi:10.51257/a-v1-af6612.

23. Nasajpour-Esfahani, N. *et al.* Comprehensive review of lithium-ion battery materials and development challenges. *Renew. Sustain. Energy Rev.* **203**, 114783 (2024).

24. Deng, C. *et al.* Recent advances in rocking chair batteries and beyond. *Energy Storage Mater.* **60**, 102820 (2023).

25. Jow, T. R., Delp, S. A., Allen, J. L., Jones, J.-P. & Smart, M. C. Factors Limiting Li^+ Charge Transfer Kinetics in Li-Ion Batteries. *J. Electrochem. Soc.* **165**, A361–A367 (2018).

26. Yao, Y. *et al.* Unlocking Charge Transfer Limitations for Extreme Fast Charging of Li-Ion Batteries. *Angew. Chem.* **135**, (2023).

27. Xu, K. "Charge-Transfer" Process at Graphite/Electrolyte Interface and the Solvation Sheath Structure of Li[sup +] in Nonaqueous Electrolytes. *J. Electrochem. Soc.* **154**, A162 (2007).

28. Schwarz, W. H. E. The Full Story of the Electron Configurations of the Transition Elements. *J. Chem. Educ.* **87**, 444–448 (2010).

29. Marinho, B., Ghislandi, M., Tkalya, E., Koning, C. E. & De With, G. Electrical conductivity of compacts of graphene, multi-wall carbon nanotubes, carbon black, and graphite powder. *Powder Technol.* **221**, 351–358 (2012).

30. Pantea, D., Darmstadt, H., Kaliaguine, S. & Roy, C. Electrical conductivity of conductive carbon blacks: influence of surface chemistry and topology. *Appl. Surf. Sci.* **217**, 181–193 (2003).

31. Ma, Y. *et al.* A practical high-energy lithium-ion capacitor enabled by multiple conducting bridges triggered electrode current reallocation. *Energy Storage Mater.* **62**, 102946 (2023).

32. Logan, E. R. & Dahn, J. R. Electrolyte Design for Fast-Charging Li-Ion Batteries. *Trends Chem.* **2**, 354–366 (2020).

33. Cavers, H., Molaiyan, P., Abdollahifar, M., Lassi, U. & Kwade, A. Perspectives on Improving the Safety and Sustainability of High Voltage Lithium-Ion Batteries Through the Electrolyte and Separator Region. *Adv. Energy Mater.* **12**, 2200147 (2022).

34. Wang, Y. & Zhong, W. Development of Electrolytes towards Achieving Safe and High-Performance Energy-Storage Devices: A Review. *ChemElectroChem* **2**, 22–36 (2015).

35. Diederichsen, K. M., McShane, E. J. & McCloskey, B. D. Promising Routes to a High Li^+ Transference Number Electrolyte for Lithium Ion Batteries. *ACS Energy Lett.* **2**, 2563–2575 (2017).

36. Ghanbarian, B., Hunt, A. G., Ewing, R. P. & Sahimi, M. Tortuosity in Porous Media: A Critical Review. *Soil Sci. Soc. Am. J.* 77, 1461–1477 (2013).

37. DuBeshter, T., Sinha, P. K., Sakars, A., Fly, G. W. & Jorne, J. Measurement of Tortuosity and Porosity of Porous Battery Electrodes. *J. Electrochem. Soc.* **161**, A599–A605 (2014).

38. Patel, K. K., Paulsen, J. M. & Desilvestro, J. Numerical simulation of porous networks in relation to battery electrodes and separators. *J. Power Sources* **122**, 144–152 (2003).

39. Tjaden, B., Cooper, S. J., Brett, D. J., Kramer, D. & Shearing, P. R. On the origin and application of the Bruggeman correlation for analysing transport phenomena in electrochemical systems. *Curr. Opin. Chem. Eng.* **12**, 44–51 (2016).

40. Zhang, Y., Yang, Z., Wang, F. & Zhang, X. Comparison of soil tortuosity calculated by different methods. *Geoderma* **402**, 115358 (2021).

41. Ebner, M., Chung, D., García, R. E. & Wood, V. Tortuosity Anisotropy in Lithium-Ion Battery Electrodes. *Adv. Energy Mater.* **4**, 1301278 (2014).

42. Mayer, S. F. *et al.* Understanding Interphases and Interfaces of Battery Materials at the Nanoscale. (2025).

43. Wang, A., Kadam, S., Li, H., Shi, S. & Qi, Y. Review on modeling of the anode solid electrolyte interphase (SEI) for lithium-ion batteries. *Npj Comput. Mater.* **4**, (2018).

44. An, S. J. *et al.* The state of understanding of the lithium-ion-battery graphite solid electrolyte interphase (SEI) and its relationship to formation cycling. *Carbon* **105**, 52–76 (2016).

45. Verma, P., Maire, P. & Novák, P. A review of the features and analyses of the solid electrolyte interphase in Li-ion batteries. *Electrochimica Acta* **55**, 6332–6341 (2010).

46. Agubra, V. A. & Fergus, J. W. The formation and stability of the solid electrolyte interface on the graphite anode. *J. Power Sources* **268**, 153–162 (2014).

47. Cheng, X. *et al.* A Review of Solid Electrolyte Interphases on Lithium Metal Anode. *Adv. Sci.* **3**, (2016).

48. Van Der Ven, A., Bhattacharya, J. & Belak, A. A. Understanding Li Diffusion in Li-Intercalation Compounds. *Acc. Chem. Res.* **46**, 1216–1225 (2013).

49. Liu, D. *et al.* Spinel materials for high-voltage cathodes in Li-ion batteries. *RSC Adv* **4**, 154–167 (2014).

50. Tang, X.-C., Song, X.-W., Shen, P.-Z. & Jia, D.-Z. Capacity intermittent titration technique (CITT): A novel technique for determination of Li+ solid diffusion coefficient of LiMn2O4. *Electrochimica Acta* **50**, 5581–5587 (2005).

51. Thackeray, M. M. & Amine, K. LiMn2O4 spinel and substituted cathodes. *Nat. Energy* **6**, 566–566 (2021).

52. Morgan, D., Van Der Ven, A. & Ceder, G. Li Conductivity in Li[sub x]MPO[sub 4] (M = Mn, Fe, Co, Ni) Olivine Materials. *Electrochem. Solid-State Lett.* **7**, A30 (2004).

53. Tian, C., Lin, F. & Doeff, M. M. Electrochemical Characteristics of Layered Transition Metal Oxide Cathode Materials for Lithium Ion Batteries: Surface, Bulk Behavior, and Thermal Properties. *Acc. Chem. Res.* **51**, 89–96 (2018).

54. Peljo, P., Villevieille, C. & Girault, H. H. The redox aspects of lithium-ion batteries. *Energy Environ. Sci.* **18**, 1658–1672 (2025).

55. Holzwarth, N. A. W. & Rabii, S. Energy band structure of lithium—graphite intercalation compound. *Mater. Sci. Eng.* **31**, 195–200 (1977).

56. Hazrati, E., De Wijs, G. A. & Brocks, G. Li intercalation in graphite: A van der Waals density-functional study. *Phys. Rev. B* **90**, 155448 (2014).

57. Kganyago, K. R. & Ngoepe, P. E. Structural and electronic properties of lithium intercalated graphite LiC 6. *Phys. Rev. B* **68**, 205111 (2003).

58. Ellis, B. L., Lee, K. T. & Nazar, L. F. Positive Electrode Materials for Li-Ion and Li-Batteries. *Chem. Mater.* **22**, 691–714 (2010).

59. Koech, A. K., Mwandila, G., Mulolani, F. & Mwaanga, P. Exploring the anode materials for lithium-ion batteries: A review. *Res.* **2**, 100442 (2025).

60. Villevieille, C. The challenge of studying interfaces in battery materials. *Nat. Nanotechnol.* **20**, 2–5 (2025).

61. An, Q., Sun, X., Guo, J., Cai, S. & Zheng, C. Review—Key Strategies to Increase the Rate Capacity of Cathode Materials for High Power Lithium-Ion Batteries. *J. Electrochem. Soc.* **167**, 140528 (2020).

62. Eftekhari, A. Lithium-Ion Batteries with High Rate Capabilities. *ACS Sustain. Chem. Eng.* **5**, 2799–2816 (2017).

63. Sivakkumar, S. R., Nerkar, J. Y. & Pandolfo, A. G. Rate capability of graphite materials as negative electrodes in lithium-ion capacitors. *Electrochimica Acta* **55**, 3330–3335 (2010).

64. Ma, M., Mansour, A. N., Ko, J. K., Waller, G. H. & Hendricks, C. E. Characterization of Li Diffusion and Solid Electrolyte Interface for $Li_4 Ti_5 O_{12}$ Electrode Cycled with an Organosilicon Additive Electrolyte. *J. Electrochem. Soc.* **167**, 110549 (2020).

65. Sarkar, T., Prakasha, K. R., Bharadwaj, M. D. & Prakash, A. S. Lithium diffusion study in $Li_2 MnO_3$ and $Li_{1.17} Ni_{0.17} Mn_{0.67} O_2$: a combined experimental and computational approach. *Phys. Chem. Chem. Phys.* **19**, 31724–31730 (2017).

66. Dees, D. W., Kawauchi, S., Abraham, D. P. & Prakash, J. Analysis of the Galvanostatic Intermittent Titration Technique (GITT) as applied to a lithium-ion porous electrode. *J. Power Sources* **189**, 263–268 (2009).

67. Churikov, A. V. *et al.* Determination of lithium diffusion coefficient in LiFePO4 electrode by galvanostatic and potentiostatic intermittent titration techniques. *Electrochimica Acta* **55**, 2939–2950 (2010).

68. Liu, W. *et al.* Improved Li-ion diffusion and stability of a $LiNi_{0.5} Mn_{1.5} O_4$ cathode through in situ co-doping with dual-metal cations and incorporation of a superionic conductor. *J. Mater. Chem. A* **5**, 145–154 (2017).

69. Zheng, J. *et al.* Characteristics of xLiFePO4·y Li3V2(PO4)3 electrodes for lithium batteries. *Ionics* **15**, 753–759 (2009).

70. Seyyedhosseinzadeh, H., Mahboubi, F. & Azadmehr, A. Diffusion mechanism of lithium ions in LiNi0.5Mn1.5O4. *Electrochimica Acta* **108**, 867–875 (2013).

71. Tian, T. *et al.* Trace Doping of Multiple Elements Enables Stable Cycling of High Areal Capacity $LiNi_{0.5} Mn_{1.5} O_4$ Cathode. *Small* **18**, 2106898 (2022).

72. Prosini, P. Determination of the chemical diffusion coefficient of lithium in LiFePO4. *Solid State Ion.* **148**, 45–51 (2002).

73. Tang, K., Yu, X., Sun, J., Li, H. & Huang, X. Kinetic analysis on LiFePO4 thin films by CV, GITT, and EIS. *Electrochimica Acta* **56**, 4869–4875 (2011).

74. Zhang, H. *et al.* $Li_4 Ti_5 O_{12}$ spinel anode: Fundamentals and advances in rechargeable batteries. *InfoMat* **4**, e12228 (2022).

75. Padhi, A. K., Nanjundaswamy, K. S. & Goodenough, J. B. Phospho-olivines as Positive-Electrode Materials for Rechargeable Lithium Batteries. *J. Electrochem. Soc.* **144**, 1188–1194 (1997).

76. Ravet, N. *et al.* Electroactivity of natural and synthetic triphylite. *J. Power Sources* **97–98**, 503–507 (2001).

77. Zhao, Y., Peng, L., Liu, B. & Yu, G. Single-Crystalline $LiFePO_4$ Nanosheets for High-Rate Li-Ion Batteries. *Nano Lett.* **14**, 2849–2853 (2014).

78. Van Den Bergh, W. *et al.* Single Crystal Layered Oxide Cathodes: The Relationship between Particle Size, Rate Capability, and Stability. *ChemElectroChem* **10**, e202300165 (2023).

79. Cabana, J., Monconduit, L., Larcher, D. & Palacín, M. R. Beyond Intercalation-Based Li-Ion Batteries: The State of the Art and Challenges of Electrode Materials Reacting Through Conversion Reactions. *Adv. Mater.* **22**, (2010).

80. Scrosati, B., Hassoun, J. & Sun, Y.-K. Lithium-ion batteries. A look into the future. *Energy Environ. Sci.* **4**, 3287 (2011).

81. Megahed, S. & Scrosati, B. Lithium-ion rechargeable batteries. *J. Power Sources* **51**, 79–104 (1994).

82. Shu, Z. X., McMillan, R. S. & Murray, J. J. Electrochemical Intercalation of Lithium into Graphite. *J. Electrochem. Soc.* **140**, 922–927 (1993).

83. Li, N. *et al.* Non-equilibrium insertion of lithium ions into graphite. *J. Mater. Chem. A* **9**, 12080–12086 (2021).

84. McKinnon, W. R. Insertion electrodes I: Atomic and electronic structure of the hosts and their insertion compounds. in *Solid State Electrochemistry* (ed. Bruce, P. G.) 163–198 (Cambridge University Press, 1994). doi:10.1017/CBO9780511524790.008.

85. Hess, M., Sasaki, T., Villevieille, C. & Novák, P. Combined operando X-ray diffraction–electrochemical impedance spectroscopy detecting solid solution reactions of LiFePO4 in batteries. *Nat. Commun.* **6**, 8169 (2015).

86. Quilty, C. D. *et al.* Multimodal electrochemistry coupled microcalorimetric and X-ray probing of the capacity fade mechanisms of Nickel rich NMC – progress and outlook. *Phys. Chem. Chem. Phys.* **24**, 11471–11485 (2022).

87. Nipan, G. D. & Klyndyuk, A. I. Solid Solutions in the Li–Ni–Mn–Co–O System. *Inorg. Mater.* **55**, 135–142 (2019).

88. Buchberger, I. *et al.* Aging Analysis of Graphite/$LiNi_{1/3}Mn_{1/3}Co_{1/3}O_2$ Cells Using XRD, PGAA, and AC Impedance. *J. Electrochem. Soc.* **162**, A2737–A2746 (2015).

89. European Carbon and Graphite Association. Graphite in batteries. *ECGA* (2022).

90. Li, M., Lu, J., Chen, Z. & Amine, K. 30 Years of Lithium-Ion Batteries. *Adv. Mater.* **30**, 1800561 (2018).

91. Li, Y., Lu, Y., Adelhelm, P., Titirici, M.-M. & Hu, Y.-S. Intercalation chemistry of graphite: alkali metal ions and beyond. *Chem. Soc. Rev.* **48**, 4655–4687 (2019).

92. Kim, J., Chae, O. B. & Lucht, B. L. Perspective—Structure and Stability of the Solid Electrolyte Interphase on Silicon Anodes of Lithium-ion Batteries. *J. Electrochem. Soc.* **168**, 030521 (2021).

93. Lin, X., Khosravinia, K., Hu, X., Li, J. & Lu, W. Lithium Plating Mechanism, Detection, and Mitigation in Lithium-Ion Batteries. *Prog. Energy Combust. Sci.* **87**, 100953 (2021).

94. Shi, H., Barker, J., Saïdi, M. Y., Koksbang, R. & Morris, L. Graphite structure and lithium intercalation. *J. Power Sources* **68**, 291–295 (1997).

95. Park, J., Xu, Z.-L. & Kang, K. Solvated Ion Intercalation in Graphite: Sodium and Beyond. *Front. Chem.* **8**, 432 (2020).

96. Herold, A. Recherches sur les composés d'insertion du graphite. *Bull Soc Chim Fr.* **187**, 999–1012 (1955).

97. Juza, R. & Wehle, V. Lithium-Graphit-Einlagerungsverbindungen. *Naturwissenschaften* **52**, 560–560 (1965).

98. Fischer, J. E., Fuerst, C. D. & Woo, K. C. Staging transitions in intercalated graphite. *Synth. Met.* **7**, 1–12 (1983).

99. Guerard, D. & Herold, A. Intercalation of lithium into graphite and other carbons. *Carbon* **13**, 337–345 (1975).

100. Dahn, J. R. Phase diagram of Li x C 6. *Phys. Rev. B* **44**, 9170–9177 (1991).

101. Ohzuku, T., Iwakoshi, Y. & Sawai, K. Formation of Lithium-Graphite Intercalation Compounds in Nonaqueous Electrolytes and Their Application as a Negative Electrode for a Lithium Ion (Shuttlecock) Cell. *J. Electrochem. Soc.* **140**, 2490–2498 (1993).

102. Dahn, J. R., Fong, R. & Spoon, M. J. Suppression of staging in lithium-intercalated carbon by disorder in the host. *Phys. Rev. B* **42**, 6424–6432 (1990).

103. Levi, M. D. & Aurbach, D. Simultaneous Measurements and Modeling of the Electrochemical Impedance and the Cyclic Voltammetric Characteristics of Graphite Electrodes Doped with Lithium. *J. Phys. Chem. B* **101**, 4630–4640 (1997).

104. Billaud, D. & Henry, F. X. Structural studies of the stage III lithium–graphite intercalation compound. *Solid State Commun.* **124**, 299–304 (2002).

105. Didier, C., Pang, W. K., Guo, Z., Schmid, S. & Peterson, V. K. Phase Evolution and Intermittent Disorder in Electrochemically Lithiated Graphite Determined Using in Operando Neutron Diffraction. *Chem. Mater.* **32**, 2518–2531 (2020).

106. Billaud, D., Henry, F. X., Lelaurain, M. & Willmann, P. Revisited structures of dense and dilute stage II lithium-graphite intercalation compounds. *J. Phys. Chem. Solids* **57**, 775–781 (1996).

107. Yazami, R. & Touzain, Ph. A reversible graphite-lithium negative electrode for electrochemical generators. *J. Power Sources* **9**, 365–371 (1983).

108. Reynier, Y., Yazami, R. & Fultz, B. The entropy and enthalpy of lithium intercalation into graphite. *J. Power Sources* **119–121**, 850–855 (2003).

109. Fujimoto, H. *et al.* Synchronized Operando Analysis of Graphite Negative Electrode of Li-Ion Battery. *J. Electrochem. Soc.* **168**, 080508 (2021).

110. Fujimoto, H. *et al.* Phase Diagram of Li-Graphite Intercalation Compound Formed by the Charge/Discharge Reaction in Li-Ion Battery. *J. Electrochem. Soc.* **169**, 070507 (2022).

111. Schmitt, C., Kube, A., Wagner, N. & Friedrich, K. A. Understanding the Influence of Temperature on Phase Evolution during Lithium-Graphite (De-)Intercalation Processes: An Operando X-ray Diffraction Study. *ChemElectroChem* **9**, (2022).

112. Takagi, S. *et al.* Operando structural analysis of phase transition of graphite electrode during Li de-intercalation process using neutron and synchrotron radiation X-ray diffraction. *Carbon* **215**, 118414 (2023).

113. Hess, M. Kinetics and stage transitions of graphite for lithium-ion batteries. 1 Band (ETH Zurich, 2013). doi:10.3929/ETHZ-A-010000442.

114. Yang, Y. *et al. Operando*Methods in Electrocatalysis. *ACS Catal.* **11**, 1136–1178 (2021).

115. Hofmann, U. & Rüdorff, W. The formation of salts from graphite by strong acids. *Trans Faraday Soc* **34**, 1017–1021 (1938).

116. Daumas, N. & Hérold, A. Relation between phase concept and reaction mechanics in graphite insertion compounds. *CR Acad Sci Paris Ser C* **268**, 373 (1969).

117. Hérold, C. & Lagrange, P. Composés d'intercalation du graphite : des binaires aux ternaires. *Comptes Rendus Chim.* **6**, 457–465 (2003).

118. Weng, S. *et al.* Localized-domains staging structure and evolution in lithiated graphite. *Carbon Energy* **5**, e224 (2023).

119. Heß, M. & Novák, P. Shrinking annuli mechanism and stage-dependent rate capability of thin-layer graphite electrodes for lithium-ion batteries. *Electrochimica Acta* **106**, 149–158 (2013).

120. Advanced Energy Materials - 2021 - Zhang - A Review of Lithium-Ion Battery Electrode Drying Mechanisms and Metrology.pdf.

121. Li, C.-C. & Wang, Y.-W. Binder Distributions in Water-Based and Organic-Based LiCoO2 Electrode Sheets and Their Effects on Cell Performance. *J. Electrochem. Soc.* **158**, A1361 (2011).

122. Stein, M., Mistry, A. & Mukherjee, P. P. Mechanistic Understanding of the Role of Evaporation in Electrode Processing. *J. Electrochem. Soc.* **164**, A1616–A1627 (2017).

123. Hwang, J. H., Yoo, H., Oh, S. & Kim, H. Relationship between particle shape and fast-charging capability of a dry-processed graphite electrode in lithium-ion batteries. *Electrochem. Commun.* **165**, 107761 (2024).

124. Zhang, Y. *et al.* Revisiting Polytetrafluorethylene Binder for Solvent-Free Lithium-Ion Battery Anode Fabrication. *Batteries* **8**, 57 (2022).

125. Suh, Y., Koo, J. K., Im, H. & Kim, Y.-J. Astonishing performance improvements of dry-film graphite anode for reliable lithium-ion batteries. *Chem. Eng. J.* **476**, 146299 (2023).

126. Billaud, J., Bouville, F., Magrini, T., Villevieille, C. & Studart, A. R. Magnetically aligned graphite electrodes for high-rate performance Li-ion batteries. *Nat. Energy* **1**, 16097 (2016).

127. Abdollahifar, M. *et al.* Insights into Influencing Electrode Calendering on the Battery Performance. *Adv. Energy Mater.* **13**, 2300973 (2023).

128. Antartis, D., Dillon, S. & Chasiotis, I. Effect of porosity on electrochemical and mechanical properties of composite Li-ion anodes. *J. Compos. Mater.* **49**, 1849–1862 (2015).

129. Singh, M., Kaiser, J. & Hahn, H. Effect of Porosity on the Thick Electrodes for High Energy Density Lithium Ion Batteries for Stationary Applications. *Batteries* **2**, 35 (2016).

130. Guo, Y. *et al.* Determination of the tortuosity and contact resistances in thick graphite anodes via electrochemical impedance spectroscopy. *J. Power Sources* **569**, 233003 (2023).

131. Tran, T. *et al.* Thermal and electrochemical studies of carbons for Li-ion batteries. *J. Power Sources* **85**, 269–278 (2000).

132. Peled, E., Golodnitsky, D., Menachem, C. & Bar-Tow, D. An Advanced Tool for the Selection of Electrolyte Components for Rechargeable Lithium Batteries. *J. Electrochem. Soc.* **145**, 3482–3486 (1998).

133. Peled, E. & Menkin, S. Review—SEI: Past, Present and Future. *J. Electrochem. Soc.* **164**, A1703–A1719 (2017).

134. Asenbauer, J. *et al.* The success story of graphite as a lithium-ion anode material – fundamentals, remaining challenges, and recent developments including silicon (oxide) composites. *Sustain. Energy Fuels* **4**, 5387–5416 (2020).

135. Zaghib, K., Nadeau, G. & Kinoshita, K. Effect of Graphite Particle Size on Irreversible Capacity Loss. *J. Electrochem. Soc.* **147**, 2110 (2000).

136. Zaghib, K., Brochu, F., Guerfi, A. & Kinoshita, K. Effect of particle size on lithium intercalation rates in natural graphite. *J. Power Sources* **103**, 140–146 (2001).

137. Zaghib, K., Song, X., Guerfi, A., Rioux, R. & Kinoshita, K. Purification process of natural graphite as anode for Li-ion batteries: chemical versus thermal. *J. Power Sources* **119–121**, 8–15 (2003).

138. Fischer, S., Doose, S., Müller, J., Höfels, C. & Kwade, A. Impact of Spheroidization of Natural Graphite on Fast-Charging Capability of Anodes for LIB. *Batteries* **9**, 305 (2023).

139. Gottschalk, L., Müller, J., Schoo, A., Baasch, E. & Kwade, A. Spherical Graphite Anodes: Influence of Particle Size Distribution and Multilayer Structuring in Lithium-Ion Battery Cells. *Batteries* **10**, 40 (2024).

140. Bryan, A. M., Santino, L. M., Lu, Y., Acharya, S. & D'Arcy, J. M. Conducting Polymers for Pseudocapacitive Energy Storage. *Chem. Mater.* **28**, 5989–5998 (2016).

141. Dresselhaus, M. S. & Dresselhaus, G. Intercalation compounds of graphite. *Adv. Phys.* **51**, 1–186 (2002).

142. Bruno, T. J. *CRC Handbook of Fundamental Spectroscopic Correlation Charts.* (CRC Press, Boca Raton, FL, 2006).

143. Ghannoum, A. Optical Properties of Lithiated Graphite In Relation to a Lithium Ion Battery Fiber Optic Sensor. *PhD Thesis Univ. Waterloo* (2018).

144. Basu, S. *et al.* Synthesis and properties of lithium-graphite intercalation compounds. *Mater. Sci. Eng.* **38**, 275–283 (1979).

145. Kang, S., Yeom, S. J. & Lee, H. Side-View Operando Optical Microscopy Analysis of a Graphite Anode to Study Its Kinetic Hysteresis. *ChemSusChem* **13**, 1480–1484 (2020).

146. Hardwick, L., Buqa, H. & Novak, P. Graphite surface disorder detection using in situ Raman microscopy. *Solid State Ion.* **177**, 2801–2806 (2006).

147. Sole, C., Drewett, N. E. & Hardwick, L. J. *In situ* Raman study of lithium-ion intercalation into microcrystalline graphite. *Faraday Discuss* **172**, 223–237 (2014).

148. Inaba, M. *et al.* In Situ Raman Study on Electrochemical Li Intercalation into Graphite. *J. Electrochem. Soc.* **142**, 20–26 (1995).

149. Panitz, J.-C., Joho, F. & Novák, P. *In situ* Characterization of a Graphite Electrode in a Secondary Lithium-Ion Battery Using Raman Microscopy. *Appl. Spectrosc.* **53**, 1188–1199 (1999).

150. Yadegari, H. *et al. Operando* Measurement of Layer Breathing Modes in Lithiated Graphite. *ACS Energy Lett.* 1633–1638 (2021) doi:10.1021/acsenergylett.1c00494.

151. Maruyama, S. Operando Raman observation of lithium-ion battery graphite composite electrodes with various densities and thicknesses. *Electrochimica Acta* **498**, 144611 (2024).

152. Yao, K. P. C., Okasinski, J. S., Kalaga, K., Shkrob, I. A. & Abraham, D. P. Quantifying lithium concentration gradients in the graphite electrode of Li-ion cells using *operando* energy dispersive X-ray diffraction. *Energy Environ. Sci.* **12**, 656–665 (2019).

153. Finegan, D. P. *et al.* Spatial dynamics of lithiation and lithium plating during high-rate operation of graphite electrodes. *Energy Environ. Sci.* **13**, 2570–2584 (2020).

154. Tardif, S. *et al.* Combining *operando* X-ray experiments and modelling to understand the heterogeneous lithiation of graphite electrodes. *J. Mater. Chem. A* **9**, 4281–4290 (2021).

155. Xue, Z. *et al.* Research on the assembly process of full coin cells: key factors affecting data reliability. *Ionics* **29**, 5285–5293 (2023).

156. Buqa, H., Goers, D., Holzapfel, M., Spahr, M. E. & Novák, P. High Rate Capability of Graphite Negative Electrodes for Lithium-Ion Batteries. *J. Electrochem. Soc.* **152**, A474 (2005).

157. Heubner, C. *et al.* Comparison of chronoamperometric response and rate-performance of porous insertion electrodes: Towards an accelerated rate capability test. *J. Power Sources* **397**, 11–15 (2018).

158. Montella, C. Discussion of the potential step method for the determination of the diffusion coefficients of guest species in host materials Part I. Influence of charge transfer kinetics and ohmic potential drop. *J. Electroanal. Chem.* (2002).

159. Levi, M. D. & Aurbach, D. Potentiostatic and Galvanostatic Intermittent Titration Techniques. in *Characterization of Materials* (ed. Kaufmann, E. N.) 1–21 (Wiley, 2012). doi:10.1002/0471266965.com125.

160. Levi, M. D., Markevich, E. & Aurbach, D. The Effect of Slow Interfacial Kinetics on the Chronoamperometric Response of Composite Lithiated Graphite Electrodes and on the Calculation of the Chemical Diffusion Coefficient of Li Ions in Graphite. *J. Phys. Chem. B* **109**, 7420–7427 (2005).

161. Landesfeind, J., Hattendorff, J., Ehrl, A., Wall, W. A. & Gasteiger, H. A. Tortuosity Determination of Battery Electrodes and Separators by Impedance Spectroscopy. *J. Electrochem. Soc.* **163**, A1373–A1387 (2016).

162. Morasch, R., Keilhofer, J., Gasteiger, H. A. & Suthar, B. Methods—Understanding Porous Electrode Impedance and the Implications for the Impedance Analysis of Li-Ion Battery Electrodes. *J. Electrochem. Soc.* **168**, 080519 (2021).

163. Portalis, G. Compréhension des phénomènes de ` cross-talking ' ' au sein des accumulateurs Li-ion. *PhD Thesis Sorbonne Univ.* (2020).

164. Seid, K. A. *et al.* Multiscale electronic transport mechanism and true conductivities in amorphous carbon–$LiFePO_4$ nanocomposites. *J Mater Chem* **22**, 2641–2649 (2012).

165. Martínez-Criado, G. *et al.* ID16B: a hard X-ray nanoprobe beamline at the ESRF for nano-analysis. *J. Synchrotron Radiat.* **23**, 344–352 (2016).

166. Cloetens, P. *et al.* Holotomography: Quantitative phase tomography with micrometer resolution using hard synchrotron radiation x rays. *Appl. Phys. Lett.* **75**, 2912–2914 (1999).

167. Mirone, A., Brun, E., Gouillart, E., Tafforeau, P. & Kieffer, J. The PyHST2 hybrid distributed code for high speed tomographic reconstruction with iterative reconstruction and a priori knowledge capabilities. *Nucl. Instrum. Methods Phys. Res. Sect. B Beam Interact. Mater. At.* **324**, 41–48 (2014).

168. Lyckegaard, A., Johnson, G. & Tafforeau, P. Correction of Ring Artifacts in X-ray Tomographic Images. *Int. J. Tomogr. Stat.* **18**, (2011).

169. Schindelin, J. *et al.* Fiji: an open-source platform for biological-image analysis. *Nat. Methods* **9**, 676–682 (2012).

170. Berg, S. *et al.* ilastik: interactive machine learning for (bio)image analysis. *Nat. Methods* **16**, 1226–1232 (2019).

171. Kieffer, J. & Wright, J. P. PyFAI: a Python library for high performance azimuthal integration on GPU. *Powder Diffr.* **28**, S339–S350 (2013).

172. Newville, M., Stensitzki, T., Allen, D. B. & Ingargiola, A. LMFIT: Non-Linear Least-Square Minimization and Curve-Fitting for Python. Zenodo https://doi.org/10.5281/ZENODO.11813 (2014).

173. Erb, D. pybaselines: A Python library of algorithms for the baseline correction of experimental data. Zenodo https://doi.org/10.5281/ZENODO.5608581 (2024).

174. Jake, L. Split Pseudo-Voigt Modelling with Drop-In Modules (WIP). https://github.com/orgs/lmfit/discussions/946#discussion-6410820 (2024).

175. Delgado, T. *et al.* Evidencing size-dependent cooperative effects on spin crossover nanoparticles following their HS→LS relaxation. *J. Mater. Chem. C* **6**, 12698–12706 (2018).

176. Almakki, M. *et al.* Mantid 6.12.0: Manipulation and Analysis Toolkit for Instrument Data. Mantid Project https://doi.org/10.5286/SOFTWARE/MANTID6.12 (2025).

177. Harris, R. K., Becker, E. D., de Menezes, S. C., Goodfellow, R. & Granger, P. Provisional recommendations for NMR nomenclature: nuclear spin properties and conventions for chemical shifts. *Pure Appl. Chem.* **73**, 1795–1818 (2001).

178. Azcarate, I. *et al.* Assessing the Oxidation Behavior of EC:DMC Based Electrolyte on Non-Catalytically Active Surface. *J. Electrochem. Soc.* **167**, 080530 (2020).

179. Renais, C. *et al.* Understanding Fast Charging Ability Limitation in Graphite Electrode for Li-Ion Batteries: Quasi-Thermodynamic Approach and Methodology. *Chem. Mater.* https://doi.org/10.1021/acs.chemmater.5c00722 (2025) doi:10.1021/acs.chemmater.5c00722.

180. Van Der Ven, A., See, K. A. & Pilon, L. Hysteresis in electrochemical systems. *Battery Energy* **1**, (2022).

181. Binder, K. Theory of first-order phase transitions. *Rep. Prog. Phys.* **50**, 783–859 (1987).

182. Bigg, E. K. The Supercooling of Water. *Proc. Phys. Soc. Sect. B* **66**, 688–694 (1953).

183. Jahn, L., Mößle, P., Röder, F. & Danzer, M. A. A physically motivated voltage hysteresis model for lithium-ion batteries using a probability distributed equivalent circuit. *Commun. Eng.* **3**, 74 (2024).

184. Dreyer, W. *et al.* The thermodynamic origin of hysteresis in insertion batteries. *Nat. Mater.* **9**, 448–453 (2010).

185. Li, D. & Zhou, H. Two-phase transition of Li-intercalation compounds in Li-ion batteries. *Mater. Today* **17**, 451–463 (2014).

186. Foster, J. M. *et al.* The Newman Model for Phase-Change Electrodes: Physics-Based Hysteresis. *J. Electrochem. Soc.* **172**, 040501 (2025).

187. Mercer, M. P., Peng, C., Soares, C., Hoster, H. E. & Kramer, D. Voltage hysteresis during lithiation/delithiation of graphite associated with meta-stable carbon stackings. *J. Mater. Chem. A* **9**, 492–504 (2021).

188. Peng, J. *et al.* High Current Density and Long Cycle Life Enabled by Sulfide Solid Electrolyte and Dendrite-Free Liquid Lithium Anode. *Adv. Funct. Mater.* **32**, 2105776 (2022).

189. Lu, Y. *et al.* Critical Current Density in Solid-State Lithium Metal Batteries: Mechanism, Influences, and Strategies. *Adv. Funct. Mater.* **31**, 2009925 (2021).

190. Levi, M. D. & Aurbach, D. Frumkin intercalation isotherm Ð a tool for the description of lithium insertion into host materials: a review. *Electrochimica Acta* (1999).

191. Chien, Y.-C. *et al.* Rapid determination of solid-state diffusion coefficients in Li-based batteries via intermittent current interruption method. *Nat. Commun.* **14**, 2289 (2023).

192. Lacey, M. J., Edström, K. & Brandell, D. Visualising the problems with balancing lithium–sulfur batteries by "mapping" internal resistance. *Chem. Commun.* **51**, 16502–16505 (2015).

193. Charbonneau, V., Lasia, A. & Brisard, G. Impedance studies of Li+ diffusion in nickel manganese cobalt oxide (NMC) during charge/discharge cycles. *J. Electroanal. Chem.* **875**, 113944 (2020).

194. Gao, Y. *et al.* Accurate Calculation of Solid-State Li^+ Diffusion Coefficient and Kinetic Activation Energies for an Artificial Graphite Anode. *J. Electrochem. Soc.* **171**, 020558 (2024).

195. Yu, P., Popov, B. N., Ritter, J. A. & White, R. E. Determination of the Lithium Ion Diffusion Coefficient in Graphite. *J. Electrochem. Soc.* **146**, 8–14 (1999).

196. Mathiesen, J. K., Johnsen, R. E., Blennow, A. S. & Norby, P. Understanding the structural changes in lithiated graphite through high-resolution operando powder X-ray diffraction. *Carbon* **153**, 347–354 (2019).

197. Filhol, J.-S., Combelles, C., Yazami, R. & Doublet, M.-L. Phase Diagrams for Systems with Low Free Energy Variation: A Coupled Theory/Experiments Method Applied to Li-Graphite. *J. Phys. Chem. C* **112**, 3982–3988 (2008).

198. Schweidler, S. *et al.* Volume Changes of Graphite Anodes Revisited: A Combined *Operando* X-ray Diffraction and *In Situ* Pressure Analysis Study. *J. Phys. Chem. C* **122**, 8829–8835 (2018).

199. Boulet-Roblin, L. *et al.* Operando Neutron Powder Diffraction Using Cylindrical Cell Design: The Case of $LiNi_{0.5}Mn_{1.5}O_4$ vs Graphite. *J. Phys. Chem. C* **120**, 17268–17273 (2016).

200. Cho, Seo-Rin & Cho, Han-Gook. Characterization of Black Carbon Collected from Candle Light and Automobile Exhaust Pipe. *J. Korean Chem. Soc.* **57**, 691–696 (2013).

201. Hardwick, L. J. *et al.* Behaviour of highly crystalline graphitic materials in lithium-ion cells with propylene carbonate containing electrolytes: An in situ Raman and SEM study. *Electrochimica Acta* **52**, 4884–4891 (2007).

202. Neale, A. R., Milan, D. C., Braga, F., Sazanovich, I. V. & Hardwick, L. J. Lithium Insertion into Graphitic Carbon Observed via Operando Kerr-Gated Raman Spectroscopy Enables High State of Charge Diagnostics. *ACS Energy Lett.* **7**, 2611–2618 (2022).

203. Wang, Z., Huang, X., Xue, R. & Chen, L. A new possible mechanism of lithium insertion and extraction in low-temperature pyrolytic carbon electrode. *Carbon* **37**, 685–692 (1999).

204. Fano, U. Effects of Configuration Interaction on Intensities and Phase Shifts. *Phys. Rev.* **124**, 1866–1878 (1961).

205. Scott, J. F. Soft-mode spectroscopy: Experimental studies of structural phase transitions. *Rev. Mod. Phys.* **46**, 83–128 (1974).

206. Eklund, P. C., Dresselhaus, G., Dresselhaus, M. S. & Fischer, J. E. Raman scattering from in-plane lattice modes in low-stage graphite-alkali-metal compounds. *Phys. Rev. B* **16**, 3330–3333 (1977).

207. Yoon, D. *et al.* Fano resonance in Raman scattering of graphene. *Carbon* **61**, 373–378 (2013).

208. Schmitz, R. *et al.* SEI investigations on copper electrodes after lithium plating with Raman spectroscopy and mass spectrometry. *J. Power Sources* **233**, 110–114 (2013).

209. Maccio-Figgemeier, V., Eshetu, G. G., Mroz, D., Joo, H. & Figgemeier, E. Establishing Li-acetylide (Li2C2) as functional element in solid-electrolyte interphases in lithium-ion batteries. *J. Power Sources Adv.* **28**, 100152 (2024).

210. Drüe, M. *et al.* Thermodynamic stability of Li2C2 and LiC6. *J. Alloys Compd.* **575**, 403–407 (2013).

211. Basu, S. *et al.* Synthesis and properties of lithium-graphite intercalation compounds. *Mater. Sci. Eng.* **38**, 275–283 (1979).

212. Renais, C. *et al.* Understanding fast charging limitation in graphite electrode for Li-ion batteries. 2. Heterogeneities of lithiation in conventionnal electrodes. *Chemistry of Materials* Under review (2025).

213. Lu, Y. *et al.* Critical Current Density in Solid-State Lithium Metal Batteries: Mechanism, Influences, and Strategies. *Adv. Funct. Mater.* **31**, 2009925 (2021).

214. Landesfeind, J., Ebner, M., Eldiven, A., Wood, V. & Gasteiger, H. A. Tortuosity of Battery Electrodes: Validation of Impedance-Derived Values and Critical Comparison with 3D Tomography. *J. Electrochem. Soc.* **165**, A469–A476 (2018).

215. Malifarge, S., Delobel, B. & Delacourt, C. Determination of Tortuosity Using Impedance Spectra Analysis of Symmetric Cell. *J. Electrochem. Soc.* **164**, E3329–E3334 (2017).

216. Zacharias, N. A. *et al.* Direct Measurements of Effective Ionic Transport in Porous Li-Ion Electrodes. *J. Electrochem. Soc.* **160**, A306–A311 (2013).

217. Arregui-Mena, J. D., Edmondson, P. D., Campbell, A. A. & Katoh, Y. Site specific, high-resolution characterisation of porosity in graphite using FIB-SEM tomography. *J. Nucl. Mater.* **511**, 164–173 (2018).

218. Perrenot, P., Bayle-Guillemaud, P., Jouneau, P.-H., Boulineau, A. & Villevieille, C. *Operando* Focused Ion Beam–Scanning Electron Microscope (FIB-SEM) Revealing Microstructural and Morphological Evolution in a Solid-State Battery. *ACS Energy Lett.* **9**, 3835–3840 (2024).

219. Kroll, M. *et al.* Reconstruction–Simulation Approach Verifies Impedance-Derived Ion Transport Tortuosity of a Graphite Battery Electrode. *J. Electrochem. Soc.* **165**, A3156–A3163 (2018).

220. Gu, H. Mathematical Analysis of a Zn / NiOOH Cell. *J. Electrochem. Soc.* **130**, 1459–1464 (1983).

221. Dufour, N., Chandesris, M., Geniès, S., Cugnet, M. & Bultel, Y. Lithiation heterogeneities of graphite according to C-rate and mass-loading: A model study. *Electrochimica Acta* **272**, 97–107 (2018).

222. Renais, C. *et al.* Understanding fast charging limitation in graphite electrode for Li-ion batteries. 1. Quasi-thermodynamic approach and methodology. *Chemistry of Materials* Accepted (2025).

223. Pietsch, P. *et al.* Quantifying microstructural dynamics and electrochemical activity of graphite and silicon-graphite lithium ion battery anodes. *Nat. Commun.* 7, (2016).

224. Chen, Z., Danilov, D. L., Eichel, R.-A. & Notten, P. H. L. Li+ concentration waves in a liquid electrolyte of Li-ion batteries with porous graphite-based electrodes. *Energy Storage Mater.* **48**, 475–486 (2022).

225. Renais, C. *et al.* Exploring electrochemical dynamics in graphite||LiNi0.8Mn0.1Co0.1O2 cells via operando ultrasound and multiprobe approaches. *Nat. Commun.* **16**, 7774 (2025).

226. Qi, Y. & Harris, S. J. In Situ Observation of Strains during Lithiation of a Graphite Electrode. *J. Electrochem. Soc.* **157**, A741 (2010).

227. Hahn, M. *et al.* A Dilatometric Study of Lithium Intercalation into Powder-Type Graphite Electrodes. *Electrochem. Solid-State Lett.* **11**, A151 (2008).

228. Michael, H. *et al.* A Dilatometric Study of Graphite Electrodes during Cycling with X-ray Computed Tomography. *J. Electrochem. Soc.* **168**, 010507 (2021).

229. Colchester, R. J. *et al.* Broadband miniature optical ultrasound probe for high resolution vascular tissue imaging. *Biomed. Opt. Express* **6**, 1502 (2015).

230. Juengert, A. *et al.* Advanced ultrasonic techniques for nondestructive testing of austenitic and dissimilar welds in nuclear facilities. in *AIP Conference Proceedings* (Author(s), Provo, Utah, USA, 2018). doi:10.1063/1.5031581.

231. Robinson, J. B. *et al.* Spatially resolved ultrasound diagnostics of Li-ion battery electrodes. *Phys. Chem. Chem. Phys.* **21**, 6354–6361 (2019).

232. Liu, X. *et al.* Decoupling of the anode and cathode ultrasonic responses to the state of charge of a lithium-ion battery. *Phys. Chem. Chem. Phys.* **25**, 21730–21735 (2023).

233. Tian, Y., Yang, S., Zhang, R., Tian, J. & Li, X. State of charge estimation of lithium-ion batteries based on ultrasonic guided waves by chirped signal excitation. *J. Energy Storage* **84**, 110897 (2024).

234. Bommier, C. *et al.* In Operando Acoustic Detection of Lithium Metal Plating in Commercial LiCoO2/Graphite Pouch Cells. *Cell Rep. Phys. Sci.* **1**, 100035 (2020).

235. Gupta, P., Üçel, İ. B., Gudmundson, P. & Olsson, E. Characterization of the Constitutive Behavior of a Cathode Active Layer in Lithium-Ion Batteries Using a Bending Test Method. *Exp. Mech.* **60**, 847–860 (2020).

236. Yamamoto, M., Terauchi, Y., Sakuda, A., Kato, A. & Takahashi, M. Effects of volume variations under different compressive pressures on the performance and microstructure of all-solid-state batteries. *J. Power Sources* **473**, 228595 (2020).

237. Laufen, H. *et al.* Correlation between Voltage, Strain, and Impedance as a Function of Pressure of a Nickel-Rich NMC Lithium-Ion Pouch Cell. *Adv. Mater. Technol.* **9**, 2301965 (2024).

238. Aufschläger, A. *et al.* High precision measurement of reversible swelling and electrochemical performance of flexibly compressed 5 Ah NMC622/graphite lithium-ion pouch cells. *J. Energy Storage* **59**, 106483 (2023).

239. Mohtat, P., Lee, S., Sulzer, V., Siegel, J. B. & Stefanopoulou, A. G. Differential Expansion and Voltage Model for Li-ion Batteries at Practical Charging Rates. *J. Electrochem. Soc.* **167**, 110561 (2020).

240. Davies, G. *et al.* State of Charge and State of Health Estimation Using Electrochemical Acoustic Time of Flight Analysis. *J. Electrochem. Soc.* **164**, A2746–A2755 (2017).

241. Xu, R., Sun, H., De Vasconcelos, L. S. & Zhao, K. Mechanical and Structural Degradation of $LiNi_xMn_yCo_zO_2$ Cathode in Li-Ion Batteries: An Experimental Study. *J. Electrochem. Soc.* **164**, A3333–A3341 (2017).

242. Qi, Y., Guo, H., Hector, L. G. & Timmons, A. Threefold Increase in the Young's Modulus of Graphite Negative Electrode during Lithium Intercalation. *J. Electrochem. Soc.* **157**, A558 (2010).

243. Cheng, E. J., Taylor, N. J., Wolfenstine, J. & Sakamoto, J. Elastic properties of lithium cobalt oxide ($LiCoO_2$). *J. Asian Ceram. Soc.* **5**, 113–117 (2017).

244. He, X., Ding, X. & Xu, R. Anisotropic mechanical properties of LiNi Mn Co1O2 cathodes for Li-ion batteries: A first-principles theoretical study. *Acta Mater.* **267**, 119751 (2024).

245. Qi, Y., Hector, L. G., James, C. & Kim, K. J. Lithium Concentration Dependent Elastic Properties of Battery Electrode Materials from First Principles Calculations. *J. Electrochem. Soc.* **161**, F3010–F3018 (2014).

246. Üçel, İ. B., Gupta, P. & Gudmundson, P. Experimental determination of the constitutive properties of a graphite anode layer in lithium-ion batteries using a bending test method. *J. Energy Storage* **46**, 103845 (2022).

247. Liu, S. *et al.* Origin of Phase Separation in Ni-Rich Layered Oxide Cathode Materials During Electrochemical Cycling. *Chem. Mater.* **35**, 8857–8871 (2023).

248. Quilty, C. D. *et al.* Probing Sources of Capacity Fade in $LiNi_{0.6}Mn_{0.2}Co_{0.2}O_2$ (NMC622): An *Operando* XRD Study of Li/NMC622 Batteries during Extended Cycling. *J. Phys. Chem. C* **124**, 8119–8128 (2020).

249. Butler, A. The Coordination and Redox Chemistry of Vanadium in Aqueous Solution. in *Vanadium in Biological Systems* (ed. Chasteen, N. D.) 25–49 (Springer Netherlands, Dordrecht, 1990). doi:10.1007/978-94-009-2023-1_2.

250. Choi, C. *et al.* A review of vanadium electrolytes for vanadium redox flow batteries. *Renew. Sustain. Energy Rev.* **69**, 263–274 (2017).

251. Chen, G., Huang, Q., Wu, T. & Lu, L. Polyanion Sodium Vanadium Phosphate for Next Generation of Sodium-Ion Batteries—A Review. *Adv. Funct. Mater.* **30**, 2001289 (2020).

252. Downard, K. M. Francis William Aston: The Man Behind the Mass Spectrograph. *Eur. J. Mass Spectrom.* **13**, 177–190 (2007).

253. Macklin, R. L. & Banta, H. E. Tritium Production from Lithium by Deuteron Bombardment. *Phys. Rev.* **97**, 753–757 (1955).

254. Lapp, R. E. The "Humanitarian" H-Bomb. *Bull. At. Sci.* **12**, 261–264 (1956).

255. Seltzer, S. Tables of X-Ray Mass Attenuation Coefficients and Mass Energy-Absorption Coefficients, NIST Standard Reference Database 126. National Institute of Standards and Technology https://doi.org/10.18434/T4D01F (1995).

256. Sears, V. F. Neutron scattering lengths and cross sections. *Neutron News* **3**, 26–37 (1992).

257. Penniston-Dorland, S., Liu, X.-M. & Rudnick, R. L. Lithium Isotope Geochemistry. *Rev. Mineral. Geochem.* **82**, 165–217 (2017).

258. Young, E. D., Galy, A. & Nagahara, H. Kinetic and equilibrium mass-dependent isotope fractionation laws in nature and their geochemical and cosmochemical significance. *Geochim. Cosmochim. Acta* **66**, 1095–1104 (2002).

259. Dauphas, N. & Schauble, E. A. Mass Fractionation Laws, Mass-Independent Effects, and Isotopic Anomalies. *Annu. Rev. Earth Planet. Sci.* **44**, 709–783 (2016).

260. Buchachenko, A. L. Mass-Independent Isotope Effects. *J. Phys. Chem. B* **117**, 2231–2238 (2013).

261. Marcus, R. A. Mass-Independent Oxygen Isotope Fractionation in Selected Systems. Mechanistic Considerations. in *Advances in Quantum Chemistry* vol. 55 5–19 (Elsevier, 2008).

262. Conway, B. E. Kinetics of electrolytic hydrogen and deuterium evolution. *Proc. R. Soc. Lond. Ser. Math. Phys. Sci.* **256**, 128–144 (1960).

263. Shaner, S. E. & Stone, K. L. Determination of Stretching Frequencies by Isotopic Substitution Using Infrared Spectroscopy: An Upper-Level Undergraduate Experiment for an In-Person or Online Laboratory. *J. Chem. Educ.* **100**, 2347–2352 (2023).

264. Gerhards, L., Brand, I. & Wittstock, G. H/D Isotope Effects in the Electrochemistry of Electrochromic Iron Hexacyanoruthenate. *ChemElectroChem* **11**, e202300824 (2024).

265. Audi, G. & Wapstra, A. H. The 1995 update to the atomic mass evaluation. *Nucl. Phys. A* **595**, 409–480 (1995).

266. Vocke, R. D. Atomic Weights of the Elements 1997. *Pure Appl. Chem.* **71**, 1593–1607 (1999).

267. Berthault, M. Etude de la dynamique du lithium dans un système électrochimique Li-ion par traçage isotopique en combinant les spectrométries RMN et ToF-SIMS.

268. Meyer, T. Tracing lithium mobility in polymer-ceramic solid-electrolyte: insights from lithium isotopic labelling, combined ToF-SIMS/ssNMR characterisation, and numerical simulations.

269. Diehl, M., Evertz, M., Winter, M. & Nowak, S. Deciphering the lithium ion movement in lithium ion batteries: determination of the isotopic abundances of ^{6}Li and ^{7}Li. *RSC Adv.* **9**, 12055–12062 (2019).

270. Downing, R. G., Lamaze, G. P., Langland, J. K. & Hwang, S. T. Neutron depth profiling: Overview and description of NIST facilities. *J. Res. Natl. Inst. Stand. Technol.* **98**, 109 (1993).

271. Verhallen, T. W., Lv, S. & Wagemaker, M. Operando Neutron Depth Profiling to Determine the Spatial Distribution of Li in Li-ion Batteries. *Front. Energy Res.* **6**, 62 (2018).

272. Périé, M., Périé, J. & Chemla, M. Effet isotopique de migration des électrolytes forts en solution aqueuse. *J. Chim. Phys.* **66**, 1379–1384 (1969).

273. Okada, I. The Chemla effect ---from the separation of isotopes to the modeling of binary ionic liquids. *J. Mol. Liq.* **83**, 5–22 (1999).

274. Tankeshwar, K. & Tosi, M. P. Theory of the Chemla effect in molten (Li,K)Cl. *Solid State Commun.* **84**, 245–247 (1992).

275. Yanase, S., Hayama, W. & Oi, T. Lithium Isotope Effect Accompanying Electrochemical Intercalation of Lithium into Graphite. *Z. Für Naturforschung A* **58**, 306–312 (2003).

276. Sato, K., Saito, S., Yanase, S. & Oi, T. Estimation of Reduced Partition Function Ratios of Lithium-Graphite Intercalation Compounds by Density Functional Theory. *Z. Für Naturforschung A* **69**, 122–128 (2014).

277. Li, X., Zhu, Y., Tan, S. & Xin, S. Isotope Effects in a Li–S Battery: A New Concept. *Batter. Supercaps* 7, e202300572 (2024).

278. Barah, O. O., Natukunda, F., Bori, I. & Ukagwu, K. J. Mechanisms and modelling of diffusion in solids: a multiscale framework with industrial case studies and AI enhancements. *Discov. Sustain.* **6**, 804 (2025).

279. Wang, H. *et al.* Internal pressure regulation enables reliable electrochemical performance evaluation of lithium-ion full coin cell. *J. Power Sources* **600**, 234235 (2024).

280. Müller, V., Scurtu, R.-G., Memm, M., Danzer, M. A. & Wohlfahrt-Mehrens, M. Study of the influence of mechanical pressure on the performance and aging of Lithium-ion battery cells. *J. Power Sources* **440**, 227148 (2019).

ABSTRACT

In the current climate context, significant challenges related to modes of transport and energy consumption are growing. E-mobility is one of the strategies envisaged to reduce greenhouse gas emissions; however, numerous challenges are associated with its deployment. In this regard, Li-ion batteries have established themselves as a technological pillar, providing high energy densities but suffering from limited power densities. This technological bottleneck restricts access to ultra-fast charging, with the objective of charging an electric vehicle to 80% of its capacity in less than 10 minutes, thereby achieving competitiveness with refuelling internal combustion vehicles. This power limitation primarily originates from the graphite electrode, which widely dominates the negative electrode market.

The work presented in this PhD thesis aims to determine the origin of the kinetic limitations of the graphite electrode, as well as to propose strategies to enhance its power properties. In an initial study combining electrochemical and structural characterisations *via* X-ray diffraction, a current understanding of graphite lithiation mechanisms is proposed, with particular emphasis on the formation of the LiC_6 phase (first stage of intercalation). Building on these initial results, a graphite electrode engineering study is presented to identify the origin of the electrode's power limitations. By correlating electrochemical and *in operando* structural analyses with the microstructure of the electrodes at the European Synchrotron Radiation Facility (ESRF) in Grenoble, lithium-ion diffusion through electrode porosity was identified as the limiting factor. This study particularly highlights the critical impact of ionic tortuosity on the power performance of graphite electrodes. An important aspect of graphite lithiation is also the evolution of the electrode's mechanical properties during cycling. This topic is addressed in the fifth chapter, in which the use of ultrasound waves as a probe for mechanical properties is discussed on a commercial NMC811 | graphite cell. These results are supported by a dilatometry study capturing the dynamic volumetric evolution of the electrodes. Finally, leveraging the conclusions drawn in the preceding chapters, an innovative strategy is proposed to improve the power properties of graphite electrodes. Based on the use of 6Li isotope, the concept relies on enhancing lithium transport kinetics through a 14% reduction in isotopic mass.

RÉSUMÉ

Face au contexte climatique actuel, d'important enjeux liés aux modes de déplacements et de consommation d'énergie grandissent. L'E-mobilité est une des stratégies envisagées afin de réduire les émissions de gaz à effet de serre, mais de nombreux challenges sont associés à ce développement. A ce sujet, les batteries Li-ion se sont imposées comme un pilier technologique fournissant d'importantes densités d'énergie, mais souffrant de densités de puissance limitées. Ce verrou technologique limite l'accès à la charge ultra-rapide, avec comme objectif de pouvoir charger un véhicule électrique en moins de 10 minutes à hauteur de 80% de capacité afin d'être compétitif avec le plein des véhicules thermiques. Cette limitation en puissance provient majoritairement de l'électrode de graphite qui domine largement le marché des électrodes négatives.

Les travaux de cette thèse visent à déterminer l'origine des limitations cinétiques de l'électrode de graphite, ainsi que de proposer des stratégies d'amélioration de ses propriétés de puissance. Dans une première étude combinant caractérisations électrochimiques et structurelles par diffraction des rayons X, une vision actuelle des mécanismes de lithiation du graphite est proposée, notamment concernant la formation de la phase LiC6 (stade premier d'intercalation). Sur la base de ces premiers travaux, une étude de l'ingénierie de l'électrode de graphite est présentée afin d'identifier l'origine des limitations en puissance de l'électrode. En corrélant des analyses électrochimiques et structurelles *in operando* à la microstructure des électrodes au synchrotron de Grenoble (ESRF), la diffusion des ions lithium à travers la porosité des électrodes a été identifiée comme facteur limitant. Cette étude met notamment en avant l'impact crucial de la tortuosité ionique dans les performances en puissance des électrodes de graphite. Un aspect important de la lithiation du graphite est également l'évolution des propriétés mécaniques de l'électrode pendant le cyclage. Ce sujet est abordé dans le cinquième chapitre, dans lequel l'utilisation d'ondes ultrasons comme sonde des propriétés mécaniques est discutée sur une cellule commerciale NMC811 | graphite. Ces résultats sont appuyés d'une étude par dilatométrie, capturant la dynamique d'évolution volumique des électrodes. Enfin, prenant avantage des conclusions tirées dans les chapitres précédents, une stratégie innovante est proposée afin d'améliorer les propriétés de puissance des électrodes de graphite. Basée sur l'utilisation d'isotope de 6Li, le concept repose sur l'augmentation des cinétiques de transport du lithium grâce à une masse isotopique réduite de 14%.